

© 2013 by Enric Xargay Mata. All rights reserved.

TIME-CRITICAL COOPERATIVE PATH-FOLLOWING CONTROL
OF MULTIPLE UNMANNED AERIAL VEHICLES

BY

ENRIC XARGAY MATA

DISSERTATION

Submitted in partial fulfillment of the requirements
for the degree of Doctor of Philosophy in Aerospace Engineering
in the Graduate College of the
University of Illinois at Urbana-Champaign, 2013

Urbana, Illinois

Doctoral Committee:

Prof. Naira Hovakimyan, Chair
Prof. Tamer Başar
Prof. Geir E. Dullerud
Prof. Isaac Kaminer
Prof. P.R. Kumar
Prof. Petros G. Voulgaris
Dr. Kevin A. Wise

Abstract

This thesis addresses the problem of steering a fleet of unmanned aerial vehicles (UAVs) along desired 3D spatial paths while meeting stringent relative temporal constraints. A representative example is the challenging mission scenario where the UAVs are tasked to cooperatively execute collision-free maneuvers and arrive at their final destinations at the same time, or at different times so as to meet a desired inter-vehicle schedule. In the proposed framework, the UAVs are assigned nominal spatial paths and speed profiles along those, and then the vehicles are requested to execute cooperative path following, rather than “open-loop” trajectory-tracking maneuvers. This strategy yields robust behavior against external disturbances by allowing the UAVs to negotiate their speeds along the paths in response to information exchanged over a supporting inter-vehicle communications network.

The proposed approach addresses explicitly the situation where each vehicle transmits coordination-relevant information to only a subset of the other vehicles, as determined by the time-varying communications topology. Furthermore, the thesis considers the case where the graph that captures the underlying communications topology is disconnected during some interval of time or even fails to be connected at all times. Conditions are given under which the complete time-critical cooperative path-following closed-loop system is stable and yields convergence of a conveniently defined cooperation error to a neighborhood of the origin. The thesis also derives lower bounds on the convergence rate of the coordination dynamics as a function of the quality of service of the supporting network, and proposes a coordination algorithm to improve the rate of convergence of the coordination dynamics in low-connectivity scenarios. Moreover, motivated by the exchange of information over networks with finite-rate communication links, the effect of quantization on vehicle coordination is also analyzed. Simulation and flight-test results verify the theoretical findings and demonstrate the efficacy of the multi-vehicle cooperative control framework adopted in this thesis.

Acknowledgments

First and foremost, I would like to express my profound gratitude to my adviser, Prof. Naira Hovakimyan, for her guidance, support, and encouragement throughout my PhD studies. Her constant drive for intellectual rigor, critical thinking, scholarly excellence, and academic integrity has been a source of inspiration all these years. My special thanks go to Prof. Isaac Kaminer for exciting discussions and invaluable advice during the course of my research. Prof. Kaminer's knowledge, vision, and creative thinking have always impressed me, ever since our first meeting in Torino back in 2006. I am deeply grateful to Prof. António M. Pascoal for his generous support, encouragement, and keen sense of perfection and elegance. I am also indebted to Prof. Vladimir Dobrokhodov for many insightful discussions and helpful comments on the practical aspects of this work. It has been a privilege and a pleasure to work with these four wonderful people, and I can only wish that we keep working together on exciting challenges in the years to come.

I am also grateful to Prof. Tamer Başar, Prof. Geir E. Dullerud, Prof. P.R. Kumar, Prof. Petros G. Voulgaris, and Dr. Kevin A. Wise for having kindly agreed to serve as members of my doctoral committee, and for giving me solid advice and constructive criticism on how to shape and improve my work. I am particularly thankful to Dr. Wise for sharing (always within confidentiality limits) his knowledge and insights on multi-vehicle cooperative motion control, aircraft dynamics, and flight control system design.

I would also like to acknowledge several other brilliant scholars and researchers from whom I received invaluable help and support throughout these years: Prof. Chengyu Cao, Dr. Reza Ghachcheloo, Prof. A. Pedro Aguiar, Dr. Irene M. Gregory, Prof. Giulio Avanzini, Prof. Roberto Tempo, Prof. Ramon Costa, and Dr. Lena Valavani. I would also like to thank Dapeng Li and Ronald Choe for many useful technical discussions as well as the friendship we have shared. Thanks also go to all other (past and present) officemates in MEB 349–351 for creating a pleasant and challenging working atmosphere.

Finally, I would like to thank my parents, Enric and Elvira, for their unconditional dedication, love, and support. *Gràcies pels valors que m'heu sabut transmetre i per estar al meu costat durant tots aquests anys. Mai no us podré estar prou agrair!*

* This work was supported in part by the Air Force Office of Scientific Research, the Office of Naval Research, and the Army Research Office.

Contents

List of Figures	vi
Notation, Symbols, and Acronyms	viii
Chapter 1 Introduction	1
1.1 Time-Critical Cooperative Missions	1
1.2 Motivational Mission Scenario: Cooperative Road Search	3
1.3 Related Work	4
1.3.1 Path-Following Control	4
1.3.2 Coordinated Path-Following Control	6
1.3.3 Consensus and Synchronization of Networks	7
1.4 Overview and Statement of Contributions	9
Chapter 2 General Framework and Problem Formulation	11
2.1 General Framework	11
2.2 Problem Formulation	12
2.2.1 Cooperative Trajectory Generation	12
2.2.2 Following a Virtual Target Vehicle on the Path	18
2.2.3 Time-Critical Coordination and Communications Constraints	25
2.2.4 Autonomous Vehicle with Autopilot	28
Chapter 3 3D Path-Following Control	31
3.1 Path-Following Control Law	31
3.1.1 Nonlinear Control Design using Vehicle Kinematics	31
3.1.2 Stability Analysis for Non-Ideal Inner-Loop Tracking	34
3.2 Implementation Details	35
3.3 Simulation Results	36
Chapter 4 Time-Critical Coordination	45
4.1 Coordination Control Law	45
4.1.1 Speed Control using Vehicle Kinematics	45
4.1.2 Convergence Analysis for Non-Ideal Inner-Loop Tracking	49
4.2 Combined Path Following and Time-Critical Coordination	51
4.2.1 Stability Analysis at the Kinematic Level	52
4.2.2 Stability Analysis with Inner-loop Autopilots	54
4.3 Implementation Details	56
4.4 Simulation Results	57
4.4.1 Path Following with Simultaneous Arrival	58
4.4.2 Sequential Auto-Landing	64

Chapter 5 Time-Critical Coordination under Quantization	70
5.1 Convergence with Quantized Information	70
5.1.1 Coordination Control Law and Coordination Dynamics	70
5.1.2 Krasovskii Equilibria	72
5.1.3 Stability Analysis at the Kinematic Level	74
5.1.4 Coordination with Fully Quantized Information	75
5.2 Simulation Results	77
Chapter 6 Time-Critical Coordination under Low Connectivity	82
6.1 Local Estimators and Topology Control	82
6.1.1 Estimator Dynamics	83
6.1.2 Coordination Control Law and Link-Weight Dynamics	84
6.2 Simulation Results	87
Chapter 7 Flight Tests: Cooperative Road Search	95
7.1 Road Search with Multiple Small Tactical UAVs	95
7.1.1 Airborne System Architecture	95
7.1.2 Flight-Test Results	97
7.2 Flight-Test Summary and Accessory Mission Outcomes	104
Chapter 8 Conclusions and Future Work	107
8.1 Conclusions	107
8.2 Future Work	108
Appendices	111
Appendix A The <i>Hat</i> and <i>Vee</i> Maps	112
Appendix B Coordination Dynamics	113
B.1 Time-Derivative of the Coordination States	113
B.2 The Coordination Projection Matrix	114
B.3 Closed-loop Coordination Error Dynamics	115
Appendix C Proofs	116
C.1 Proof of Lemma 1	116
C.2 Proof of Lemma 2	119
C.3 Proof of Lemma 3	122
C.4 Proof of Lemma 4	127
C.5 Proof of Theorem 1	128
C.6 Proof of Theorem 2	129
C.7 Proof of Lemma 5	133
C.8 Proof of Proposition 1	134
C.9 Proof of Theorem 3	135
C.10 Proof of Lemma 6	137
References	141

List of Figures

1.1	Cooperative road search using multiple UAVs	3
2.1	Conceptual architecture of the cooperative control framework adopted	13
2.2	Trajectory generation; collision avoidance in space	15
2.3	Trajectory generation; collision avoidance in time	16
2.4	Trajectory generation; arrival margin	17
2.5	Following a virtual target vehicle; problem geometry	19
2.6	Shaping the approach to the path	22
2.7	Inner-loop control structure with an adaptive augmentation loop	30
3.1	Path-following closed-loop system for a single vehicle solved at the kinematic level	32
3.2	Effect of the characteristic distance d on the convergence of the vehicle to the path	33
3.3	Path-following closed-loop system for a single vehicle	34
3.4	Framed 3D spatial path and main geometric properties	38
3.5	Path following of a single UAV	39
3.6	Path-following performance related to Fig. 3.5	40
3.7	Path following of a single UAV; <i>fast</i> convergence to the path ($d = 50$ m)	41
3.8	Path-following performance related to Fig. 3.7	42
3.9	Path following of a single UAV; <i>slow</i> convergence to the path ($d = 250$ m)	43
3.10	Path-following performance related to Fig. 3.9	44
3.11	Projection of versor $\hat{\mathbf{w}}_1$ onto the tangent versor to the path $\hat{\mathbf{t}}$	44
4.1	Time-critical cooperative path-following closed-loop for a single vehicle	52
4.2	Network topologies	57
4.3	Simultaneous arrival; 3D time-trajectories	59
4.4	Simultaneous arrival; path deconfliction	60
4.5	Simultaneous arrival; mission evolution	61
4.6	Simultaneous arrival; path-following performance	62
4.7	Simultaneous arrival; time-critical coordination	63
4.8	Simultaneous arrival; information flow	63
4.9	Sequential auto-landing; 3D time-trajectories	65
4.10	Sequential auto-landing; trajectory deconfliction	66
4.11	Sequential auto-landing; mission evolution	67
4.12	Sequential auto-landing; path-following performance	68
4.13	Sequential auto-landing; time-critical coordination	69
4.14	Sequential auto-landing; information flow	69
5.1	Sequential auto-landing; partially quantized control law with fine quantization	78
5.2	Sequential auto-landing; fully quantized control law with fine quantization	79
5.3	Sequential auto-landing; partially quantized control law with coarse quantization	80
5.4	Sequential auto-landing; fully quantized control law with coarse quantization	81

6.1	Extended network with local estimators.	85
6.2	Edge snapping; two-well function and forcing function for link-weight dynamics.	88
6.3	Convergence time with three different coordination algorithms.	90
6.4	Histograms and distribution fits of the normalized convergence time.	90
6.5	Sequential auto-landing; modified coordination control law (hybrid strategy).	91
6.6	Sequential auto-landing; information flow.	91
6.7	Sequential auto-landing; link weights and local connectivity (hybrid strategy).	92
6.8	Sequential auto-landing; modified coordination control law (edge snapping).	93
6.9	Sequential auto-landing; information flow.	93
6.10	Sequential auto-landing; link weights and local connectivity (edge snapping).	94
7.1	SIG Rascal UAV with two different onboard cameras.	96
7.2	Network-centric architecture of the airborne platform.	96
7.3	Cooperative road-search; trajectory generation.	99
7.4	Cooperative road-search; time-coordination during the transition phase.	100
7.5	Cooperative road-search; cooperative path-following control during the road-search phase.	101
7.6	Cooperative road-search; mission performance.	102
7.7	Cooperative road-search; coordinated vision-based target tracking.	103
7.8	Time-critical cooperation in a road-search mission.	104
7.9	High-resolution image exploitation.	106

Notation, Symbols, and Acronyms

\mathbb{R}	Field of real numbers.
\mathbb{Z}	Set of all integers.
$\text{SO}(3)$	Special orthogonal group of all rotations about the origin of three-dimensional Euclidean space \mathbb{R}^3 .
$\mathfrak{so}(3)$	Set of 3×3 skew-symmetric matrices over \mathbb{R} .
\mathbb{I}_n	Identity matrix of size n .
$\mathbf{0}$	Zero matrix of appropriate dimension.
$\mathbf{1}_n$	Vector of \mathbb{R}^n whose components are all 1.
$\{\mathcal{F}\}$	Reference frame.
$\{\mathbf{v}\}_F$	Vector \mathbf{v} resolved in frame $\{\mathcal{F}\}$.
$\{\hat{\mathbf{e}}\}_F$	Versor $\hat{\mathbf{e}}$ resolved in frame $\{\mathcal{F}\}$.
$\boldsymbol{\omega}_{F1/F2}$	Angular velocity of frame $\{\mathcal{F}1\}$ with respect to frame $\{\mathcal{F}2\}$.
R_{F1}^{F2}	Rotation matrix from frame $\{\mathcal{F}1\}$ to frame $\{\mathcal{F}2\}$.
$\dot{\mathbf{v}}]_F$	Time-derivative of vector \mathbf{v} taken in frame $\{\mathcal{F}\}$.
\mathbf{v}^\top	Transpose of vector \mathbf{v} .
$\ \mathbf{v}\ $	2-norm of vector \mathbf{v} .
$\ \mathbf{v}\ _\infty$	∞ -norm of vector \mathbf{v} .
\mathbf{M}^\top	Transpose of matrix \mathbf{M} .
$\det(\mathbf{M})$	Determinant of matrix \mathbf{M} .
$\text{tr}[\mathbf{M}]$	Trace of matrix \mathbf{M} .
$\lambda_{\max}(\mathbf{M})$	Maximum eigenvalue of matrix \mathbf{M} .
$\lambda_{\min}(\mathbf{M})$	Minimum eigenvalue of matrix \mathbf{M} .
$\ \mathbf{M}\ $	Induced 2-norm of matrix \mathbf{M} .
$\text{card}(\mathcal{S})$	Cardinality of set \mathcal{S} .
$K(\cdot)$	Krasovskii operator.
$\text{co } \mathcal{S}$	Convex hull of set \mathcal{S} .

$\text{sat}(\cdot)$	The saturation function.
$(\cdot)^\wedge$	The <i>hat map</i> . (See Appendix A.)
$(\cdot)^\vee$	The <i>vee map</i> . (See Appendix A.)

♠	End of definition.
◊	End of corollary, lemma, proposition, or theorem.
□	End of proof.
△	End of remark.

CVBTT	Coordinated Vision-Based Target Tracking.
DoD	Department of Defense.
Dof	Degree of Freedom.
FoV	Field of View.
ISS	Input-to-State Stable.
LoS	Line of Sight.
MANET	Mobile Ad-hoc Network.
NPS	Naval Postgraduate School.
PE	Persistency of Excitation.
QoS	Quality of Service.
UAV	Unmanned Aerial Vehicle.

Calligraphic, upper-case letters enclosed within curly brackets are used to denote reference frames (e.g. $\{\mathcal{F}\}$). Unless otherwise noted, bold-face, lower-case letters refer to column vectors (e.g. \mathbf{v}), while bold-face, capital letters refer to matrices (e.g. \mathbf{M}). In general, the i th component of vector \mathbf{v} is denoted by v_i , and the (i, j) entry of matrix \mathbf{M} is represented by M_{ij} . The cross product of two vectors \mathbf{v} and \mathbf{w} is denoted by $\mathbf{v} \times \mathbf{w}$, while their dot product is denoted by $\mathbf{v} \cdot \mathbf{w}$.

Chapter 1

Introduction

1.1 Time-Critical Cooperative Missions

The advent of powerful embedded systems, sensors, and communications networks has drawn widespread interest in the use of unmanned aerial vehicles (UAVs) to execute missions with limited involvement of human operators. In recent years, UAVs have been playing an increasingly important role in military reconnaissance and strike operations, border patrol missions, aerobiological sampling, forest fire detection, police surveillance, and recovery operations, to name but a few. In simple applications, a single vehicle can be managed by a crew using a ground station provided by the vehicle manufacturer. The execution of more challenging missions, however, requires the use of multiple UAVs working in cooperation to achieve a common objective. In such missions, a team of vehicles connected by means of a communications network must meet stringent spatial and temporal constraints, while possibly maneuvering in close proximity to each other. In general, success of these multi-vehicle cooperative missions depends on the ability of the fleet to exchange information in a timely and reliable manner and, therefore, the quality of service (QoS) of the supporting network becomes a factor of major importance. In addition, as pointed out in [49] and [55], in many scenarios the flow of information among vehicles may be severely restricted, either for security reasons or because of tight bandwidth limitations. As a consequence, no vehicle may be able to communicate with the entire fleet and, moreover, the amount of information that can be exchanged may be limited. Under these circumstances, a key enabling element for the effective execution of multi-UAV missions is thus the availability of cooperative motion-control strategies that can yield robust performance in the face of external disturbances and communications limitations, while ensuring at the same time collision-free maneuvers.

The range of relevant, related topics addressed in literature includes parallel computing [101], synchronization of oscillators [84, 85, 90], study of collective behavior and flocking [15, 48], multi-system consensus mechanisms [64], multi-vehicle system formations [29, 30, 35, 75], coordinated motion control [6, 42, 53, 97], cooperative path and trajectory planning [57, 66, 78, 88, 89], asynchronous protocols [34], dynamic graphs [67, 70, 77, 99], and graph-related theory [18, 55]. Especially relevant are the applications of the

theory developed in the area of multi-vehicle control: spacecraft formation flying [9, 68, 86], UAV control [10, 51, 96, 100], coordinated control of land robots [42, 87], and control of multiple autonomous marine vehicles [7, 17, 37, 46, 47, 81, 93, 98]. In spite of significant progress in the field, much work remains to be done to develop strategies capable of providing guaranteed levels of performance in the presence of complex vehicle dynamics, communications constraints, and partial vehicle failures.

It is against this backdrop of ideas that this thesis addresses the problem of *steering a fleet of UAVs along desired spatial paths while meeting relative temporal constraints*. In particular, the cooperative missions considered require that each vehicle follow a feasible collision-free path, and that all vehicles arrive at their respective final destinations at the same time, or at different times so as to meet a desired inter-vehicle schedule. Representative examples of such *time-critical missions* are sequential auto-landing and coordinated ground target suppression. The first refers to the situation where a fleet of UAVs must break up and arrive at the assigned glide path separated by pre-specified safe-guarding time-intervals and maintain this separation as they fly along the glide slope. In the case of ground-target suppression, a formation of UAVs must also break up and execute a coordinated maneuver to arrive at predefined positions over the target at the same time. In both cases, only *relative*—rather than *absolute*—temporal constraints are given a priori, a critical point that needs to be emphasized.

To solve this problem, a framework for vehicle cooperation is proposed in this thesis that brings together concepts and tools from nonlinear control, algebraic graph theory, geometry, topology control, and estimation. The framework builds on the approach to multi-vehicle cooperative motion control developed in [60] and on some of the extensions that emerged out of this work, such as [51]. In the setup adopted, the vehicles are assigned nominal paths and speed profiles along those, obtained from an appropriately formulated optimization problem. The paths are judiciously parameterized, and the vehicles are requested to execute cooperative path following, rather than “open-loop” trajectory-tracking maneuvers. This strategy allows the vehicles to react to unforeseen off-nominal situations by negotiating their speeds along the paths in response to information exchanged over the supporting communications network. In particular, the work presented here analyzes the degradation in terms of mission performance caused by the presence of dynamic communications networks arising from temporary loss of communications links and switching communications topologies, and proposes distributed coordination algorithms for improved performance in low-connectivity scenarios. Furthermore, motivated by the exchange of information over networks with finite-rate communication links, it also analyzes the effect of quantization on vehicle coordination. To better root the exposition in practical applications, next section describes a mission scenario that motivates the use of a team of cooperating UAVs.

1.2 Motivational Mission Scenario: Cooperative Road Search

Today's operational environments face a growing need for up-to-date satellite-like imagery, with enough resolution to detect humans, weapons, and other potential threats. While accurate high-resolution imagery is traditionally provided by satellites and high-end aerial intelligence surveillance and reconnaissance platforms, these assets are not always available to the end-user due to time-of-day, visibility, or mission priority. In such cases, the use of small tactical UAVs outfitted with the ability to capture actionable, high-resolution, geo-referenced imagery and full motion video, represents an economical and expeditious alternative. Moreover, the fact that the UAVs can deliver the information to the end-user in seconds or minutes, rather than hours or days, can potentially revolutionize future DoD operations.

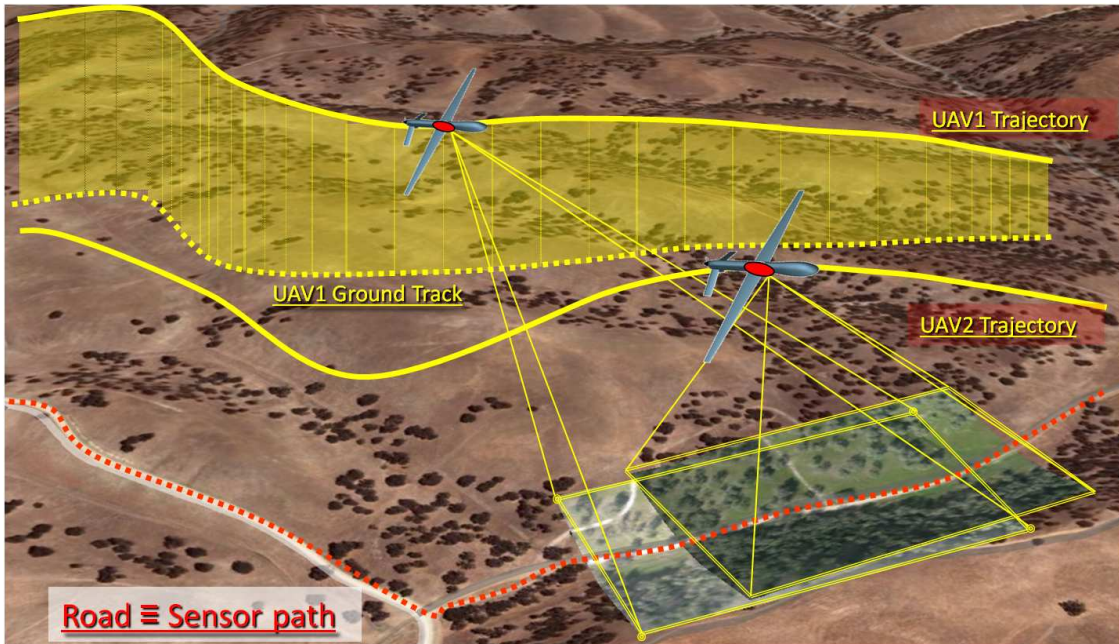


Figure 1.1: Cooperative road search using multiple UAVs. Two small tactical UAVs equipped with complementary vision sensors try to detect and identify an improvised explosive device along a road. Cooperative control can ensure a satisfactory overlap of the field-of-view footprints of the sensors along the road, thus increasing the probability of target detection.

One of the applications that motivates the use of multiple cooperative UAVs and poses several challenges to systems engineers, both from a theoretical and practical standpoint, is automatic road search for detection and identification of foes and improvised explosive devices; see Figure 1.1. The mission is initiated by a minimally trained user who scribbles a path on a digital map, generating a precise continuous ground-track for the airborne sensors to follow. This ground-track is then transmitted over the network to a fleet of small

tactical UAVs equipped with complementary visual sensors. A distributed optimization algorithm generates feasible collision-free flight trajectories that maximize road coverage and account for sensor capabilities—field of view, resolution, and gimbal constraints—as well as inter-vehicle and ground-to-air communications limitations. The fleet of UAVs starts then the cooperative road search. During this phase, the information obtained from the sensors mounted onboard the UAVs is shared over the network and retrieved by remote users in near real time. Target detection and identification can thus be done remotely on the ground, based on in-situ imagery data delivered over the network.

In this particular mission scenario, the advantages of using a cooperative group of autonomous vehicles connected by means of a mobile communications network—rather than a single, heavily equipped vehicle—can be immediately identified. In a cooperative scenario, the team can reconfigure the network in response to unplanned events as well as changing mission objectives, and optimize strategies for improved target detection and discrimination. The use of multiple vehicles also improves the robustness of the mission execution to a single-point system failure. Furthermore, in a multi-UAV approach, each vehicle of the team may be required to carry only a single sensor, making each of the vehicles in the fleet less complex, thus increasing overall reliability. This cooperative approach requires, however, a robust cooperative control algorithm for the fleet of UAVs that allows to effectively combine the capabilities of the onboard sensors. In fact, flying in a coordinated fashion is critical to maximize the overlap of the fields of view of multiple sensors while reliably maintaining a desired image resolution.

1.3 Related Work

1.3.1 Path-Following Control

The problem of path following can be briefly described as that of making a vehicle converge to and follow a desired spatial path, while tracking a desired speed profile that may be path dependent. The temporal and spatial assignments are therefore separated. Often, it is simply required that the speed of the vehicle be kept constant. Path-following control algorithms are pervasive in many robotic applications and are key to the operation of multiple vehicles undergoing cooperative missions.

There is a wealth of literature on path-following algorithms that defies a short summary. Pioneering work in the area can be found in [69], where an elegant solution to the problem of path-following control was presented for a wheeled robot at the kinematic level. In the setup adopted, the kinematic model of the vehicle is derived with respect to a Frenet-Serret frame moving along the path, while playing the role of a virtual target vehicle to be tracked by the real vehicle. The origin of the Frenet-Serret is placed at the point

on the path closest to the real vehicle.

The work in [69] spurred a great deal of activity in the literature addressing the path-following problem. A popular approach that emerged out of this research effort was to solve a trajectory-tracking problem and then reparameterize the resulting feedback controller using an independent variable other than time. See, for example, the work in [1, 5, 45] and references therein. The approach proposed in [69] was extended to UAVs with full account of its dynamics in [49], where the authors addressed the issue of path following of trimming trajectories and derived nonlinear path-following controllers that satisfy a linearization property. Related results can be found in [32] for autonomous underwater vehicles using a backstepping approach. A common feature of the latter papers is to reduce the path-following problem to that of driving the kinematic errors resolved in Frenet-Serret frame to zero. This approach ensures that path following is essentially done by proper choice of the vehicle's attitude, a strategy that is akin to that used by pilots when they fly airplanes. The same property does not necessarily hold in the case of the strategies that emerged out of the work in [1, 5, 45].

The setup used in [69] was later reformulated in [95] (and its journal version, [61]), leading to a feedback control law that steers the dynamic model of a wheeled robot along a desired path and overcomes some of the constraints present in [69]. The key to this algorithm is to explicitly control the rate of progression of the virtual target along the path. This approach effectively creates an extra degree of freedom that can be exploited to avoid the singularities that occur when the distance to the path is not well defined —this occurs, for example, when the vehicle is located exactly at the center of curvature of a circular path. Related strategies were exploited in the work in [91] and [94] on output maneuvering and also in the work in [26] and [31]. As will become clear, the path-following algorithm described in this thesis is an extension of the algorithm presented in [61] to the case of 3D spatial paths.

Other path-following methods have been presented in the literature that depart from the ideas and concepts of the algorithms described above. In [80], lateral acceleration commands are used to make a UAV converge to and follow planar curved paths. A nonlinear path-following method that generates acceleration commands to steer a holonomic vehicle towards a given 3D path is presented in [39]. Path-following algorithms based on the concept of vector fields can be found in [62] and [73]. Finally, the work reported in [82] and [83] presents an elegant approach to path following that uses Lagrange multipliers to derive path-following control laws for mechanical systems subject to both holonomic and nonholonomic constraints.

1.3.2 Coordinated Path-Following Control

The problem of coordinated path following amounts to making a fleet of vehicles converge to and follow a set of desired spatial paths, while meeting pre-specified spatial and temporal constraints. Over the last decade, there has been growing interest in the problem of coordinated path-following control of fleets of autonomous vehicles, mainly for the execution of cooperative marine missions involving multiple autonomous surface and underwater vehicles. Initial work in this topic can be found in [33, 60, 92, 93].

The coordinated path-following control problem was implicit in the early work in [33], where the authors built on and extended the single-vehicle “manoeuvre regulation” approach in [45], and presented a solution to the problem of coordinated operation of an autonomous surface vehicle and an autonomous underwater vehicle. The strategy adopted, however, requires the vehicles to exchange a large amount of information, and cannot be easily generalized to larger teams of vehicles. These drawbacks were later overcome in [60], which proposes a leader-follower cooperative approach that (almost) decouples the temporal and spatial assignments of the mission. The solution adopted is rooted in the results on path-following control of a single vehicle presented in [95], and takes advantage of the fact that, with this path-following algorithm, the speed profile of each vehicle becomes an additional degree of freedom that can be exploited for vehicle coordination. Moreover, in this setup, the two vehicles only need to exchange the (scalar) “along-path positions” of their virtual targets, which reduces drastically the amount of information to be exchanged among vehicles when compared to the solution developed in [33]. Interestingly, an approach similar to the one in [60] was proposed at approximately the same time in the work in [92] and [93], where a nonlinear control design method was presented for formation control of a fleet of ships. The approach relies on the maneuvering methodology developed in [94], which is then combined with a centralized guidance system that adjusts the speed profile of each vehicle so as to achieve and maintain the desired formation configuration. The maneuvering strategy in [94] was also exploited in [46], where a passivity framework is used to solve the problem of vehicle coordination and formation maneuvering.

In [40], the authors extended the approach in [60] and addressed the problem of steering a group of vehicles along predefined spatial paths while holding a desired (possibly time-varying) formation pattern. Using results from nonlinear systems and algebraic graph theory, conditions were derived under which the proposed algorithm solves the coordinated path-following control problem in the presence of switching communications topologies and network link latencies. In particular, stability of the closed-loop system was analyzed under two scenarios: first, networks with brief connectivity losses; and second, uniformly jointly connected communications graphs.

The approach in [60] was also extended in [51], where the authors addressed the problem of coordinated

control of multiple UAVs. To enforce the temporal constraints of the mission, the coordination algorithm relies on a distributed control law with a proportional-integral structure, which ensures that each vehicle travels along its path at the desired constant speed, and also provides disturbance rejection capabilities against steady winds. As will become clear, the approach for vehicle coordination described in this thesis is an extension of the algorithm presented in [51] to the case of arbitrary (feasible) desired speed profiles and multiple leaders.

Related work can also be found in [4], which proposes a multi-vehicle control architecture aimed at reducing the frequency at which information is exchanged among vehicles by incorporating logic-based communications. To this effect, the authors borrow from and expand some of the key ideas exposed in [104] and [105], where decentralized controllers for distributed systems are derived by using, for each system, its local state information together with estimates of the states of the systems that it communicates with.

Other relevant cooperative motion-control algorithms have been presented in the literature that address problems akin to that of coordinated path following. In [58] and [59], for example, synchronization techniques are used to develop control laws for ship rendezvous maneuvers. Also, the work in [30] presents a solution to the problem of coordinated path following for multi-agent formation control. In the setup adopted, a reference path is specified for a nonphysical point of the formation, which plays the role of a virtual leader, while a desired formation pattern is defined with respect to this nonphysical point. Control laws are then derived that ensure that the real vehicles converge to the desired reference points of the formation, while the virtual leader follows the reference path.

1.3.3 Consensus and Synchronization of Networks

As mentioned previously, this thesis aims to design algorithms that solve the time-critical cooperative missions described earlier in this chapter, as well as to analyze their stability and convergence properties in the presence of switching network topologies and quantized information exchange. To this effect, the thesis borrows tools from consensus and synchronization of networked systems. There is an extremely rich body of literature available in both these disciplines, and its discussion is well beyond the scope of this section. The reader is referred to [76] for an overview of consensus algorithms and their application to cooperative control of networked multi-agent systems, while a thorough review of the major concepts and results in the study of the structure and dynamics of complex networks is presented in [16]. In this section, instead, we will only give a brief overview of the work in these disciplines that is most directly and closely related to the developments in this thesis, namely, proportional-integral consensus protocols and quantized consensus.

Proportional-integral consensus protocols: As mentioned in the previous section, a distributed proportional-integral protocol is used in [51] to enforce the temporal constraints of cooperative missions involving multiple UAVs. The integral term in the consensus algorithm allows the follower vehicles to learn the (constant) reference speed from the leader, and provides disturbance rejection capabilities against steady winds. A generalization of a proportional-integral protocol is proposed in [8], where the authors develop an adaptive algorithm to reconstruct a time-varying reference velocity that is available only to a single leader. The paper uses a passivity framework to show that a network of nonlinear agents with fixed connected topology asymptotically achieves coordination. The work in [19] also uses a (discrete-time) proportional-integral consensus protocol to synchronize networks of clocks with fixed connected topology. In this application, the integral part of the controller is critical to eliminate the different initial clock offsets. A proportional-integral estimation algorithm is also proposed in [38] for dynamic average consensus in sensing networks. In particular, the paper analyzes the stability and convergence properties of the developed proportional-integral estimator, by deriving conditions on both constant and time-varying information flows that ensure stability of the estimator.

Quantized consensus: The exchange of information over networks with finite-rate communication links motivates the interest in quantized consensus problems. Most of the work on this topic has dealt with discrete-time dynamics; see, for example, [20, 52, 72] and references therein. Pioneering work in this area can be found in [52], where the authors analyze the distributed averaging problem on arbitrary connected graphs, and derive bounds on the expected convergence time of the collective dynamics for complete and linear networks. The results in [52] were later extended in [72] to the case of time-varying topologies. Interesting results on quantized consensus can also be found in [20], which proposes a protocol with which the network reaches consensus with arbitrarily small precision, at the expense, however, of slow convergence.

The continuous-time quantized averaging problem was studied in detail in [21], where it is proven that Carathéodory solutions might not exist for (continuous-time) quantized consensus problems, implying thus that a weaker concept of solution has to be considered. The work in [25] uses a passivity framework to extend the results in [21] to the case of agents with complex dynamics and advanced coordination tasks. Related work can also be found in [106], which investigates the multi-agent rendezvous problem under minimal sensing and actuation.

1.4 Overview and Statement of Contributions

The thesis is organized into six main chapters and has three appendices that contain definitions and derivations of intermediate results, as well as the proofs of the theoretical results. Next, we present a brief summary and thesis contributions by chapter:

- **Chapter 2** presents the framework for vehicle cooperation adopted in this thesis, and provides a rigorous formulation of the problem of time-critical cooperative path-following control of multiple UAVs in 3D space. The chapter also introduces a set of assumptions and constraints on the supporting communications network as well as on the autopilots mounted onboard the UAVs. The proposed approach builds upon the framework for cooperative path following developed in [60], and extends it to the case of 3D spatial paths and arbitrary (feasible) desired speed profiles. To this end, in the setup adopted, the path-following kinematic error dynamics of the vehicle are derived with respect to a *parallel transport frame* moving along the path. This approach is in contrast to other formulations of the problem of path-following control, which use a Frenet-Serret frame. Note that, unlike the Frenet-Serret frame, parallel transport frames are well defined when the path has a vanishing second derivative. In addition, the chapter also proposes a set of *coordination states* and *coordination maps* that allow to extend the cooperative path-following framework developed in [51] to the case of desired speed profiles that are path dependent.
- **Chapter 3** describes a path-following nonlinear control algorithm that uses vehicle angular rates to steer a UAV along a 3D spatial path for an arbitrary feasible temporal assignment along the path. Controller design builds on previous work on path-following control of small tactical UAVs, reported in [50], and puts forward a new algorithm that uses the special orthogonal group $\text{SO}(3)$ in the formulation of the attitude-control problem. This formulation avoids the geometric singularities and complexities that appear when dealing with local parameterizations of the vehicle's attitude and thus leads to a singularity-free path-following control law.
- **Chapter 4** presents a strategy for time-critical coordination of multiple UAVs that relies on the adjustment of the speed profile of each vehicle based on coordination information exchanged over a supporting communications network. This cooperative strategy was presented in [51] (and later modified in [3]) for the case of constant desired speed profiles, and stability results were derived for networks with topologies connected pointwise in time. In this thesis, the distributed proportional-integral coordination control law proposed in [51] is further modified to account for path-dependent desired speed profiles and include multiple fleet leaders. Moreover, in the setup adopted, the graph

that captures the underlying communications network topology is allowed to be disconnected during some interval of time or may even fail to be connected at all times. The chapter also borrows tools from nonlinear control and algebraic graph theory to derive lower bounds on the convergence rate of the coordination error dynamics as a function of the level of connectivity of the dynamic communications network and the number of leaders.

- Motivated by the use of networks with finite-rate communication links, **Chapter 5** analyzes the effect of quantization on the stability and convergence properties of the closed-loop coordination dynamics. The results in this chapter show that, depending on the design of the quantized coordination control law, the closed-loop kinematic coordination error dynamics have undesirable “zero-speed” attractors. A modification of the coordination control law presented in Chapter 4 is proposed that, for the case of connected network topologies and sufficiently fine quantization, retains the origin as the only equilibria on the system and prevents the existence of “zero-speed” equilibria.
- **Chapter 6** proposes a modification of the coordination control law introduced in Chapter 4, which is intended to improve the convergence rate of the closed-loop coordination dynamics in *low-connectivity scenarios*. The proposed approach, which borrows and expands tools and concepts from control of complex networks and logic-based communication protocols, leads to an evolving extended network, whose topology depends on the local exchange of information among nodes. While we have—as of now—no theoretical guarantee that the modified coordination algorithm improves the convergence rate of the coordination dynamics, the chapter provides numerical evidence suggesting that the coordination error state converges to a neighborhood of the origin in a shorter time.
- **Chapter 7** presents flight-test results for a cooperative road-search mission that show the efficacy of the multi-UAV cooperative framework presented in this thesis. The significance of these field experiments is twofold. First, the results verify the main stability and convergence properties of the developed cooperative algorithms in a realistic mission scenario, under environmental disturbances and with the limitations of a real-world communications network. And second, the results demonstrate the validity of the proposed generic theoretical framework in a specific realistic application as well as the feasibility of the onboard implementation of the algorithms. These flight tests were conducted in collaboration with Isaac Kaminer and Vladimir Dobrokhotov from the Naval Postgraduate School.

Chapter 2

General Framework and Problem Formulation

This chapter presents the framework for vehicle cooperation adopted in this thesis, and provides a rigorous formulation of the problem of time-critical cooperative path-following control of multiple UAVs in 3D space, in which a fleet of UAVs is tasked to converge to and follow a set of desired feasible paths so as to meet spatial and temporal constraints. The chapter also introduces a set of assumptions and constraints on the supporting communications network as well as on the autopilots mounted onboard the UAVs.

2.1 General Framework

The methodology adopted in this work, which was initially proposed in [60], is based on the key idea of *decoupling space and time*, and can be summarized in three basic steps. First, given a multi-vehicle cooperative mission, a set of feasible spatial paths together with a set of feasible speed profiles is generated for all the vehicles involved in the mission. This step relies on optimization methods that take explicitly into account initial and final boundary conditions, a general performance criterion to be optimized, simplified vehicle dynamics, safety rules for collision avoidance, as well as mission-specific constraints. The second step consists of making each vehicle converge to and follow its assigned path, regardless of what the desired speed profile is, as long as the latter is physically feasible. This approach takes advantage of the separation in space and time introduced during trajectory generation, and leaves the speed profile of the vehicle as an additional degree of freedom to be exploited at the time-coordination level. In this sense, path-following control is in contrast to trajectory tracking, for which it is proven in [2] that, in the presence of unstable zero dynamics, there exist fundamental performance limitations that cannot be overcome by any controller structure. Finally, in the third step, the speed of each vehicle is adjusted about its desired speed profile to enforce the temporal constraints that must be met to coordinate the fleet of vehicles. This last step relies on the underlying communications network as a means to exchange information among vehicles.

Another key feature of the framework presented in [60] and adopted in this thesis is that it exhibits a *multiloop control structure* in which an inner-loop controller stabilizes the vehicle dynamics, while a guid-

ance outer-loop controller is designed to control the vehicle kinematics, providing path-following and time-coordination capabilities. To make these ideas more precise, we notice that a typical autonomous vehicle can be modeled as a cascade system consisting of the kinematic and dynamic equations of the vehicle. Following standard notation, the kinematics \mathcal{G}_k of the vehicle can be represented as

$$\mathcal{G}_k : \quad \dot{\mathbf{x}}(t) = \mathbf{f}(\mathbf{x}(t)) + \mathbf{g}(\mathbf{x}(t))\mathbf{y}(t), \quad (2.1)$$

where $\mathbf{x}(t)$ denotes the kinematic state of the vehicle, which usually includes vehicle's position and attitude, $\mathbf{y}(t)$ represents the vector of variables driving the vehicle kinematics, such as vehicle angular and linear velocities, and $\mathbf{f}(\cdot)$ and $\mathbf{g}(\cdot)$ are known nonlinear functions. The dynamics \mathcal{G}_d of the vehicle can be expressed as

$$\mathcal{G}_d : \quad \begin{cases} \dot{\mathbf{z}}(t) &= \mathbf{h}(\mathbf{z}(t), \mathbf{u}(t), t) \\ \mathbf{y}(t) &= \mathbf{h}_o(\mathbf{z}(t), \mathbf{u}(t), t) \end{cases}, \quad (2.2)$$

where $\mathbf{z}(t)$ denotes the dynamic state of the vehicle, $\mathbf{u}(t)$ represents the control signal that drives the vehicle dynamics, and $\mathbf{h}(\cdot)$ and $\mathbf{h}_o(\cdot)$ are partially known nonlinear functions. The model above is sufficiently general to capture six-degree-of-freedom (6DoF) dynamics, together with plant uncertainty. The cooperative control algorithms presented in this thesis are derived at the kinematic level for the system \mathcal{G}_k in (2.1) and are viewed as guidance outer-loop controllers that provide reference commands to an inner-loop controller. The latter is designed to stabilize the dynamics \mathcal{G}_d in (2.2) and to ensure that the vehicle tracks the outer-loop commands. This inner/outer loop approach simplifies the design process and affords the designer a systematic approach to seamlessly tailor the algorithms for a very general class of vehicles that come equipped with inner-loop commercial autopilots. The conceptual architecture of the complete solution is shown in Figure 2.1.

2.2 Problem Formulation

2.2.1 Cooperative Trajectory Generation

Given a cooperative mission of interest involving n vehicles, the problem of *cooperative trajectory generation* can be defined as follows:

Definition 1 (Cooperative Trajectory-Generation Problem) *Find a set of n 3D time-trajectories $\mathbf{p}_{d,i} : [0, t_d^*] \rightarrow \mathbb{R}^3$, conveniently parameterized by a single time-variable $t_d \in [0, t_d^*]$, that together minimize a given cost function, satisfy desired boundary conditions, do not violate dynamic constraints of the vehicles, ensure that the vehicles maintain a predefined spatial clearance, and satisfy pre-specified mission-specific constraints.*



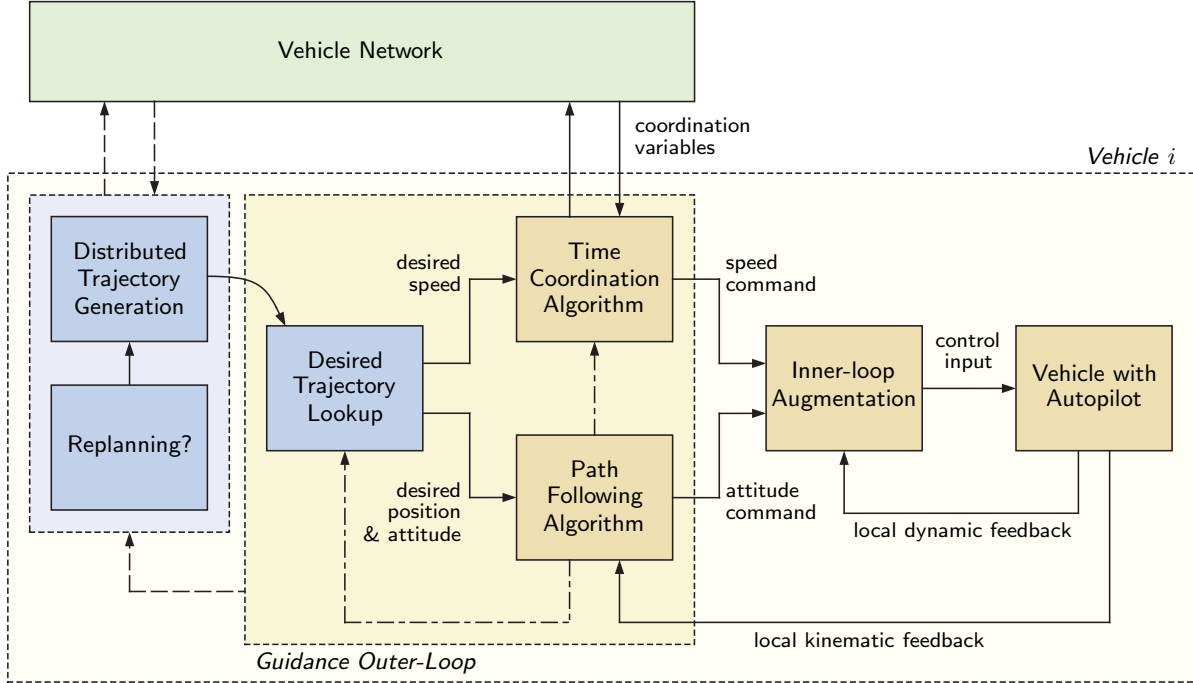


Figure 2.1: Conceptual architecture of the cooperative control framework adopted.

In this formulation, the variable t_d represents a *desired mission time*, with t_d^* being the *desired mission duration*. For a given t_d , $\mathbf{p}_{d,i}(t_d)$ defines the desired position of the i th vehicle t_d seconds after the initiation of the cooperative mission. The variable t_d is used during the trajectory-generation phase and is distinct from the actual mission time that evolves as the mission unfolds. As will become clear later, it is sometimes convenient to reparameterize these time-trajectories in terms of *path length* to obtain *spatial paths* $\mathbf{p}_{d,i}(\tau_{\ell,i}) : [0, \ell_{fi}] \rightarrow \mathbb{R}^3$, dropping thus the temporal specifications of the mission. Spatial paths are parameterized by their path length $\tau_{\ell,i}$, $i = 1, \dots, n$, with ℓ_{fi} denoting the total length of the i th path. Path length and desired mission time are related through the relation

$$\tau_{\ell,i} = \int_0^{t_d} v_{d,i}(\sigma) d\sigma,$$

where $v_{d,i}(t_d) : [0, t_d^*] \rightarrow \mathbb{R}$ represents the desired speed profile along the i th path. With this notation, we next formulate the problem of cooperative trajectory generation to compute feasible trajectories for multiple autonomous vehicles that satisfy collision-avoidance constraints.

Feasible Trajectory Generation for a Single Vehicle

Before formulating the cooperative trajectory-generation problem for multiple vehicles, we first address the problem of generating a feasible trajectory for a single vehicle. In the context of this thesis, we define a *feasible trajectory* as the one that satisfies maximum curvature, torsion, and flight-path-angle bounds, and it can be followed by a vehicle without having it exceed pre-specified bounds on the vehicle desired speed $v_{d,i}(t_d)$ and desired acceleration $a_{d,i}(t_d)$. Letting $v_{d\min}$, $v_{d\max}$, $a_{d\max}$, $\kappa_{d\max}$, $\tau_{d\max}$, $\gamma_{d\min}$, and $\gamma_{d\max}$ denote predefined bounds on the vehicle's velocity, acceleration, path curvature, torsion, and flight path angle, the trajectory $\mathbf{p}_{d,i}(t_d)$ is said to be feasible if the conditions

$$0 < v_{d\min} \leq v_{d,i}(t_d) \leq v_{d\max}, \quad |a_{d,i}(t_d)| \leq a_{d\max}, \quad (2.3a)$$

$$|\kappa_{d,i}(\tau_{\ell,i})| \leq \kappa_{d\max}, \quad |\tau_{d,i}(\tau_{\ell,i})| \leq \tau_{d\max}, \quad \gamma_{d\min} \leq \gamma_{d,i}(\tau_{\ell,i}) \leq \gamma_{d\max}, \quad (2.3b)$$

are met for all $t_d \in [0, t_d^*]$ and all $\tau_{\ell,i} \in [0, \ell_{fi}]$.

A feasible trajectory for the i th vehicle can thus be obtained by solving, for example, the optimization problem

$$\min_{\Xi_i} J(\cdot)$$

subject to initial and final boundary conditions as well as the feasibility conditions in (2.3). In the problem above, $J(\cdot)$ is a given cost function and Ξ_i represents the vector of optimization parameters for the trajectory $\mathbf{p}_{d,i}(t_d)$. The cost function $J(\cdot)$ may include terms related to mission-specific goals, while additional constraints can also be added to account for vehicle-to-ground communications limitations, sensory capabilities, collision avoidance with obstacles, and no-fly zones.

Feasible Collision-Free Trajectory Generation for Multiple Vehicles

We now formulate the problem of cooperative trajectory generation for multiple vehicles. In particular, the time-critical missions described in this article require that each vehicle follow a collision-free trajectory, and that all vehicles arrive at their respective destinations at the same time, or at different times so as to meet a desired inter-vehicle schedule. Without loss of generality, we consider in this section the problem of simultaneous arrival. For these missions, the generation of collision-free trajectories can be addressed using two complementary approaches. The first one, referred to as *collision avoidance in space*, ensures that no feasible paths intersect. Alternatively, the second approach —*collision avoidance in time*— implies that no two vehicles are at the same place at the same time. The first approach may be particularly useful in military applications, where jamming prevents vehicles from communicating with each other, and is preferable to the

current practice of separating vehicles by altitude. On the other hand, the second approach relies heavily on inter-vehicle communications to properly coordinate the vehicle motions and is thus a function of the QoS of the underlying communications network. Formally, these two strategies lead to two alternative constraints. For collision avoidance in space, the trajectories for the n vehicles need to satisfy the constraint

$$\min_{\substack{j,k=1,\dots,n \\ j \neq k}} \| \mathbf{p}_{d,j}(\tau_{\ell,j}) - \mathbf{p}_{d,k}(\tau_{\ell,k}) \|^2 \geq E^2, \quad \text{for all } (\tau_{\ell,j}, \tau_{\ell,k}) \in [0, \ell_{fj}] \times [0, \ell_{fk}],$$

whereas, for collision avoidance in time, the trajectories need to verify that

$$\min_{\substack{j,k=1,\dots,n \\ j \neq k}} \| \mathbf{p}_{d,j}(t_d) - \mathbf{p}_{d,k}(t_d) \|^2 \geq E^2, \quad \text{for all } t_d \in [0, t_d^*],$$

where E is the desired distance for spatial clearance. See Figures 2.2 and 2.3 for an illustration of these two approaches.

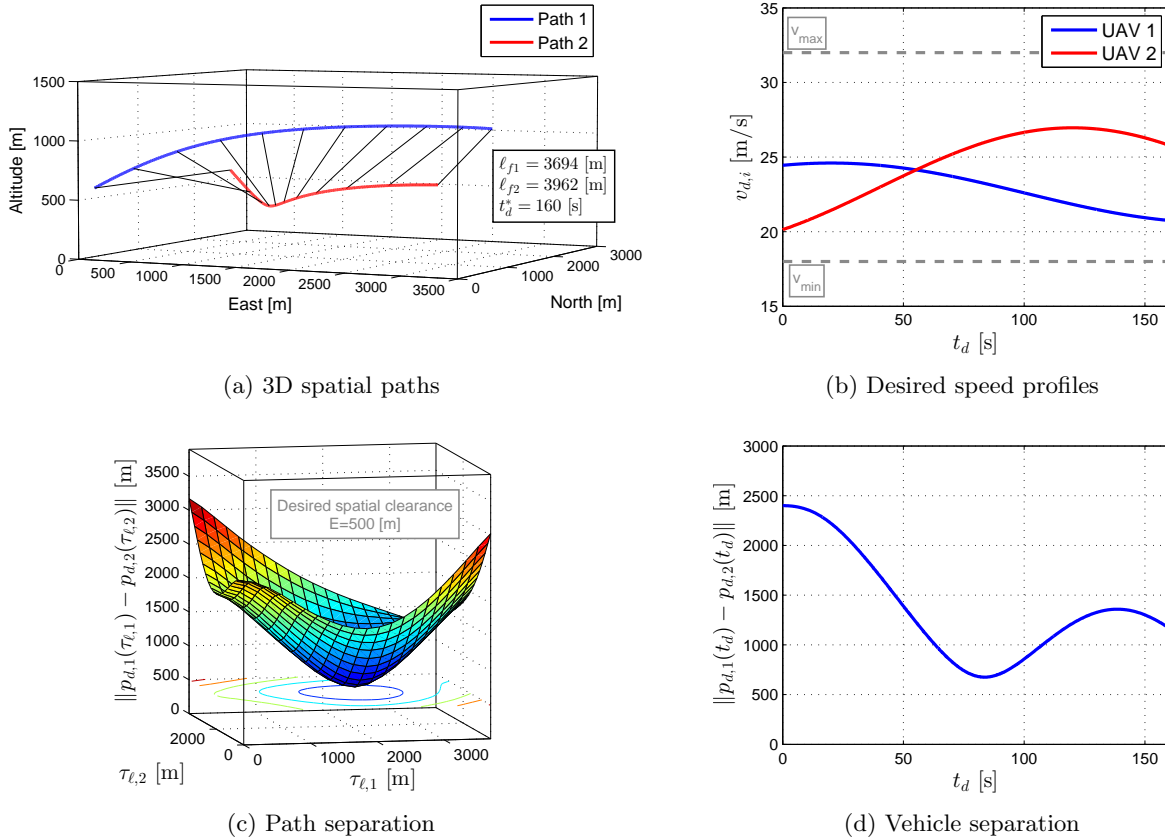


Figure 2.2: Trajectory generation; collision avoidance in space.

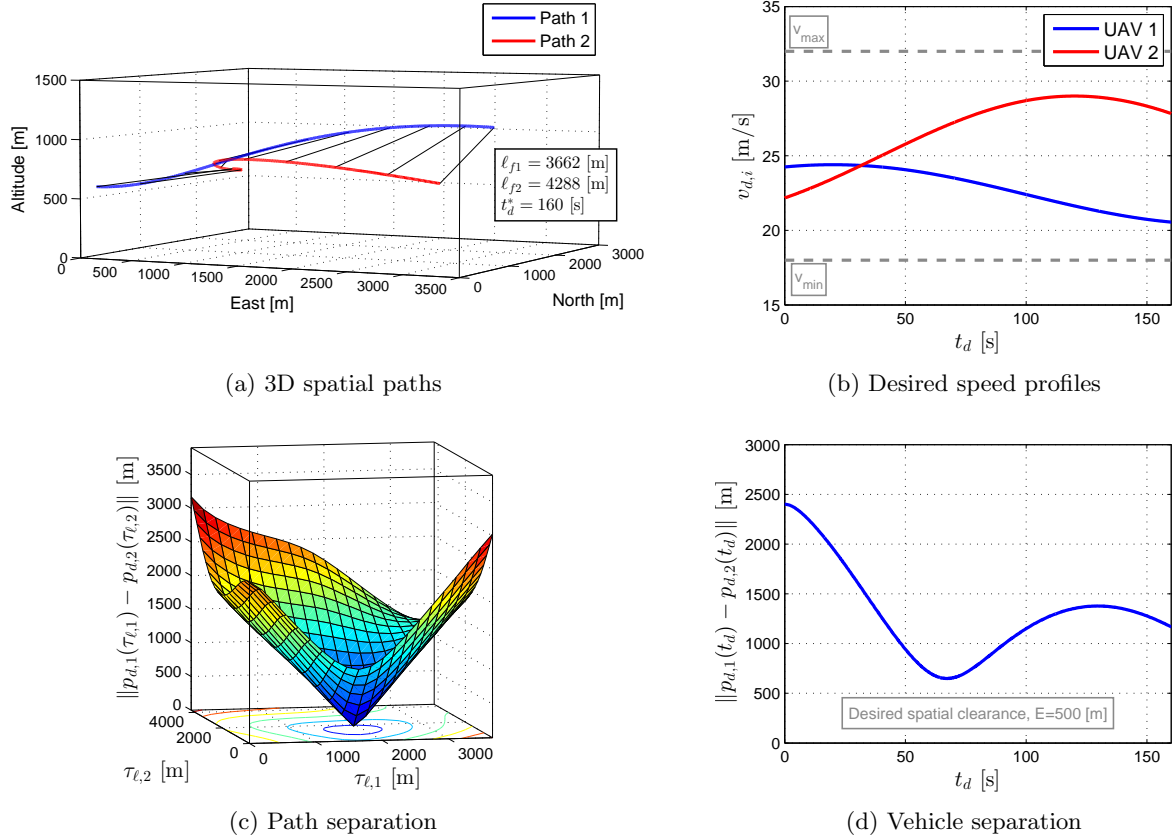


Figure 2.3: Trajectory generation; collision avoidance in time.

In addition to collision avoidance, the simultaneous time-of-arrival requirement adds an additional constraint on the trajectory-generation problem. Let $\delta w_i := [t_{d\min,i}^*, t_{d\max,i}^*]$ be the *arrival-time window* for the i th vehicle, where $t_{d\min,i}^*$ and $t_{d\max,i}^*$ represent the minimal and maximal possible durations of the mission for the i th vehicle, defined as $t_{d\min,i}^* := \frac{\ell_{f_i}}{v_{d\max}}$ and $t_{d\max,i}^* := \frac{\ell_{f_i}}{v_{d\min}}$. Then, the simultaneous arrival problem has a solution if and only if the intersection of the arrival-time windows is nonempty, that is, $\delta w_i \cap \delta w_j \neq \emptyset$ for all $i, j \in \{1, \dots, n\}$, $i \neq j$. In particular, if we define the *arrival margin* δw_{am} as

$$\delta w_{\text{am}} := \min_{i=1,\dots,n} t_{d\max,i}^* - \max_{i=1,\dots,n} t_{d\min,i}^*,$$

then nonemptiness of the intersection of arrival-time windows is implied by enforcing a positive arrival margin; see Figure 2.4. Moreover, enlarging the arrival margin adds robustness to the mission execution at the coordination level.

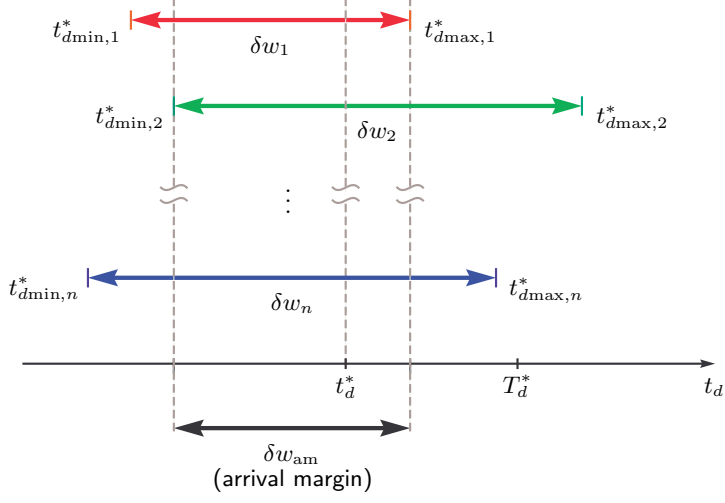


Figure 2.4: Trajectory generation; arrival margin.

Then, letting T_d^* be a predefined upper bound on the final time for the mission to be completed, and defining a cost function $J(\cdot)$ to be minimized, the cooperative *trajectory-generation problem* can be formulated as two alternative optimization problems. The first optimization problem addresses collision avoidance in space and is formulated as follows:

$$\min_{\Xi_1 \times \dots \times \Xi_n} J(\cdot) \quad (2.4)$$

subject to initial and final boundary conditions and the feasibility conditions (2.3) for all vehicles $i \in \{1, \dots, n\}$, as well as the constraints

$$\begin{aligned} \min_{\substack{j, k=1, \dots, n \\ j \neq k}} \| \mathbf{p}_{d,j}(\tau_{\ell,j}) - \mathbf{p}_{d,k}(\tau_{\ell,k}) \|^2 &\geq E^2, & \text{for all } (\tau_{\ell,j}, \tau_{\ell,k}) \in [0, \ell_{fj}] \times [0, \ell_{fk}], \\ \ell_{fi} = \int_0^{t_d^*} v_{d,i}(t_d) dt_d, && \text{for all } i \in \{1, \dots, n\}, \end{aligned}$$

$$\delta w_{\text{am}} \geq \delta W_{\text{am}},$$

$$t_d^* \leq T_d^*,$$

where Ξ_i is the set of optimization parameters for the i th trajectory, E is the minimal allowable separation distance between paths, and $\delta W_{\text{am}} > 0$ represents a requirement in the arrival margin. The second optimization problem accounts for collision avoidance in time and is posed as:

$$\min_{\Xi_1 \times \dots \times \Xi_n} J(\cdot) \quad (2.5)$$

subject to initial and final boundary conditions and the feasibility conditions (2.3) for all vehicles $i \in \{1, \dots, n\}$, as well as the constraints

$$\begin{aligned} \min_{\substack{j,k=1,\dots,n \\ j \neq k}} \| \mathbf{p}_{d,j}(t_d) - \mathbf{p}_{d,k}(t_d) \|^2 &\geq E^2, & \text{for all } t_d \in [0, t_d^*], \\ \ell_{fi} = \int_0^{t_d^*} v_{d,i}(t_d) dt_d, && \text{for all } i \in \{1, \dots, n\}, \\ \delta w_{\text{am}} &\geq \delta W_{\text{am}}, \\ t_d^* &\leq T_d^*, \end{aligned}$$

where Ξ_i is again the set of optimization parameters for the i th trajectory, while E is now the minimal allowable separation distance between vehicles. In the cooperative trajectory-generation problems above, the cost function $J(\cdot)$ includes terms related to mission-specific goals and cooperative performance criteria, while additional constraints can also be added to account, for instance, for inter-vehicle and vehicle-to-ground communications limitations, sensory capabilities, task allocation under resource constraints, and collision avoidance with obstacles.

The outcome of the optimization problems (2.4) and (2.5) is a set of n feasible spatial paths $\mathbf{p}_{d,i}(\tau_{\ell,i})$ and corresponding desired speed profiles $v_{d,i}(t_d)$ such that, if each agent follows its assigned path and speed profile, then the time-critical mission is executed optimally. However, the presence of disturbances, modeling uncertainty, and failures in the communications network require the synthesis of robust feedback laws to ensure that the mission can be accomplished with a high degree of confidence. In the remaining of this thesis, we present a general framework to synthesize path-following and coordination control laws that can address the performance of the overall time-critical mission in the presence of system uncertainty and a faulty time-varying communications network.

2.2.2 Following a Virtual Target Vehicle on the Path

As mentioned earlier, the solution to the path-following problem proposed in this thesis extends the algorithm presented in [61] to the case of 3D spatial paths, and relies on the insight that a UAV can follow a given path using only its attitude, thus leaving its linear speed as an extra degree of freedom to be used at the coordination level. The key idea of the algorithm is to use the vehicle's attitude control effectors to follow a *virtual target vehicle* running along the path. To this effect, following the approach developed in [61], we introduce a frame attached to this virtual target and define a generalized error vector between this moving coordinate system and a frame attached to the actual vehicle. With this setup, the path-following control problem is reduced to driving this generalized error vector to zero by using only the vehicle's attitude control

effectors, while following an arbitrary feasible speed profile. In this section, we characterize the dynamics of the kinematic errors between one of the n vehicles involved in the cooperative mission and its virtual target. For notational simplicity, we drop the subscript i used to denote a particular vehicle.

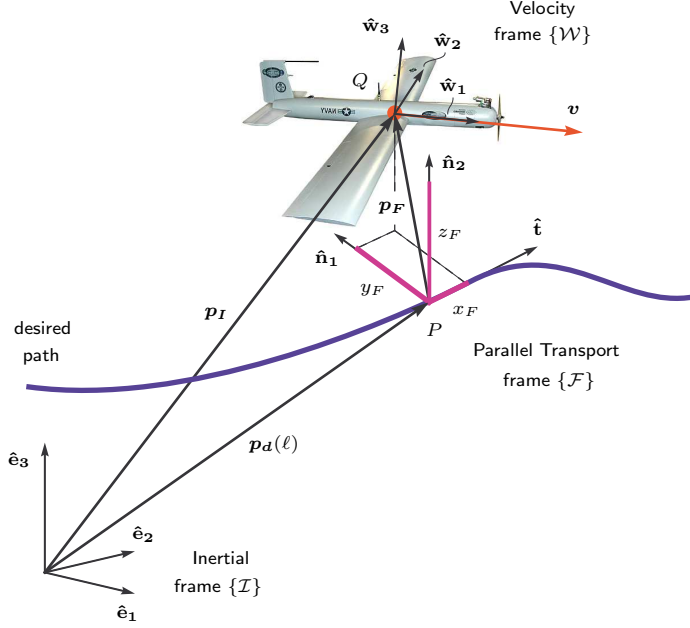


Figure 2.5: Following a virtual target vehicle; problem geometry.

Figure 2.5 captures the geometry of the problem at hand. The symbol $\{\mathcal{I}\}$ denotes an inertial reference frame $\{\hat{\mathbf{e}}_1, \hat{\mathbf{e}}_2, \hat{\mathbf{e}}_3\}$ and $\mathbf{p}_d(\cdot)$ is the desired path assigned to one of the vehicles, with ℓ_f being its total path length. Vector $\mathbf{p}_I(t)$ denotes the position of the center of mass Q of the vehicle in this inertial frame. Further, we let P be an arbitrary point on the desired path that plays the role of the virtual target, and denote by $\mathbf{p}_d(\ell)$ its position in the inertial frame. Here $\ell \in [0, \ell_f]$ is a free length-variable that defines the position of the virtual target vehicle along the path. In the setup adopted, the total rate of progression of the virtual target along the path, $\frac{d\ell(t)}{dt}$, is an additional design parameter. This approach is in striking contrast with the strategy used in the path-following algorithm introduced in [69], where P was defined as the point on the path that is closest to the vehicle. Endowing point P with an extra degree of freedom is the key to the path-following algorithm presented in [61] and its extension to the 3D case described in this thesis.

For our purposes, it is convenient to define a *parallel transport frame* $\{\mathcal{F}\}$ attached to point P on the path and characterized by the orthonormal vectors $\{\hat{\mathbf{t}}(\ell), \hat{\mathbf{n}}_1(\ell), \hat{\mathbf{n}}_2(\ell)\}$, which satisfy the following frame

equations [14, 44]:

$$\begin{bmatrix} \frac{d\hat{\mathbf{t}}}{d\ell}(\ell) \\ \frac{d\hat{\mathbf{n}}_1}{d\ell}(\ell) \\ \frac{d\hat{\mathbf{n}}_2}{d\ell}(\ell) \end{bmatrix} = \begin{bmatrix} 0 & k_1(\ell) & k_2(\ell) \\ -k_1(\ell) & 0 & 0 \\ -k_2(\ell) & 0 & 0 \end{bmatrix} \begin{bmatrix} \hat{\mathbf{t}}(\ell) \\ \hat{\mathbf{n}}_1(\ell) \\ \hat{\mathbf{n}}_2(\ell) \end{bmatrix},$$

where $k_1(\ell)$ and $k_2(\ell)$ define the *normal development* of the path, and are related to the polar coordinates of curvature $\kappa(\ell)$ and torsion $\tau(\ell)$ as

$$\kappa(\ell) = (k_1^2(\ell) + k_2^2(\ell))^{\frac{1}{2}}, \quad \tau(\ell) = -\frac{d}{d\ell} \left(\tan^{-1} \left(\frac{k_2(\ell)}{k_1(\ell)} \right) \right).$$

Vectors $\hat{\mathbf{t}}(\ell)$, $\hat{\mathbf{n}}_1(\ell)$, and $\hat{\mathbf{n}}_2(\ell)$ define an orthonormal basis for $\{\mathcal{F}\}$, in which the unit vector $\hat{\mathbf{t}}(\ell)$ defines the tangent direction to the path at the point determined by ℓ , while $\hat{\mathbf{n}}_1(\ell)$ and $\hat{\mathbf{n}}_2(\ell)$ define the normal plane perpendicular to $\hat{\mathbf{t}}(\ell)$. We note that, unlike the Frenet-Serret frame, parallel transport frames are well defined when the path has a vanishing second derivative. This orthonormal basis can be used to construct the rotation matrix $\mathbf{R}_F^I(\ell) = [\{\hat{\mathbf{t}}(\ell)\}_I; \{\hat{\mathbf{n}}_1(\ell)\}_I; \{\hat{\mathbf{n}}_2(\ell)\}_I]$ from $\{\mathcal{F}\}$ to $\{\mathcal{I}\}$. Furthermore, the angular velocity of $\{\mathcal{F}\}$ with respect to $\{\mathcal{I}\}$, resolved in $\{\mathcal{F}\}$, can be easily expressed in terms of the parameters $k_1(\ell)$ and $k_2(\ell)$ as

$$\{\boldsymbol{\omega}_{F/I}\}_F = [0, -k_2(\ell) \dot{\ell}, k_1(\ell) \dot{\ell}]^\top.$$

The position of the vehicle's center of mass Q in the parallel transport frame $\{\mathcal{F}\}$ is denoted by $\mathbf{p}_F(t)$, and $x_F(t)$, $y_F(t)$, and $z_F(t)$ are the components of this vector with respect to the basis $\{\hat{\mathbf{t}}, \hat{\mathbf{n}}_1, \hat{\mathbf{n}}_2\}$, that is,

$$\{\mathbf{p}_F\}_F = [x_F, y_F, z_F]^\top.$$

Finally, let $\{\mathcal{W}\}$ denote a vehicle-carried velocity frame $\{\hat{\mathbf{w}}_1, \hat{\mathbf{w}}_2, \hat{\mathbf{w}}_3\}$ with its origin at the vehicle's center of mass Q and its x axis aligned with the velocity vector of the vehicle. The z axis is chosen to lie in the plane of symmetry of the vehicle, and the y axis is determined by completing the right-hand system. In this thesis, $q(t)$ and $r(t)$ are the y -axis and z -axis components, respectively, of the vehicle's rotational velocity resolved in the $\{\mathcal{W}\}$ frame. With a slight abuse of notation, $q(t)$ and $r(t)$ will be referred here to as *pitch rate* and *yaw rate*, respectively, in the $\{\mathcal{W}\}$ frame.

With the above notation, we next characterize the path-following kinematic error dynamics of the vehicle with respect to the virtual target. We start by deriving the position-error dynamics. To this effect, we note that

$$\mathbf{p}_I = \mathbf{p}_d(\ell) + \mathbf{p}_F,$$

from which it follows that

$$\dot{\mathbf{p}}_I]_I = \dot{\ell} \hat{\mathbf{t}} + \boldsymbol{\omega}_{F/I} \times \mathbf{p}_F + \dot{\mathbf{p}}_F]_F,$$

where $\cdot |_I$ and $\cdot |_F$ are used to indicate that the derivatives are taken in the inertial and parallel transport frames, respectively. Because

$$\dot{\mathbf{p}}_I]_I = v \hat{\mathbf{w}}_1,$$

where $v(t)$ denotes the magnitude of the vehicle's ground velocity vector, the path-following kinematic position-error dynamics of the vehicle with respect to the virtual target can be written as

$$\dot{\mathbf{p}}_F]_F = -\dot{\ell} \hat{\mathbf{t}} - \boldsymbol{\omega}_{F/I} \times \mathbf{p}_F + v \hat{\mathbf{w}}_1. \quad (2.6)$$

With respect to the basis $\{\hat{\mathbf{t}}, \hat{\mathbf{n}}_1, \hat{\mathbf{n}}_2\}$, the above equation takes the following form:

$$\begin{bmatrix} \dot{x}_F \\ \dot{y}_F \\ \dot{z}_F \end{bmatrix} = -\begin{bmatrix} \dot{\ell} \\ 0 \\ 0 \end{bmatrix} - \left(\begin{bmatrix} 0 \\ -k_2(\ell) \dot{\ell} \\ k_1(\ell) \dot{\ell} \end{bmatrix} \times \begin{bmatrix} x_F \\ y_F \\ z_F \end{bmatrix} \right) + \mathbf{R}_W^F \begin{bmatrix} v \\ 0 \\ 0 \end{bmatrix}.$$

To derive the attitude-error dynamics of the vehicle with respect to its virtual target, we first introduce an auxiliary frame $\{\mathcal{D}\}$, which will be used to shape the approach attitude to the path as a function of the *cross-track error* components y_F and z_F . Frame $\{\mathcal{D}\}$ has its origin at the vehicle center of mass and is characterized by vectors $\hat{\mathbf{b}}_{1D}(t)$, $\hat{\mathbf{b}}_{2D}(t)$, and $\hat{\mathbf{b}}_{3D}(t)$, which are defined as

$$\hat{\mathbf{b}}_{1D} := \frac{d \hat{\mathbf{t}} - y_F \hat{\mathbf{n}}_1 - z_F \hat{\mathbf{n}}_2}{(d^2 + y_F^2 + z_F^2)^{\frac{1}{2}}}, \quad \hat{\mathbf{b}}_{2D} := \frac{y_F \hat{\mathbf{t}} + d \hat{\mathbf{n}}_1}{(d^2 + y_F^2)^{\frac{1}{2}}}, \quad \hat{\mathbf{b}}_{3D} := \hat{\mathbf{b}}_{1D} \times \hat{\mathbf{b}}_{2D}, \quad (2.7)$$

with $d > 0$ being a constant *characteristic distance* that plays the role of a design parameter, as will become clear later. In particular, the basis vector $\hat{\mathbf{b}}_{1D}(t)$ defines the desired direction of the vehicle's velocity vector. As illustrated in Figure 2.6, when the vehicle is far from the desired path, vector $\hat{\mathbf{b}}_{1D}(t)$ becomes perpendicular to $\hat{\mathbf{t}}(\ell)$. As the vehicle comes closer to the path and the cross-track error becomes smaller, then $\hat{\mathbf{b}}_{1D}(t)$ tends to $\hat{\mathbf{t}}(\ell)$. Vectors $\hat{\mathbf{b}}_{1D}(t)$, $\hat{\mathbf{b}}_{2D}(t)$, and $\hat{\mathbf{b}}_{3D}(t)$ can be used to compute the rotation matrix $\mathbf{R}_D^F(t)$, which is given by

$$\mathbf{R}_D^F = \begin{bmatrix} \frac{d}{(d^2 + y_F^2 + z_F^2)^{\frac{1}{2}}} & \frac{y_F}{(d^2 + y_F^2)^{\frac{1}{2}}} & \frac{z_F d}{(d^2 + y_F^2 + z_F^2)^{\frac{1}{2}}(d^2 + y_F^2)^{\frac{1}{2}}} \\ \frac{-y_F}{(d^2 + y_F^2 + z_F^2)^{\frac{1}{2}}} & \frac{d}{(d^2 + y_F^2)^{\frac{1}{2}}} & \frac{-y_F z_F}{(d^2 + y_F^2 + z_F^2)^{\frac{1}{2}}(d^2 + y_F^2)^{\frac{1}{2}}} \\ \frac{-z_F}{(d^2 + y_F^2 + z_F^2)^{\frac{1}{2}}} & 0 & \frac{(d^2 + y_F^2)^{\frac{1}{2}}}{(d^2 + y_F^2 + z_F^2)^{\frac{1}{2}}} \end{bmatrix}.$$

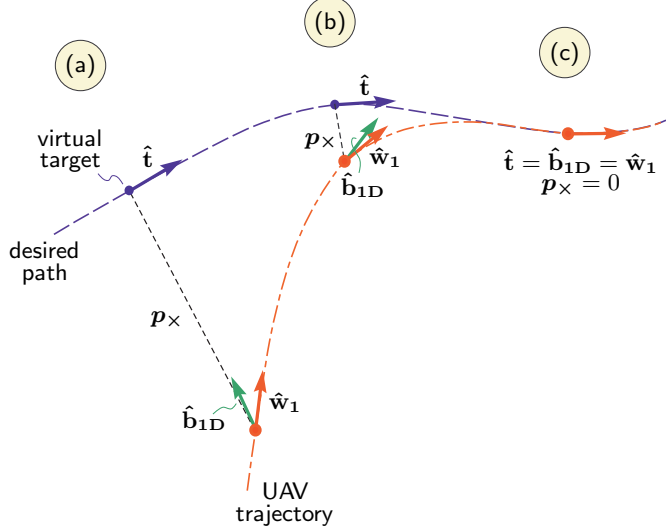


Figure 2.6: Shaping the approach to the path as a function of the cross-track error p_x . (For simplicity, the plot above assumes that the along-path error $x_F(t)$ is zero.)

Next, let $\tilde{\mathbf{R}}(t)$ be the rotation matrix from $\{\mathcal{W}\}$ to $\{\mathcal{D}\}$, that is,

$$\tilde{\mathbf{R}} := \mathbf{R}_W^D = \mathbf{R}_F^D \mathbf{R}_W^F = (\mathbf{R}_D^F)^\top \mathbf{R}_W^F,$$

and define the real-valued error function on $\text{SO}(3)$

$$\Psi(\tilde{\mathbf{R}}) := \frac{1}{2} \text{tr} \left[(\mathbb{I}_3 - \boldsymbol{\Pi}_R^\top \boldsymbol{\Pi}_R) (\mathbb{I}_3 - \tilde{\mathbf{R}}) \right], \quad (2.8)$$

where $\boldsymbol{\Pi}_R := [\begin{smallmatrix} 0 & 1 & 0 \\ 0 & 0 & 1 \end{smallmatrix}]$. The function $\Psi(\tilde{\mathbf{R}})$ in (2.8) can be expressed in terms of the entries of $\tilde{\mathbf{R}}(t)$ as

$$\Psi(\tilde{\mathbf{R}}) = \frac{1}{2} (1 - \tilde{R}_{11}),$$

where $\tilde{R}_{11}(t)$ denotes the $(1, 1)$ entry of $\tilde{\mathbf{R}}(t)$. Therefore, $\Psi(\tilde{\mathbf{R}})$ is a positive-definite function about $\tilde{R}_{11} = 1$. We note that $\tilde{R}_{11} = 1$ corresponds to the situation where the velocity vector of the vehicle is aligned with the basis vector $\hat{\mathbf{b}}_{1D}(t)$, which as mentioned earlier defines the desired attitude of the vehicle.

The attitude kinematics equation

$$\dot{\tilde{\mathbf{R}}} = \dot{\mathbf{R}}_W^D = \mathbf{R}_W^D (\{\omega_{W/D}\}_W)^\wedge = \tilde{\mathbf{R}} (\{\omega_{W/D}\}_W)^\wedge,$$

where $(\cdot)^\wedge : \mathbb{R}^3 \rightarrow \mathfrak{so}(3)$ denotes the *hat map* (see Appendix A), can now be used to derive the time-derivative

of $\Psi(\tilde{\mathbf{R}})$, which is given by

$$\dot{\Psi}(\tilde{\mathbf{R}}) = -\frac{1}{2}\text{tr}\left[\left(\mathbb{I}_3 - \Pi_R^\top \Pi_R\right)\dot{\tilde{\mathbf{R}}}\right] = -\frac{1}{2}\text{tr}\left[\left(\mathbb{I}_3 - \Pi_R^\top \Pi_R\right)\tilde{\mathbf{R}}(\{\omega_{W/D}\}_W)^\wedge\right].$$

Property (A.1) of the hat map leads to

$$\dot{\Psi}(\tilde{\mathbf{R}}) = \frac{1}{2}\left(\left(\left(\mathbb{I}_3 - \Pi_R^\top \Pi_R\right)\tilde{\mathbf{R}} - \tilde{\mathbf{R}}^\top\left(\mathbb{I}_3 - \Pi_R^\top \Pi_R\right)\right)^\vee\right)^\top\{\omega_{W/D}\}_W,$$

where $(\cdot)^\vee : \mathfrak{so}(3) \rightarrow \mathbb{R}^3$ denotes the *vee map*, which is defined as the inverse of the hat map (see Appendix A). Moreover, since the first component of $\left(\left(\mathbb{I}_3 - \Pi_R^\top \Pi_R\right)\tilde{\mathbf{R}} - \tilde{\mathbf{R}}^\top\left(\mathbb{I}_3 - \Pi_R^\top \Pi_R\right)\right)^\vee$ is equal to zero, we can also write

$$\begin{aligned}\dot{\Psi}(\tilde{\mathbf{R}}) &= \frac{1}{2}\left(\left(\left(\mathbb{I}_3 - \Pi_R^\top \Pi_R\right)\tilde{\mathbf{R}} - \tilde{\mathbf{R}}^\top\left(\mathbb{I}_3 - \Pi_R^\top \Pi_R\right)\right)^\vee\right)^\top\Pi_R^\top \Pi_R\{\omega_{W/D}\}_W \\ &= \left(\frac{1}{2}\Pi_R\left(\left(\mathbb{I}_3 - \Pi_R^\top \Pi_R\right)\tilde{\mathbf{R}} - \tilde{\mathbf{R}}^\top\left(\mathbb{I}_3 - \Pi_R^\top \Pi_R\right)\right)^\vee\right)^\top\Pi_R\{\omega_{W/D}\}_W.\end{aligned}\quad (2.9)$$

Next, we define the attitude error $e_{\tilde{\mathbf{R}}}(t)$ as

$$e_{\tilde{\mathbf{R}}} := \frac{1}{2}\Pi_R\left(\left(\mathbb{I}_3 - \Pi_R^\top \Pi_R\right)\tilde{\mathbf{R}} - \tilde{\mathbf{R}}^\top\left(\mathbb{I}_3 - \Pi_R^\top \Pi_R\right)\right)^\vee,$$

which allows us to rewrite (2.9) in the more compact form

$$\dot{\Psi}(\tilde{\mathbf{R}}) = e_{\tilde{\mathbf{R}}} \cdot (\Pi_R\{\omega_{W/D}\}_W).$$

We note that the attitude error $e_{\tilde{\mathbf{R}}}(t)$ can also be expressed in terms of the entries of $\tilde{\mathbf{R}}(t)$ as

$$e_{\tilde{\mathbf{R}}} = \frac{1}{2}[\tilde{R}_{13}, -\tilde{R}_{12}]^\top$$

and, therefore, within the region where $\Psi(\tilde{\mathbf{R}}) < 1$, we have that if $\|e_{\tilde{\mathbf{R}}}\| = 0$, then $\Psi(\tilde{\mathbf{R}}) = 0$. Finally, noting that $\{\omega_{W/D}\}_W$ can be expressed as

$$\begin{aligned}\{\omega_{W/D}\}_W &= \{\omega_{W/I}\}_W + \{\omega_{I/F}\}_W + \{\omega_{F/D}\}_W \\ &= \{\omega_{W/I}\}_W - \mathbf{R}_F^W\{\omega_{F/I}\}_F - \mathbf{R}_D^W\{\omega_{D/F}\}_D \\ &= \{\omega_{W/I}\}_W - \tilde{\mathbf{R}}^\top(\mathbf{R}_F^D\{\omega_{F/I}\}_F + \{\omega_{D/F}\}_D),\end{aligned}$$

we obtain

$$\dot{\Psi}(\tilde{\mathbf{R}}) = \mathbf{e}_{\tilde{\mathbf{R}}} \cdot \left(\Pi_{\mathbf{R}} \left(\{\omega_{W/I}\}_W - \tilde{\mathbf{R}}^\top (\mathbf{R}_F^D \{\omega_{F/I}\}_F + \{\omega_{D/F}\}_D) \right) \right),$$

or equivalently

$$\dot{\Psi}(\tilde{\mathbf{R}}) = \mathbf{e}_{\tilde{\mathbf{R}}} \cdot \left(\begin{bmatrix} q \\ r \end{bmatrix} - \Pi_{\mathbf{R}} \tilde{\mathbf{R}}^\top (\mathbf{R}_F^D \{\omega_{F/I}\}_F + \{\omega_{D/F}\}_D) \right). \quad (2.10)$$

This equation describes the path-following kinematic attitude-error dynamics of frame $\{\mathcal{W}\}$ with respect to frame $\{\mathcal{D}\}$. The overall path-following kinematic error dynamics can now be obtained by combining (2.6) and (2.10), yielding

$$\begin{aligned} \dot{\mathbf{p}}_F]_F &= -\dot{\ell} \hat{\mathbf{t}} - \omega_{F/I} \times \mathbf{p}_F + v \hat{\mathbf{w}}_1, \\ \dot{\Psi}(\tilde{\mathbf{R}}) &= \mathbf{e}_{\tilde{\mathbf{R}}} \cdot \left(\begin{bmatrix} q \\ r \end{bmatrix} - \Pi_{\mathbf{R}} \tilde{\mathbf{R}}^\top (\mathbf{R}_F^D \{\omega_{F/I}\}_F + \{\omega_{D/F}\}_D) \right). \end{aligned} \quad (2.11)$$

In the kinematic error model (2.11), $q(t)$ and $r(t)$ play the role of control inputs, while the rate of progression $\dot{\ell}(t)$ of point P along the path becomes an additional variable that can be manipulated at will. At this point, we formally define the path-following generalized error vector $\mathbf{x}_{pf}(t)$ as

$$\mathbf{x}_{pf} := [\mathbf{p}_F^\top, \mathbf{e}_{\tilde{\mathbf{R}}}^\top]^\top.$$

Notice that, within the region where $\Psi(\tilde{\mathbf{R}}) < 1$, if $\mathbf{x}_{pf} = \mathbf{0}$, then both the path-following position error and the path-following attitude error are equal to zero, that is, $\mathbf{p}_F = \mathbf{0}$ and $\Psi(\tilde{\mathbf{R}}) = 0$.

Using the above formulation, and given a spatially defined feasible path $\mathbf{p}_d(\cdot)$, the problem of *path following* for a single vehicle can now be defined accordingly.

Definition 2 (Path-Following Problem) *For a given vehicle, design feedback control laws for pitch rate $q(t)$, yaw rate $r(t)$, and rate of progression $\dot{\ell}(t)$ of the virtual target along the path such that all closed-loop signals are bounded and the path-following generalized error vector $\mathbf{x}_{pf}(t)$ converges to a neighborhood of the origin, regardless of the (feasible) temporal assignments of the mission.* ♠

Stated in simple terms, the problem above amounts to designing feedback laws so that a vehicle converges to and remains inside a tube centered on the desired path curve assigned to this vehicle, for an arbitrary speed profile (subject to feasibility constraints).

2.2.3 Time-Critical Coordination and Communications Constraints

To enforce the temporal constraints that must be met to coordinate the entire fleet of vehicles, following the approach presented in [51], the speed profile of each vehicle is adjusted based on coordination information exchanged among the vehicles over a supporting communications network. In this section, we formulate the coordination problem as a consensus problem, in which the objective of the fleet of vehicles is to reach agreement on some distributed variables of interest. An appropriate coordination variable needs thus to be defined for each vehicle that captures the objective of the cooperative mission, which in the context of this thesis translates to satisfying relative temporal constraints.

To this effect, we start by defining $\ell'_{d,i}(t_d)$ as the desired normalized curvilinear abscissa of the i th vehicle along its corresponding path at the desired mission time t_d , which is given by

$$\ell'_{d,i}(t_d) := \frac{1}{\ell_{fi}} \int_0^{t_d} v_{d,i}(\tau) d\tau, \quad i = 1, \dots, n,$$

with ℓ_{fi} and $v_{d,i}(\cdot)$ being, respectively, the length of the path and the desired speed profile corresponding to the i th vehicle. The trajectory-generation algorithm ensures that the desired speed profiles $v_{d,i}(\cdot)$ satisfy feasibility conditions, which implies that the following bounds hold for all vehicles:

$$0 < v_{\min} \leq v_{d,\min} \leq v_{d,i}(t_d) \leq v_{d,\max} \leq v_{\max}, \quad \text{for all } t_d \in [0, t_d^*], \quad \text{and all } i \in \{1, \dots, n\}, \quad (2.12)$$

where v_{\min} and v_{\max} denote, respectively, the minimum and maximum operating speeds of the vehicle, while $v_{d,\min}$ and $v_{d,\max}$ denote lower and upper bounds on the desired speed profiles of the vehicles; see Equation (2.3). From the definition of $\ell'_{d,i}(t_d)$ and the bounds in (2.12), it follows that $\ell'_{d,i}(t_d)$ is a strictly increasing continuous function of t_d mapping $[0, t_d^*]$ onto $[0, 1]$, and satisfying $\ell'_{d,i}(0) = 0$ and $\ell'_{d,i}(t_d^*) = 1$. We also define $\eta_i : [0, 1] \rightarrow [0, t_d^*]$ to be the inverse function of $\ell'_{d,i}(t_d)$. Clearly, $\eta_i(\cdot)$ is also a strictly increasing continuous function of its argument. Then, letting $\ell'_i(t)$ be the normalized curvilinear abscissa at time t of the i th virtual target vehicle running along its path, defined as

$$\ell'_i := \frac{\ell_i}{\ell_{fi}}, \quad i = 1, \dots, n,$$

we define the time-variables

$$\xi_i := \eta_i(\ell'_i), \quad i = 1, \dots, n. \quad (2.13)$$

From this definition, it follows that $\xi_i(t) \in [0, t_d^*]$, and therefore this variable characterizes the status of the

mission for the i th vehicle at time t in terms of the desired mission time t_d .

We note that, for any two vehicles i and j , if $\xi_i(t) = \xi_j(t) = t'_d$ at a given time t , then $\ell'_i(t) = \ell'_{d,i}(t'_d)$ and $\ell'_j(t) = \ell'_{d,j}(t'_d)$, which implies that at time t the target vehicles corresponding to vehicles i and j have the desired relative position along their paths at the desired mission time t'_d . Clearly, if $\xi_i(t) = \xi_j(t)$ for all $t \geq 0$, then the i th and j th virtual target vehicles maintain desired relative position along their paths at all times and, therefore, these two target vehicles satisfy the relative temporal constraints as provided by the trajectory-generation algorithm. Also, in the case of collision avoidance in time (see Section 2.2.1), if $\xi_i(t) = \xi_j(t)$ for all $t \geq 0$, then the solution to the trajectory-generation problem ensures that the virtual targets i and j are not at the same place at the same time during the entire duration of the mission. Moreover, it can be shown that if the i th coordination state evolves at rate 1 at a given time t , that is $\dot{\xi}_i(t) = 1$, then we have that the i th virtual target travels at the desired speed, $\dot{\ell}_i(t) = v_{d,i}(\xi_i(t))$ (see Appendix B.1). The variables $\xi_i(t)$ represent thus an appropriate measure of vehicle coordination and will be referred to as *coordination states*, while the functions $\eta_i(\cdot)$ will be called *coordination maps*. We notice that the use of these specific coordination variables is motivated by the work in [41].

To reach agreement on these coordination states and ensure that the desired temporal assignments of the mission are met, coordination information is to be exchanged among the vehicles over the supporting communications network. Next, we use tools and facts from algebraic graph theory to model the information exchange over the network as well as the constraints imposed by the communications topology. The reader is referred to [13] for key concepts and details on algebraic graph theory.

First, it is assumed that the i th vehicle can only exchange information with a neighboring set of vehicles, denoted here by $\mathcal{N}_i(t)$. It is also assumed that communications between two vehicles are bidirectional and, for simplicity, that information is transmitted continuously with no delays. Moreover, since the flow of information among vehicles may be severely restricted, either for security reasons or because of tight bandwidth limitations, we impose the constraint that each vehicle only exchanges its coordination state $\xi_i(t)$ with its neighbors. Finally, we assume that the connectivity of the communications graph $\Gamma(t)$ that captures the underlying bidirectional communications network topology of the fleet at time t satisfies the persistency of excitation (PE)-like condition [6]

$$\frac{1}{n} \frac{1}{T} \int_t^{t+T} \mathbf{Q} \mathbf{L}(\tau) \mathbf{Q}^\top d\tau \geq \mu \mathbb{I}_{n-1}, \quad \text{for all } t \geq 0, \quad (2.14)$$

where $\mathbf{L}(t) \in \mathbb{R}^{n \times n}$ is the Laplacian of the graph $\Gamma(t)$, and \mathbf{Q} is an $(n - 1) \times n$ matrix such that $\mathbf{Q}\mathbf{1}_n = \mathbf{0}$ and $\mathbf{Q}\mathbf{Q}^\top = \mathbb{I}_{n-1}$, with $\mathbf{1}_n$ being the vector in \mathbb{R}^n whose components are all 1. Parameters $T > 0$ and $\mu > 0$

characterize the QoS of the communications network, which in the context of this thesis represents a measure of the level of connectivity of the communications graph. We note that the PE-like condition (2.14) requires the communications graph $\Gamma(t)$ to be connected only in an integral sense, not pointwise in time. In fact, the graph may be disconnected during some interval of time or may even fail to be connected at all times. A similar type of condition can be found, for example, in [64].

Using the formulation above, we next define the problem of time-critical cooperative path following for a fleet of n vehicles.

Definition 3 (Time-Critical Cooperative Path-Following Problem) *Given a fleet of n vehicles supported by an inter-vehicle communications network and a set of desired 3D time-trajectories $\mathbf{p}_{d,i}(t_d)$, design feedback control laws for pitch rate $q(t)$, yaw rate $r(t)$, and speed $v(t)$ for all vehicles such that*

1. *all closed-loop signals are bounded;*
2. *for each vehicle i , $i = 1, \dots, n$, the path-following generalized error vector $\mathbf{x}_{pf,i}(t)$ converges to a neighborhood of the origin; and*
3. *for each pair of vehicles i and j , $i, j = 1, \dots, n$, the coordination errors $(\xi_i(t) - \xi_j(t))$ and $(\dot{\xi}_i(t) - \dot{\xi}_j(t))$ converge to a neighborhood of the origin, guaranteeing that the temporal assignments of the mission are satisfied.*



Remark 1 *If the desired speed profiles $v_{d,i}(t_d)$ obtained from the trajectory-generation algorithm are constant along the corresponding paths, that is,*

$$v_{d,i}(t_d) = v_{d,i}, \quad \text{for all } t_d \in [0, t_d^*], \quad \text{and all } i \in \{1, \dots, n\},$$

then the following equalities hold:

$$\begin{aligned} \ell'_{d,i}(t_d) &= \ell'_{d,j}(t_d), & \text{for all } t_d \in [0, t_d^*], \quad \text{and all } i, j \in \{1, \dots, n\}, \\ \frac{v_{d,i}}{\ell_{f_i}} &= \frac{d\ell'_{d,i}(t_d)}{dt_d} = \frac{d\ell'_{d,j}(t_d)}{dt_d} = \frac{v_{d,j}}{\ell_{f_j}}, & \text{for all } t_d \in [0, t_d^*], \quad \text{and all } i, j \in \{1, \dots, n\}. \end{aligned}$$

This implies that, in the case of constant desired speed profiles, the normalized curvilinear abscissas $\ell'_i(t)$ can be equivalently used as coordination states, while $(\ell'_i(t) - \ell'_j(t))$ and $(\dot{\ell}'_i(t) - \frac{v_{d,i}}{\ell_{f_i}})$ can be used to characterize the coordination errors. This is, in fact, the setup for vehicle coordination adopted in [51]. \triangle

Remark 2 In mission scenarios in which the various vehicles are required to follow their respective paths separated by pre-specified time-intervals, the coordination states in (2.13) need to be defined differently so as to capture the desired inter-vehicle schedule. It would be the case, for example, of a sequential auto-landing scenario, in which several UAVs are required to follow a common glide slope with a given speed profile and separated by pre-specified safe-guarding time-intervals. In Chapter 4, we will illustrate through an example how the coordination states can be defined for this type of time-critical missions. \triangle

Remark 3 The formulation of the time-critical cooperative path-following problem described above assumes only relative temporal constraints in the execution of a given mission. Absolute temporal constraints, such as specifications in the desired final time of the mission, are not considered. Such constraints can, nevertheless, be easily incorporated in the problem formulation, and enforced by judiciously modifying the coordination control laws presented later in this thesis. \triangle

2.2.4 Autonomous Vehicle with Autopilot

At this point, it is important to stress that this thesis addresses the design of control algorithms for path following and time coordination of a fleet of vehicles executing time-critical cooperative missions. The design of inner-loop onboard autopilots that are capable of tracking reference commands generated by outer-loop controllers and providing uniform performance across the operational envelope is, however, beyond the scope of the work presented here. This section presents a set of assumptions on the inner closed-loop performance of the vehicles with their autopilots, which will be useful to analyze the convergence properties of the path-following and coordination control laws developed later.

To this effect, we assume that each vehicle involved in the cooperative mission is equipped with an autopilot designed to stabilize the vehicle and to provide angular-rate as well as speed tracking capabilities. In particular, we make the assumption that the onboard autopilots ensure that each vehicle is able to track bounded pitch-rate and yaw-rate commands, denoted here by $q_c(t)$ and $r_c(t)$, with guaranteed performance bounds γ_q and γ_r . Stated mathematically,

$$\begin{aligned} |q_c(t) - q(t)| &\leq \gamma_q, & \text{for all } t \geq 0, \\ |r_c(t) - r(t)| &\leq \gamma_r, & \text{for all } t \geq 0. \end{aligned} \tag{2.15}$$

Similarly, we assume that if the speed command $v_c(t)$ satisfies the bounds

$$v_{\min} \leq v_c(\tau) \leq v_{\max}, \quad \text{for all } \tau \in [0, t], \tag{2.16}$$

then the autopilots ensure that each vehicle tracks its corresponding speed command with guaranteed performance bound γ_v :

$$|v_c(\tau) - v(\tau)| \leq \gamma_v, \quad \text{for all } \tau \in [0, t]. \quad (2.17)$$

The bounds γ_q , γ_r , and γ_v characterize thus the level of tracking performance that the inner-loop autopilot is able to provide. It is important to note that, in this setup, it is the autopilot that determines the bank angle required to track the angular-rate commands $q_c(t)$ and $r_c(t)$. Therefore, it is justified to assume that the roll dynamics of the vehicle (roll rate and bank angle) are bounded for bounded angular-rate commands corresponding to the set of feasible paths considered.

Remark 4 *The bounds in (2.15) and (2.17) will be used later in the thesis to set constraints on the inner-loop tracking performance requirements that guarantee stability of the complete cooperative control architecture. As will become clear from the algorithms for path following and time coordination proposed later, a proper choice of the initial boundary conditions for the trajectory-generation problem may be required to ensure that these bounds can be satisfied at all times. A more relaxed—and realistic—assumption would be ultimate boundedness of the inner-loop tracking errors; under this assumption, the results in this thesis would still hold with a few modifications, especially affecting the initial transient phase. For simplicity, however, we assume that the performance bounds in (2.15) and (2.17) hold uniformly in time. From a practical perspective, these performance bounds—as well as the constraints on them derived in the following sections—should be seen as guidelines/specifications for the design of the inner-loop autopilots.* \triangle

Remark 5 *For the missions of interest, typical off-the-shelf autopilots are capable of providing uniform performance across the operational envelope of small autonomous vehicles while operating in nominal conditions. However, these commercial autopilots may fail to provide adequate performance in the event of actuator failures, partial vehicle damage, or in the presence of adverse environmental disturbances. Under these unfavorable circumstances, adaptive augmentation loops are seen as an appealing technology that can improve vehicle performance. In [28] and [50], for example, an \mathcal{L}_1 adaptive control architecture for UAV autopilot augmentation is presented that retains the properties of the onboard commercial autopilot and adjusts the autopilot commands only when the tracking performance degrades. Figure 2.7 shows the inner-loop control architecture considered in [28] and [50], with the adaptive augmentation loop wrapped around the autopilot. In this setup, the adaptive controller uses angular-rate and speed measurements to modify the commands generated by the outer-loop algorithms, which are then sent to the autopilot as references to be tracked. This structure for autopilot augmentation does not require any modifications to the autopilot itself, and at the same time it does not use internal states of the autopilot for control design purposes.* \triangle

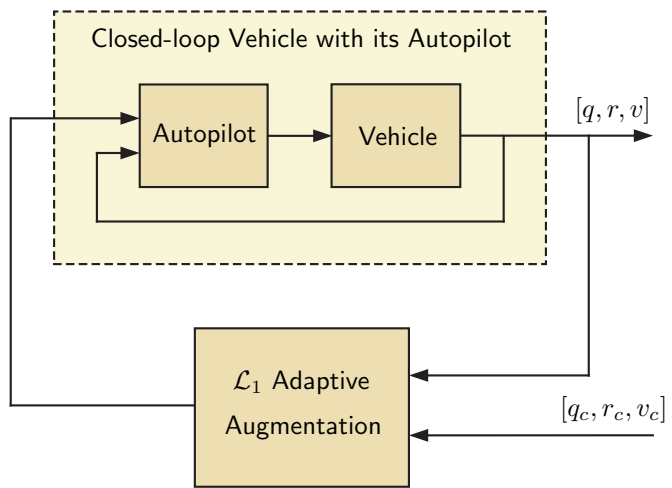


Figure 2.7: Inner-loop control structure with an \mathcal{L}_1 adaptive augmentation loop [28,50].

Chapter 3

3D Path-Following Control

This chapter describes an outer-loop path-following nonlinear control algorithm that uses vehicle angular rates to steer the i th vehicle along a 3D spatial path $\mathbf{p}_{d,i}(\cdot)$ for an arbitrary feasible temporal assignment along the path. Controller design builds on previous work on path-following control of small tactical UAVs, reported in [50], and derives a novel path-following control law on $\text{SO}(3)$ that avoids the geometric singularities and complexities that appear when dealing with local parameterizations of the vehicle's attitude. First, we address only the kinematic equations of the vehicle by taking pitch rate and yaw rate as virtual outer-loop control inputs. In particular, we show that there exist stabilizing functions for $q(t)$ and $r(t)$ leading to local exponential stability of the origin of the kinematic error dynamics with a prescribed domain of attraction. Then, we perform a stability analysis for the case of non-ideal inner-loop tracking and show that the path-following errors are locally uniformly ultimately bounded with the same domain of attraction. The results yield an efficient methodology to design path-following controllers for autonomous vehicles with due account for the vehicle kinematics and the characteristics of their inner-loop autopilots. For notational simplicity, in this chapter, we again drop the subscript i used to denote a particular vehicle.

3.1 Path-Following Control Law

3.1.1 Nonlinear Control Design using Vehicle Kinematics

Recall from Chapter 2 (Section 2.2.2) that the main objective of the path-following control algorithm is to drive the position error $\mathbf{p}_F(t)$ and the attitude error $\mathbf{e}_{\tilde{\mathbf{R}}}(t)$ to (a neighborhood of) zero. At the kinematic level, this objective can be achieved by determining feedback control laws for $q(t)$, $r(t)$, and $\dot{\ell}(t)$ that ensure that the origin of the kinematic error dynamics (2.11) is exponentially stable with a given domain of attraction. Figure 3.1 presents the kinematic closed-loop system considered in this section.

To solve the path-following problem, we first let the rate of progression of point P along the path be governed by

$$\dot{\ell} = (v \hat{\mathbf{w}}_1 + k_\ell \mathbf{p}_F) \cdot \hat{\mathbf{t}}, \quad (3.1)$$

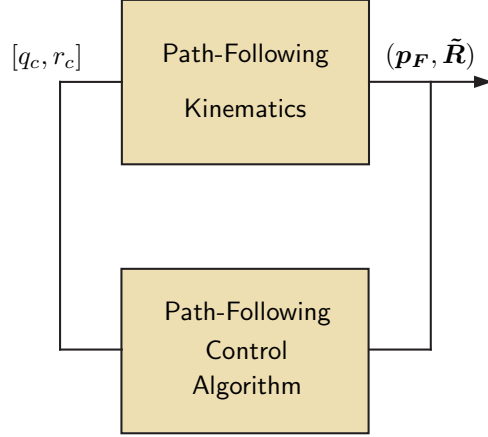


Figure 3.1: Path-following closed-loop system for a single vehicle solved at the kinematic level.

where k_ℓ is a positive constant gain. Then, the rate commands $q_c(t)$ and $r_c(t)$ given by

$$\begin{bmatrix} q_c \\ r_c \end{bmatrix} := \boldsymbol{\Pi}_R \tilde{\mathbf{R}}^\top (\mathbf{R}_F^D \{\omega_{F/I}\}_F + \{\omega_{D/F}\}_D) - 2k_{\tilde{R}} \mathbf{e}_{\tilde{\mathbf{R}}}, \quad (3.2)$$

where $k_{\tilde{R}}$ is also a positive constant gain, drive the path-following generalized error vector $\mathbf{x}_{pf}(t)$ to zero with a guaranteed rate of convergence. A formal statement of this result is given in the lemma below.

Lemma 1 *Assume that the vehicle speed $v(t)$ verifies the following bounds:*

$$0 < v_{\min} \leq v(t) \leq v_{\max}, \quad \text{for all } t \geq 0. \quad (3.3)$$

If, for given positive constants $c < \frac{1}{\sqrt{2}}$ and c_1 , we choose the path-following control parameters k_ℓ , $k_{\tilde{R}}$, and d such that

$$k_{\tilde{R}} \tilde{k}_\ell > \frac{v_{\max}^2}{c_1^2 (1 - 2c^2)^2}, \quad (3.4)$$

where \tilde{k}_ℓ is defined as

$$\tilde{k}_\ell := \min \left\{ k_\ell, \frac{v_{\min}}{(d^2 + c^2 c_1^2)^{\frac{1}{2}}} \right\}, \quad (3.5)$$

then the rate commands (3.2), together with the law (3.1) for the rate of progression of the virtual target along the path, ensure that the origin of the kinematic error equations (2.11) is exponentially stable with

guaranteed rate of convergence

$$\bar{\lambda}_{pf} := \frac{\tilde{k}_\ell + k_{\tilde{R}}(1 - c^2)}{2} - \frac{1}{2} \left(\left(\tilde{k}_\ell - k_{\tilde{R}}(1 - c^2) \right)^2 + \frac{4(1 - c^2)}{c_1^2(1 - 2c^2)^2} v_{\max}^2 \right)^{\frac{1}{2}} \quad (3.6)$$

and domain of attraction

$$\Omega_{pf} := \left\{ (\mathbf{p}_F, \tilde{\mathbf{R}}) \in \mathbb{R}^3 \times \text{SO}(3) \mid \Psi(\tilde{\mathbf{R}}) + \frac{1}{c_1^2} \|\mathbf{p}_F\|^2 \leq c^2 < \frac{1}{2} \right\}. \quad (3.7)$$

◇

Proof: The proof of this result, which uses some insight from [63], is given in Appendix C.1.

Remark 6 The choice of the characteristic distance d in the definition of auxiliary frame $\{\mathcal{D}\}$ (see Equation (2.7)) can be used to adjust the rate of convergence of the path-following error vector. This is consistent with the fact that a large parameter d reduces the penalty for cross-track position errors, which results in a small rate of convergence of the vehicle to the path. Figure 3.2 illustrates this point. When $d \sim \infty$, the vehicle never converges to the path, since $\omega_{D/F} = \mathbf{0}$. For large values of d , the term $\omega_{D/F}$ introduces only small corrections to the “feedforward” term $\omega_{F/I}$, and therefore the convergence of the vehicle to the desired path is slow. On the other hand, small values of d allow for higher rates of convergence (subject to the design of the gains k_ℓ and $k_{\tilde{R}}$), which however might result in oscillatory path-following behavior.

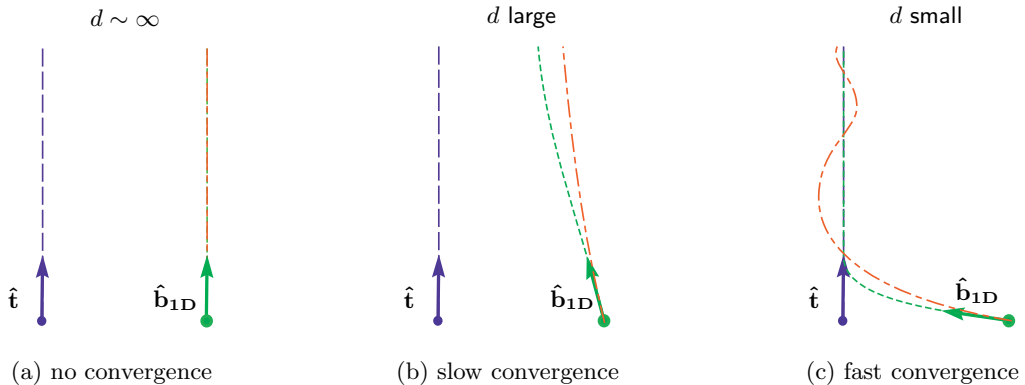


Figure 3.2: Effect of the characteristic distance d on the convergence of the vehicle to the path. In these plots, the blue line is the desired path, the green line represents the desired approach curve, and the red line corresponds to the resulting vehicle trajectory.

△

3.1.2 Stability Analysis for Non-Ideal Inner-Loop Tracking

The stabilizing control laws (3.1) and (3.2) lead to local exponential stability of the origin of the path-following kinematic error dynamics (2.11) with a prescribed domain of attraction. In general, this result does not hold when the dynamics of the vehicle are included in the problem formulation; see Figure 3.3. In this section, we perform a stability analysis of the path-following closed-loop system for the case of non-ideal inner-loop tracking. In particular, we assume that the onboard autopilot ensures that the vehicle is able to track bounded pitch-rate and yaw-rate commands with the performance bounds (2.15) and show that the path-following errors $\mathbf{p}_F(t)$ and $\mathbf{e}_{\tilde{\mathbf{R}}}(t)$ are locally uniformly ultimately bounded with the same domain of attraction Ω_{pf} . The next lemma states this result formally.

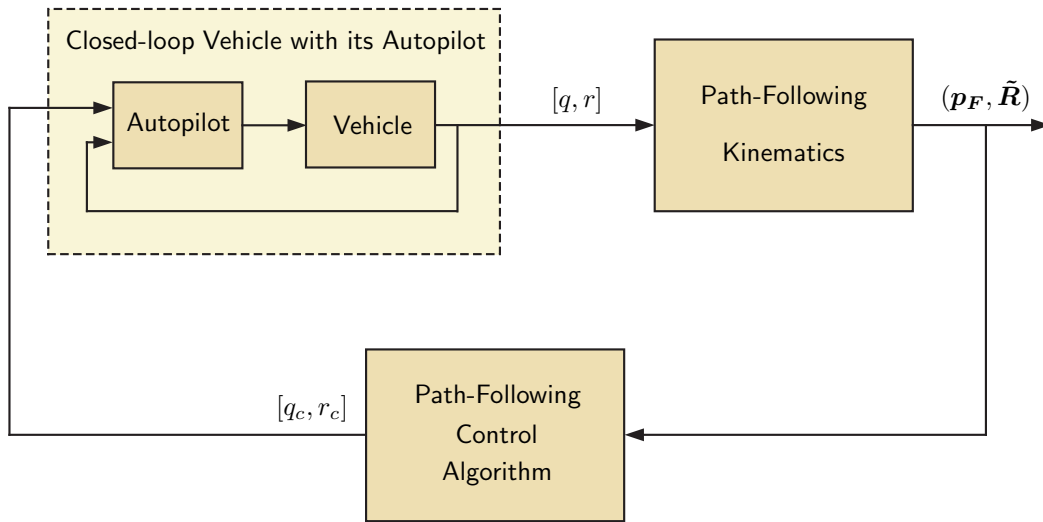


Figure 3.3: Path-following closed-loop system for a single vehicle.

Lemma 2 Assume that the vehicle speed $v(t)$ verifies the bounds in (3.3). For given positive constants $c < \frac{1}{\sqrt{2}}$ and c_1 , choose the path-following control parameters k_ℓ , $k_{\tilde{\mathbf{R}}}$, and d according to the design constraint (3.4). Further, let $\lambda_{pf} := \bar{\lambda}_{pf}(1 - \delta_\lambda)$, where $\bar{\lambda}_{pf}$ was defined in (3.6) and δ_λ is a positive constant verifying $0 < \delta_\lambda < 1$. If the performance bounds γ_q and γ_r in (2.15) satisfy the following inequality:

$$\gamma_\omega := (\gamma_q^2 + \gamma_r^2)^{\frac{1}{2}} < \frac{2c}{(1 - c^2)^{\frac{1}{2}}} \bar{\lambda}_{pf} \delta_\lambda, \quad (3.8)$$

then, for any initial state $(\mathbf{p}_F(0), \tilde{\mathbf{R}}(0)) \in \Omega_{pf}$, the rate commands (3.2), together with the law (3.1) for the rate of progression of the virtual target along the path, ensure that there is a time $T_b \geq 0$ such that the

path-following errors $\mathbf{p}_F(t)$ and $\mathbf{e}_{\tilde{\mathbf{R}}}(t)$ satisfy

$$\|\mathbf{e}_{\tilde{\mathbf{R}}}(t)\|^2 + \frac{1}{c_1^2} \|\mathbf{p}_F(t)\|^2 \leq \left(\frac{1}{1-c^2} \|\mathbf{e}_{\tilde{\mathbf{R}}}(0)\|^2 + \frac{1}{c_1^2} \|\mathbf{p}_F(0)\|^2 \right) e^{-2\lambda_{pf} t}, \quad \text{for all } 0 \leq t < T_b, \quad (3.9a)$$

$$\|\mathbf{e}_{\tilde{\mathbf{R}}}(t)\|^2 + \frac{1}{c_1^2} \|\mathbf{p}_F(t)\|^2 \leq \frac{(1-c^2) \gamma_\omega^2}{4\bar{\lambda}_{pf}^2 \delta_\lambda^2}, \quad \text{for all } t \geq T_b. \quad (3.9b)$$

◇

Proof: The proof of this result is given in Appendix C.2.

Remark 7 Inequalities (3.9) show that the path-following errors $\mathbf{p}_F(t)$ and $\mathbf{e}_{\tilde{\mathbf{R}}}(t)$ are uniformly bounded for all $t \geq 0$ and uniformly ultimately bounded with ultimate bounds

$$\|\mathbf{e}_{\tilde{\mathbf{R}}}(t)\| \leq \frac{(1-c^2)^{\frac{1}{2}}}{2\bar{\lambda}_{pf} \delta_\lambda} \gamma_\omega, \quad \|\mathbf{p}_F(t)\| \leq \frac{c_1(1-c^2)^{\frac{1}{2}}}{2\bar{\lambda}_{pf} \delta_\lambda} \gamma_\omega, \quad \text{for all } t \geq T_b.$$

These ultimate bounds are proportional to the inner-loop tracking performance bound γ_ω and, in the limit ideal case of perfect inner-loop tracking, one recovers the exponential stability result derived in Lemma 1. △

Remark 8 An implicit assumption in the results and derivations above is that the presence of wind and gusts does not result in the UAV flying at zero or “negative” groundspeed. This assumption also holds throughout the remainder of the thesis for all of the UAVs involved in the cooperative mission. In the case of strong winds that would violate this assumption, trajectory replanning with due account of wind conditions will be required. △

3.2 Implementation Details

In this section we briefly discuss some details about the practical implementation of the path-following control law proposed in this chapter:

- The strategy for path-following control adopted requires the definition of a parallel transport frame $\{\mathcal{F}\}$ attached to the virtual target on the path. This frame need not be computed online as the mission unfolds and, instead, the path can be framed before the actual execution of the mission. Path framing can, in fact, be implemented as a post-processing routine of trajectory generation. Algorithms for computation of parallel transport frames on a spatial 3D curve are discussed in [44]. Similarly, the normal development of the path, required to determine $\{\boldsymbol{\omega}_{F/I}\}_F$, can also be pre-computed as part of the trajectory-generation algorithm.

- The implementation of the law (3.1) and the rate commands (3.2) also requires the estimation of the inertial velocity vector of the UAV, which is necessary to define frame $\{\mathcal{W}\}$ and compute the rotation matrix $\tilde{\mathbf{R}}(t)$ as well as the attitude error $\mathbf{e}_{\tilde{\mathbf{R}}}(t)$. The inertial velocity vector can be estimated from inertial sensors and GPS measurements, generally available on UAVs.
- We also note that the control law (3.2) produces angular-rate commands defined in the $\{\mathcal{W}\}$ frame. However, typical commercial off-the-self autopilots accept rate commands defined in body-fixed frame. These two frames can differ significantly, especially for the case of small UAVs operating in high winds, which implies that the rate commands (3.2) need to be transformed to the body-fixed frame before they are sent to the onboard autopilot.
- Finally, since the path-following control law (3.1)-(3.2) is only guaranteed to work locally (see Lemmas 1 and 2), a secondary guidance loop is to be implemented that complements the angular-rate command (3.2) and, as soon as external disturbances push the vehicle outside the domain of attraction Ω_{pf} defined in (3.7), drives the vehicle's position and velocity vector back inside this domain.

3.3 Simulation Results

This section presents simulation results that illustrate the performance of the path-following algorithm proposed in this chapter. The simulations are based on the following kinematic model of the UAV:

$$\begin{aligned} \dot{\mathbf{p}}_I]_I &= v \hat{\mathbf{w}}_1, \\ \dot{\mathbf{R}}_W^I &= \mathbf{R}_W^I (\{\omega_{W/I}\}_W)^\wedge, \end{aligned} \tag{3.10}$$

along with a simplified, decoupled linear model describing the roll, pitch, yaw, and speed dynamics of the closed-loop UAV with its autopilot. In particular, the linear model used here corresponds to an identified second-order model of the SIG Rascal 110 research aircraft operated by the Naval Postgraduate School; see Chapter 7.

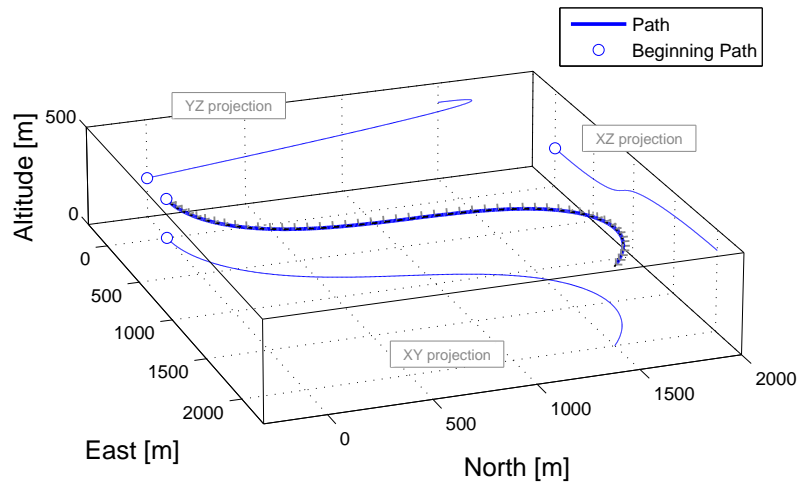
Figure 3.4 presents the desired path with the parallel transport frame, which is shown in light gray. The path consists of a left turn followed by a right turn, and climbs steadily from 200 m to 400 m. The total length of the path is 2,998.5 m, and its beginning is indicated with a circle. The figure also shows the normal development of the path (parameters k_1 and k_2) as well as the flight path angle along the path. For speeds within the operating range of the small UAVs considered here (ranging from 18 m/s to 32 m/s), the angular rates required to follow the path are well within feasible bounds.

Simulation results for this scenario are presented next. The path-following controller gains are selected as follows:

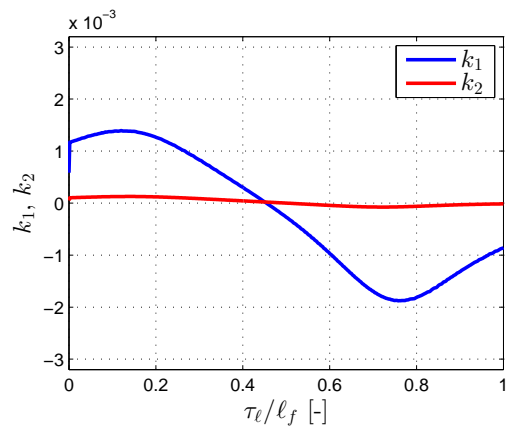
$$k_\ell = 0.20 \text{ [1/s]}, \quad k_{\tilde{R}} = 0.50 \text{ [1/s]}, \quad d = 125 \text{ [m]},$$

while the speed command is set to $v_c = 20 \text{ m/s}$. The angular-rate commands are saturated to $\pm 0.3 \text{ rad/s}$. Figure 3.5 illustrates the evolution of the UAV (blue) as well as the virtual target (red) moving along the path (green). This figure also includes the $\{\mathcal{W}\}$ frame attached to the UAV (blue) as well as the $\{\mathcal{F}\}$ frame attached to the virtual target (gray). Both the initial position and attitude of the UAV present an initial offset with respect to the beginning of the framed desired path. As can be seen in the figure, the path-following control algorithm eliminates this initial offset and steers the UAV along the path. Details about the performance of the path-following algorithm are shown in Figure 3.6; the path-following attitude and position errors, $\Psi(\tilde{\mathbf{R}}(t))$ and $\mathbf{p}_F(t)$, converge to a neighborhood of zero within 10 s and 40 s, respectively. The figure also presents the angular-rate commands, $q_c(t)$ and $r_c(t)$, the actual angular rates, $q(t)$ and $r(t)$, as well as the rate of progression, $\dot{\ell}(t)$, of the virtual target along the path.

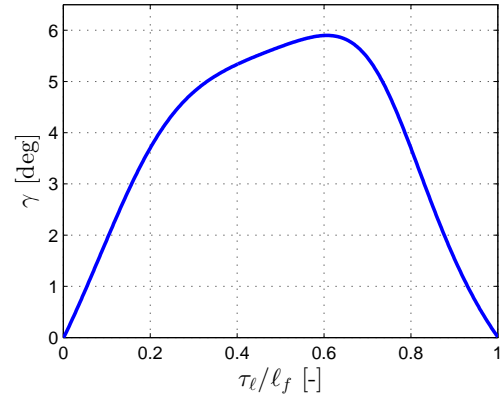
To illustrate the effect of the characteristic distance d on the convergence of the UAV to the path, Figures 3.7-3.8 and 3.9-3.10 show simulation results for the same scenario as Figures 3.5-3.6, but now with $d = 50 \text{ m}$ and $d = 250 \text{ m}$, respectively. As expected, a smaller characteristic distance leads to a faster convergence to the path; in fact, as can be seen in Figure 3.8, the cross-track error components $y_F(t)$ and $z_F(t)$ converge now to a neighborhood of zero in about 30 s, which also requires more aggressive angular-rate commands in order to align the UAV's velocity vector with the tangent vector to the path. Instead, a larger characteristic distance yields a slower convergence to the path; Figure 3.10 shows that the path-following cross-track error converges to a neighborhood of zero in about 60 s, with a much gentler angular-rate response. The ability of the characteristic distance d to shape the approach to the path can also be illustrated through the time-history of the projection of versor $\hat{\mathbf{w}}_1(t)$ onto the tangent versor to the path $\hat{\mathbf{t}}(t)$; see Figure 3.11. Clearly, as the characteristic distance decreases, the approach to the path becomes more aggressive, with UAV trajectories that run nearly perpendicular to the desired path.



(a) Framed 3D path



(b) Normal development, k_1 and k_2



(c) Flight path angle, γ

Figure 3.4: Framed 3D spatial path and main geometric properties.

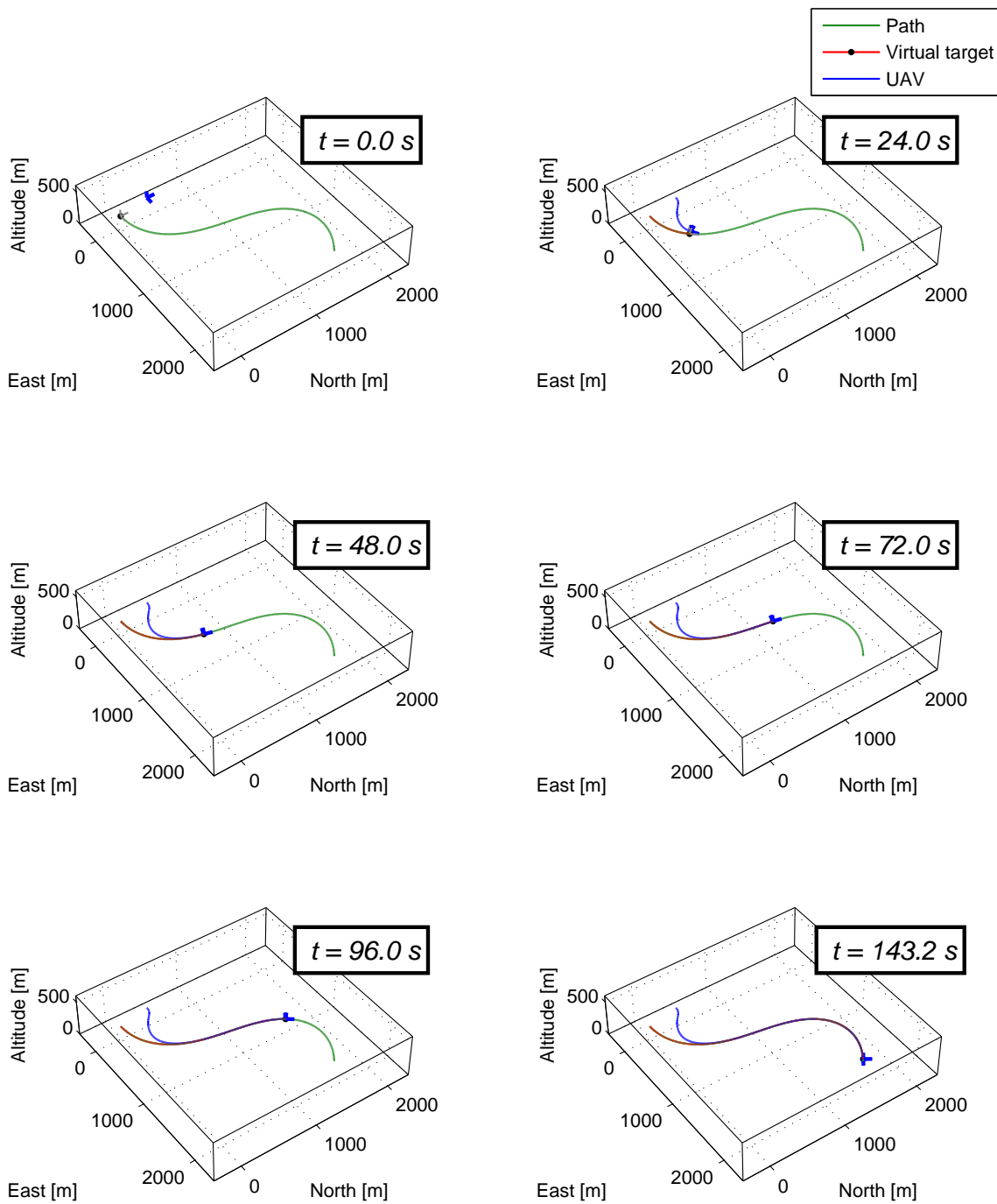


Figure 3.5: Path following of a single UAV.

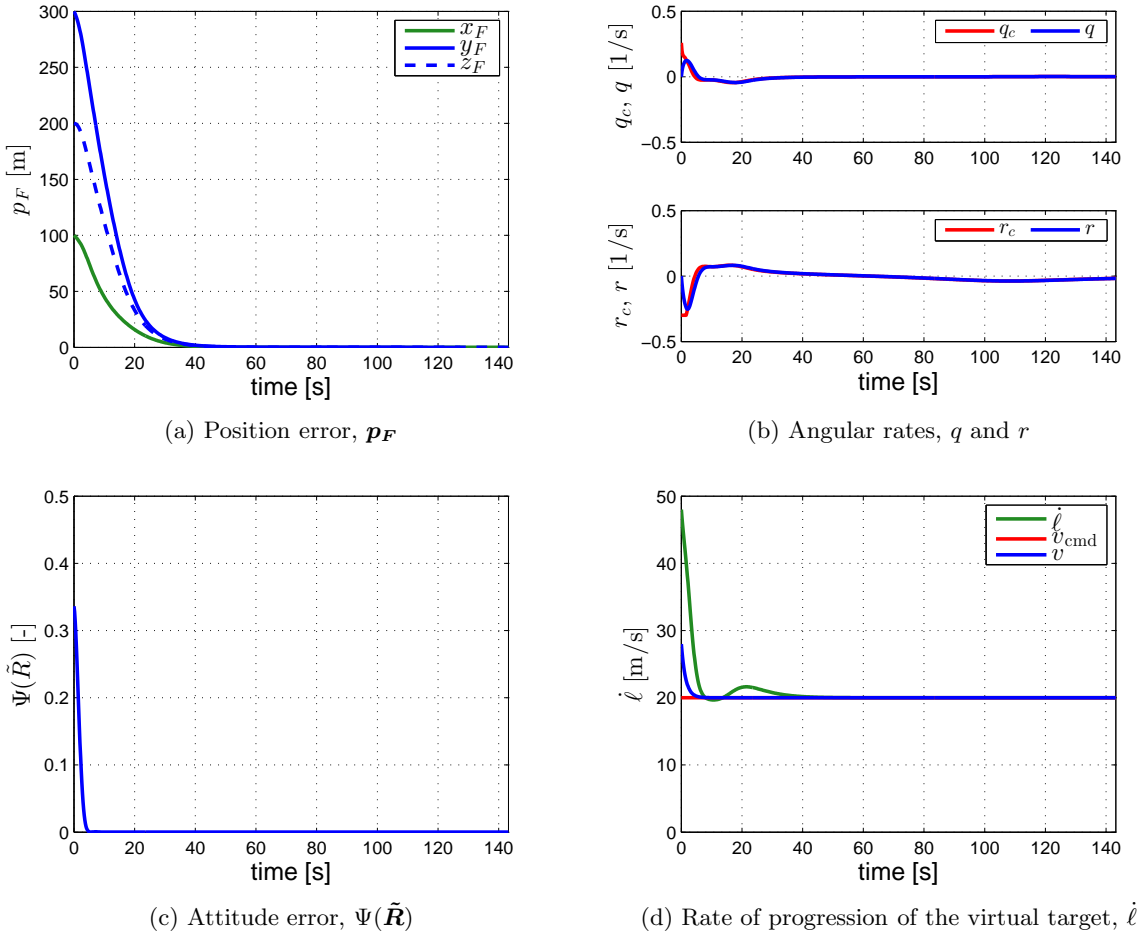


Figure 3.6: Path-following performance related to Figure 3.5.

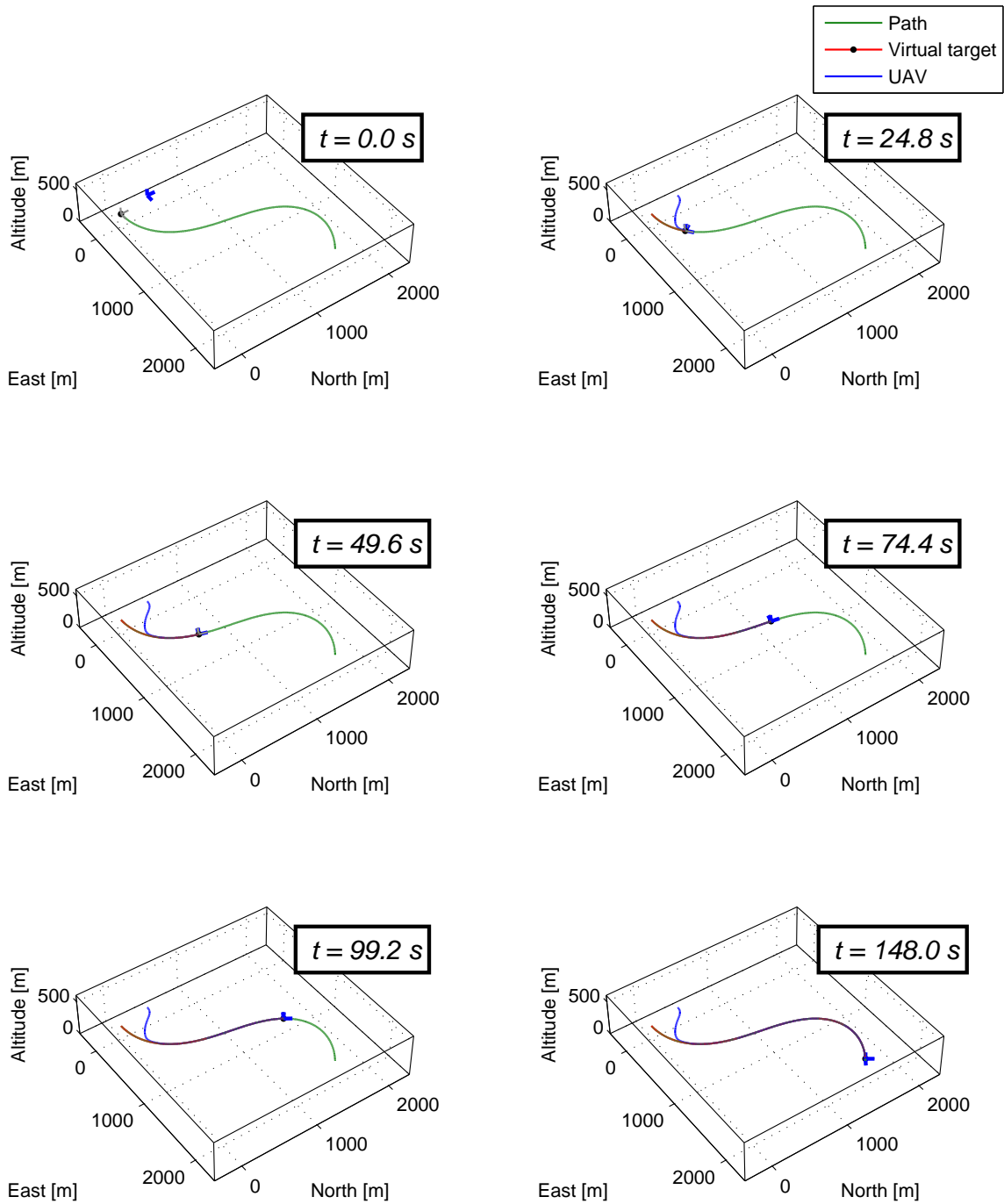


Figure 3.7: Path following of a single UAV; *fast* convergence to the path ($d = 50$ m).

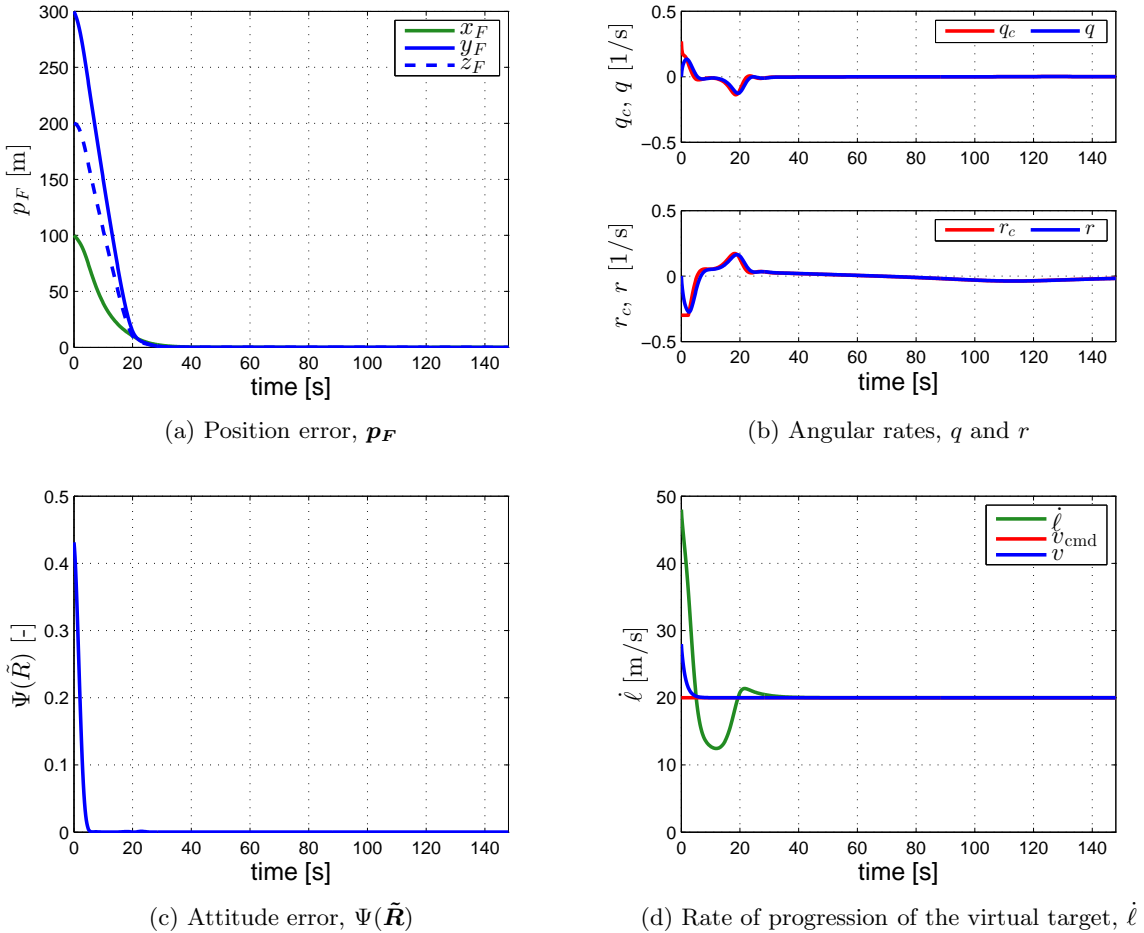


Figure 3.8: Path-following performance related to Figure 3.7.

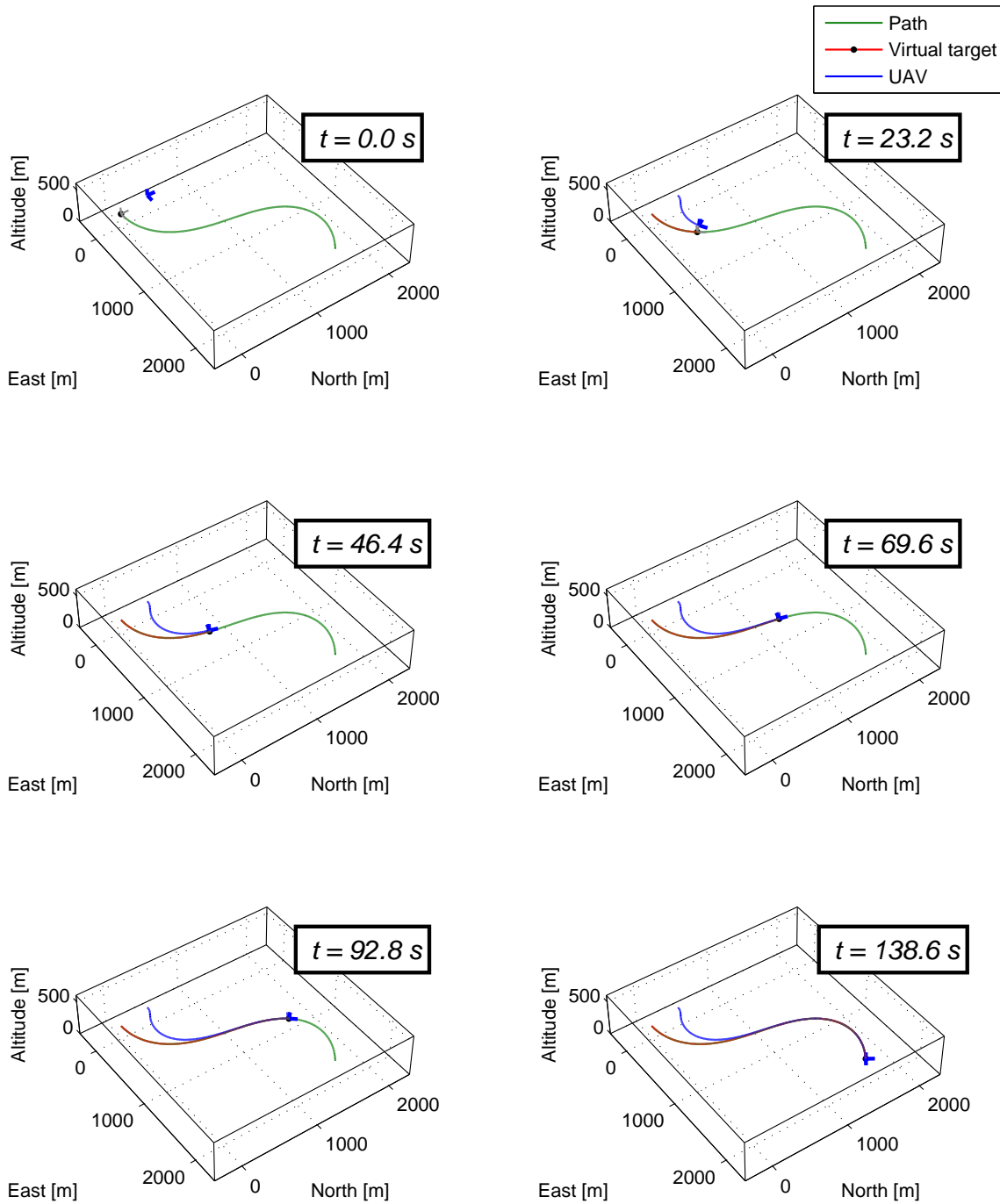


Figure 3.9: Path following of a single UAV; slow convergence to the path ($d = 250 \text{ m}$).

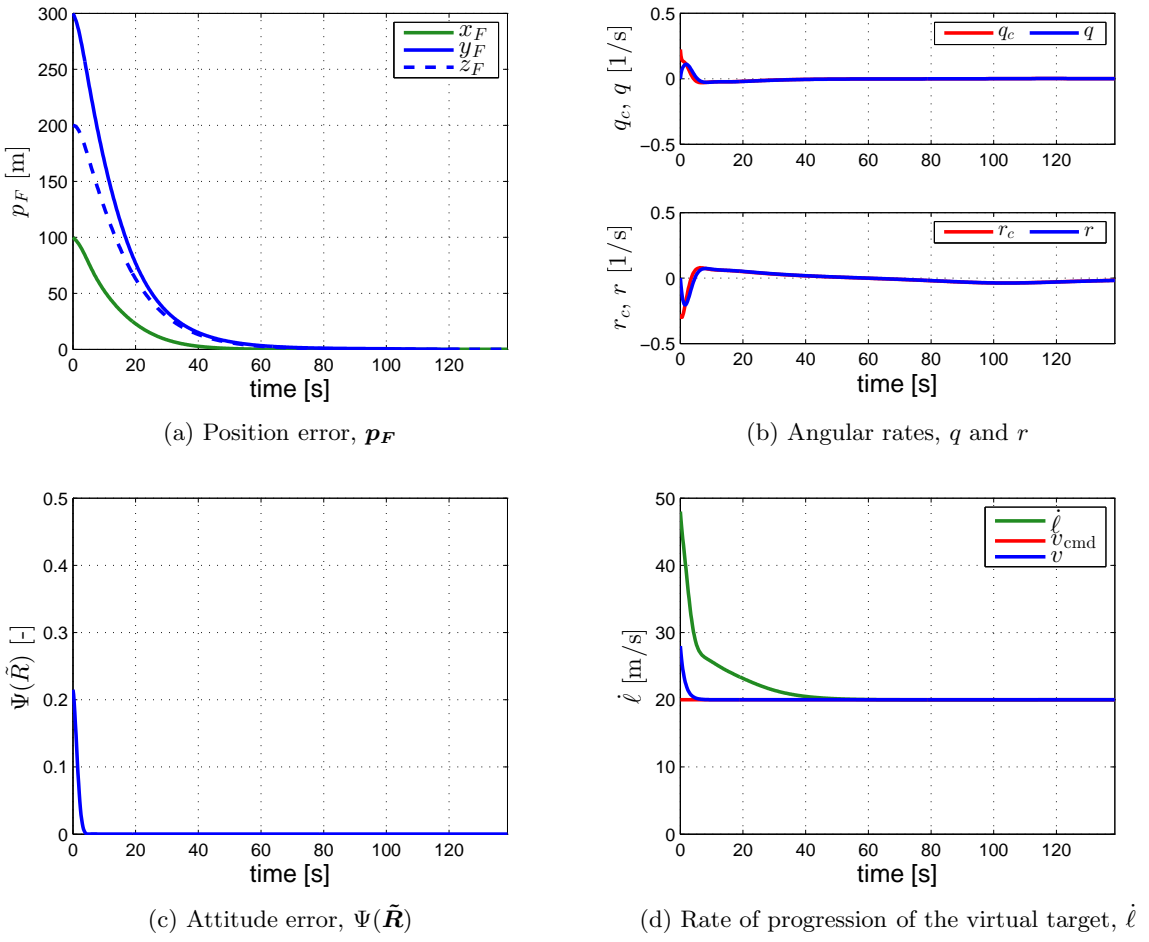


Figure 3.10: Path-following performance related to Figure 3.9.

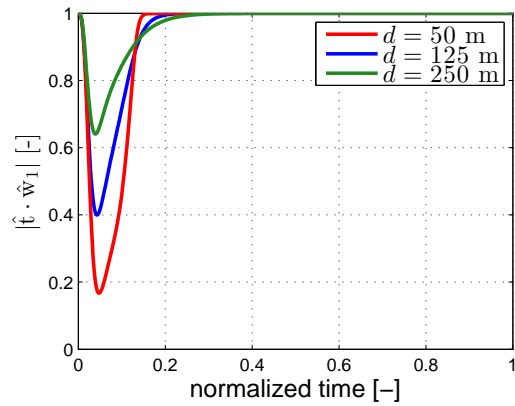


Figure 3.11: Projection of versor \hat{w}_1 onto the tangent versor to the path \hat{t} .

Chapter 4

Time-Critical Coordination

The previous chapter offered a solution to the path-following problem for a single vehicle and an arbitrary feasible speed profile by using a control strategy in which the vehicle's attitude control effectors are used to follow a virtual target running along the path. We now address the problem of time-critical cooperative control of multiple vehicles. To this effect, following the approach in [51], the speeds of the vehicles are adjusted based on coordination information exchanged among the vehicles over a supporting communications network. In particular, the outer-loop coordination control law derived in this chapter is intended to provide a correction to the desired speed profile $v_{d,i}(\cdot)$ obtained in the trajectory-generation step, and to generate a total speed command $v_{c,i}(t)$. This speed command is then to be tracked by the i th vehicle to achieve coordination in time.

4.1 Coordination Control Law

4.1.1 Speed Control using Vehicle Kinematics

As stated in Chapter 2 (Section 2.2.3), the main objective of the time-critical cooperative algorithm is to drive the coordination errors $(\xi_i(t) - \xi_j(t))$ and $(\dot{\xi}_i(t) - 1)$ to a neighborhood of the origin. To solve this coordination problem, we first note that the evolution of the i th coordination state is given by (see Appendix B.1)

$$\dot{\xi}_i = \frac{\dot{\ell}_i}{v_{d,i}(\xi_i)}.$$

Next, we recall from the solution to the path-following problem in Chapter 3 that the evolution of the i th virtual target vehicle along the path is given by

$$\dot{\ell}_i = (v_i \hat{\mathbf{w}}_{1,i} + k_\ell \mathbf{p}_{F,i}) \cdot \hat{\mathbf{t}}_i,$$

where for simplicity we keep k_ℓ without indexing. The dynamics of the i th coordination state can thus be

rewritten as

$$\dot{\xi}_i = \frac{(v_i \hat{\mathbf{w}}_{1,i} + k_\ell \mathbf{p}_{F,i}) \cdot \hat{\mathbf{t}}_i}{v_{d,i}(\xi_i)}.$$

At this point, it is important to note that, if the path-following control law can guarantee that, for every vehicle, the quantity $(\hat{\mathbf{w}}_{1,i} \cdot \hat{\mathbf{t}}_i)$ is positive and bounded away from zero for all $t \geq 0$, that is,

$$\hat{\mathbf{w}}_{1,i} \cdot \hat{\mathbf{t}}_i \geq c_2 > 0, \quad \text{for all } t \geq 0, \quad \text{and all } i \in \{1, \dots, n\}, \quad (4.1)$$

where c_2 is any constant satisfying $0 < c_2 \leq 1$, then we can use dynamic inversion and define the speed command for the i th vehicle as

$$v_{c,i} := \frac{u_{\text{coord},i} v_{d,i}(\xi_i) - k_\ell \mathbf{p}_{F,i} \cdot \hat{\mathbf{t}}_i}{\hat{\mathbf{w}}_{1,i} \cdot \hat{\mathbf{t}}_i}, \quad (4.2)$$

where $u_{\text{coord},i}(t)$ is a coordination control law to be defined later. At the kinematic level, this speed command leads to the following dynamics for the i th coordination state:

$$\dot{\xi}_i = u_{\text{coord},i}. \quad (4.3)$$

In the remainder of this section we assume that the bound in (4.1) holds for every vehicle and derive a coordination control law $u_{\text{coord},i}(t)$ that achieves coordination for the entire fleet of vehicles. This assumption will be verified later in Section 4.2, where we prove stability of the combined time-critical cooperative path-following closed-loop system and derive an expression for the constant c_2 .

Recall now that each vehicle is allowed to exchange only its coordination parameter $\xi_i(t)$ with its neighbors $\mathcal{N}_i(t)$, which are defined by the (possibly time-varying) communications topology. To observe this constraint, we propose the distributed coordination law

$$\begin{aligned} u_{\text{coord},i}(t) &= -k_P \sum_{j \in \mathcal{N}_i(t)} (\xi_i(t) - \xi_j(t)) + 1, & i = 1, \dots, n_\ell, \\ u_{\text{coord},i}(t) &= -k_P \sum_{j \in \mathcal{N}_i(t)} (\xi_i(t) - \xi_j(t)) + \chi_{I,i}(t), & i = n_\ell + 1, \dots, n, \\ \dot{\chi}_{I,i}(t) &= -k_I \sum_{j \in \mathcal{N}_i(t)} (\xi_i(t) - \xi_j(t)), \quad \chi_{I,i}(0) = 1, \end{aligned} \quad (4.4)$$

where vehicles 1 through n_ℓ , $n_\ell \leq n$, are elected as fleet leaders (which can be *virtual leaders*), and k_P and k_I are positive coordination control gains. Note that the coordination control law for the follower vehicles has a proportional-integral structure, which provides disturbance rejection capabilities at the coordination

level [102]. We also note that the leaders adjust their dynamics according to information exchanged with their neighboring vehicles, rather than running as isolated agents. Finally, we notice that the presence of multiple leaders can improve the robustness of the cooperative control architecture to a single-point vehicle failure.

The coordination law (4.4) can be rewritten in compact form as

$$\begin{aligned} \mathbf{u}_{\text{coord}} &= -k_P \mathbf{L}(t) \boldsymbol{\xi} + \begin{bmatrix} \mathbf{1}_{n_\ell} \\ \boldsymbol{\chi}_I \end{bmatrix}, \\ \dot{\boldsymbol{\chi}}_I &= -k_I \mathbf{C}^\top \mathbf{L}(t) \boldsymbol{\xi}, \quad \boldsymbol{\chi}_I(0) = \mathbf{1}_{n-n_\ell}, \end{aligned}$$

where $\mathbf{u}_{\text{coord}}(t)$, $\boldsymbol{\xi}(t)$, and $\boldsymbol{\chi}_I(t)$ are defined as

$$\begin{aligned} \mathbf{u}_{\text{coord}}(t) &:= [u_{\text{coord},1}(t), \dots, u_{\text{coord},n}(t)]^\top \in \mathbb{R}^n, \\ \boldsymbol{\xi}(t) &:= [\xi_1(t), \dots, \xi_n(t)]^\top \in \mathbb{R}^n, \\ \boldsymbol{\chi}_I(t) &:= [\chi_{I,n_\ell+1}(t), \dots, \chi_{I,n}(t)]^\top \in \mathbb{R}^{n-n_\ell}, \end{aligned}$$

the matrix \mathbf{C} is defined as $\mathbf{C}^\top := [\mathbf{0} \quad \mathbb{I}_{n-n_\ell}] \in \mathbb{R}^{(n-n_\ell) \times n}$, and $\mathbf{L}(t)$ is the Laplacian of the undirected graph $\Gamma(t)$ that captures the underlying bidirectional communications network topology of the fleet at time t . It is well known that the Laplacian of an undirected graph is symmetric, $\mathbf{L}^\top(t) = \mathbf{L}(t)$, and positive semi-definite, $\mathbf{L}(t) \geq 0$; $\lambda_1(\mathbf{L}(t)) = 0$ is an eigenvalue with eigenvector $\mathbf{1}_n$, $\mathbf{L}(t)\mathbf{1}_n = \mathbf{0}$; and the second smallest eigenvalue of $\mathbf{L}(t)$ is positive if and only if the graph $\Gamma(t)$ is connected.

At the kinematic level, the coordination law (4.4) leads to the closed-loop coordination dynamics

$$\begin{aligned} \dot{\boldsymbol{\xi}} &= -k_P \mathbf{L}(t) \boldsymbol{\xi} + \begin{bmatrix} \mathbf{1}_{n_\ell} \\ \boldsymbol{\chi}_I \end{bmatrix}, \quad \boldsymbol{\xi}(0) = \boldsymbol{\xi}_0, \\ \dot{\boldsymbol{\chi}}_I &= -k_I \mathbf{C}^\top \mathbf{L}(t) \boldsymbol{\xi}, \quad \boldsymbol{\chi}_I(0) = \mathbf{1}_{n-n_\ell}. \end{aligned} \tag{4.5}$$

To analyze the convergence properties of these collective dynamics, we reformulate the coordination problem stated above into a stabilization problem. To this end, we define the *coordination projection matrix* $\boldsymbol{\Pi}_{\boldsymbol{\xi}}$ as

$$\boldsymbol{\Pi}_{\boldsymbol{\xi}} := \mathbb{I}_n - \frac{\mathbf{1}_n \mathbf{1}_n^\top}{n},$$

and we note that $\boldsymbol{\Pi}_{\boldsymbol{\xi}} = \boldsymbol{\Pi}_{\boldsymbol{\xi}}^\top = \boldsymbol{\Pi}_{\boldsymbol{\xi}}^2$ and also that $\mathbf{Q}^\top \mathbf{Q} = \boldsymbol{\Pi}_{\boldsymbol{\xi}}$, where \mathbf{Q} is the $(n-1) \times n$ matrix introduced in (2.14)¹. Moreover, we have that $\mathbf{L}(t) \boldsymbol{\Pi}_{\boldsymbol{\xi}} = \boldsymbol{\Pi}_{\boldsymbol{\xi}} \mathbf{L}(t) = \mathbf{L}(t)$, and the spectrum of the matrix $\bar{\mathbf{L}}(t) := \mathbf{Q} \mathbf{L}(t) \mathbf{Q}^\top$ is equal to the spectrum of $\mathbf{L}(t)$ without the eigenvalue $\lambda_1 = 0$ corresponding to the

¹A proof of the equality $\mathbf{Q}^\top \mathbf{Q} = \boldsymbol{\Pi}_{\boldsymbol{\xi}}$ can be found in Appendix B.2.

eigenvector $\mathbf{1}_n$. Finally, we define the coordination error state $\zeta(t) := [\zeta_1^\top(t), \zeta_2^\top(t)]^\top$ as

$$\begin{aligned}\zeta_1(t) &:= \mathbf{Q} \xi(t) && \in \mathbb{R}^{n-1}, \\ \zeta_2(t) &:= \chi_I(t) - \mathbf{1}_{n-n_\ell} && \in \mathbb{R}^{n-n_\ell}.\end{aligned}\tag{4.6}$$

Note that, at the kinematic level, $\zeta(t) = \mathbf{0}$ is equivalent to $\xi(t) \in \text{span}\{\mathbf{1}_n\}$ and $\dot{\xi}(t) = \mathbf{1}_n$, which implies that, if $\zeta(t) = \mathbf{0}$, then at time t all target vehicles are coordinated and travel at the desired speed. With the above notation, the closed-loop coordination dynamics (4.5) can be reformulated as (see Appendix B.3)

$$\dot{\zeta} = \mathbf{A}_\zeta(t) \zeta, \quad \zeta(0) = \zeta_0, \tag{4.7}$$

where $\mathbf{A}_\zeta(t)$ is given by

$$\mathbf{A}_\zeta(t) := \begin{bmatrix} -k_P \bar{\mathbf{L}}(t) & \mathbf{Q} \mathbf{C} \\ -k_I \mathbf{C}^\top \mathbf{Q}^\top \bar{\mathbf{L}}(t) & \mathbf{0} \end{bmatrix} \in \mathbb{R}^{(2n-n_\ell-1) \times (2n-n_\ell-1)}. \tag{4.8}$$

Next we show that, if the connectivity of the communications graph $\Gamma(t)$ verifies the PE-like condition (2.14), then the coordination control law (4.4) solves the coordination control problem at the kinematic level. The next lemma summarizes this result.

Lemma 3 *Assume that the Laplacian of the graph that models the communications topology satisfies the PE-like condition (2.14) for some parameters $\mu, T > 0$. Then, there exist coordination control gains k_P and k_I such that the origin of the kinematic coordination error dynamics (4.7) is exponentially stable with guaranteed rate of convergence*

$$\bar{\lambda}_{cd} := \frac{k_P n \mu}{(1 + k_P n T)^2} \left(1 + \rho_k \frac{n}{n_\ell}\right)^{-1}, \quad \rho_k \geq 2. \tag{4.9}$$

Furthermore, the coordination states $\xi_i(t)$ and their rates of change $\dot{\xi}_i(t)$ satisfy

$$|\xi_i(t) - \xi_j(t)| \leq \kappa_{\xi 0} \|\zeta(0)\| e^{-\bar{\lambda}_{cd} t}, \quad \text{for all } i, j \in \{1, \dots, n\}, \tag{4.10}$$

$$|\dot{\xi}_i(t) - 1| \leq \kappa_{\dot{\xi} 0} \|\zeta(0)\| e^{-\bar{\lambda}_{cd} t}, \quad \text{for all } i \in \{1, \dots, n\}, \tag{4.11}$$

for some constants $\kappa_{\xi 0}, \kappa_{\dot{\xi} 0} \in (0, \infty)$. \diamondsuit

Proof: The proof of this result is given in Appendix C.3.

Remark 9 The proof of Lemma 3 is constructive and explicitly specifies a particular choice for the coordination control gains k_P and k_I that ensures exponential stability of the kinematic coordination error dynamics; see Equation (C.18) in Appendix C.3. \triangle

Remark 10 Lemma 3 above indicates that the guaranteed rate of convergence of the coordination control loop is limited by the QoS of the network (characterized by parameters T and μ). According to the lemma, for a given QoS of the network, the maximum (guaranteed) rate of convergence $\bar{\lambda}_{cd}^*$ is achieved by setting $k_P = \frac{1}{Tn}$, which results in

$$\bar{\lambda}_{cd}^* := \frac{\mu}{4T} \left(1 + \rho_k \frac{n}{n_\ell} \right)^{-1}, \quad \rho_k \geq 2.$$

Note that the convergence rate $\bar{\lambda}_c^*$ scales with the ratio (n_ℓ/n) . We also note that, as the parameter T goes to zero (and the graph becomes connected pointwise in time), the convergence rate can be set arbitrarily high by increasing the coordination control gains k_P and k_I . This is consistent with results obtained in previous work on cooperative path-following control; see [3, Lemma 2].

Finally, we notice that

$$\bar{\lambda}_{cd}^p := \frac{k_P n \mu}{(1 + k_P n T)^2}$$

represents the (guaranteed) convergence rate for the coordination loop with a proportional control law, rather than a proportional-integral control law (see Appendix C.3). It is straightforward to verify that, for a given proportional gain k_P , we have that $\bar{\lambda}_{cd} < \bar{\lambda}_{cd}^p$, which implies that a proportional control law can provide higher rates of convergence than the proportional-integral control law used in this thesis. However, as mentioned earlier and proven in [102], the integral term in the coordination control law is important in the current application as it improves the disturbance rejection capabilities at the coordination level. \triangle

4.1.2 Convergence Analysis for Non-Ideal Inner-Loop Tracking

When the dynamics of the vehicle are included in the problem formulation, the evolution of the i th coordination state with the speed command (4.2) becomes

$$\dot{\xi}_i = u_{\text{coord},i} + \frac{e_{v,i}}{v_{d,i}(\xi_i)} \hat{\mathbf{w}}_{1,i} \cdot \hat{\mathbf{t}}_i,$$

where $e_{v,i}(t) := v_i(t) - v_{c,i}(t)$ denotes the speed tracking error for the i th vehicle. In this case, the coordi-

nation law (4.4) leads to the closed-loop coordination dynamics

$$\begin{aligned}\dot{\boldsymbol{\xi}} &= -k_P \mathbf{L}(t) \boldsymbol{\xi} + \begin{bmatrix} \mathbf{1}_{n_\ell} \\ \boldsymbol{\chi}_I \end{bmatrix} + \mathbf{e}'_v, & \boldsymbol{\xi}(0) &= \boldsymbol{\xi}_0, \\ \dot{\boldsymbol{\chi}}_I &= -k_I \mathbf{C}^\top \mathbf{L}(t) \boldsymbol{\xi}, & \boldsymbol{\chi}_I(0) &= \mathbf{1}_{n-n_\ell},\end{aligned}$$

with $\mathbf{e}'_v(t) \in \mathbb{R}^n$ being a vector whose i th component is equal to $e'_{v,i} := \frac{e_{v,i}}{v_{d,i}(\xi_i)} \hat{\mathbf{w}}_{1,i} \cdot \hat{\mathbf{t}}_i$. Similar to the previous section, we can now derive the closed-loop coordination error dynamics, which become

$$\dot{\boldsymbol{\zeta}} = \mathbf{A}_\zeta(t) \boldsymbol{\zeta} + \mathbf{B}_\zeta \mathbf{e}'_v, \quad \boldsymbol{\zeta}(0) = \boldsymbol{\zeta}_0, \quad (4.12)$$

where $\mathbf{A}_\zeta(t)$ was defined in (4.8) and \mathbf{B}_ζ is given by

$$\mathbf{B}_\zeta := \begin{bmatrix} \mathbf{Q} \\ \mathbf{0} \end{bmatrix} \in \mathbb{R}^{(2n-n_\ell-1) \times n}.$$

The next lemma shows that, if the connectivity of the communications graph $\Gamma(t)$ verifies the PE-like condition (2.14), the coordination control law (4.4) solves the coordination control problem in a practical sense, and proves that the coordination error vector degrades gracefully with the size of the speed tracking error vector $\mathbf{e}_v(t) := [e_{v,1}(t), \dots, e_{v,n}(t)]^\top$.

Lemma 4 *Consider the coordination error dynamics (4.12) and suppose that the information flow satisfies the PE-like condition (2.14) for some parameters $\mu, T > 0$. Moreover, assume that the speed tracking error vector $\mathbf{e}_v(t)$ is a piecewise continuous, bounded function of t for all $t \geq 0$. Then, there exist coordination control gains k_P and k_I such that system (4.12) is input-to-state stable (ISS) with respect to $\mathbf{e}_v(t)$, satisfying*

$$\|\boldsymbol{\zeta}(t)\| \leq \kappa_{\zeta 0} \|\boldsymbol{\zeta}(0)\| e^{-\lambda_{cd} t} + \kappa_{\zeta 1} \sup_{\tau \in [0,t)} \|\mathbf{e}_v(\tau)\|, \quad \text{for all } t \geq 0, \quad (4.13)$$

for some constants $\kappa_{\zeta 0}, \kappa_{\zeta 1} \in (0, \infty)$, and with $\lambda_{cd} := \bar{\lambda}_{cd}(1 - \theta_\lambda)$, where $\bar{\lambda}_{cd}$ was defined in (4.9) and θ_λ is a constant verifying $0 < \theta_\lambda < 1$. Further, the coordination states $\xi_i(t)$ and their rates of change $\dot{\xi}_i(t)$ satisfy

$$|\xi_i(t) - \xi_j(t)| \leq \kappa_{\xi 0} \|\boldsymbol{\zeta}(0)\| e^{-\lambda_{cd} t} + \kappa_{\xi 1} \sup_{\tau \in [0,t)} \|\mathbf{e}_v(\tau)\|, \quad \text{for all } t \geq 0, \quad \text{and all } i, j \in \{1, \dots, n\}, \quad (4.14)$$

$$|\dot{\xi}_i(t) - 1| \leq \kappa_{\dot{\xi} 0} \|\boldsymbol{\zeta}(0)\| e^{-\lambda_{cd} t} + \kappa_{\dot{\xi} 1} \sup_{\tau \in [0,t)} \|\mathbf{e}_v(\tau)\|, \quad \text{for all } t \geq 0, \quad \text{and all } i \in \{1, \dots, n\}, \quad (4.15)$$

for some constants $\kappa_{\xi 0}, \kappa_{\xi 1}, \kappa_{\dot{\xi} 0}, \kappa_{\dot{\xi} 1} \in (0, \infty)$. ◊

Proof: The proof of this result is given in Appendix C.4.

Remark 11 If the desired speed profiles of all vehicles are constant along the corresponding paths, that is, $v_{d,i}(t_d) = v_{d,i}$ for all $t_d \in [0, t_d^*]$ and all $i \in \{1, \dots, n\}$, we have shown in Remark 1 that the normalized curvilinear abscissas $\ell'_i(t)$ can be used as coordination states. In this case, the dynamics of the i th coordination state can be written as

$$\dot{\ell}'_i = \frac{(v_i \hat{\mathbf{w}}_{1,i} + k_\ell \mathbf{p}_{F,i}) \cdot \hat{\mathbf{t}}_i}{\ell_{fi}}, \quad i = 1, \dots, n,$$

which implies that the speed commands $v_{c,i}(t)$ can be generated as

$$v_{c,i} := \frac{u_{\text{coord},i} \ell_{fi} - k_\ell \mathbf{p}_{F,i} \cdot \hat{\mathbf{t}}_i}{\hat{\mathbf{w}}_{1,i} \cdot \hat{\mathbf{t}}_i}, \quad i = 1, \dots, n,$$

where $u_{\text{coord},i}(t)$ is now given by

$$\begin{aligned} u_{\text{coord},i}(t) &= -k_P \sum_{j \in \mathcal{N}_i(t)} (\ell'_i(t) - \ell'_j(t)) + \frac{v_{d,i}}{\ell_{fi}}, \quad i = 1, \dots, n_\ell, \\ u_{\text{coord},i}(t) &= -k_P \sum_{j \in \mathcal{N}_i(t)} (\ell'_i(t) - \ell'_j(t)) + \chi_{I,i}(t) \\ \dot{\chi}_{I,i}(t) &= -k_I \sum_{j \in \mathcal{N}_i(t)} (\ell'_i(t) - \ell'_j(t)), \quad \chi_{I,i}(0) = \frac{v_{d,i}}{\ell_{fi}}, \quad i = n_\ell + 1, \dots, n. \end{aligned}$$

This formulation admits analyses similar to the ones in Lemmas 3 and 4 with analogous results. \triangle

Remark 12 To effectively solve the coordination problem in the presence of winds and gusts, it is beneficial to implement the fleet leaders as virtual agents with “uncertainty-free dynamics” (in our case, no groundspeed tracking error). This fact was illustrated through simulation in [102], where we also proposed a methodology to add these virtual agents and derived a lower bound on the QoS of the resulting extended communications network. In the setup adopted in [102], the virtual agents (along with the corresponding coordination control law) act as local controllers that ensure that the fleet of vehicles reaches the desired agreement. \triangle

4.2 Combined Path Following and Time-Critical Coordination

Chapter 3 and Section 4.1 have shown that, under an appropriate set of assumptions, the path-following and coordination control laws are able to ensure stability of the path-following and time-critical coordination dynamics when treated separately. In particular, the solution developed for the path-following problem assumes that the speed of the vehicle is bounded above and below, while the control law designed for vehicle coordination relies on the assumption that the angle between the vehicle’s velocity vector and the

tangent direction to the path is less than 90 deg (see Equations (3.3) and (4.1)). This section addresses the convergence properties of the combined cooperation and path-following systems, and derives design constraints for the inner-loop tracking performance bounds that guarantee stability of the complete system. The overall cooperative path-following control architecture for the i th vehicle is presented in Figure 4.1.

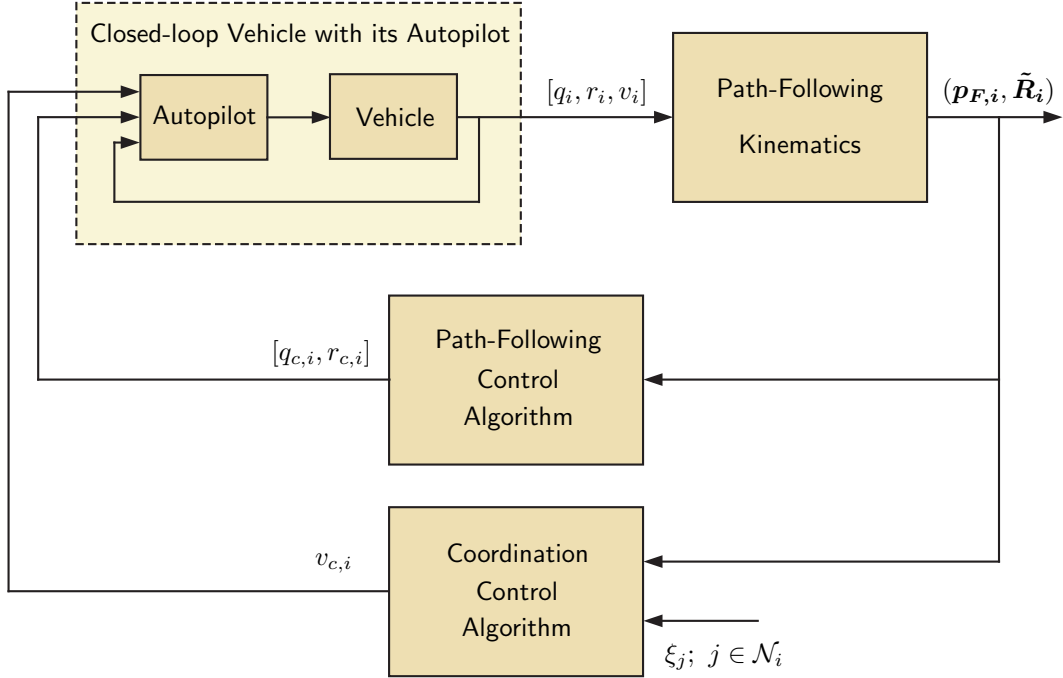


Figure 4.1: Time-critical cooperative path-following closed-loop for a single vehicle.

4.2.1 Stability Analysis at the Kinematic Level

We start by analyzing the stability of the cooperative path-following closed-loop system at the kinematic level. To this effect, we consider the path-following kinematic error dynamics (2.11) and the coordination-state dynamics (4.3), and show that the rate commands (3.2) and the speed command (4.2) with the coordination control law (4.4) solve the time-critical cooperative path-following problem with guaranteed rates of convergence. The next theorem states this result formally for the case of spatially deconflicted trajectories (see Chapter 2, Section 2.2.1). Stability conditions for the case of time-deconflicted trajectories are given in Remark 13.

Theorem 1 Consider a fleet of n vehicles supported by a communications network that verifies the PE-like condition (2.14), and a set of desired spatially deconflicted 3D time-trajectories. Let c and c_1 be positive constants satisfying $c < \frac{1}{\sqrt{2}}$ and $c_1 < \frac{E}{2c}$ and, for each UAV, choose the path-following control parameters k_ℓ , $k_{\tilde{R}}$, and d such that

$$d > \frac{2(1 - c^2)^{\frac{1}{2}}}{1 - 2c^2} cc_1, \quad k_{\tilde{R}} \tilde{k}_\ell > \frac{v_{\max}^2}{c_1^2(1 - 2c^2)^2}, \quad (4.16)$$

where \tilde{k}_ℓ was defined in (3.5). Also, let $\rho_k \geq 2$ and set the coordination control gains k_P and k_I such that

$$k_P > 0, \quad \frac{k_I}{k_P} = \frac{k_P n \mu}{(1 + k_P n T)^2} \frac{\rho_k \frac{n}{n_\ell}}{1 + \rho_k \frac{n}{n_\ell}}. \quad (4.17)$$

Then, for all initial conditions

$$(\mathbf{p}_{F,i}(0), \tilde{\mathbf{R}}_i(0)) \in \Omega_{pf}, \quad i = 1, \dots, n, \quad (4.18)$$

$$\|\zeta(0)\| \leq \frac{1}{\kappa_{\zeta 0} \kappa_1} \min \left\{ \left(1 - \frac{v_{\min} + k_\ell c c_1}{v_{d \min}} \right), \left(\frac{v_{\max} c_2 - k_\ell c c_1}{v_{d \max}} - 1 \right) \right\}, \quad (4.19)$$

where $\kappa_1 = 2k_P \left(\frac{(n-1)^3}{n} \right)^{\frac{1}{2}} + 1$ and $c_2 = \frac{(1-2c^2)d-2c(1-c^2)^{\frac{1}{2}}cc_1}{(d^2+(cc_1)^2)^{\frac{1}{2}}}$, the progression law (3.1), the angular-rate commands (3.2), and the speed commands (4.2) with the coordination control law (4.4) ensure, first, that the speed of each vehicle satisfies

$$v_{\min} \leq v_i(t) \leq v_{\max}, \quad \text{for all } t \geq 0, \quad \text{and all } i \in \{1, \dots, n\}, \quad (4.20)$$

and, second, that the origin of the path-following kinematic error dynamics (2.11) and the origin of the kinematic coordination error dynamics (4.7) are exponentially stable with guaranteed rates of convergence $\bar{\lambda}_{pf}$ and $\bar{\lambda}_{cd}$, respectively. \diamond

Proof: The proof of this result is given in Appendix C.5.

Remark 13 In the case of time-deconflicted trajectories, the initial conditions of the kinematic coordination error dynamics have to satisfy the following additional inequality:

$$\|\zeta(0)\| < \frac{E - 2cc_1}{\kappa_{\zeta 0} v_{d \max}},$$

which ensures that no two vehicles are at the same place at the same time. \triangle

4.2.2 Stability Analysis with Inner-loop Autopilots

Next, we analyze stability of the cooperative path-following dynamics assuming that each UAV is equipped with an onboard autopilot designed to stabilize the vehicle and to provide angular-rate as well as speed tracking capabilities. In particular, in this section, we make the assumption that each vehicle is able to track bounded pitch-rate, yaw-rate, as well as speed commands with the performance bounds (2.15) and (2.17).

At this point, we note that, while the pitch-rate and yaw-rate commands (3.2) are continuous in time, the same cannot be said about the speed command (4.2). In fact, due to the time-varying nature of the network topology, the coordination law (4.4) is discontinuous, which implies that the speed command $v_{c,i}(t)$ is also discontinuous. Note that, if the bound

$$|v_{c,i}(t) - v_i(t)| \leq \gamma_v \quad (4.21)$$

holds for all $t \geq 0$ and all vehicles, implying that $\sup_{t \geq 0} \|e_v(t)\| \leq \sqrt{n} \gamma_v$, then an upper bound $\Delta v_{c,i}$ on jumps in the speed command $v_{c,i}(t)$ can be derived from (4.2), (4.4), and the results of Lemma 4, and is given by

$$\Delta v_{c,i} = \frac{k_P(n-1)(\kappa_{\xi_0}\|\zeta(0)\| + \kappa_{\xi_1}\sqrt{n}\gamma_v)v_{d\max}}{c_2}, \quad i = 1, \dots, n.$$

A necessary (but by no means sufficient!) condition for the bound in (4.21) to hold is thus:

$$\Delta v_{c,i} < \gamma_v, \quad i = 1, \dots, n.$$

The above condition limits the choice of the coordination control gains, which in particular need to satisfy the following inequality:

$$k_P(n-1)\kappa_{\xi_1}\sqrt{n}v_{d\max} < c_2.$$

The derivation of sufficient conditions ensuring that the bound in (2.17) holds for all $t \geq 0$ requires, however, assumptions on vehicle dynamics and autopilot design, and is thus beyond the scope of this thesis. Hence, for the subsequent developments, we make the assumption that the bound in (2.17) holds —provided the speed command $v_{c,i}(t)$ satisfies the bounds in (2.16)—, and derive design constraints for this inner-loop tracking performance bound that ensure that the overall time-critical cooperative path-following control system is stable and has desired convergence properties.

The next theorem summarizes the stability and convergence properties of the time-critical cooperative path-following control system for the case of spatially deconflicted trajectories.

Theorem 2 Consider a fleet of n vehicles supported by a communications network that verifies the PE-like condition (2.14), and a set of desired spatially deconflicted 3D time-trajectories. For given positive constants c and c_1 satisfying $c < \frac{1}{\sqrt{2}}$ and $c_1 < \frac{E}{2c}$, choose the path-following control parameters k_ℓ , $k_{\tilde{R}}$, and d according to the design constraints (4.16). Also, let $\rho_k \geq 2$, and set the coordination control gains k_P and k_I as in (4.17). Further, let $\lambda_{pf} := \bar{\lambda}_{pf}(1 - \delta_\lambda)$ and $\lambda_{cd} := \bar{\lambda}_{cd}(1 - \theta_\lambda)$, where δ_λ and θ_λ are positive constants verifying $0 < \delta_\lambda, \theta_\lambda < 1$. If the performance bounds γ_q , γ_r , and γ_v satisfy

$$(\gamma_q^2 + \gamma_r^2)^{\frac{1}{2}} < \frac{2c}{(1-c^2)^{\frac{1}{2}}} \bar{\lambda}_{pf} \delta_\lambda, \quad (4.22)$$

$$\gamma_v < \min \left\{ \frac{v_{d\min} - (v_{\min} + k_\ell c c_1)}{1 + \kappa_1 \kappa_{\zeta 1} \sqrt{n} v_{d\min}}, \frac{(v_{\max} c_2 - k_\ell c c_1) - v_{d\max}}{c_2 + \kappa_1 \kappa_{\zeta 1} \sqrt{n} v_{d\max}} \right\}, \quad (4.23)$$

then, for all initial conditions

$$(\mathbf{p}_{F,i}(0), \tilde{\mathbf{R}}_i(0)) \in \Omega_{pf}, \quad i = 1, \dots, n, \quad (4.24)$$

$$\|\zeta(0)\| \leq \frac{1}{\kappa_{\zeta 0} \kappa_1} \min \left\{ \left(1 - \frac{v_{c\min} + k_\ell c c_1}{v_{d\min}} \right), \left(\frac{v_{c\max} c_2 - k_\ell c c_1}{v_{d\max}} - 1 \right) \right\} - \frac{\kappa_{\zeta 1}}{\kappa_{\zeta 0}} \sqrt{n} \gamma_v, \quad (4.25)$$

the progression law (3.1), the rate commands (3.2), and the speed commands (4.2) with the coordination control law (4.4) ensure, first, that the speed of each vehicle satisfies

$$v_{\min} \leq v_i(t) \leq v_{\max}, \quad \text{for all } t \geq 0, \quad \text{and all } i \in \{1, \dots, n\}, \quad (4.26)$$

and, second, that there exist times $T_{b,i} \geq 0$ such that the path-following errors $\mathbf{p}_{F,i}(t)$ and $\mathbf{e}_{\tilde{\mathbf{R}},i}(t)$, $i = 1, \dots, n$, satisfy

$$\|\mathbf{e}_{\tilde{\mathbf{R}},i}(t)\|^2 + \frac{1}{c_1^2} \|\mathbf{p}_{F,i}(t)\|^2 \leq \left(\frac{1}{1-c^2} \|\mathbf{e}_{\tilde{\mathbf{R}},i}(0)\|^2 + \frac{1}{c_1^2} \|\mathbf{p}_{F,i}(0)\|^2 \right) e^{-2\lambda_{pf} t}, \quad \text{for all } 0 \leq t < T_{b,i}, \quad (4.27a)$$

$$\|\mathbf{e}_{\tilde{\mathbf{R}},i}(t)\|^2 + \frac{1}{c_1^2} \|\mathbf{p}_{F,i}(t)\|^2 \leq \frac{(1-c^2) \gamma_\omega^2}{4\bar{\lambda}_{pf}^2 \delta_\lambda^2}, \quad \text{for all } t \geq T_{b,i}, \quad (4.27b)$$

while the coordination error state $\zeta(t)$ satisfies

$$\|\zeta(t)\| \leq \kappa_{\zeta 0} \|\zeta(0)\| e^{-\lambda_{cd} t} + \kappa_{\zeta 1} \sqrt{n} \gamma_v, \quad \text{for all } t \geq 0. \quad (4.28)$$

◊

Proof: The proof of this result is given in Appendix C.6.

Remark 14 In the case of time-deconflicted trajectories, the initial conditions of the coordination error dynamics have to satisfy the following additional inequality:

$$\|\zeta(0)\| < \frac{E - 2cc_1}{\kappa_{\xi_0} v_{d\max}} - \frac{\kappa_{\zeta_1}}{\kappa_{\zeta_0}} \sqrt{n} \gamma_v ,$$

which ensures that no two vehicles are at the same place at the same time. \triangle

4.3 Implementation Details

In this section, similar to Section 3.2 in Chapter 3, we briefly discuss some details about the practical implementation of the coordination control law proposed in this chapter:

- The strategy for time-coordination adopted in this thesis requires the groundspeed of each vehicle to be adjusted based on coordination information exchanged among the vehicles. However, typical commercial off-the-shelf autopilots accept airspeed commands. These two speeds can differ significantly, especially for the case of small UAVs operating in high winds, which implies that the speed command (4.2) needs to be transformed to an airspeed command before being sent to the autopilot. This transformation requires the integration of a wind estimator into the coordination control architecture. Note that some commercial autopilots, such as the Piccolo Plus autopilot², are capable of generating a rough estimate of winds aloft.
- For safety reasons, the airspeed command sent to the autopilot is first saturated between a minimum and a maximum value. Anti-windup compensation is thus needed to prevent the integral term of the coordination control law from winding up, which could lead to highly oscillatory speed commands or even closed-loop instability. A possible solution is to feed back the difference between the saturated airspeed command and the unsaturated airspeed command to the input of the integrator:

$$\dot{\chi}_{I,i}(t) = -k_I \sum_{j \in \mathcal{N}_i(t)} (\xi_i(t) - \xi_j(t)) + k_{aw} [G_{aw}(s)] (\text{sat}(v_{c,i}(t)) - v_{c,i}(t)) , \quad \chi_{I,i}(0) = 1 ,$$

where k_{aw} is the anti-windup feedback gain and $G_{aw}(s)$ is a stable, low-pass transfer function.

- In addition, to prevent division by zero when computing the speed command (4.2), the quantity $\hat{\mathbf{w}}_{1,i} \cdot \hat{\mathbf{t}}_i$ is to be saturated below a certain (small) positive value.

²Information available online at http://www.cloudcaptech.com/piccolo_system.shtml [Online; accessed 8 March 2013].

4.4 Simulation Results

This section presents simulation results of two cooperative multi-vehicle mission scenarios that show the efficacy of the cooperative framework proposed in this thesis. In the first mission, three UAVs must execute a coordinated maneuver to arrive at predefined positions at the same time. We then consider a second mission in which three UAVs must execute sequential auto-landing while maintaining a pre-specified safe-guarding separation along the glide slope. Similar to the results presented in Chapter 3, simulations here are based on the kinematic model of the UAV in (3.10) along with a simplified, decoupled linear model describing the roll, pitch, yaw, and speed dynamics of the closed-loop UAV with its autopilot.

In this set of simulations, the path-following controller gains are selected as follows:

$$k_\ell = 0.20 \text{ [1/s]}, \quad k_{\tilde{R}} = 0.50 \text{ [1/s]}, \quad d = 125 \text{ [m]},$$

while the coordination control gains k_P and k_I , and the anti-windup compensation are set to

$$k_P = 1.0 \cdot 10^{-1} \text{ [1/s]}, \quad k_I = 1.0 \cdot 10^{-2} \text{ [1/s}^2], \quad k_{aw} = 2.0 \cdot 10^{-3} \text{ [1/m]}, \quad G_{aw}(s) = \frac{1}{s+1}.$$

In all of the simulations, vehicle 1 is elected as the single leader of the fleet. The angular-rate commands are saturated to ± 0.3 rad/s, and the speed commands are saturated between 18 m/s and 32 m/s. To achieve coordination, the UAVs rely on a supporting communications network. The information flow is assumed to be time-varying and, at any given time t , is characterized by one of the graphs in Figure 4.2.

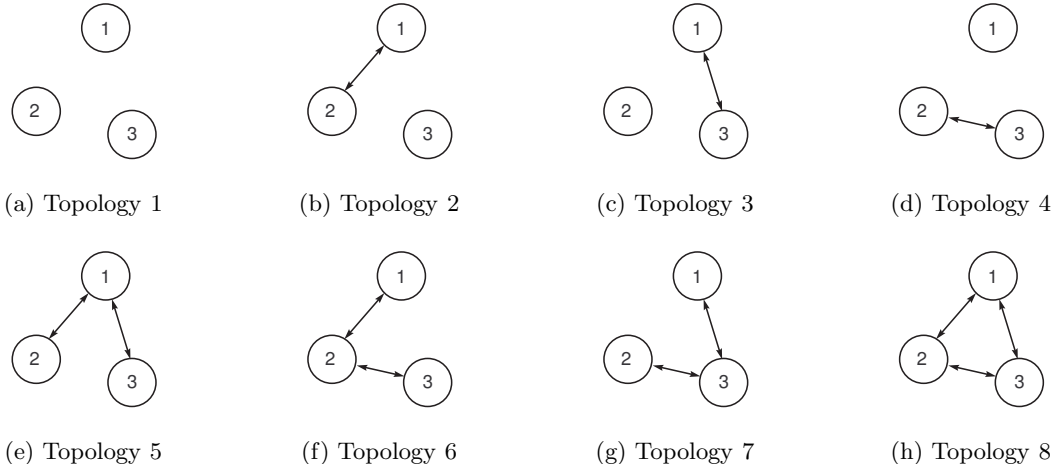


Figure 4.2: Network topologies. At any given time t , the dynamic information flow is characterized by one of these graphs.

4.4.1 Path Following with Simultaneous Arrival

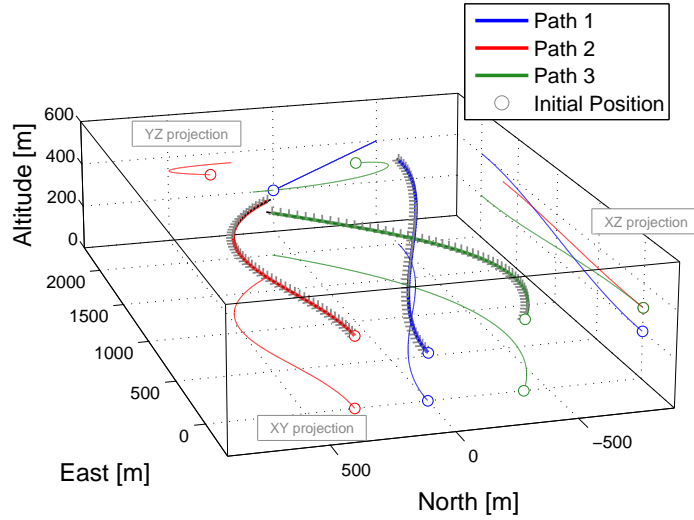
In this mission scenario, three UAVs are tasked to converge to and follow three spatially deconflicted paths and arrive at their final destinations at the same time. A representative example of such mission is simultaneous suppression of multiple targets located at different positions. Note that this mission imposes only *relative* temporal constraints on the arrival of the UAVs.

Figure 4.3 shows the three paths with the parallel transport frames as well as the corresponding desired speed profiles, which assume a final desired speed of 20 m/s for all UAVs. The beginning of each path is indicated in this figure with a circle. The figure also shows the coordination maps η_i relating the desired normalized curvilinear abscissa $\ell'_{d,i}$ to the desired mission time t_d . The paths have lengths $\ell_{f1} = 2,084.8$ m, $\ell_{f2} = 1,806.4$ m, and $\ell_{f3} = 2,221.0$ m, and the desired time of arrival is $t_d^* = 85.0$ s. Figure 4.4 presents the path separations, which show a minimum spatial clearance between paths of approximately 125 m, and the desired inter-vehicle separations for this particular mission.

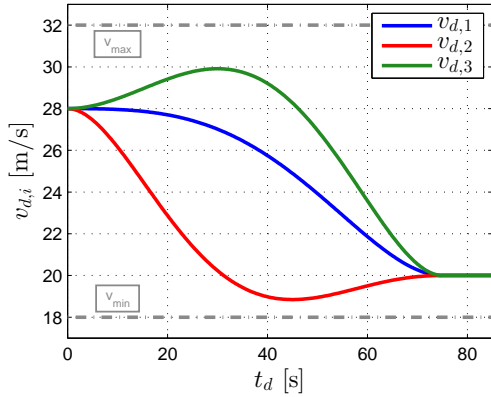
Simulation results are presented next. Figure 4.5 illustrates the evolution of the UAVs (blue) as well as the virtual targets (red) moving along the paths (green). This figure also includes the $\{\mathcal{W}\}$ frame attached to each UAV (blue) as well as the $\{\mathcal{F}\}$ frame attached to the virtual targets (gray). The UAVs start the mission with an initial offset in both position and attitude with respect to the beginning of the framed paths. As can be seen in the figure, the path-following algorithm eliminates this initial offset and steers the UAVs along the corresponding paths, while the coordination algorithm ensures simultaneous arrival at the end of the path at $t = 84.1$ s.

Details about the performance of the path-following algorithm are shown in Figure 4.6; the path-following attitude and position errors, $\Psi(\tilde{\mathbf{R}}_i(t))$ and $\mathbf{p}_{\mathcal{F},i}(t)$, converge to a neighborhood of zero within 10 s and 30 s, respectively. The figure also presents the angular-rate commands, $q_{c,i}(t)$ and $r_{c,i}(t)$, the actual angular rates, $q_i(t)$ and $r_i(t)$, as well as the rate of progression $\dot{\ell}_i(t)$ of the virtual targets along the path.

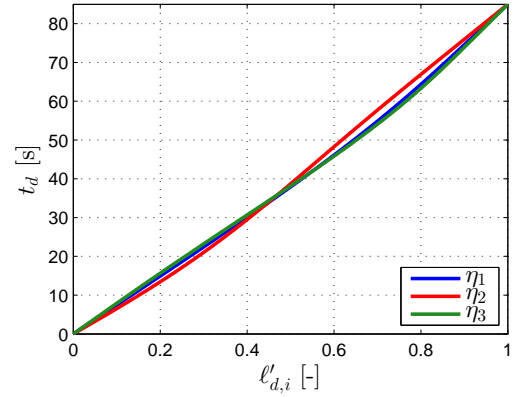
The evolution of both the coordination errors ($\xi_i(t) - \xi_j(t)$) and the rate of change of the coordination states $\dot{\xi}_i(t)$ is illustrated in Figure 4.7, along with the resulting UAV speeds and the integral states implemented on the follower vehicles. The figure shows that the coordination errors converge to a neighborhood of zero, while the rate of change of the coordination states converges to the desired rate of 1 s/s. In particular, Figure 4.7b illustrates how the vehicles adjust their speeds (with respect to the desired speed profile) to achieve coordination. The figure also shows that, as a result of the switching nature of the network topology, the speed commands of the three vehicles are discontinuous. Finally, Figure 4.8 describes the evolution of



(a) Framed 3D paths



(b) Desired speed profiles



(c) Coordination maps

Figure 4.3: Simultaneous arrival. Framed 3D spatial paths along with the corresponding desired speed profiles and coordination maps.

the information flow as the mission unfolds, and presents an estimate of the QoS of the network, computed as

$$\hat{\mu}(t) := \lambda_{\min} \left(\frac{1}{3} \frac{1}{T} \int_{t-T}^t \mathbf{Q}_3 \mathbf{L}(\tau) \mathbf{Q}_3^\top d\tau \right), \quad t \geq T, \quad (4.29)$$

with $T = 5$ s. The network topology changes every 0.5 s and, as can be seen in the figure, the QoS estimate is always greater than 0.15.

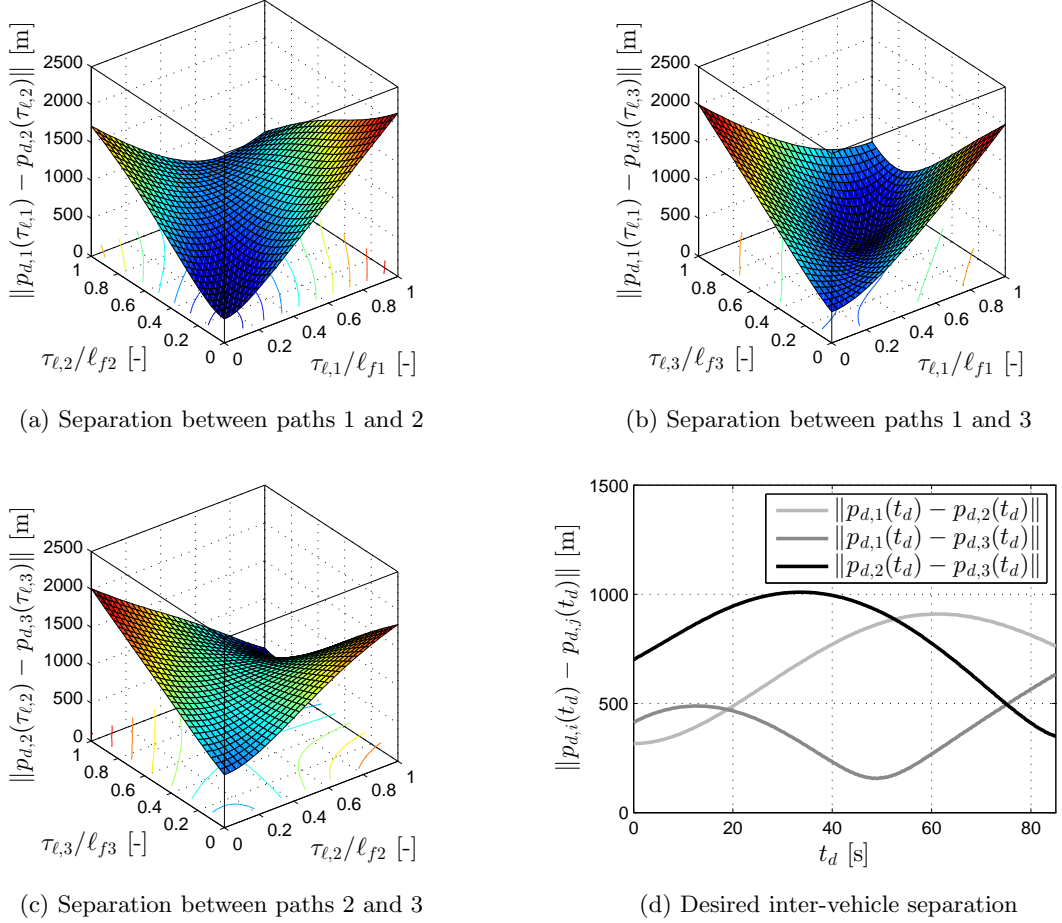


Figure 4.4: Simultaneous arrival. Path separation and desired inter-vehicle separation; the three paths are spatially deconflicted with a minimum clearance of 125 m.

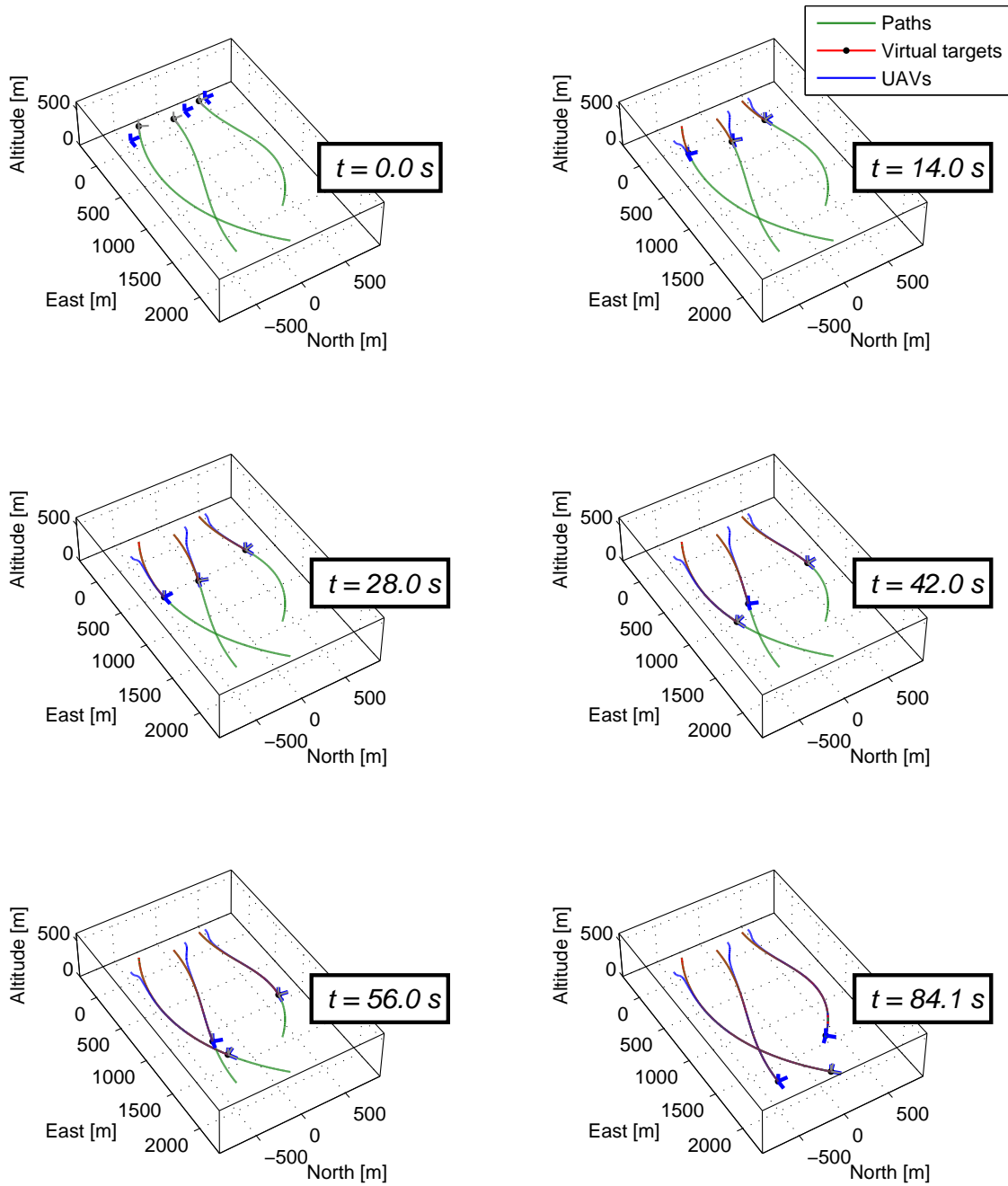


Figure 4.5: Simultaneous arrival. The three UAVs achieve simultaneous arrival at their final destinations at $t = 84.1 \text{ s}$.

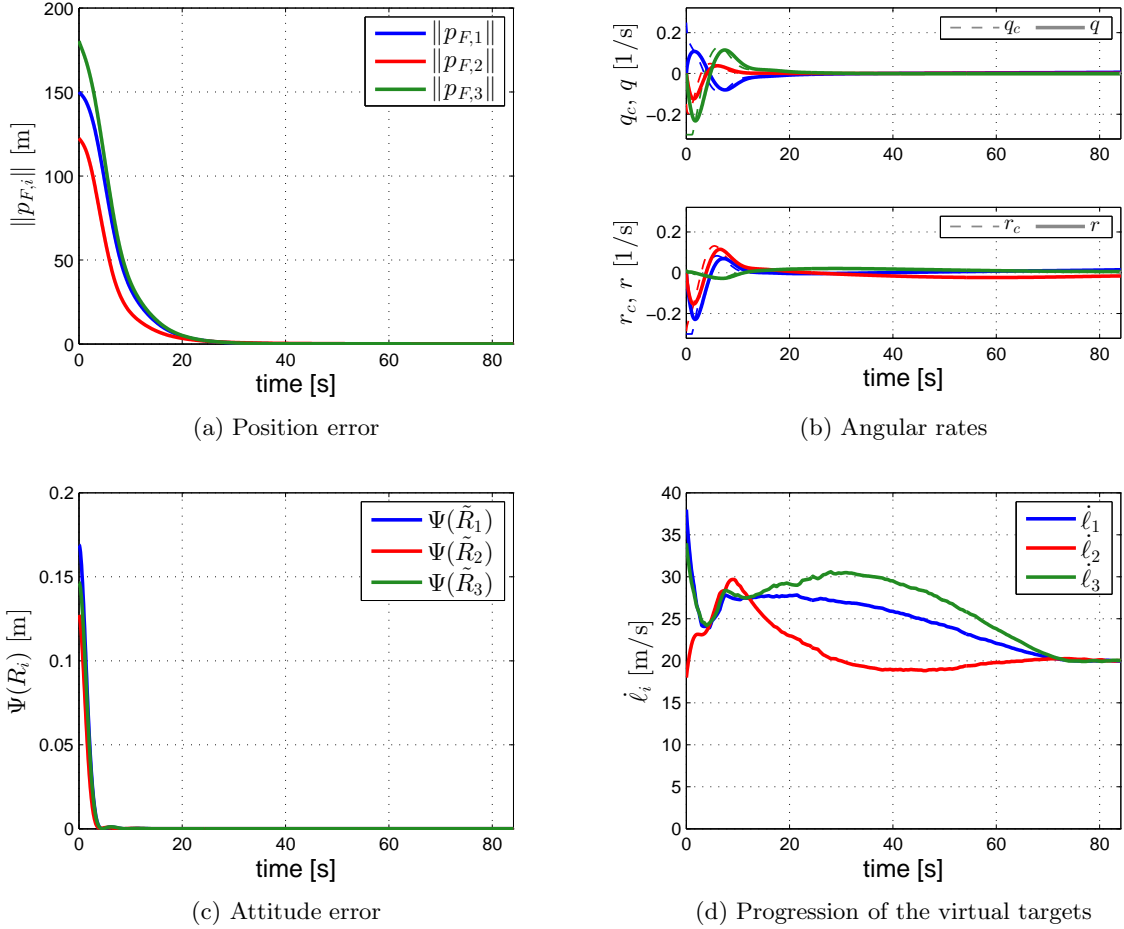


Figure 4.6: Simultaneous arrival. The path-following algorithm drives the path-following position and attitude errors to a neighborhood of zero.

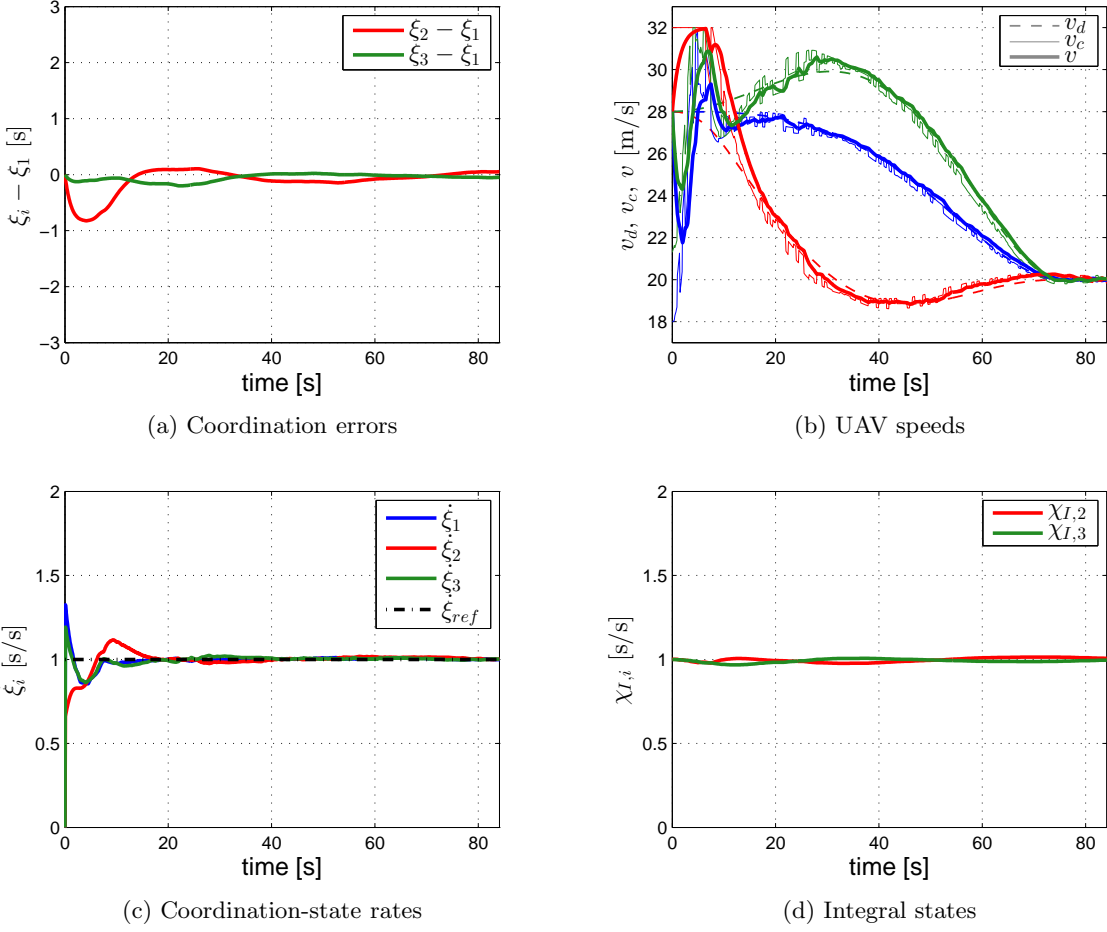


Figure 4.7: Simultaneous arrival. The coordination control law ensures that the coordination errors converge to a neighborhood of zero and also that the rate of change of the coordination states evolves at about the desired rate of 1 s/s.

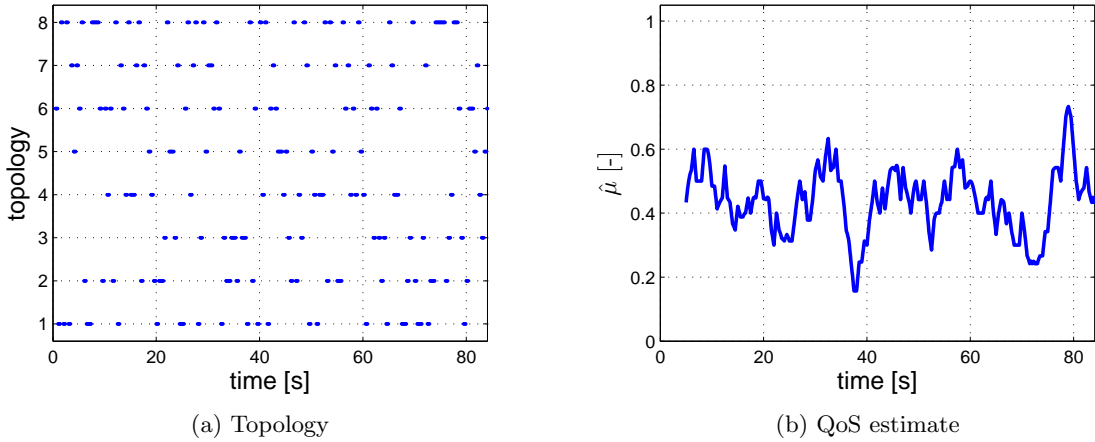


Figure 4.8: Simultaneous arrival. At a given time instant, the information flow is characterized by one of the topologies in Figure 4.2. The resulting graph is only connected in an integral sense, and not pointwise in time.

4.4.2 Sequential Auto-Landing

Here, three UAVs must arrive at the assigned glide slope separated by pre-specified safe-guarding time-intervals, and then follow the glide path at a constant approach speed while maintaining the safe-guarding separation. To this end, time-deconflicted transition trajectories are generated from pre-specified initial conditions to the beginning of the glide path, satisfying the desired inter-vehicle arrival schedule and taking the UAVs to the desired approach speed. Again, this mission imposes only *relative* temporal constraints on the arrival of the UAVs.

Figure 4.9 shows the three transition paths with the parallel transport frames as well as the framed 3-deg glide path. The beginning of each transition path is indicated with a circle, while the beginning of the glide path is indicated with a triangle. The figure also presents the desired speed profiles for the initial transition phase that ensure a desired safe-guarding arrival separation of 30 s, trajectory deconfliction, as well as a final approach speed of 20 m/s. The transition coordination maps are shown in Figure 4.9c. Finally, the figure also includes the desired speed profile for the approach along the glide slope as well as the corresponding coordination map. The transition paths have lengths $\ell_{f1} = 1,609.0$ m, $\ell_{f2} = 1,962.7$ m, and $\ell_{f3} = 2,836.7$ m, and the desired times of arrival at the glide slope are $t_{d1}^* = 65.0$ s, $t_{d2}^* = 95.0$ s, and $t_{d3}^* = 125.0$ s. Figure 4.10 presents the path separations, which show that the three transition paths meet at their end positions (beginning of the glide slope), whereas the desired inter-vehicle separations for this particular mission are never less than 350 m.

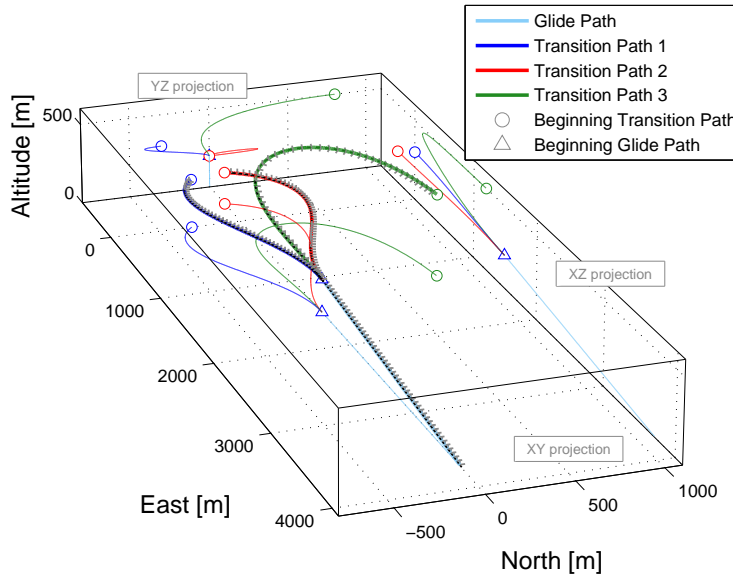
The cooperative motion-control algorithms described in this thesis can be used to solve this sequential auto-landing problem. In this case, however, since the UAVs are required to maintain a safe-guarding separation during the approach along the glide path, the coordination states have to be redefined as the vehicles reach the glide slope. Hence, while the i th UAV is flying along its transition path, its coordination state is defined as

$$\xi_i(t) = \eta_i(\ell'_i(t)) , \quad i = 1, 2, 3 ,$$

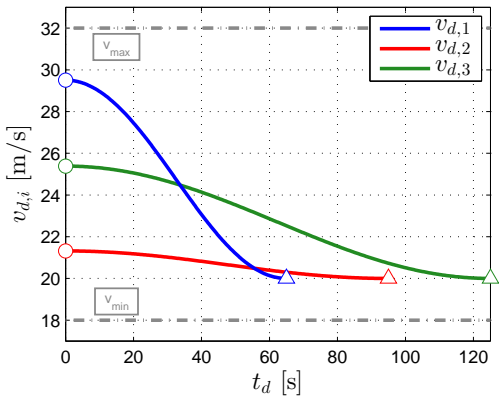
where $\ell'_i(t)$ is the normalized curvilinear abscissa of the i th virtual target along the corresponding transition path. When the UAV reaches the beginning of the glide path, then its coordination state is (re)defined as

$$\xi_i(t) = \eta_{\text{gs}}(\ell'_i(t)) + t_{di}^* , \quad i = 1, 2, 3 ,$$

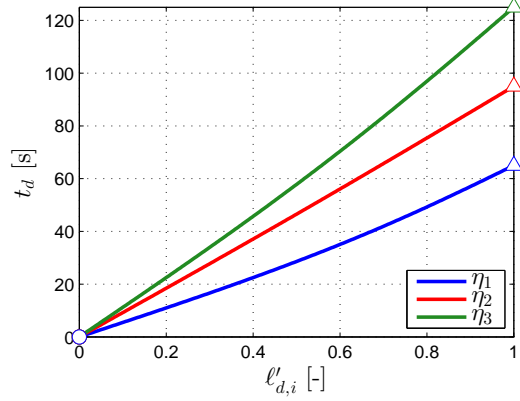
where $\ell'_i(t)$ is now the normalized curvilinear abscissa of the i th virtual target along the glide path, and t_{di}^* is the desired time of arrival of the i th UAV at the beginning of the glide slope. Note that, with the above definitions, the coordination states $\xi_i(t)$ are continuous, as $\eta_i(1) = t_{di}^*$ and $\eta_{\text{gs}}(0) = 0$.



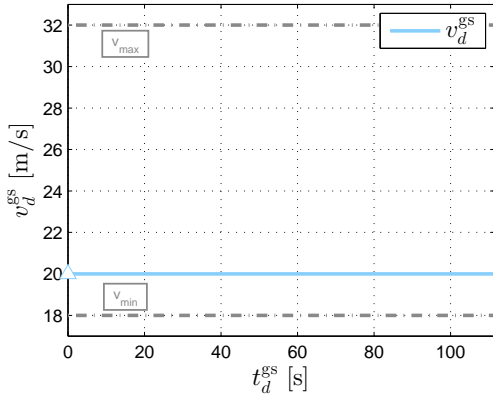
(a) Framed 3D paths



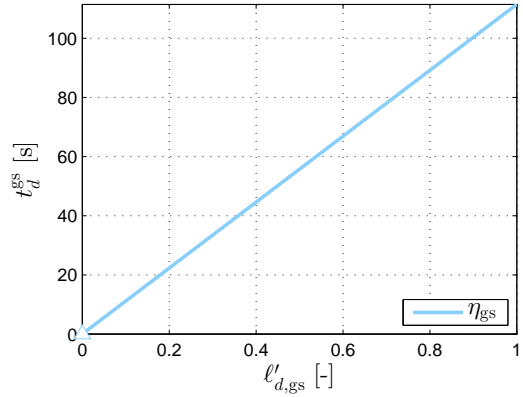
(b) Transition: Desired speed profiles



(c) Transition: Coordination maps



(d) Glide slope: Desired speed profile



(e) Glide slope: Coordination map

Figure 4.9: Sequential auto-landing. Framed 3D paths along with the corresponding desired speed profiles and coordination maps for both the transition trajectories and the glide slope.

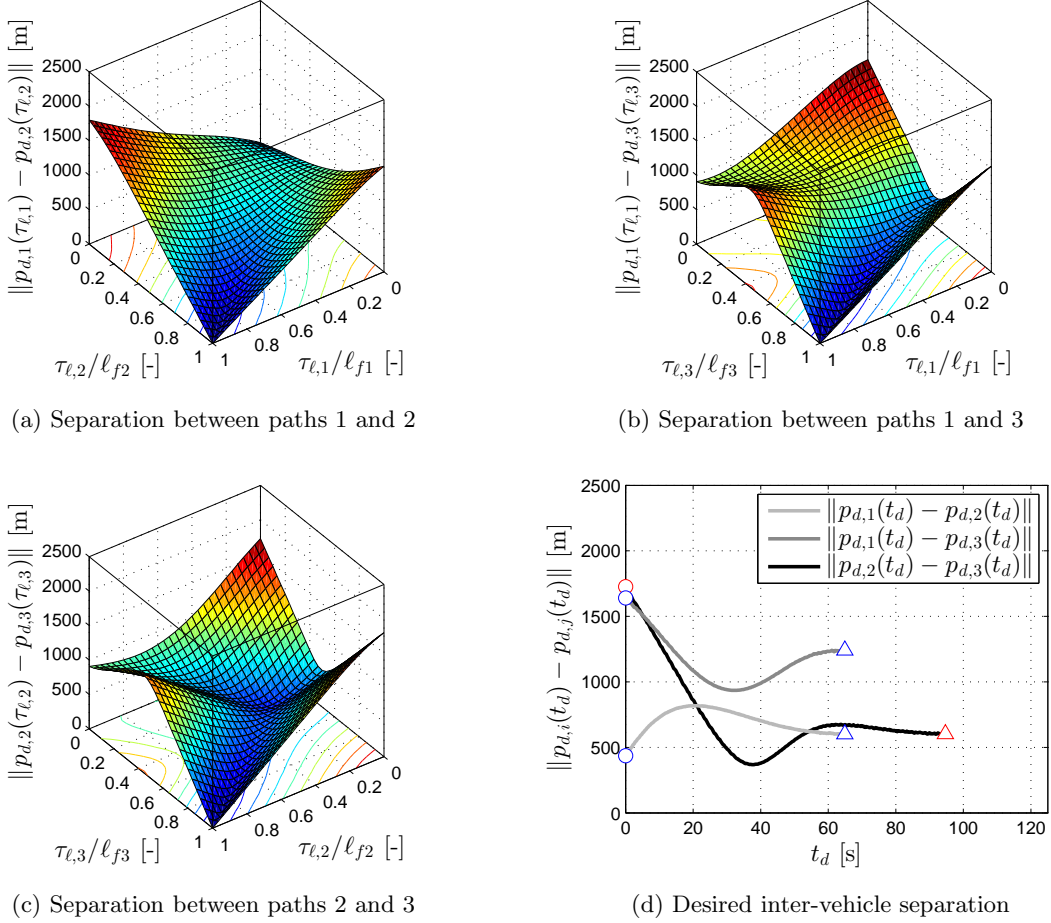


Figure 4.10: Sequential auto-landing. Path separation and desired inter-vehicle separation during the transition phase; the speed profiles ensure deconfliction of the three desired trajectories with a minimum clearance of 350 m.

Next, we present simulation results for this mission scenario. Figure 4.11 illustrates the evolution of the UAVs (blue) as well as the virtual targets (red) moving along the paths (green and light blue). Similar to the previous scenario, the UAVs start the mission with an initial offset in both position and attitude with respect to the beginning of the transition paths. As can be seen in the figure, the path-following algorithm eliminates this initial offset and steers the UAVs along the corresponding transition paths, while the coordination algorithm ensures that the UAVs reach the glide slope separated by the desired time-interval. The UAVs reach the glide slope at $t = 67.2$ s, $t = 97.1$ s, and $t = 127.1$ s, approximately meeting the desired 30 s inter-vehicle separation. After reaching the glide slope, the path-following algorithm ensures that the UAVs stay on the glide path as the coordination algorithm maintains the safe-guarding separation. The simulation is stopped when the first UAV reaches the end of the glide path.

Figure 4.12 shows the path-following position and attitude errors, $\mathbf{p}_{F,i}(t)$ and $\Psi(\tilde{\mathbf{R}}_i(t))$, the angular-rate

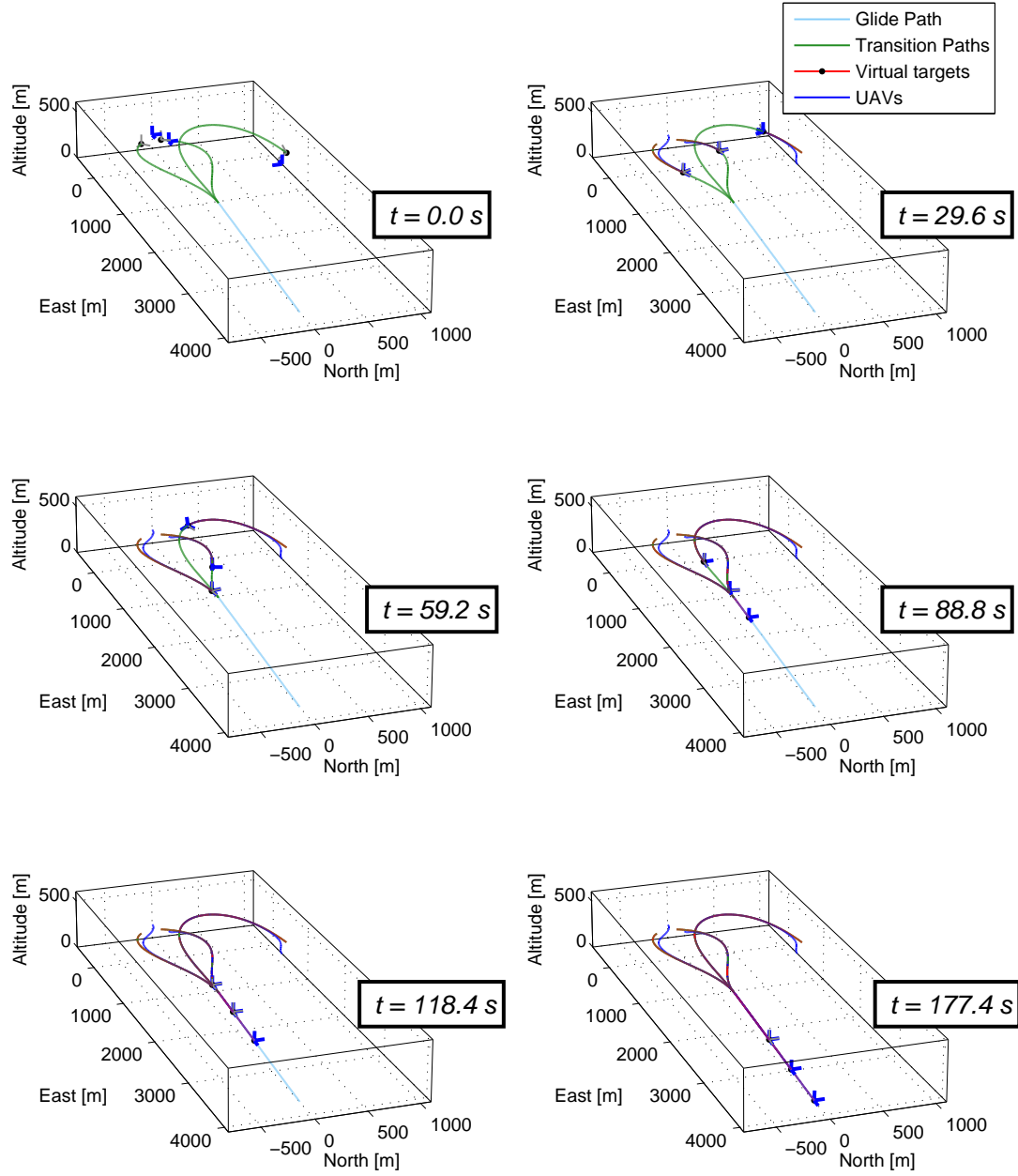


Figure 4.11: Sequential auto-landing. The three UAVs arrive at the beginning of the glide path separated by approximately 30 s and maintain this safe-guarding separation as they fly along the glide slope.

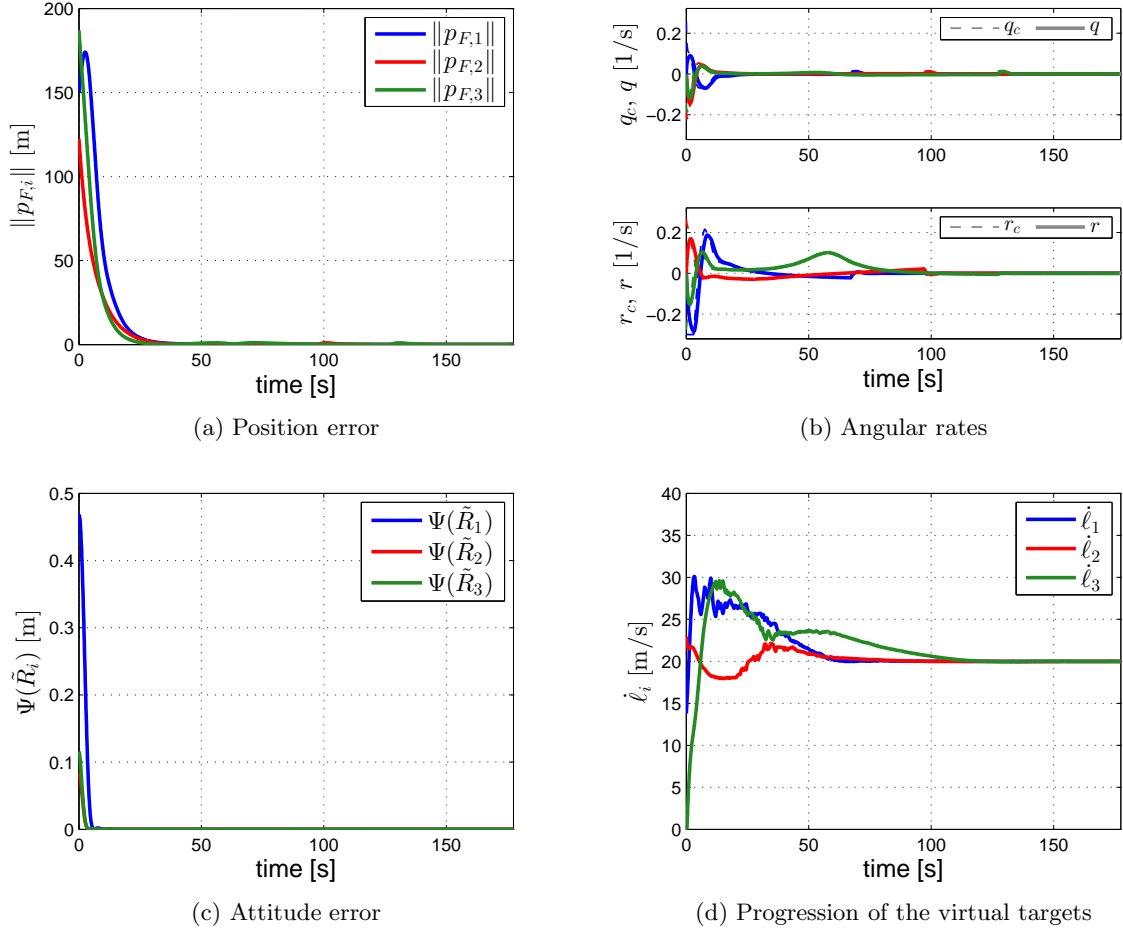


Figure 4.12: Sequential auto-landing. The path-following algorithm drives the path-following position and attitude errors to a neighborhood of zero.

commands, $q_{c,i}(t)$ and $r_{c,i}(t)$, the actual angular rates, $q_i(t)$ and $r_i(t)$, and the rate of progression of the virtual targets $\dot{\ell}_i(t)$. The path-following errors converge to a neighborhood of zero within 40 s.

The coordination errors ($\xi_i(t) - \xi_j(t)$) also converge to a neighborhood of zero, while the rate of change of the coordination states $\dot{\xi}_i(t)$ converges to neighborhood of the desired rate of 1 s/s; see Figure 4.13. This figure also shows the UAV speeds and the integral states implemented on the follower vehicles. In particular, Figure 4.13b shows that, after a transient caused by the initial path-following errors as well as the speed corrections introduced by the coordination control law, the speed of each UAV converges to its desired speed and, as the vehicles enter the glide path, their speeds converge to the desired approach speed of 20 m/s. Again, as a result of the switching nature of the network topology, the speed commands of the three vehicles are discontinuous. Finally, Figure 4.14 shows the evolution of the time-varying network topology along with an estimate of the QoS of the network, computed as in (4.29).

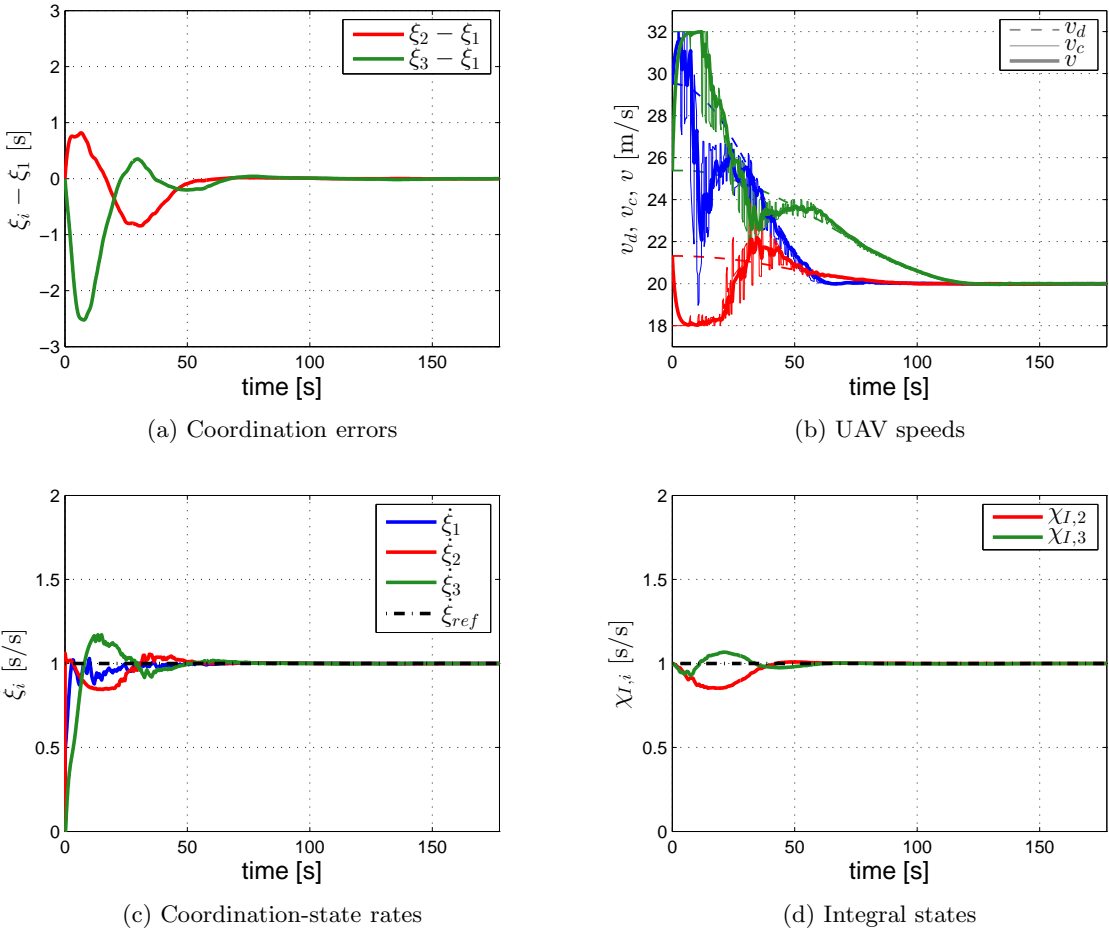


Figure 4.13: Sequential auto-landing. The coordination control law ensures that the coordination errors converge to a neighborhood of zero, thus ensuring trajectory deconfliction, and also that the rate of change of the coordination states evolves at about the desired rate of 1 s/s.

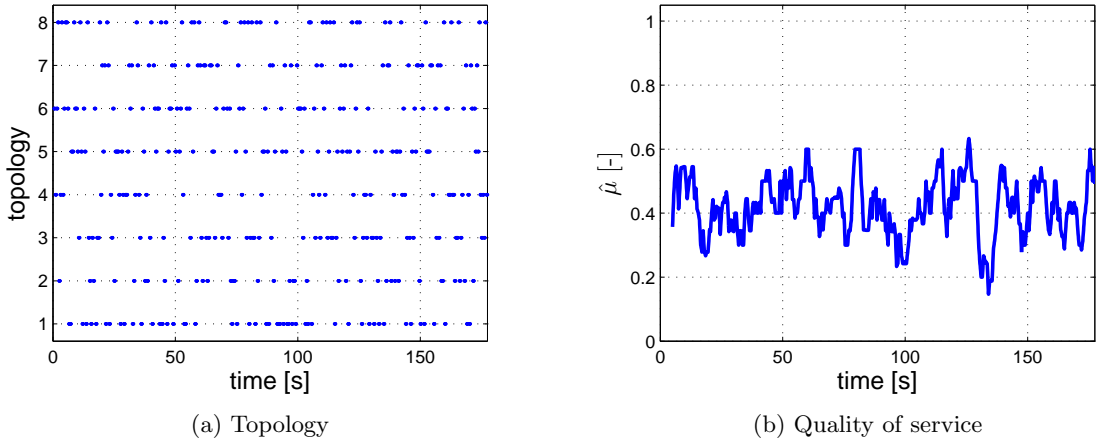


Figure 4.14: Sequential auto-landing. At a given time instant, the information flow is characterized by one of the topologies in Figure 4.2. The resulting graph is only connected in an integral sense, and not pointwise in time.

Chapter 5

Time-Critical Coordination under Quantization

When vehicles communicate over a network with finite-rate communication links, the exchanged information is to be quantized into an appropriate finite number of bits. In this chapter, we analyze the effect of quantization on the stability and convergence properties of the closed-loop coordination dynamics. In particular, we restrict the analysis to the problem of time-critical coordination at the kinematic level; stability of the combined cooperation and path-following systems with vehicle dynamics can be investigated following an approach similar to that of Chapter 4. Also, for the sake of simplicity, we consider only the case of *uniform quantization* with step size Δ . The results in this chapter show that, under sufficiently fine quantization, the (quantized) coordination control law solves the coordination control problem in a practical sense, and the coordination error degrades gracefully with the value of the quantizer step size. In addition, we also prove that, depending on the design of the quantized coordination control law, the closed-loop kinematic coordination error dynamics have undesirable “zero-speed” attractors. From a mathematical point of view, a consequence of quantization is that the resulting dynamics are not guaranteed to admit solutions either in the classical sense or in the sense of Carathéodory. This implies that a weaker concept of solution has to be considered for the derivations in this chapter.

5.1 Convergence with Quantized Information

5.1.1 Coordination Control Law and Coordination Dynamics

When only quantized information from the other vehicles is available, the distributed coordination control law (4.4) becomes

$$\begin{aligned} \mathbf{u}_{\text{coord}} &= -k_P (\mathbf{D}(t) \boldsymbol{\xi} - \mathbf{A}(t) \mathbf{q}(\boldsymbol{\xi})) + \begin{bmatrix} \mathbf{1}_{n_\ell} \\ \boldsymbol{\chi}_I \end{bmatrix}, \\ \dot{\boldsymbol{\chi}}_I &= -k_I \mathbf{C}^\top (\mathbf{D}(t) \boldsymbol{\xi} - \mathbf{A}(t) \mathbf{q}(\boldsymbol{\xi})), \quad \boldsymbol{\chi}_I(0) = \mathbf{1}_{n-n_\ell}, \end{aligned} \tag{5.1}$$

where the time-varying matrices $\mathbf{D}(t)$ and $\mathbf{A}(t)$ are respectively the *degree* and *adjacency matrices* of $\mathbf{L}(t)$, while $\mathbf{q}(\xi(t)) \in \mathbb{Z}^n \Delta$ is the quantized coordination state

$$\mathbf{q}(\xi(t)) := [\mathbf{q}_\Delta(\xi_1(t)), \dots, \mathbf{q}_\Delta(\xi_n(t))]^\top,$$

with $\mathbf{q}_\Delta(\cdot) : \mathbb{R} \rightarrow \mathbb{Z}\Delta$ being defined as

$$\mathbf{q}_\Delta(\phi) := \text{sgn}(\phi)\Delta \left\lfloor \frac{|\phi|}{\Delta} + \frac{1}{2} \right\rfloor, \quad \phi \in \mathbb{R}.$$

Then, the closed-loop kinematic coordination dynamics can be written as

$$\begin{aligned} \dot{\xi} &= -k_P (\mathbf{D}(t)\xi - \mathbf{A}(t)\mathbf{q}(\xi)) + \begin{bmatrix} \mathbf{1}_{n_\ell} \\ \chi_I \end{bmatrix}, & \xi(0) &= \xi_0, \\ \dot{\chi}_I &= -k_I \mathbf{C}^\top (\mathbf{D}(t)\xi - \mathbf{A}(t)\mathbf{q}(\xi)), & \chi_I(0) &= \mathbf{1}_{n-n_\ell}. \end{aligned} \tag{5.2}$$

In terms of the coordination error state $\zeta(t)$, and noting that $\mathbf{L}(t) = \mathbf{D}(t) - \mathbf{A}(t)$, the closed-loop coordination error dynamics can be expressed as

$$\dot{\zeta} = \mathbf{A}_\zeta(t)\zeta + \mathbf{f}_q, \quad \zeta(0) = \zeta_0, \tag{5.3}$$

where $\mathbf{A}_\zeta(t)$ was defined in (4.8), and $\mathbf{f}_q(t)$ is given by

$$\mathbf{f}_q(t) := \begin{bmatrix} k_P \mathbf{Q} \mathbf{A}(t) \mathbf{e}_\xi(t) \\ k_I \mathbf{C}^\top \mathbf{A}(t) \mathbf{e}_\xi(t) \end{bmatrix} \in \mathbb{R}^{2n-n_\ell-1},$$

with $\mathbf{e}_\xi(t) := \mathbf{q}(\xi(t)) - \xi(t)$ being the *quantization error vector*.

Note that, in this case, the right-hand side of the kinematic coordination error dynamics (5.3) is discontinuous not only due to the switching network topology, but also due to the presence of quantized states. As proven in [21], Carathéodory solutions might not exist for quantized consensus problems, implying that a weaker concept of solution has to be considered. Similar to [21], in this chapter we will consider solutions *in the sense of Krasovskii*, which we define next.

Definition 4 (Krasovskii solution [43]) Let $\phi : J \rightarrow \mathbb{R}^n$ (J an interval in \mathbb{R}) be absolutely continuous on each compact subinterval of J . Then, ϕ is called a Krasovskii solution of the vector differential equation $\dot{\phi} = \mathbf{f}(t, \phi)$ if

$$\dot{\phi}(t) \in \mathbf{K}(\mathbf{f}(t, \phi(t))) \quad \text{almost everywhere in } J,$$

where the operator $K(\cdot)$ is defined as

$$K(f(t, \phi)) := \bigcap_{\epsilon > 0} \overline{\text{co}} f(t, \phi + \epsilon \mathcal{B}),$$

with \mathcal{B} being the open unit ball in \mathbb{R}^n . ♠

To show that Krasovskii solutions to (5.3) exist (at least) locally, we note that, during continuous evolution of the system between “quantization jumps”, the quantized coordination error dynamics (5.3) are linear, with the quantized state $\mathbf{q}(\xi(t))$ acting as a bounded exogenous input. This implies that the solutions $\xi(t)$ are locally bounded (no *finite escape time* occurs). Then, local existence of Krasovskii solutions is guaranteed by the fact that the right-hand side of (5.3) is measurable and locally bounded [43]. At this point, however, we cannot claim that Krasovskii solutions to (5.3) are complete; for this, we will need to prove that solutions are bounded (see Theorem 3, Section 5.1.3).

5.1.2 Krasovskii Equilibria

Before investigating the convergence properties of the quantized coordination error dynamics (5.3), in this section we analyze the existence of equilibria for these dynamics. In particular, we show that (i) unlike the unquantized case, $\zeta_{\text{eq}} = \mathbf{0}$ is not an equilibrium point of the quantized kinematic coordination error dynamics; and (ii) other (undesirable) equilibria might exist, depending on the step size of the quantizers. The former follows easily from the error dynamics (5.3) and recalling that, at the kinematic level, $\zeta(t) = \mathbf{0}$ is equivalent to $\xi(t) \in \text{span}\{\mathbf{1}_n\}$ and $\dot{\xi}(t) = \mathbf{1}_n$. The proof of the latter result is, instead, more involved, and we only show it here for the case of static and connected network topologies.

To this effect, we start by noting that $\dot{\zeta}(t) \equiv \mathbf{0}$ is equivalent to $\dot{\xi}(t) \in \text{span}\{\mathbf{1}_n\}$ and $\dot{\chi}_{\mathcal{I}}(t) \equiv \mathbf{0}$ holding simultaneously. This implies that $\zeta_{\text{eq}} = [\zeta_{1\text{eq}}^\top, \zeta_{2\text{eq}}^\top]^\top$ is an equilibrium of (5.3) if the following inclusions hold for all $t \geq 0$:

$$\begin{aligned} \beta(t)\mathbf{1}_n &\in K\left(-k_P(D\xi_{\text{eq}}(t) - A\mathbf{q}(\xi_{\text{eq}}(t))) + \begin{bmatrix} \mathbf{1}_{n_\ell} \\ \chi_{\mathcal{I},\text{eq}} \end{bmatrix}\right), \\ \mathbf{0} &\in K\left(-k_I C^\top(D\xi_{\text{eq}}(t) - A\mathbf{q}(\xi_{\text{eq}}(t)))\right), \end{aligned}$$

where $\beta(t) \in \mathbb{R}$ is an arbitrary time-varying signal; $\xi_{\text{eq}}(t)$ is a continuous coordination-state trajectory satisfying $\zeta_{1\text{eq}} = Q\xi_{\text{eq}}(t)$; while $\chi_{\mathcal{I},\text{eq}} = \zeta_{2\text{eq}} + \mathbf{1}_{n-n_\ell}$. The second inclusion above and continuity of $\xi_{\text{eq}}(t)$, along with the fact that the network is assumed to be static and connected, preclude the existence of equilibria involving time-varying coordination-state trajectories, that is, $\beta(t) \equiv 0$ (or equivalently $\dot{\xi}_{\text{eq}}(t) \equiv 0$). Then,

the set of (Krasovskii) equilibria of the error dynamics (5.3) can be defined as

$$\Theta := \left\{ (\zeta_{1\text{eq}}, \zeta_{2\text{eq}}) \in \mathbb{R}^{n-1} \times \mathbb{R}^{n-n_\ell} : \right. \\ \left. \zeta_{1\text{eq}} = Q\xi_{\text{eq}}, \quad \zeta_{2\text{eq}} = \chi_{I,\text{eq}} - \mathbf{1}_{n-n_\ell}, \quad \mathbf{0} \in K \left(\begin{bmatrix} -k_P(D\xi_{\text{eq}} - A\mathbf{q}(\xi_{\text{eq}})) + \begin{bmatrix} \mathbf{1}_{n_\ell} \\ \chi_{I,\text{eq}} \end{bmatrix} \\ -k_I C^\top(D\xi_{\text{eq}} - A\mathbf{q}(\xi_{\text{eq}})) \end{bmatrix} \right) \right\}. \quad (5.4)$$

Next, we show that, under sufficiently fine quantization, set Θ is empty. We also prove, on the contrary, the existence of other (undesirable) “zero-speed” equilibria in the presence of coarse quantization.

Lemma 5 *Consider the quantized kinematic coordination error dynamics (5.3), and assume that the network topology is static and connected. If the step size of the quantizers satisfies*

$$\Delta < \frac{2n_\ell}{(3n - 2n_\ell)(n - 1)} \frac{1}{k_P}, \quad (5.5)$$

then the set of equilibria Θ is empty. \diamond

Proof: The proof of this result is given in Appendix C.7.

The next corollary follows from the proof of Lemma 5.

Corollary 1 *Consider the quantized kinematic coordination dynamics (5.2), and assume that the network topology is static and connected. If the step size of the quantizers is such that*

$$\left\| \frac{1}{k_P} D^{-1} \begin{bmatrix} \mathbf{1}_{n_\ell} \\ \mathbf{0} \end{bmatrix} \right\|_\infty < \frac{\Delta}{2}, \quad (5.6)$$

then, for any $k \in \mathbb{Z}$, the point

$$(\hat{\xi}, \hat{\chi}_I) = \left(k\Delta \mathbf{1}_n + \frac{1}{k_P} D^{-1} \begin{bmatrix} \mathbf{1}_{n_\ell} \\ \mathbf{0} \end{bmatrix}, \mathbf{0} \right) \quad (5.7)$$

is a “zero-speed” equilibrium point of system (5.2). \diamond

Proposition 1 *Consider the quantized kinematic coordination dynamics (5.2), and assume that the network topology is static and connected. Further, assume that the step size of the quantizers satisfies inequality (5.6). Then, the “zero-speed” equilibrium points defined in (5.7) are locally asymptotically stable.* \diamond

Proof: The proof of this result is given in Appendix C.8.

Remark 15 The equilibrium points characterized by (5.7) correspond to solutions in which the vehicles have zero groundspeed and, therefore, are to be avoided. Unfortunately, as shown in Proposition 1, these equilibrium points are asymptotically stable, which implies that the quantizers are to be designed to preclude the existence of such equilibria. The bound in (5.5) should thus be understood as a design constraint for the quantizers that prevents the existence of such undesirable equilibria. \triangle

Remark 16 From inequality (5.6), it follows that all of the components of $\hat{\xi}$ fall into the same quantization level, with the components corresponding to the follower vehicles at its center. Moreover, note that all of the equilibrium points characterized by (5.7) map to the same coordination error state

$$(\hat{\zeta}_1, \hat{\zeta}_2) = \left(\frac{1}{k_P} \mathbf{D}^{-1} \begin{bmatrix} \mathbf{1}_{n_\ell} \\ \mathbf{0} \end{bmatrix}, -\mathbf{1}_{n-n_\ell} \right). \quad \triangle$$

5.1.3 Stability Analysis at the Kinematic Level

Next we show that, if the connectivity of graph $\Gamma(t)$ verifies the PE-like condition (2.14), then the coordination control law (5.1) solves—at the kinematic level—the coordination control problem in a practical sense and, in addition, the coordination error vector degrades gracefully with the value of the quantizer step size. The next theorem summarizes this result.

Theorem 3 Consider the closed-loop kinematic coordination error dynamics (5.3) and suppose that the information flow satisfies the PE-like condition (2.14) for some parameters $\mu, T > 0$. Then, there exist coordination control gains k_P and k_I such that the solution of the quantized coordination error dynamics (5.3) satisfies

$$\|\zeta(t)\| \leq \kappa'_{\zeta 0} \|\zeta(0)\| e^{-\lambda'_{cd} t} + \kappa'_{\zeta 1} \Delta, \quad \text{for all } t \geq 0, \quad (5.8)$$

for some constants $\kappa'_{\zeta 0}, \kappa'_{\zeta 1} \in (0, \infty)$, and with $\lambda'_{cd} := \bar{\lambda}_{cd}(1 - \theta'_\lambda)$, where $\bar{\lambda}_{cd}$ was defined in (4.9) and θ'_λ is a constant verifying $0 < \theta'_\lambda < 1$. \diamond

Proof: The proof of this result is given in Appendix C.9.

Remark 17 The theorem above admits a slightly stronger version. In fact, from the proof of the theorem it follows that the coordination error state $\zeta(t)$ is uniformly bounded for all $t \geq 0$ and uniformly ultimately bounded with ultimate bound proportional to the step size of the quantizers. However, we prefer to present here an ISS-type result similar to the one in Lemma 4, for such a bound is more convenient when proving stability of the overall cooperative path-following system. \triangle

Remark 18 As mentioned earlier, in this chapter we only investigate the stability and convergence properties of the time-coordination problem at the kinematic level. Stability of the overall cooperative control architecture, including vehicle dynamics, is not addressed here and can be analyzed following an approach similar to that of Chapter 4 (Sections 4.1.2 and 4.2). This analysis should yield additional design constraints for the step size of the quantizers, similar to the constraints on the performance bounds in Theorem 2. \triangle

5.1.4 Coordination with Fully Quantized Information

In this section we propose a modification of the coordination control law (5.1) that retains $\zeta_{\text{eq}} = \mathbf{0}$ as an equilibrium point of the resulting quantized kinematic coordination error dynamics. In addition, we will show that, for the case of connected network topologies and sufficiently fine quantization, $\zeta_{\text{eq}} = \mathbf{0}$ is the only equilibrium point.

To this effect, consider the following distributed control law:

$$\begin{aligned} \mathbf{u}_{\text{coord}} &= -k_P \mathbf{L}(t) \mathbf{q}(\xi) + \begin{bmatrix} \mathbf{1}_{n_\ell} \\ \chi_I \end{bmatrix}, \\ \dot{\chi}_I &= -k_I \mathbf{C}^\top \mathbf{L}(t) \mathbf{q}(\xi), \quad \chi_I(0) = \mathbf{1}_{n-n_\ell}, \end{aligned} \tag{5.9}$$

which, unlike control law (5.1), uses only quantized information. The kinematic coordination dynamics can now be written as

$$\begin{aligned} \dot{\xi} &= -k_P \mathbf{L}(t) \mathbf{q}(\xi) + \begin{bmatrix} \mathbf{1}_{n_\ell} \\ \chi_I \end{bmatrix}, \quad \xi(0) = \xi_0, \\ \dot{\chi}_I &= -k_I \mathbf{C}^\top \mathbf{L}(t) \mathbf{q}(\xi), \quad \chi_I(0) = \mathbf{1}_{n-n_\ell}, \end{aligned} \tag{5.10}$$

leading to the quantized kinematic coordination error dynamics

$$\dot{\zeta} = \mathbf{A}_\zeta(t) \zeta + \mathbf{f}'_{\mathbf{q}}, \quad \zeta(0) = \zeta_0, \tag{5.11}$$

where $\mathbf{A}_\zeta(t)$ was defined in (4.8) and $\mathbf{f}'_{\mathbf{q}}(t)$ is given by

$$\mathbf{f}'_{\mathbf{q}}(t) := \begin{bmatrix} k_P \mathbf{Q} \mathbf{L}(t) \mathbf{e}_\xi(t) \\ k_I \mathbf{C}^\top \mathbf{L}(t) \mathbf{e}_\xi(t) \end{bmatrix} \in \mathbb{R}^{2n-n_\ell-1}.$$

In this case, it can be shown that the set of (Krasovskii) equilibria of (5.11) is characterized by:

$$\Theta' := \left\{ (\zeta_{1\text{eq}}, \zeta_{2\text{eq}}) \in \mathbb{R}^{n-1} \times \mathbb{R}^{n-n_\ell} : \right. \\ \left. \zeta_{1\text{eq}} = Q\xi_{\text{eq}}(t), \ zeta_{2\text{eq}} = \chi_{I,\text{eq}} - \mathbf{1}_{n-n_\ell}, \begin{bmatrix} \beta(t)\mathbf{1}_n \\ \mathbf{0} \end{bmatrix} \in K \left(\begin{bmatrix} -k_P \mathbf{L}(t) \mathbf{q}(\xi_{\text{eq}}(t)) + \begin{bmatrix} \mathbf{1}_{n_\ell} \\ \chi_{I,\text{eq}} \end{bmatrix} \\ -k_I \mathbf{C}^\top \mathbf{L}(t) \mathbf{q}(\xi_{\text{eq}}(t)) \end{bmatrix} \right) \right\},$$

where $\beta(t) \in \mathbb{R}$ is an arbitrary time-varying signal. Next, we provide some insights into the set of equilibria Θ' defined above. Moreover, similar to Theorem 3, we show that the coordination error state degrades gracefully with the value of the quantizer step size.

Lemma 6 *Consider the quantized kinematic coordination error dynamics (5.11). We have that:*

- (i) $\zeta_{\text{eq}} = \mathbf{0}$ is an equilibrium point, independently of the quantizer resolution and the information flow;
- (ii) for the case of connected (undirected) network topologies, if the step size of the quantizers satisfies

$$\Delta < \frac{1}{2(n-n_\ell)} \frac{1}{k_P}, \quad (5.12)$$

then $\zeta_{\text{eq}} = \mathbf{0}$ is the only equilibrium point, that is $\Theta' = \{(\mathbf{0}, \mathbf{0})\}$. \diamond

Proof: The proof is given in Appendix C.10.

Remark 19 *The bound in (5.12) should be understood as a design constraint for the quantizers that prevents the existence of equilibria other than $\zeta_{\text{eq}} = \mathbf{0}$.* \triangle

Theorem 4 *Consider the closed-loop kinematic coordination error dynamics (5.11) and suppose that the information flow satisfies the PE-like condition (2.14) for some parameters $\mu, T > 0$. Then, there exist coordination control gains k_P and k_I such that the solution of the quantized coordination error dynamics (5.11) satisfies*

$$\|\zeta(t)\| \leq \kappa''_{\zeta_0} \|\zeta(0)\| e^{-\lambda''_{cd} t} + \kappa''_{\zeta_1} \Delta, \quad \text{for all } t \geq 0,$$

for some constants $\kappa''_{\zeta_0}, \kappa''_{\zeta_1} \in (0, \infty)$, and with $\lambda''_{cd} := \bar{\lambda}_{cd}(1 - \theta''_\lambda)$, where $\bar{\lambda}_{cd}$ was defined in (4.9) and θ''_λ is a constant verifying $0 < \theta''_\lambda < 1$. \diamond

Proof: The proof of this result is similar to the proof of Theorem 3, and is therefore omitted.

5.2 Simulation Results

We now present simulation results that illustrate the performance of the two coordination control laws introduced in this chapter: the *partially quantized* control law (5.1) and the *fully quantized* control law (5.9). To this end, we consider the sequential auto-landing mission scenario described in Section 4.4.2 of Chapter 4, and assume that the information exchanged among UAVs is quantized. Similar to the results presented in Chapters 3 and 4, simulations in this section are based on the kinematic model of the UAV in (3.10) along with a simplified, decoupled linear model of the UAV with its autopilot.

Figures 5.1 and 5.2 present the computed evolution of the quantized coordination dynamics for the two control laws with quantizer step size $\Delta = 1$ s (note that this step size verifies inequalities (5.5) and (5.12)). In particular, the figures show the time-evolution of the coordination errors ($\xi_i(t) - \xi_j(t)$), the rate of change of the coordination states $\dot{\xi}_i(t)$, the UAV speeds $v_i(t)$, and the integral states $\chi_{I,i}(t)$ implemented on the follower vehicles. As can be seen in the figure, for this resolution of the quantizers, the two control laws lead to similar results, with comparable levels of performance in terms of vehicle coordination. However, note that the partially quantized control law results in a speed command with high-frequency content, whereas the fully quantized control law generates a much smoother speed command with a much less wiggling speed response. From this perspective, the fully quantized control law seems to be preferable to the partially quantized control law, in which each vehicle uses its own unquantized coordination state.

Next, we illustrate the behavior of the two protocols in the presence of coarse quantization. To this end, we consider the same simulation scenario as in Figures 5.1-5.2, but change the quantizer step size to $\Delta = 5$ s, which does not verify inequalities (5.5) or (5.12). The computed responses of the quantized coordination dynamics for the two control laws are shown in Figures 5.3 and 5.4, respectively. In this case, the coordination control law with partially quantized information achieves the desired agreement (in a practical sense); the response is, however, highly oscillatory with speed commands exhibiting large high-frequency content. Meanwhile, when using the control law with fully quantized feedback, the vehicles seem to asymptotically converge to the desired agreement, and the response is again much smoother than the one achieved with the partially quantized control law. Interestingly, note that asymptotic convergence is a much stronger result than that of Theorem 4, which instead derives an ISS-type bound for the coordination error state. These simulation results seem to indicate that a stronger version of Theorem 4 may hold and, hence, point out to the need to conduct a more in-depth analysis of the fully quantized coordination control law.

Finally, we notice that convergence of the fleet to one of the “zero-speed” equilibria characterized in Corollary 1 cannot be illustrated by this simulation scenario, as the speed command of each vehicle is saturated below 18 m/s. Simulation results illustrating this undesirable phenomenon can be found in [102].

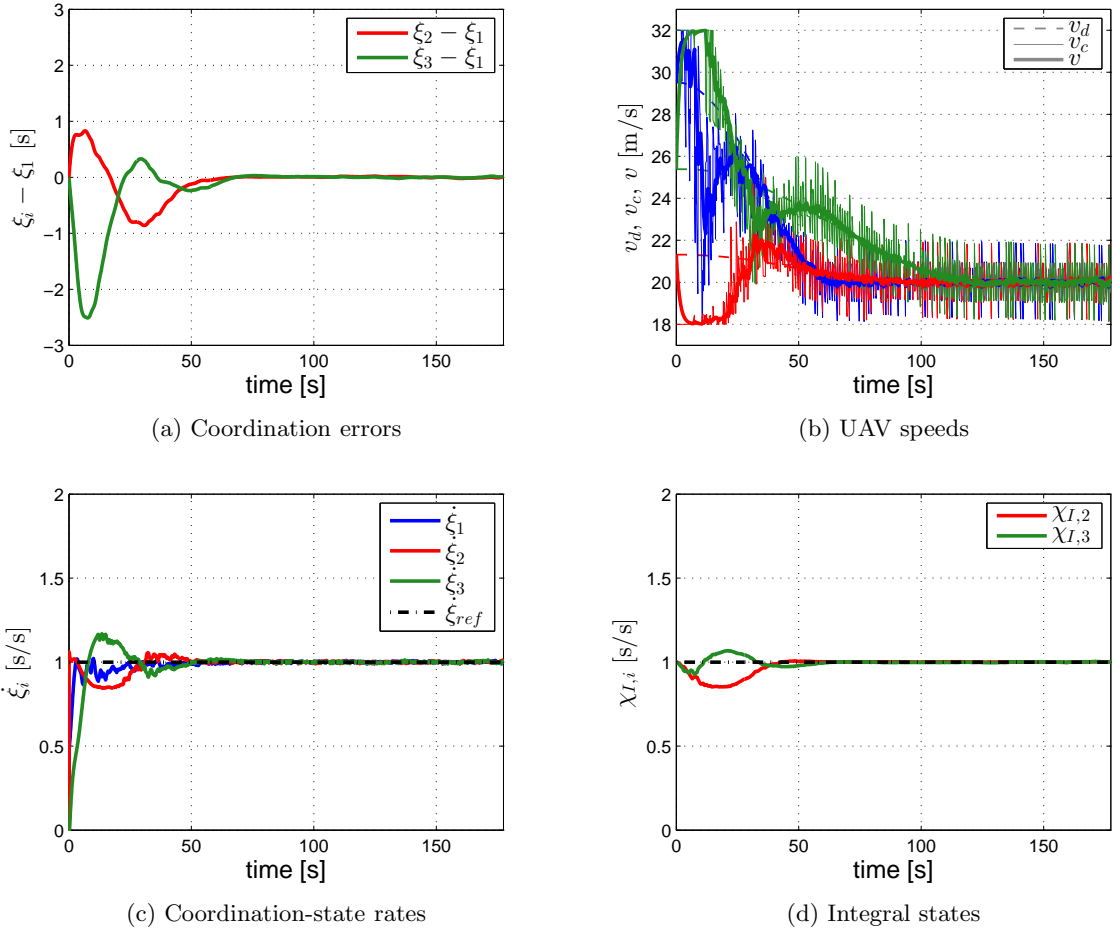


Figure 5.1: Sequential auto-landing. Closed-loop coordination dynamics for the partially quantized control law under fine quantization.

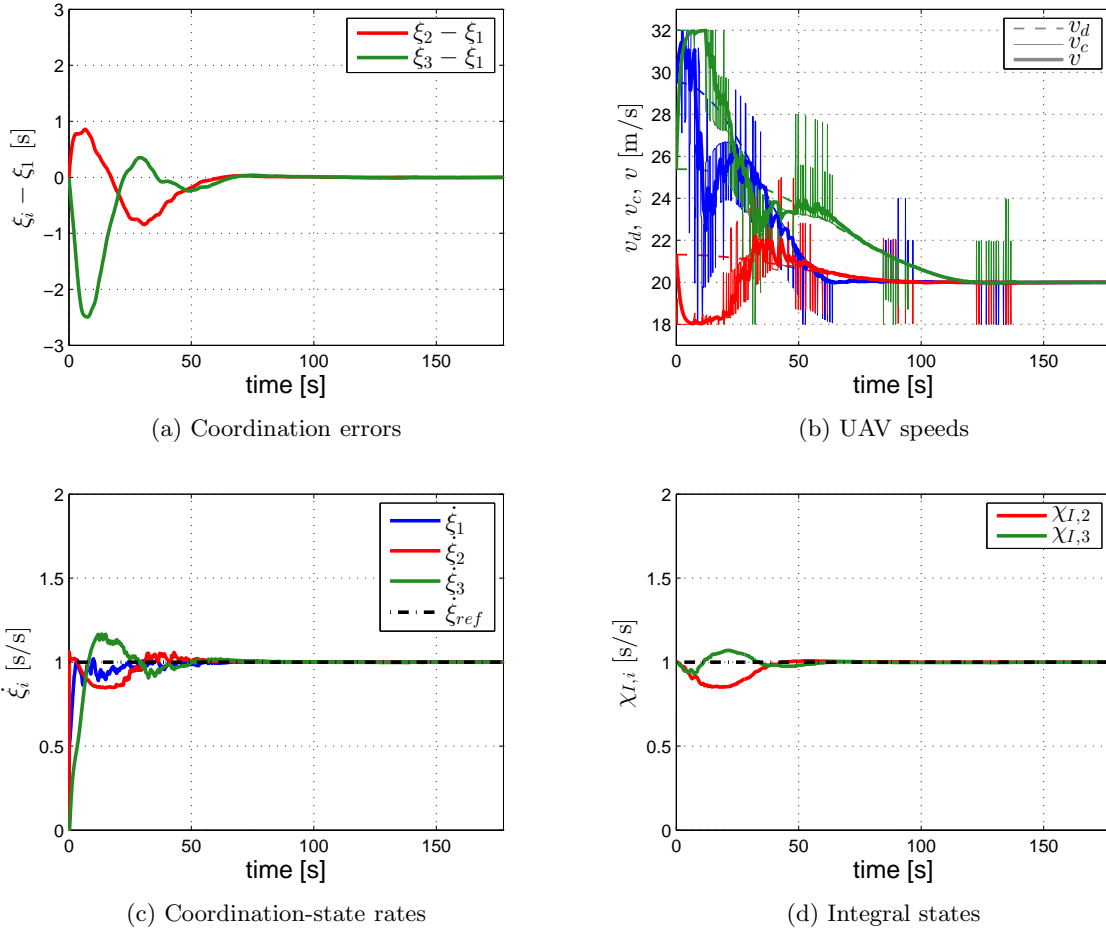


Figure 5.2: Sequential auto-landing. Closed-loop coordination dynamics for the fully quantized control law under fine quantization.

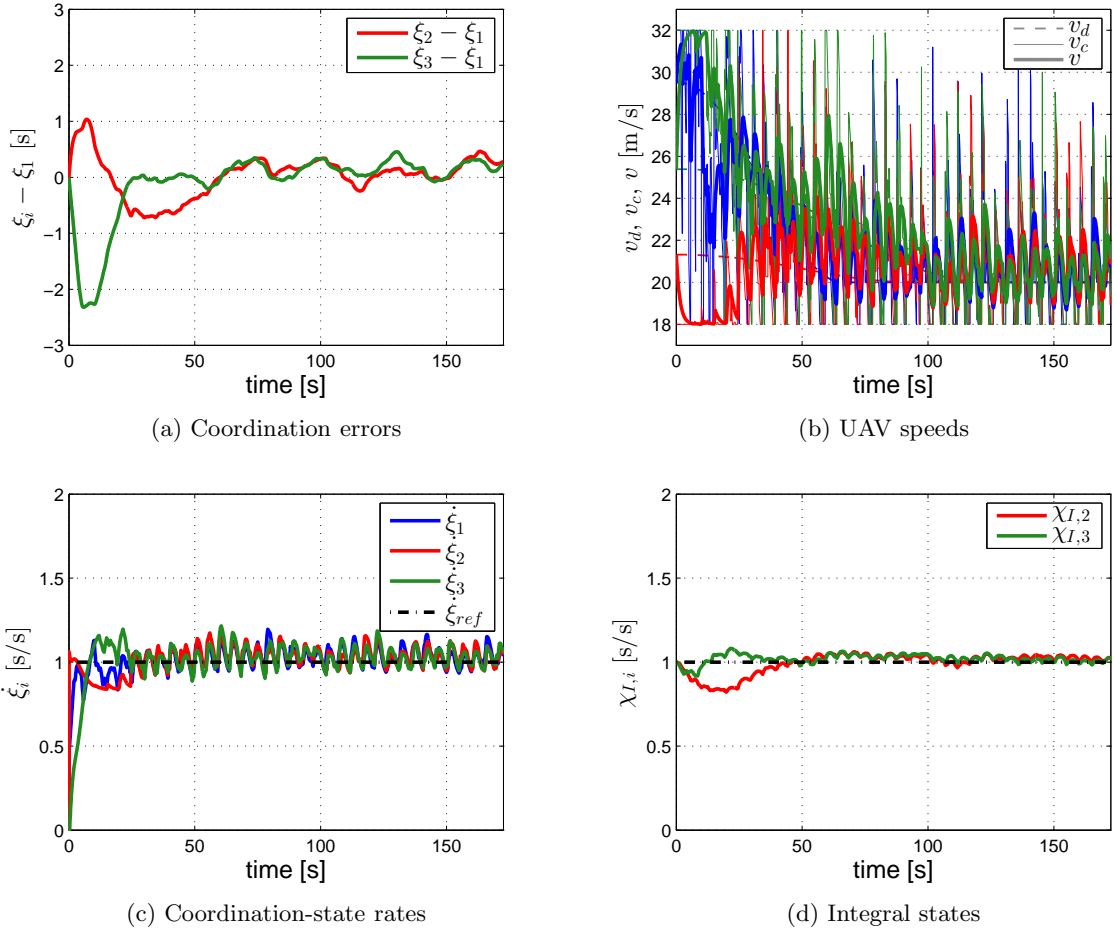


Figure 5.3: Sequential auto-landing. Closed-loop coordination dynamics for the partially quantized control law under coarse quantization.

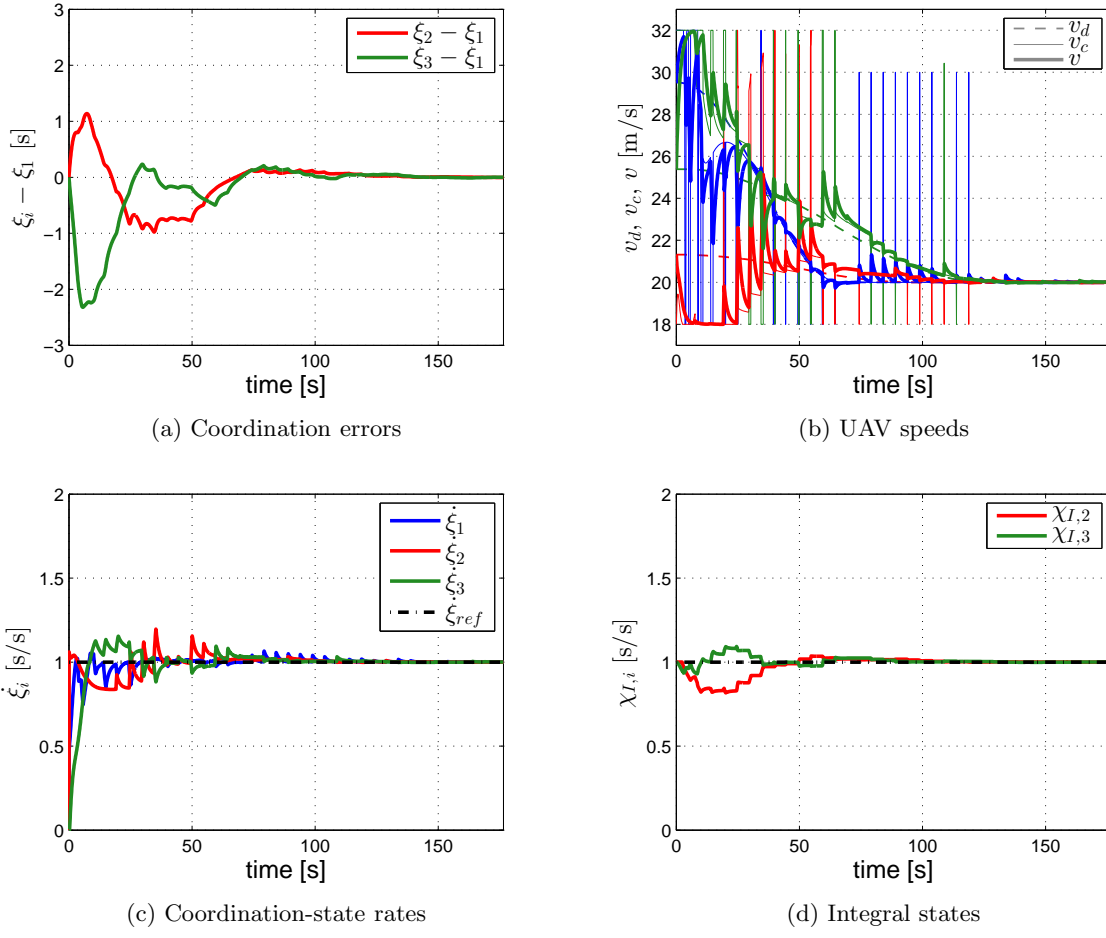


Figure 5.4: Sequential auto-landing. Closed-loop coordination dynamics for the fully quantized control law under coarse quantization.

Chapter 6

Time-Critical Coordination under Low Connectivity

In Chapter 4 we have proven that the (guaranteed) rate of convergence of the coordination control loop is limited by the QoS of the communications network; see Lemmas 3 and 4. This implies that in communication-limited environments, characterized by small parameters μ and large parameters T , long times might be required for the vehicles to reach agreement and coordinate their positions along the paths. In this chapter, we propose a modification of the coordination control law introduced in Chapter 4 (Section 4.1.1), which is intended to improve the convergence rate of the closed-loop coordination dynamics in *low-connectivity scenarios*. While we have—as of now—no theoretical guarantee that the modified coordination algorithm achieves this objective, we provide numerical evidence suggesting that the coordination error state converges to a neighborhood of the origin in a shorter time.

6.1 Local Estimators and Topology Control

The problem of designing a control law that speeds up the convergence of the coordination dynamics under low connectivity can be seen as the dual problem of determining a logic-based communication protocol that is able to reduce the amount of information exchanged over the network while maintaining a desired level of performance. These logic-based protocols use banks of local estimators and communication logics to determine when each node should communicate its own state to the neighboring nodes, and have been shown to significantly reduce the required channel bandwidth [103, 105]. Here, instead, we propose the use of local estimators to improve the *knowledge* that each vehicle (or node) has about the coordination states of other vehicles, while continuously broadcasting its own coordination state to its neighbors, as determined by the time-varying communications topology. The states of the local estimators can then be used by the coordination control law to enforce vehicle coordination even during time-intervals when the actual coordination states of other vehicles are not available.

In this approach, the estimators are useful only if vehicles receive “enough” information from the corresponding neighboring vehicles; if this is not the case, then each vehicle is just carrying a bag of estimators

with worthless information, which may reduce the convergence rate of the coordination error dynamics due to a “large network effect”.¹ This implies that precise a priori knowledge about the (local) structure of the network topology would be beneficial for an effective implementation of such estimators. The framework adopted in this thesis, however, assumes no information about the structure of the network topology, other than the—rather general—PE-like connectivity assumption in (2.14). This means that the vehicles involved in the mission do not know in advance which neighbors they are going to exchange information with or the amount of information received from each neighbor. The question is thus how to design a protocol that can take advantage of the additional information provided by the estimators without experiencing the drawbacks associated with a large extended network.

To address this problem, in this chapter we borrow and expand tools and concepts from control of complex networks, and develop strategies to control the communication links between each vehicle and its estimators. These topology-control strategies are thus responsible for deciding when a vehicle should “listen” to a particular estimator and adjusting the corresponding link weight accordingly. This approach leads to an evolving network, whose topology depends on the local exchange of information among nodes.

6.1.1 Estimator Dynamics

Recalling that, at the kinematic level, the evolution of the coordination states is described by single integrators (see Equation (4.3)), the estimate of the coordination state of vehicle j implemented at the i th vehicle, denoted here by $\hat{\xi}_j^i(t)$, is obtained from the following dynamics:

$$\dot{\hat{\xi}}_j^i(t) = u_j^i(t), \quad \hat{\xi}_j^i(0) = \xi_i(0),$$

with the control law

$$u_j^i(t) = -\hat{k}_P(\hat{\xi}_j^i(t) - \xi_i(t)) - a_{ij}(t)\hat{l}_P(\hat{\xi}_j^i(t) - \xi_j(t)) + \hat{\chi}_j^i(t), \quad (6.1a)$$

$$\dot{\hat{\chi}}_j^i(t) = -\hat{k}_I(\hat{\xi}_j^i(t) - \xi_i(t)) - a_{ij}(t)\hat{l}_I(\hat{\xi}_j^i(t) - \xi_j(t)), \quad \hat{\chi}_j^i(0) = 1, \quad (6.1b)$$

where $\hat{k}_P, \hat{k}_I > 0$ are consensus gains, $\hat{l}_P, \hat{l}_I > 0$ are learning gains, and $a_{ij}(t)$ is the (i, j) entry of the time-varying adjacency matrix $\mathbf{A}(t)$ of graph $\Gamma(t)$. On the one hand, the first term in (6.1a) and (6.1b) ensures that the estimate $\hat{\xi}_j^i(t)$ follows the coordination state of vehicle i and is not left behind in the absence of information from vehicle j . On the other hand, the second term in these equations incorporates the

¹As will become clear later, the implementation of these estimators on each vehicle creates an extended network, which can have a significantly larger number of nodes and a smaller connectivity degree than the original vehicle network.

information available from vehicle j into the estimator dynamics, and is thus responsible for learning the evolution of its coordination state. From a practical perspective, the learning gains \hat{l}_P and \hat{l}_I should be larger than the consensus gains \hat{k}_P and \hat{k}_I so that the learning component dominates the estimator dynamics as soon as new information from vehicle j is available. Note, however, that the choice of (large) learning gains is constrained by the presence of channel noise in real-world applications.

6.1.2 Coordination Control Law and Link-Weight Dynamics

To improve the convergence rate of the closed-loop coordination dynamics, we propose the following modification of the distributed coordination control law (4.4):

$$\begin{aligned} u_{\text{coord},i}(t) &= -k_P \sum_{j \in \mathcal{N}_i(t)} (\xi_i(t) - \xi_j(t)) - \hat{k}_P \sum_{j \in \mathcal{S}_i} \alpha_{ij}(t)(\xi_i(t) - \hat{\xi}_j^i(t)) + 1 \quad , \quad i = 1, \dots, n_\ell , \\ u_{\text{coord},i}(t) &= -k_P \sum_{j \in \mathcal{N}_i(t)} (\xi_i(t) - \xi_j(t)) - \hat{k}_P \sum_{j \in \mathcal{S}_i} \alpha_{ij}(t)(\xi_i(t) - \hat{\xi}_j^i(t)) + \chi_{I,i}(t) \quad , \quad i = n_\ell + 1, \dots, n , \\ \dot{\chi}_{I,i}(t) &= -k_I \sum_{j \in \mathcal{N}_i(t)} (\xi_i(t) - \xi_j(t)) - \hat{k}_I \sum_{j \in \mathcal{S}_i} \alpha_{ij}(t)(\xi_i(t) - \hat{\xi}_j^i(t)) , \quad \chi_{I,i}(0) = 1 \end{aligned}$$

where \mathcal{S}_i represents the group of vehicles for which vehicle i runs an estimator, and $\alpha_{ij}(t)$ are time-varying link weights that can be manipulated at will. The control law above adjusts the speed commands for the vehicles based not only on the actual coordination states of the neighboring vehicles (when available), but also on the information provided uninterruptedly by the estimators. This setup leads to an extended network of $(n + \sum_i \text{card}(\mathcal{S}_i))$ nodes with a time-varying directed topology of small connectivity degree. Figure 6.1 presents a simple example illustrating the node configuration and the information flow of this extended network.

Effective use of the estimators requires a careful design of the dynamics of the link weights $\alpha_{ij}(t)$, which should ensure that only the states of the estimators with useful information are included in the coordination control law. The blind addition of coordination-state estimates to the control law, without consideration of the quality of such estimates, is likely to slow down the convergence of the coordination error dynamics by forcing the vehicles to carry a bag of estimators with no valuable information. To prevent this undesirable “large network effect”, we propose to dynamically adjust the weights $\alpha_{ij}(t)$ as a function of the quality of

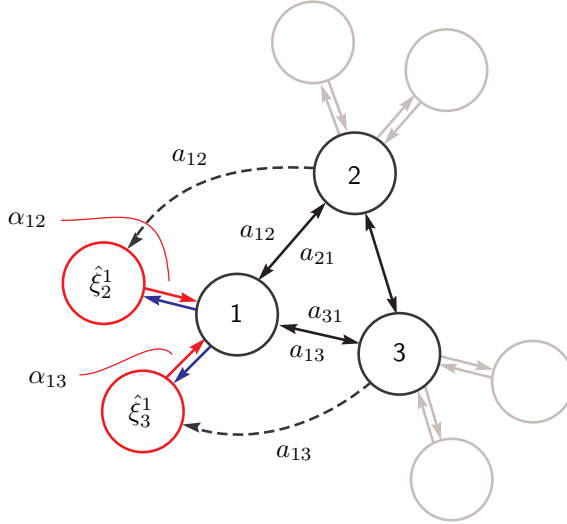


Figure 6.1: Extended network with local estimators. Example of a network of three vehicles running each one two estimators and the resulting information flow for vehicle 1.

the local estimates. To this effect, we define the following variables:

$$\hat{\mu}_{ij}(t) := \frac{1}{T_\mu} \int_{t-T_\mu}^t a_{ij}(\tau) d\tau, \quad j \in \mathcal{S}_i, \quad i = 1, \dots, n,$$

where $T_\mu > 0$ is a constant *characteristic time*. From its definition, it follows that the variable $\hat{\mu}_{ij}(t)$ represents a measure of the quality of the communication link between vehicle i and vehicle j and, hence, can be used to characterize the quality of the coordination-state estimate of the j th vehicle. For example, if $\hat{\mu}_{ij}(t) \approx 0$, then the i th vehicle has received little information from vehicle j in the time-interval $[t - T_\mu, t]$, which implies that the estimate of the coordination state of vehicle j is likely to be inaccurate; instead, if $\hat{\mu}_{ij}(t) \approx 1$, then vehicles i and j have constantly been exchanging information during the interval $[t - T_\mu, t]$, which suggests that the coordination-state estimate of vehicle j is accurate. As a practical note, it is important to emphasize that the variables $\hat{\mu}_{ij}(t)$ can be easily computed locally by the vehicles if each packet exchanged over the network contains the source vehicle's identifier.

At this point, various strategies can be adopted to judiciously design the dynamics of the weight links $\alpha_{ij}(t)$ as a function of the variables $\hat{\mu}_{ij}(t)$. Here, we investigate two different approaches for topology control: (i) a *hybrid strategy* in which links switch between different activation/deactivation modes; and (ii) a continuous strategy based on *edge snapping* [23, 24]. Next, we provide details about these two strategies:

- *Hybrid Strategy:* Letting μ_{\min} and μ_{\max} be a priori defined activation thresholds, the link weights $\alpha_{ij}(t)$

can be assigned as follows:

$$\alpha_{ij}(t) = \begin{cases} 0, & \text{if } \hat{\mu}_{ij}(t) < \mu_{\min}, \\ 1, & \text{if } \mu_{\min} \leq \hat{\mu}_{ij}(t) \leq \mu_{\max}, \\ 0, & \text{if } \mu_{\max} < \hat{\mu}_{ij}(t). \end{cases}$$

According to this strategy, vehicle i only “listens” to its j th estimator if the variable $\hat{\mu}_{ij}(t)$ is between the thresholds μ_{\min} and μ_{\max} . If $\hat{\mu}_{ij}(t) < \mu_{\min}$, it is considered that the estimator does not contain valuable information about the coordination state of vehicle j and, therefore, the corresponding estimate is not included in the control law. If $\hat{\mu}_{ij}(t) > \mu_{\max}$, then it is considered that there is enough communication between vehicles i and j to ensure a fast convergence of the coordination error dynamics, and the information from the estimator can thus be ignored.

- *Edge Snapping:* In this strategy, the evolution of each link weight $\alpha_{ij}(t)$ is modeled as a second-order dynamical system subject to the action of a two-well potential and driven by an appropriately designed forcing signal. More precisely, this approach sets

$$\alpha_{ij}(t) = \sigma_{ij}^2(t), \quad j \in \mathcal{S}_i, \quad i = 1, \dots, n,$$

where $\sigma_{ij}(t)$ is generated through the following dynamics:

$$\ddot{\sigma}_{ij}(t) + d_\sigma \dot{\sigma}_{ij}(t) + \frac{dU(\sigma_{ij})}{d\sigma_{ij}}(t) = g(\hat{\mu}_{ij}(t), \hat{e}_j^i(t)), \quad j \in \mathcal{S}_i, \quad i = 1, \dots, n.$$

In the above equation, d_σ is the damping coefficient, $U(\cdot)$ is a two-well potential function, while $g : \mathbb{R} \times \mathbb{R} \rightarrow \mathbb{R}$ is the forcing function, which—for the purpose of our problem—we take to depend on the variable $\hat{\mu}_{ij}(t)$ as well as the error $\hat{e}_j^i(t) := \hat{\xi}_j^i(t) - \xi_i(t)$. This strategy yields a bistable dynamical behavior of the link weights, which leads to self-emerging unweighted topologies and, unlike the hybrid approach discussed previously, results in a continuous evolution of the link weights.

Finally, we note that the estimators and topology-control algorithms proposed here do not require any a priori knowledge about the structure of the network topology and can be implemented in a distributed fashion onboard the autonomous vehicles. The main drawback of this approach is an increase in the computational demands of the system, as these algorithms have to be run onboard the vehicles in real time. There is, thus, a trade-off between the overall coordination performance and the onboard computational requirements. In the next section, we present simulation results that illustrate the benefits of the modified coordination control law proposed here for low-connectivity scenarios.

6.2 Simulation Results

In this section, we consider again the sequential auto-landing mission scenario described in Section 4.4.2 of Chapter 4, and augment the proportional-integral coordination control law developed in Chapter 4 with the onboard estimators (two per vehicle) as well as the two strategies for topology control and link assignment. Similar to the results presented in previous chapters, simulations in this section are based on the kinematic model of the UAV in (3.10) along with a simplified, decoupled linear model of the UAV with its autopilot.

In this set of simulations, the path-following controller gains are selected as follows:

$$k_\ell = 0.20 \text{ [1/s]}, \quad k_{\tilde{R}} = 0.50 \text{ [1/s]}, \quad d = 125 \text{ [m]},$$

while the control gains for the (extended) coordination algorithm are chosen as

$$\begin{aligned} k_P &= 1.0 \cdot 10^{-1} \text{ [1/s]}, & k_I &= 1.0 \cdot 10^{-2} \text{ [1/s}^2], & k_{aw} &= 2.0 \cdot 10^{-3} \text{ [1/m]}, & G_{aw}(s) &= \frac{1}{s+1}, \\ \hat{k}_P &= 1.0 \cdot 10^{-1} \text{ [1/s]}, & \hat{k}_I &= 2.0 \cdot 10^{-2} \text{ [1/s}^2], & \hat{k}_P &= 1.0 \cdot 10^0 \text{ [1/s]}, & \hat{k}_I &= 1.0 \cdot 10^{-1} \text{ [1/s}^2], \end{aligned}$$

with the following settings for the link-weight dynamics:

- *Hybrid Strategy:* The characteristic time is set to $T_\mu = 5$ s, and the activation thresholds are set to $\mu_{\min} = 0.05$ and $\mu_{\max} = 0.6$.
- *Edge Snapping:* The characteristic time is also set to $T_\mu = 5$ s, and the damping coefficient d_σ , the two-well potential function $U(\cdot)$, and the forcing function $g(\cdot, \cdot)$ are given by

$$\begin{aligned} d_\sigma &= 4, & U(\sigma_{ij}) &= 0.01 (\sigma_{ij} - 1)^2 (15\sigma_{ij}^2 + 2\sigma_{ij} + 1), \\ g(\hat{\mu}_{ij}, \hat{e}_j^i) &= 4 (\mu_{\max} - \hat{\mu}_{ij})(\hat{\mu}_{ij} - \mu_{\min}) |\hat{e}_j^i|, & \mu_{\min} &= 0.05, \quad \mu_{\max} = 0.6. \end{aligned}$$

The two-well potential function and the forcing function are illustrated in Figure 6.2.

In all of the simulations, vehicle 1 is elected as the single leader of the fleet. The angular-rate commands are saturated to ± 0.3 rad/s, and the speed commands are saturated between 18 m/s and 32 m/s. The information flow is assumed to be time-varying and, at any given time t , is characterized by one of the first four graphs in Figure 4.2 (that is, topologies 1 through 4).

To analyze the convergence properties of the proposed algorithms, a set of Monte Carlo simulations has been conducted for a total of 1024 simulation configurations, consisting of different initial conditions of

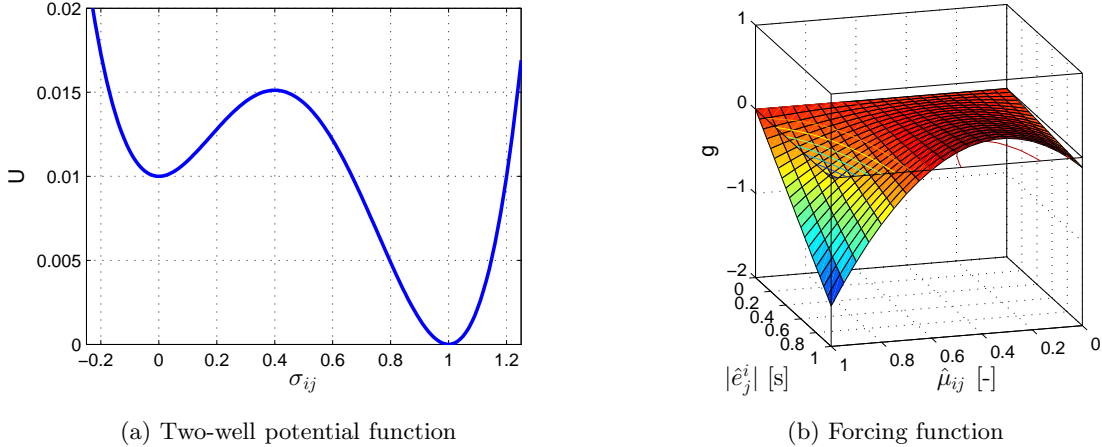


Figure 6.2: Edge snapping; two-well function and forcing function for link-weight dynamics.

the UAVs and different switching topologies. For each configuration (initial condition and switching topology), three simulation runs are performed with the following three coordination algorithms: (i) the “basic” proportional-integral coordination control law described in Chapter 4; (ii) the modified coordination control law with node estimators and binary link weights (hybrid strategy); and (iii) the modified coordination control law with node estimators and continuous link weights (edge snapping). For each run we compute the amount of time it takes for the 2-norm of the coordination error state $\zeta(t)$ to converge to a 0.1-error band, which corresponds to a maximum coordination error ($\xi_i(t) - \xi_j(t)$) of approximately 0.2 s (see Equation (C.23) in Appendix C.3). We represent each of these convergence times as T_k^m , $k = 1, \dots, 1024$ and $m = \{\text{b}, \text{h}, \text{e}\}$, where ‘b’ stands for *basic*, ‘h’ stands for *hybrid*, and ‘e’ stands for *edge snapping*.

The data obtained from these Monte Carlo runs is shown in Figure 6.3a. To remove the dependency of convergence time on the initial conditions of the UAVs, the figure also presents the convergence times T_k^h and T_k^e normalized to the corresponding T_k^b ; see Figure 6.3b. As can be observed in the figure, all of the normalized convergence times for the hybrid approach are below 1 (except for one, which we will discuss shortly), which suggests that the proposed approach is effective for speeding up coordination in low-connectivity scenarios. The single normalized convergence time above 1 corresponds to sample #546, with convergence times $T_{546}^b = 12.5$ s and $T_{546}^h = 18.4$ s. This sample corresponds thus to a configuration in which the UAVs start the mission almost coordinated, and the modified control law delays convergence of the coordination error dynamics to the 0.1-error band by roughly 6 s for a mission with a desired duration of approximately 175 s. This isolated anomaly is, hence, of no particular concern. Similar conclusions can be drawn for the coordination control law with edge snapping. In fact, only three runs present a normalized convergence time

above 1, while the remaining 1021 samples are below 1. One of these runs also corresponds to sample #546, with convergence time $T_{546}^e = 23.6$ s. The other two runs correspond to samples #517 and #971, with convergence times $T_{517}^b = 50.8$ s and $T_{517}^e = 54.9$ s, and $T_{971}^b = 44.2$ s and $T_{971}^e = 46.9$ s, respectively, which represent an increase of approximately 6% and 8%. Despite these three samples, the data seems to support the observation that the edge-snapping strategy is also capable of speeding up coordination of the fleet in low-connectivity scenarios, albeit not as effectively as the hybrid approach.

To provide further insight into these results, Figure 6.4 presents histograms of the normalized convergence time of the coordination error dynamics with both the hybrid approach and the edge-snapping strategy. In addition, the figure also shows *generalized extreme value* (GEV) distribution fits to these histograms [56]. The location, scale, and shape parameters (conventionally denoted in the literature as μ , σ , and ξ) characterizing these two GEV distribution fits are summarized in Table 6.1. The table also contains estimates of the mean of both distributions, which indicate that, in average, the hybrid approach is able to reduce the convergence time to a 43% of the original value, while the edge-snapping strategy shortens the convergence time to a 51% of this value.

Finally, we present time-history responses of the control algorithms proposed in this chapter. In particular, Figures 6.5-6.7 show the results obtained for one of the Monte Carlo runs obtained with the hybrid approach, while Figures 6.8-6.10 illustrate the results obtained with the coordination algorithm with edge snapping for the same scenario. The figures show the time-evolution of the coordination errors ($\xi_i(t) - \xi_j(t)$), the rate of change of the coordination states $\dot{\xi}_i(t)$, the UAV speeds $v_i(t)$, the integral states $\chi_{I,i}(t)$ implemented on the follower vehicles, the time-evolution of the link weights between the vehicles and their estimators $\hat{\alpha}_{ij}(t)$, as well as the variables $\hat{\mu}_{ij}(t)$. As a reference for comparison, the figures also present (in pale dashed lines) the time-responses of the coordination errors ($\xi_i(t) - \xi_j(t)$) as well as the rate of change of the coordination states $\dot{\xi}_i(t)$ obtained with the “basic” proportional-integral coordination control law described in Chapter 4. The figures also show the evolution of the time-varying network topology along with an estimate of the QoS of the network, computed as in (4.29). This set of simulation results illustrates the benefits of the proposed algorithms in terms of coordination performance, and evidences the different nature of the two topology-control strategies developed in this chapter. While the hybrid approach forces the link weights to continuously switch back and forth from 0 to 1 (Figure 6.7), the edge-snapping strategy leads to an extended, stable, unweighted network topology with a total of 9 nodes (Figure 6.10).

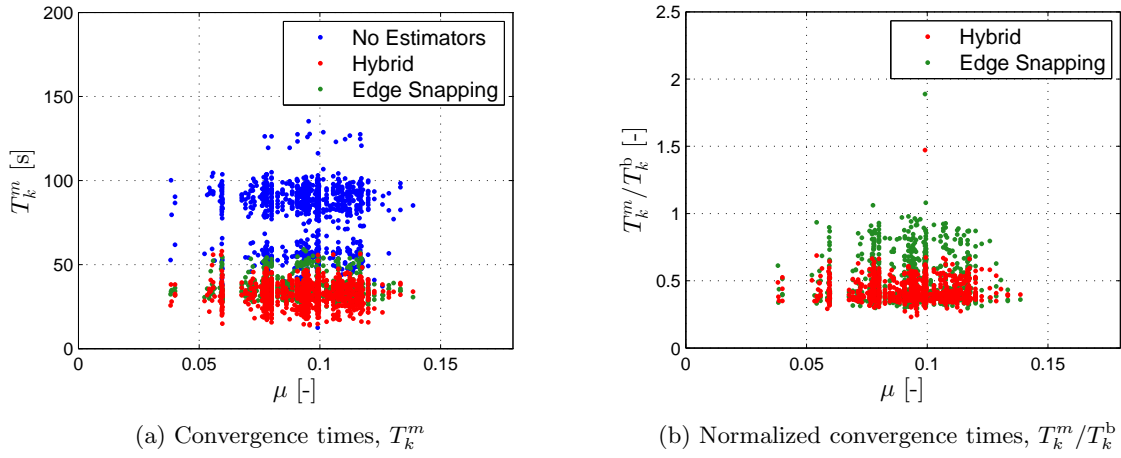


Figure 6.3: Convergence time of the coordination error dynamics to a 0.1-error band with three different coordination algorithms.

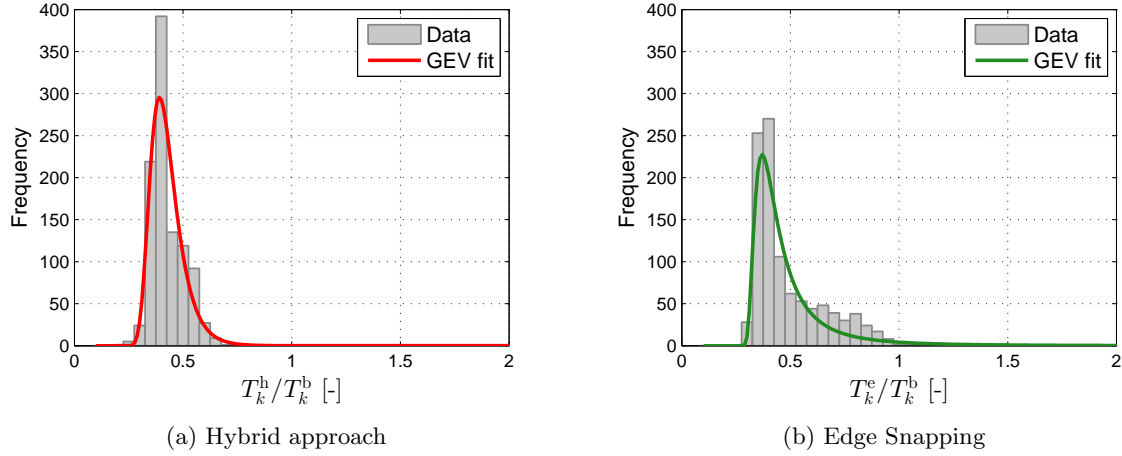


Figure 6.4: Histograms and distribution fits of the normalized convergence time of the coordination error dynamics with both the hybrid approach and the edge-snapping strategy.

Table 6.1: Mean, variance, as well as location, scale, and shape parameters characterizing the two GEV distributions in Figure 6.4.

	Hybrid		Edge Snapping	
	Estimate	95% confidence	Estimate	95% confidence
μ	0.3925	(0.3887, 0.3964)	0.3967	(0.3914, 0.4020)
σ	0.0583	(0.0556, 0.0611)	0.0763	(0.0714, 0.0815)
ξ	0.0152	(-0.0139, 0.0442)	0.4656	(0.4072, 0.5239)
Mean	0.4270	—	0.5051	—
Variance	0.0058	—	0.3021	—

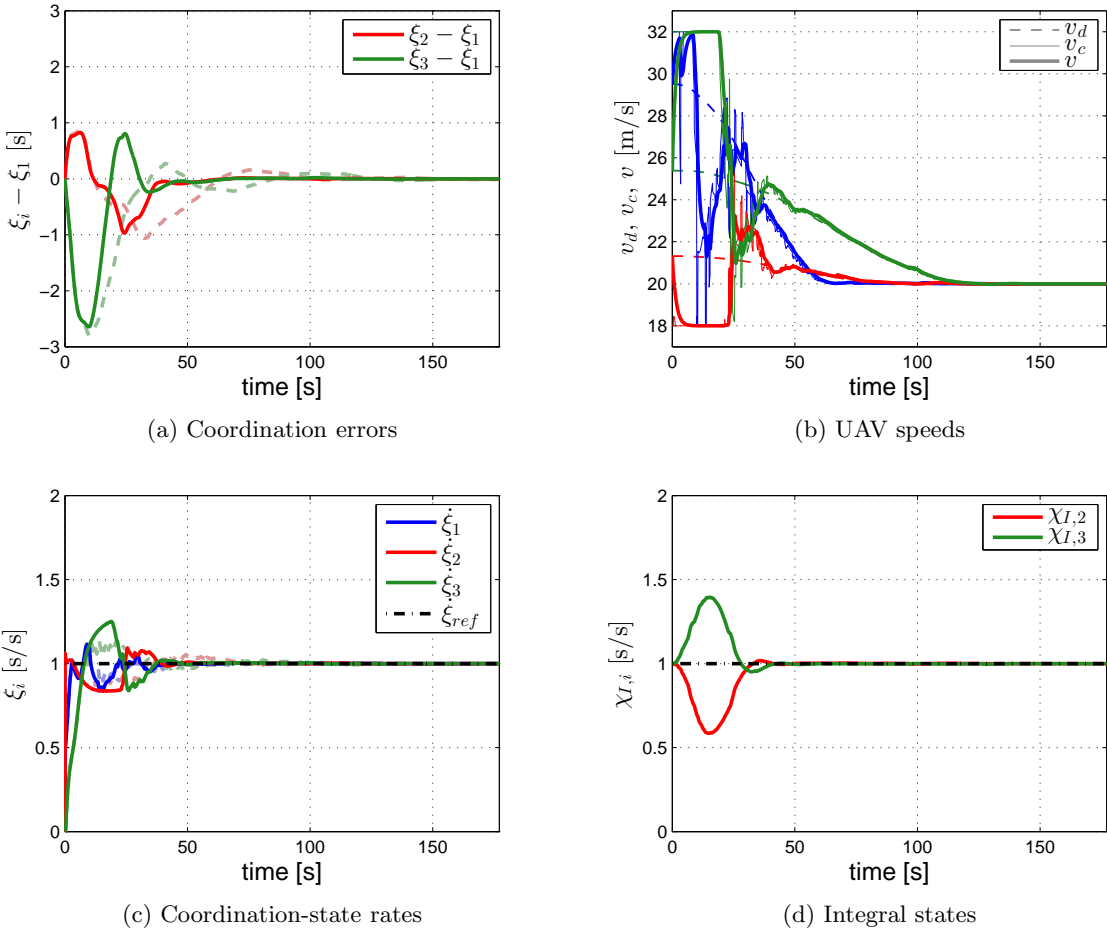


Figure 6.5: Sequential auto-landing. Closed-loop coordination dynamics for the modified control law with node estimators and binary link weights (hybrid strategy).

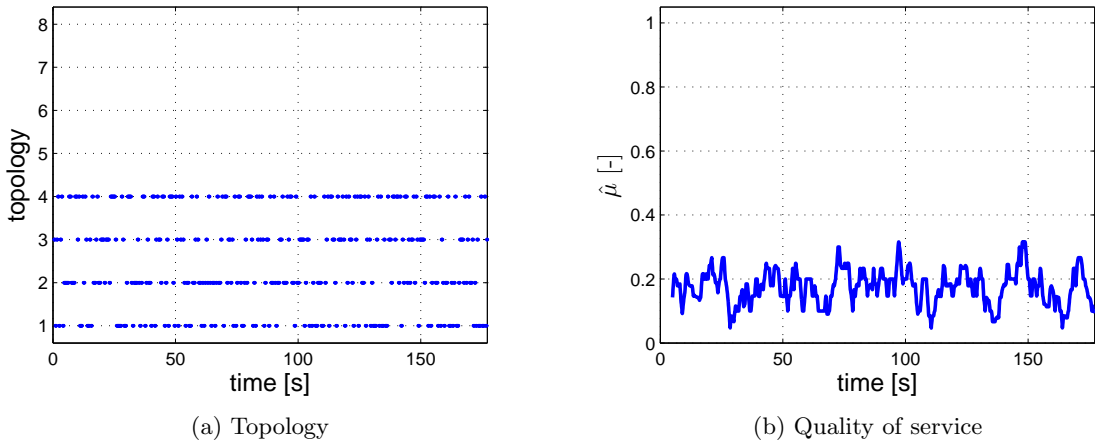


Figure 6.6: Sequential auto-landing. At a given time instant, the information flow is characterized by one of the first four topologies in Figure 4.2. The resulting graph is only connected in an integral sense, and not pointwise in time.

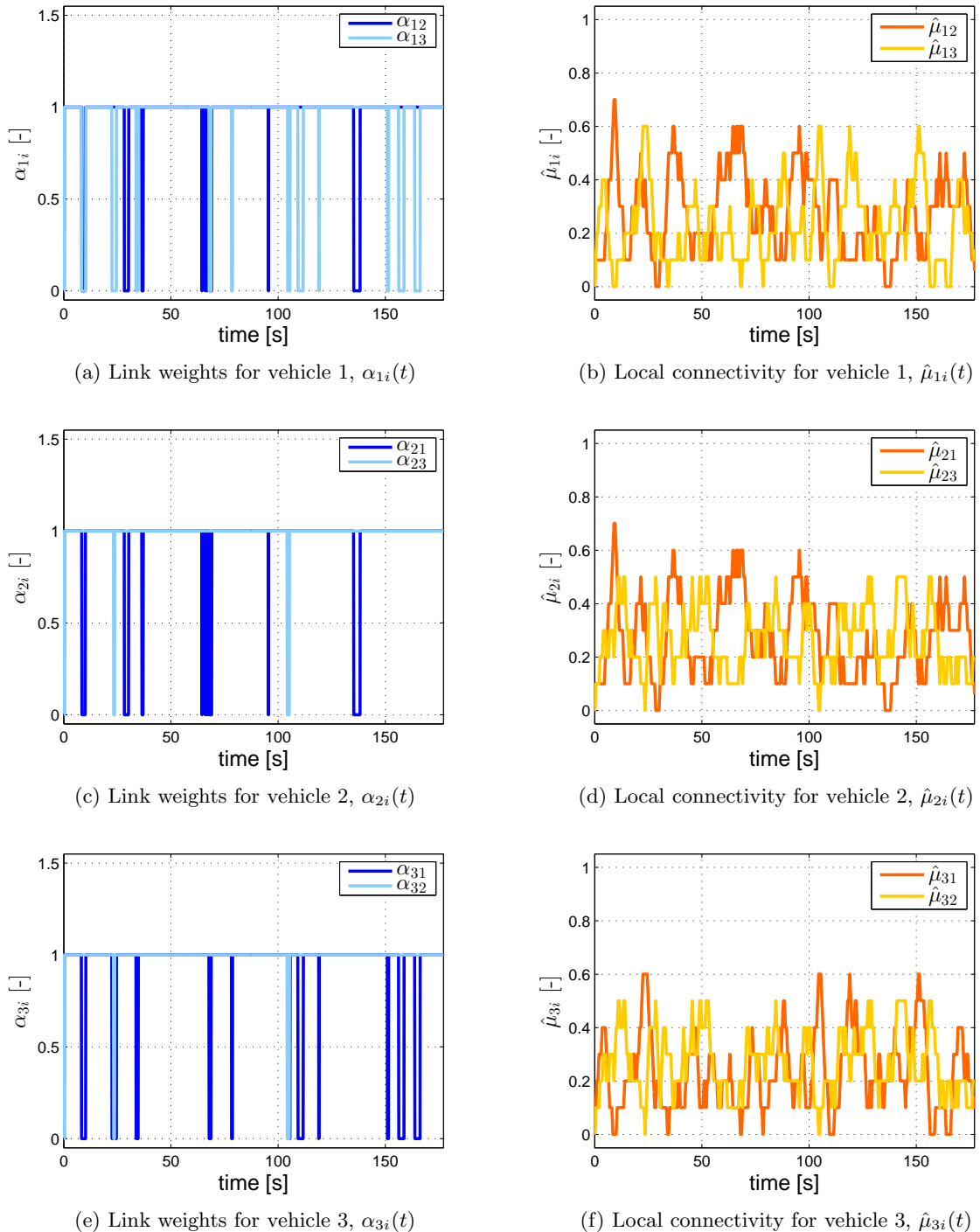


Figure 6.7: Sequential auto-landing. Time-evolution of link weights and local connectivity (hybrid strategy).

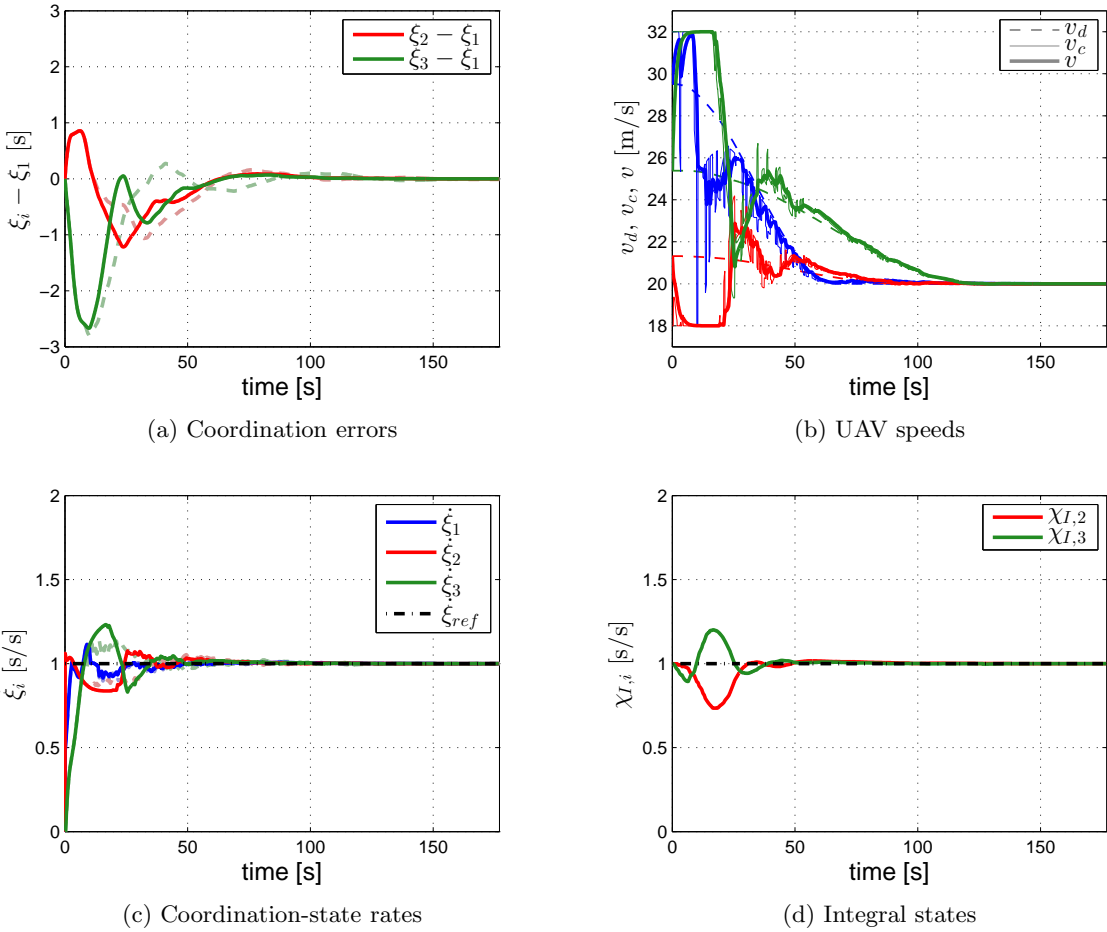


Figure 6.8: Sequential auto-landing. Closed-loop coordination dynamics for the modified control law with node estimators and continuous link weights (edge snapping).

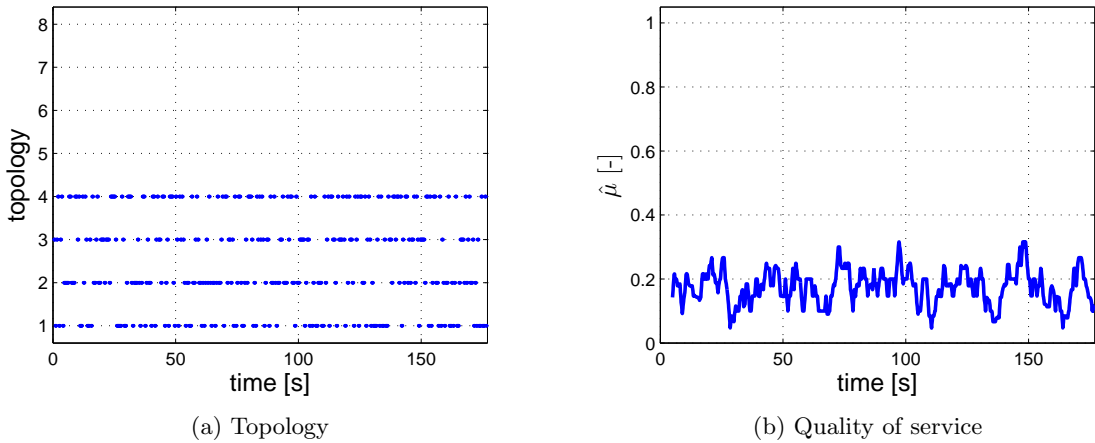


Figure 6.9: Sequential auto-landing. At a given time instant, the information flow is characterized by one of the first four topologies in Figure 4.2. The resulting graph is only connected in an integral sense, and not pointwise in time.

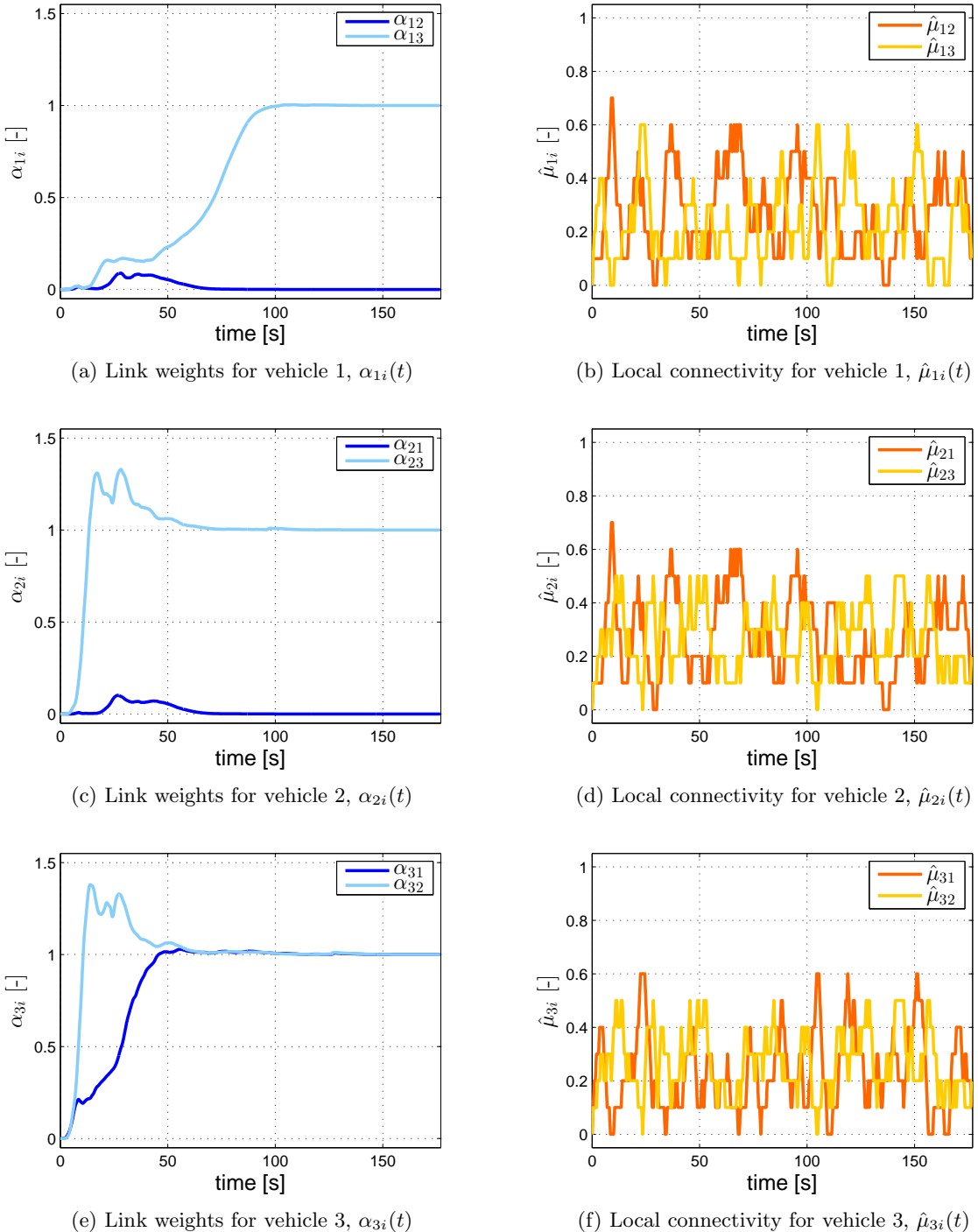


Figure 6.10: Sequential auto-landing. Time-evolution of link weights and local connectivity (edge snapping).

Chapter 7

Flight Tests: Cooperative Road Search

This chapter presents flight-test results for a cooperative road-search mission that show the efficacy of the multi-UAV cooperative framework presented in this thesis. The flight tests were performed during the quarterly run Tactical Network Topology¹ field experiments conducted through the Field Experimentation Cooperative Program, which is being led by the U.S. Special Operations Command and the Naval Post-graduate School (NPS). The significance of these experiments is twofold. First, the results verify the main stability and convergence properties of the developed cooperative algorithms in a realistic mission scenario, under environmental disturbances and with the limitations of a real-world communications network. And second, the results demonstrate the validity of the proposed generic theoretical framework in a specific realistic application as well as the feasibility of the onboard implementation of the algorithms.

7.1 Road Search with Multiple Small Tactical UAVs

7.1.1 Airborne System Architecture

The small tactical UAVs employed in this particular mission are two SIG Rascals 110 operated by NPS; see Figure 7.1. The two UAVs have the same avionics and the same instrumentation onboard, the only difference being the vision sensors. The first UAV has a 1DoF bank-stabilized high-resolution 12-MPx camera, while the second UAV has a full-motion video camera suspended on a 2DoF pan-tilt gimbal. Due to weight and power constraints, each UAV is allowed to carry only one camera at a time and, therefore, the two cameras need to be mounted on different platforms. The rest of the onboard avionics, common to both platforms, includes two PC-104 industrial embedded computers² assembled in a stack, a wireless Mobile Ad-hoc Network (MANET) link³, and the Piccolo Plus autopilot⁴ with its dedicated 900-MHz command and control channel. Details of the complete airborne network-centric architecture are presented in Figure 7.2.

¹Information available online at <http://www.nps.edu/Academics/Schools/GSOIS/Departments/IS/Research/FX/CBETNT/CBE/TNT.html> [Online; accessed 8 March 2013]. See also [74].

²Information available online at <http://www.adl-usa.com/products/cpu/index.php> [Online; accessed 8 March 2013].

³Information available online at <http://www.persistentsystems.com> [Online; accessed 8 March 2013].

⁴Information available online at http://www.cloudcaptech.com/piccolo_system.shtml [Online; accessed 8 March 2013].

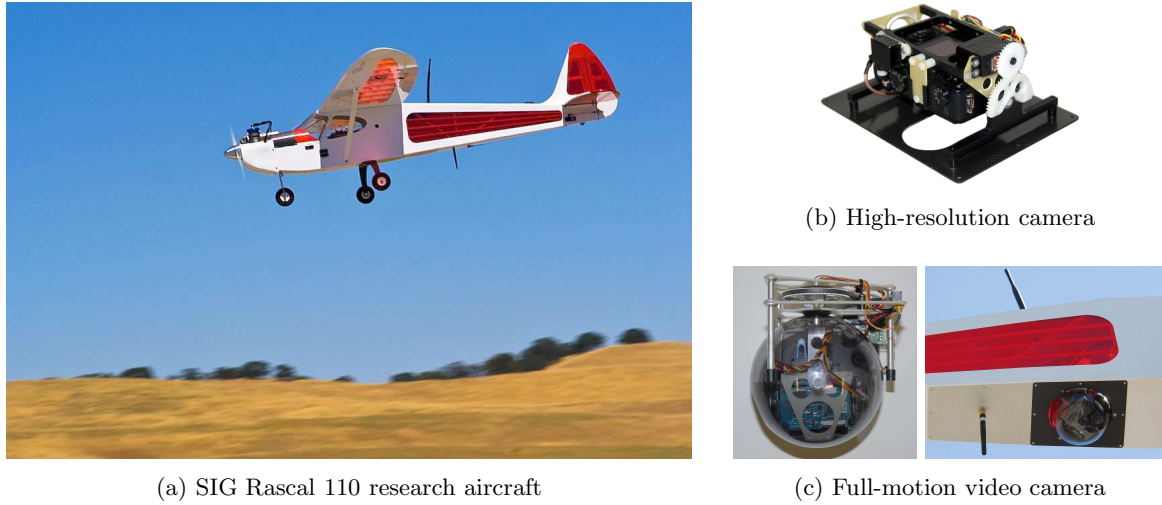


Figure 7.1: SIG Rascal UAV with two different onboard cameras. The SIG Rascal UAVs (a) used for cooperative path-following missions are equipped with complementary vision sensors. The first UAV has a bank-stabilized high-resolution 12-MPx camera (b), while the second UAV has a full-motion video camera suspended on a pan-tilt gimbal (c).

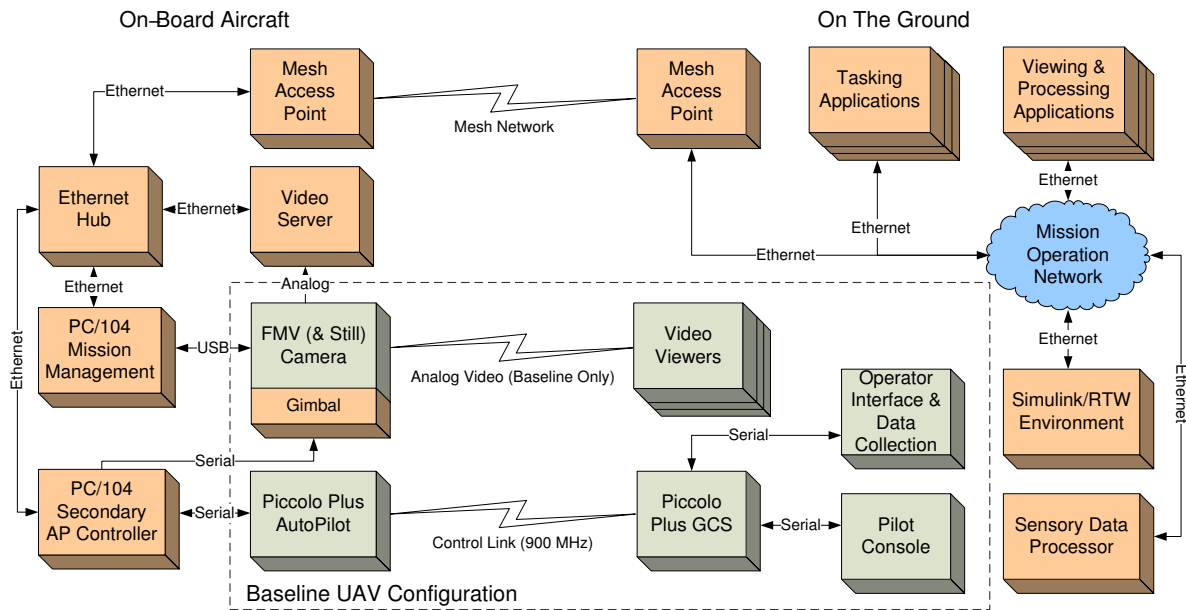


Figure 7.2: Network-centric architecture of the airborne platform. The Rascal UAV avionics include two PC-104 industrial embedded computers assembled in a stack, a wireless Mobile Ad-hoc Network link, and the Piccolo Plus autopilot with its dedicated 900-MHz command and control channel. The PC-104 computers are used to run the cooperative control algorithms in hard real time as well as mission management routines enabling onboard preprocessing and retrieval of sensory data.

The first PC-104 computer runs the cooperative-control algorithms in hard real time at 100 Hz. The computer directly communicates with the Piccolo Plus autopilot at 50 Hz over a dedicated bidirectional serial link. The second PC-104 acts as a mission management computer that implements a set of non-real-time routines enabling onboard preprocessing and retrieval of the sensory data —high-resolution imagery or video— in near real time over the network. Integration of the MANET link allows for robust, transparent inter-vehicle and ground communication, which is needed for both the coordination algorithms and the expedited sensory data delivery to a remote mission operator. In fact, the MANET link provides “any-to-any” connectivity capability, allowing every node —vehicle or ground station— to communicate with every other node. Details on the flight-test architecture and the supporting network infrastructure for coordination control and data dissemination can be found in [22].

7.1.2 Flight-Test Results

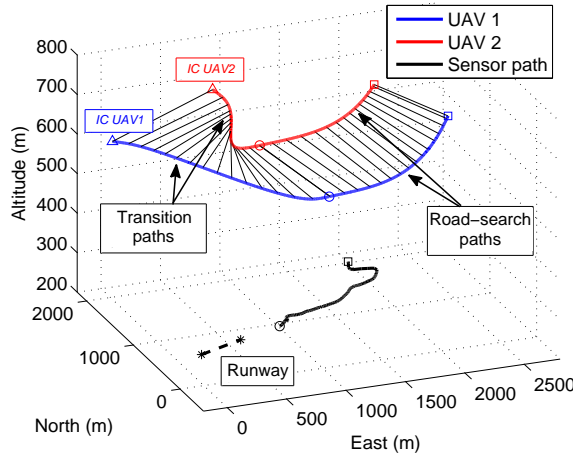
The flight-test results for a cooperative road-search mission executed by the two SIG Rascal UAVs are presented next. The objective of the mission is to detect a stationary or moving target along a pre-specified road and, if detection occurs, to collect information about the target. This information is then to be shared over a MANET link so that it can be retrieved by remote mission operators in near real time. Success of the mission relies on the ability to overlap the footprint of the FoVs of the two cameras along the road, which increases the probability of target detection [36]. Next, we provide details about the execution of this coordinated road-search mission, which we divide in four consecutive phases, namely, *initialization*, *transition*, *road search*, and *vision-based target tracking*. The description is supported by one of the flight-test results performed during a Tactical Network Topology field experiment at Camp Roberts, CA.

In the *initialization phase*, an operator specifies on a digital map the road of interest. Then, a centralized optimization algorithm generates road-search (sub)optimal paths and desired speed profiles for the two UAVs that explicitly account for UAV dynamic constraints, collision-avoidance constraints, and mission-specific constraints such as inter-vehicle and vehicle-to-ground communications limitations as well as sensory capabilities. In particular, for this mission scenario, the trajectory-generation algorithm is designed to maximize the overlap of the footprints of the FoVs of the high-resolution camera and the full-motion video during the road search, while minimizing at the same time gimbal actuation. In addition to the road-search paths and the corresponding desired speed profiles, the outcome of the trajectory-generation algorithm includes a *sensor trajectory* on the ground to be followed by the vision sensors. The two road-search paths and the sensor path, along with the three corresponding speed profiles, are then transmitted to the UAVs over the MANET link.

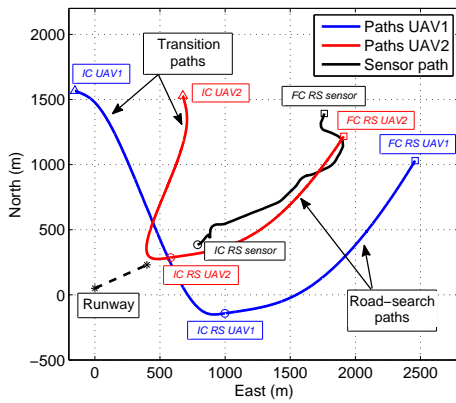
In the *transition phase*, the two UAVs fly from their standby starting positions to the initial points of the respective road-search paths. For this purpose, distributed optimization algorithms generate feasible collision-free 3D trajectories to ensure that the two UAVs arrive at the initial points of the road-search paths at the same time. Once these transition trajectories are generated, the two vehicles start operating in cooperative path-following mode. From that moment on, the UAVs follow the transition paths while adjusting their speeds based on coordination information exchanged over the MANET link in order to achieve simultaneous arrival at the starting point of the road-search paths. The transition and road-search paths obtained for this particular mission scenario, together with the corresponding desired speed profiles and the path separations, are shown in Figure 7.3. Figure 7.4 illustrates the performance of the coordination control algorithm during the transition phase of the mission. As can be observed, the inter-vehicle separation remains above 100 m and the coordination error remains below 13% during the entire duration of the transition phase, with an 11% error in coordination at the end of this phase.

The third phase addresses the *cooperative road-search mission* itself, in which the two UAVs follow the road-search paths generated in the initialization phase while adjusting their speeds to ensure the required overlap of the FoV footprints of the cameras. In this phase, a virtual target vehicle running along the sensor path is implemented on one of the UAVs. For this road-search mission, a natural choice for this sensor path is the road itself, and the virtual vehicle determines thus the spot of the road being observed by the vision sensors mounted onboard the UAVs at a given time. The virtual vehicle is in fact used as a leader in the coordination algorithm, and its speed is also adjusted based on the coordination states of the two UAVs. The coordination state of this virtual vehicle is also transmitted over the tactical network and used in the coordination control laws of the two “real” vehicles. The performance of the cooperative path-following control algorithm is illustrated in Figure 7.5. For this particular scenario, the path-following cross-track errors converge to a 3-m tube around the desired spatial paths, while the coordination errors remain below 7% during the entire duration of the road search. It is worth noting that significant data dropouts occurred between 145 s and 170 s, especially effecting UAV 1; these data dropouts cause sudden jumps in the normalized coordination states, as can be seen in Figures 7.5a and 7.5c.

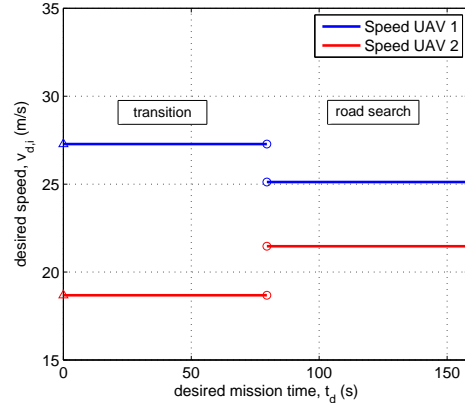
As mentioned above, maintaining a tight coordination along the paths is important to ensure a desired level of FoV overlap with desired image resolution, two key elements for reliable target detection. Figure 7.6 illustrates the performance of the road-search mission from this perspective. On the one hand, Figure 7.6a shows a set of estimates of the ground FoV footprints assuming a flat Earth with known ground elevation. These estimates assume a trapezoidal footprint, and are based on experimental data including the inertial position and orientation of the two UAVs, orientation of their cameras, as well as the line-of-sight range to



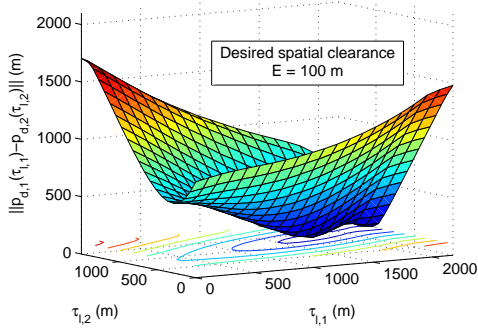
(a) Desired 3D spatial paths



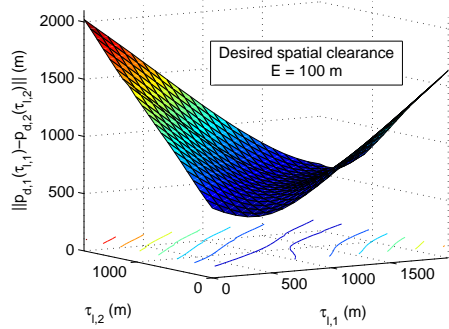
(b) 2D projections



(c) Desired speed profiles

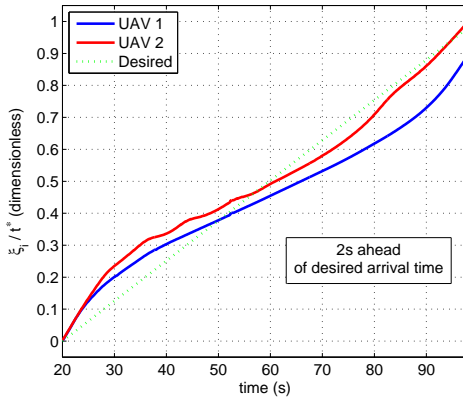


(d) Path separation for transition phase

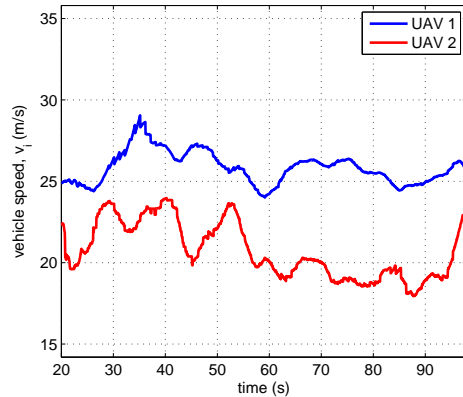


(e) Path separation for road-search phase

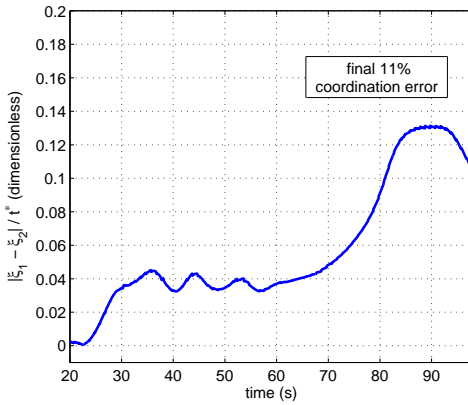
Figure 7.3: Cooperative road-search; trajectory generation.



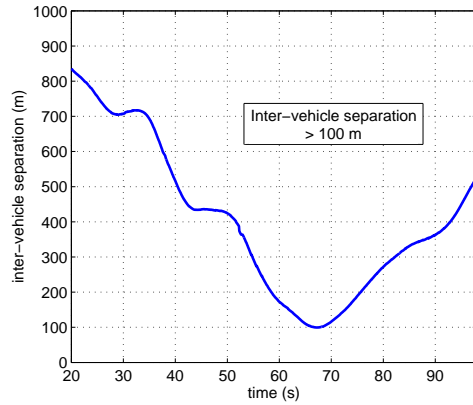
(a) Normalized coordination states



(b) UAV speeds



(c) Normalized coordination error

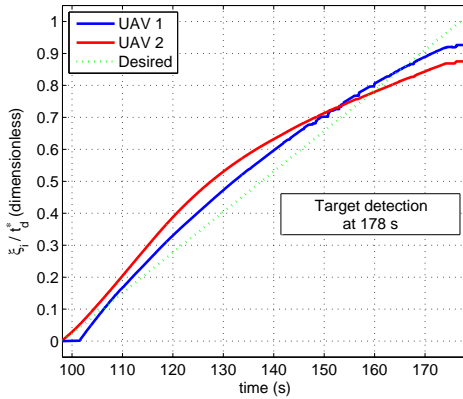


(d) Inter-vehicle separation

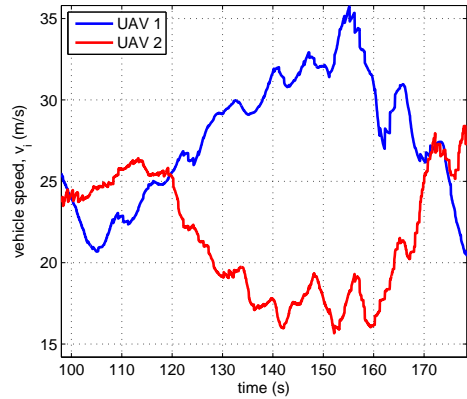
Figure 7.4: Cooperative road-search; time-coordination during the transition phase. The two UAVs arrive at the starting point of the road-search paths with an 11%-error difference.

the ground. To provide a quantitative measure of the FoV overlap, Figure 7.6b presents an image-overlap coefficient, sampled at 1 Hz. This coefficient is calculated offline using proprietary technology⁵, and is based on semi-automated alignment and differencing of two synchronous images. As can be seen, except for a 5-s initial transient, the overlap coefficient stays above 0.7 during the cooperative road search. This figure also includes a side-by-side image comparison of the imagery data obtained from the two cameras at approximately 160 s after initiation of the mission; one can easily observe that the two images correspond to the same road segment. On the other hand, Figure 7.6c shows the range for the two vision sensors to the virtual vehicle on the sensor path; these ranges are always below 1,000 m for UAV 1 and 500 m for UAV 2, therefore ensuring desired image resolution for the targets of interest given the characteristics of the two cameras.

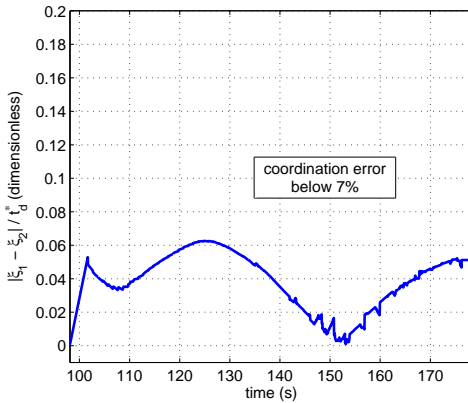
⁵Information available online at <http://perceptivu.com/TargetTrackingSoftware.html> [Online; accessed 8 March 2013].



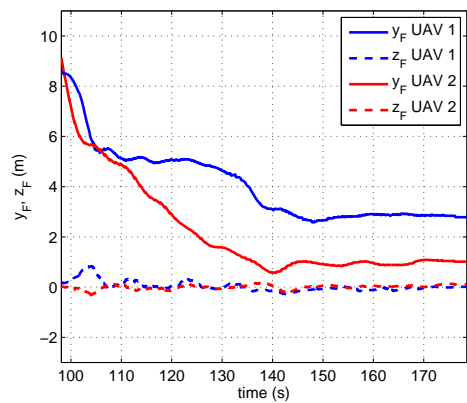
(a) Normalized coordination states



(b) UAV speeds



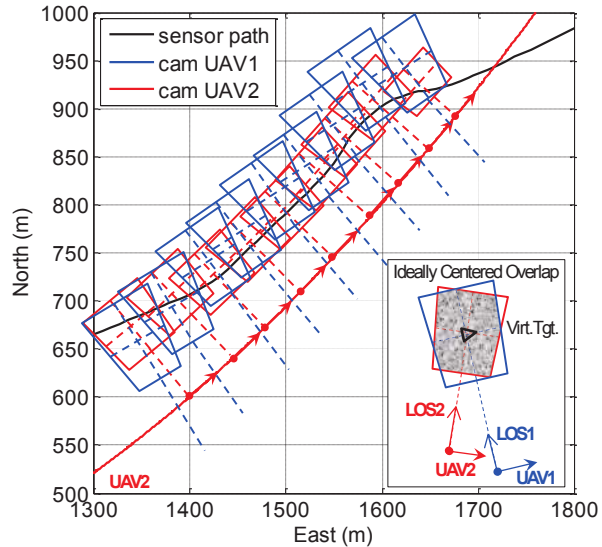
(c) Normalized coordination error



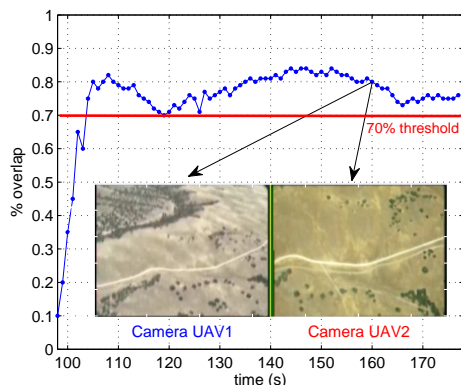
(d) Path-following cross-track errors

Figure 7.5: Cooperative road-search; cooperative path-following control during the road-search phase. The coordination errors remain below 7% during the entire duration of the road search, while the path-following cross-track errors converge to a 3-m tube around the desired spatial paths.

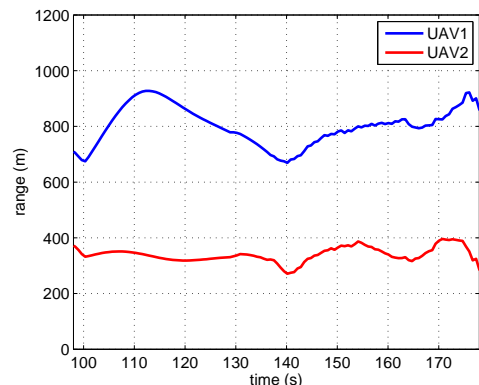
Finally, when a target is detected, the two UAVs switch to *cooperative vision-based tracking* mode. In this phase, the UAVs track the target by means of guidance loops that use visual information for feedback, while simultaneously providing in-situ imagery for precise geo-location of the point of interest. During this target-tracking phase, a coordination algorithm ensures that the two UAVs keep a predefined phase separation of $\frac{\pi}{2}$ rad while “orbiting” around the target. This coordination algorithm uses the distributed control law described in Chapter 4 to adjust the speed of the UAVs, with the main difference that *phase on orbit* is now used as a coordination state, rather than the time-variable $\xi_i(t)$. Besides collision avoidance, cooperation through phase-on-orbit coordination allows for several additional benefits, including reduced sensitivity to target escape maneuvers [71]. Performance of the cooperative control algorithm is illustrated in Figure 7.7, which shows the trajectories of the two UAVs while tracking the target as well as the phase-coordination error. Details about the vision-based guidance loop used in this phase can be found in [27].



(a) 2D flat-Earth field-of-view footprints

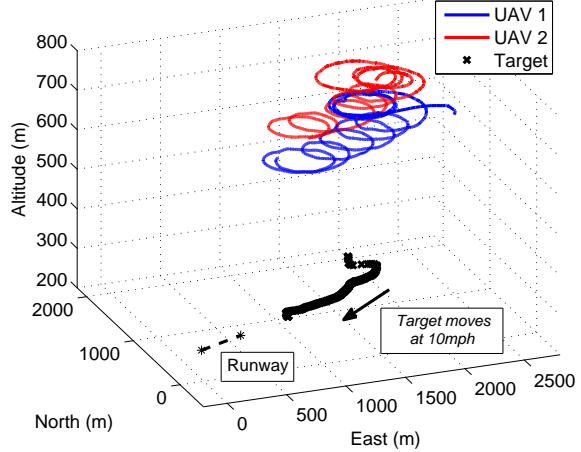


(b) FoV-overlap coefficient

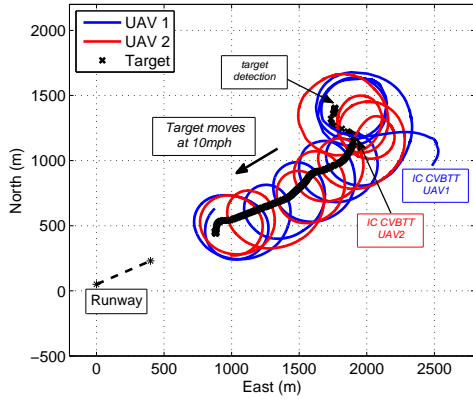


(c) Range to the virtual vehicle on the sensor path

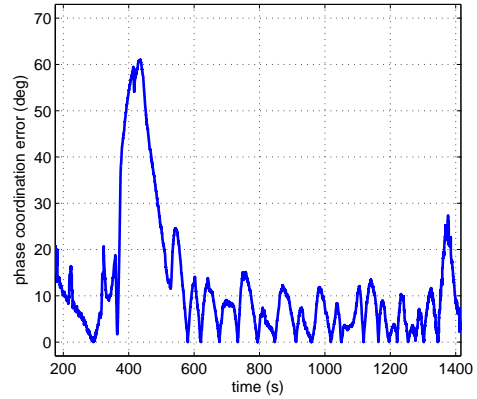
Figure 7.6: Cooperative road-search; mission performance. Field-of-view (FoV) overlap and range to the virtual vehicle on the sensor path. ([Watch video](#))



(a) 3D trajectories



(b) 2D projections



(c) Phase coordination error

Figure 7.7: Cooperative road-search; coordinated vision-based target tracking (CVBTT). Upon target detection, the two UAVs start tracking the target by means of guidance loops that use visual information for feedback, while simultaneously providing in-situ imagery for precise geo-location of the point of interest. During the target-tracking phase, a coordination algorithm ensures that the two UAVs keep a predefined phase separation of $\frac{\pi}{2}$ rad while “orbiting” around the target.

7.2 Flight-Test Summary and Accessory Mission Outcomes

The results presented in the previous section illustrate the benefits of using cooperative control based on the algorithms described in this thesis when dealing with missions involving multiple vehicles. Such cooperative strategies ensure collision-free maneuvers, and efficiently combine heterogeneous information provided by complementary sensors.

To visually illustrate the effect of time-critical cooperation among the UAVs, Figure 7.8 presents a mosaic of four consecutive high-resolution images taken during a flight experiment. In this experiment, the road-search paths are intentionally separated by altitude and optimized such that, if the coordination algorithm adequately adjusts the speed of the two UAVs, then the UAV flying at a lower altitude is expected to be continuously present in the FoV of the camera flying at a higher altitude. The figure schematically represents the progression of the lines of sight connecting the two cameras with the virtual target vehicle running along the sensor path. Time-coordination ensures that cameras observe the same spot on the road and thus maximize the overlap of the footprints of their FoVs, which is critical to provide reliable target discrimination.

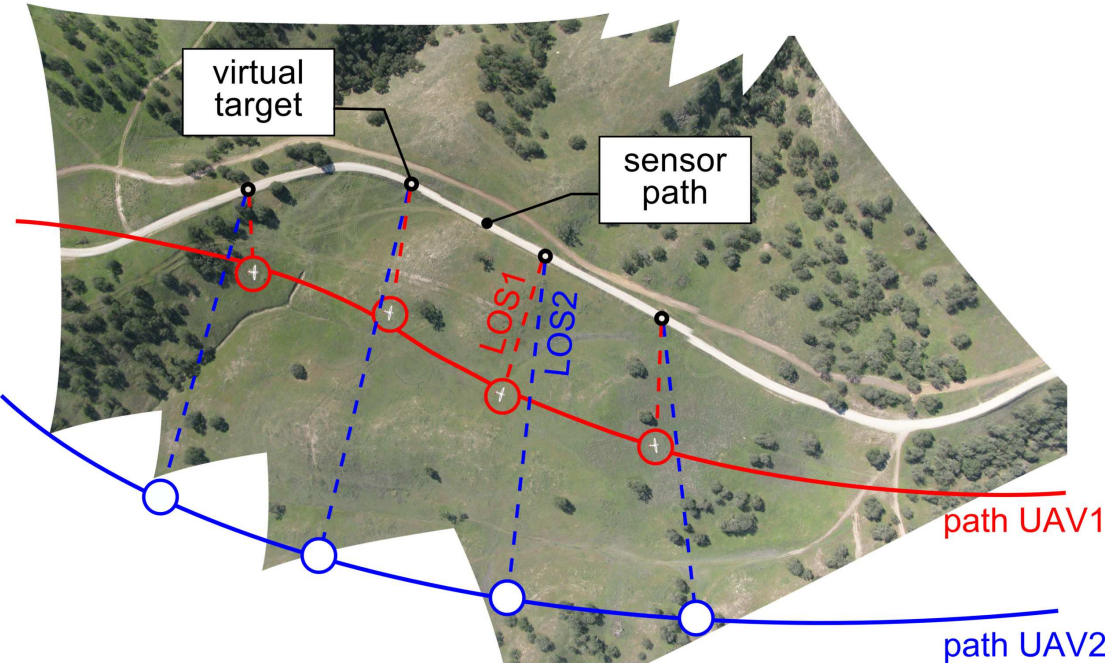


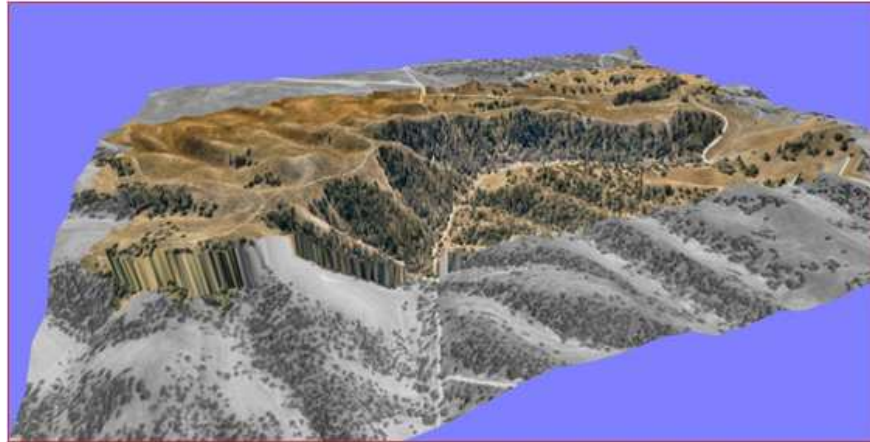
Figure 7.8: Time-critical cooperation in a road-search mission. In this experiment, the road-search paths are intentionally separated by altitude and optimized such that the UAV flying at a lower altitude is continuously present in the field of view of the camera flying at a higher altitude. A mosaic of four consecutive high-resolution images illustrates the progression of the lines of sight (LoSs) connecting the two onboard cameras with the virtual target vehicle running along the sensor path.

Also, in order to illustrate possible accessory mission outcomes, Figure 7.9 presents examples of imagery data exploitation. In Figure 7.9a, for example, the 3D geo-referenced model of the operational environment is built from 2D high-resolution frames using proprietary technology⁶. In Figure 7.9b, a geo-referenced mosaic is obtained in near real time from high-resolution frames sent by one of the UAVs through the MANET link while in mission⁷.

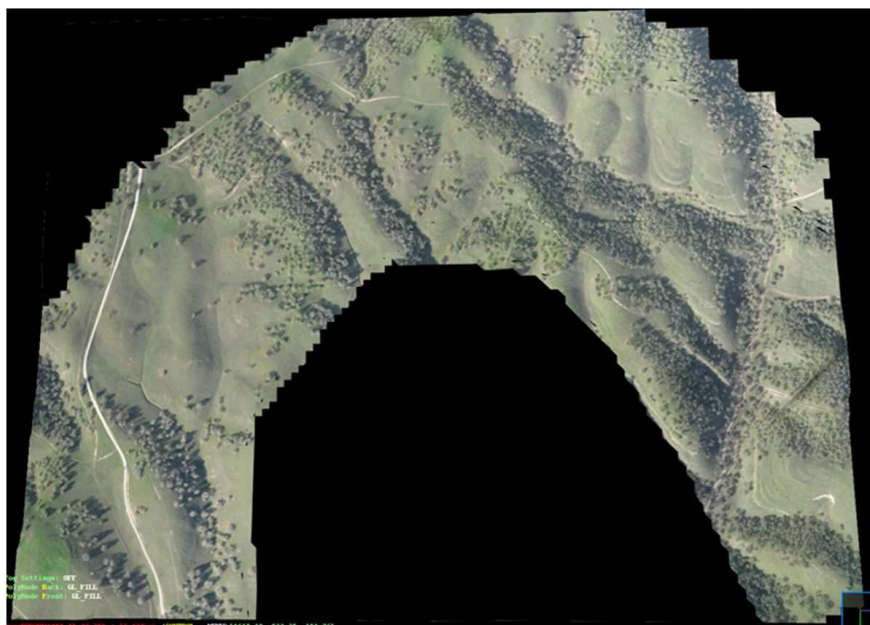
In summary, the results presented above demonstrate the feasibility and efficacy of the onboard integration of the nonlinear path-following and time-critical coordination algorithms. This cooperative control approach applies to teams of heterogeneous systems and does not necessarily lead to swarming behavior, which is unsuitable for many of the mission scenarios envisioned in this research. At the same time, the achieved functionality of the UAV following 3D curves in an inertial space outperforms the conventional waypoint navigation method typically implemented on off-the-shelf commercial autopilots. These results provide also a roadmap for further development and onboard implementation of advanced cooperative algorithms.

⁶Information available online at <http://www.urbanrobots.com/home.php> [Online; accessed 8 March 2013].

⁷Information available online at <http://www.2d3.com/application> [Online; accessed 8 March 2013].



(a) Automated 3D terrain extraction from 2D high-resolution data (Courtesy of Urban Robotics)



(b) Near-real-time geo-referenced map obtained from high-resolution data (Courtesy of 2D3)

Figure 7.9: High-resolution image exploitation. The use cooperative algorithms in missions involving multiple UAVs can provide accessory mission outcomes, such as (a) 3D geo-referenced models of the operational environment, or (b) geo-referenced maps obtained in near real time from high-resolution imagery.

Chapter 8

Conclusions and Future Work

8.1 Conclusions

This thesis addressed the problem of steering a fleet of unmanned aerial vehicles (UAVs) along desired 3D spatial paths while meeting relative temporal constraints. The methodology adopted unfolds in three basic steps. Initially, each vehicle is assigned a feasible path with a desired speed profile that together satisfy the mission requirements and the vehicle dynamic constraints, while ensuring collision-free maneuvers. Then, a path-following algorithm ensures that every vehicle follows its own path independently of the temporal assignments of the mission. Finally, the vehicles coordinate their position along the path with the remaining vehicles engaged in the mission by exchanging coordination information over the supporting communications network. These three steps are accomplished by judiciously decoupling space and time in the formulation of the path-following and coordination problems, and by relying on the existing inner-loop controllers for nominal control of the autonomous systems. As a result, the developed work yields a systematic framework for integration of various tools and concepts from a broad spectrum of disciplines, leading to a streamlined design procedure for time-critical cooperative path-following control. The approach presented applies to teams of heterogeneous systems and does not necessarily lead to swarming behavior, which is unsuitable for many of the mission scenarios envisioned in this work.

The thesis put forward a new singularity-free path-following control law on $\text{SO}(3)$, and introduced a set of coordination states that can accommodate path-dependent desired speed profiles. Using results from nonlinear systems, differential inclusions, and algebraic graph theory, conditions were derived under which the proposed algorithms solve the coordinated path-following control problem in the presence of switching communications topologies and quantized information exchange. The thesis also derived lower bounds on the convergence rate of the network dynamics as a function of the number of leaders included in the coordination control law and the quality of service (QoS) of the supporting network, which in the context of this thesis represents a measure of the level of connectivity of the communications graph. In particular, it was proven that the (guaranteed) rate of convergence of the coordination control loop is limited by the QoS of the

communications network, which implies that in communication-limited environments long times might be required for the vehicles to reach agreement and coordinate their positions along the paths. To address this issue and improve the convergence rate of the coordination dynamics in low-connectivity scenarios, a coordination algorithm was proposed that integrates network estimators with topology-control strategies. The proposed approach leads to an evolving extended network, whose topology depends on the local exchange of information among nodes. Numerical evidence was provided suggesting that, with this new approach, the coordination error state converges to a neighborhood of the origin in a shorter time.

The thesis bridged the gap between theory and practice, and included flight-test results of a cooperative road-search mission involving multiple small tactical UAVs that illustrate the benefits of some of the developed algorithms. In particular, the results demonstrated the validity of the proposed generic theoretical framework in a specific realistic application as well as the feasibility of the onboard implementation of the algorithms. Moreover, it is also important to emphasize that the achieved functionality of a UAV following 3D curves in an inertial space outperforms the conventional waypoint navigation method typically implemented on off-the-shelf commercial autopilots.

8.2 Future Work

Cooperative Trajectory Generation: To have a complete solution to the problem of time-critical cooperative path following, it is necessary to develop and integrate efficient *trajectory-generation algorithms* that are capable of computing trajectories for teams of autonomous vehicles that do not violate the dynamic constraints of each vehicle, ensure that the vehicles maintain a predefined spatial clearance, account for communication constraints, verify desired temporal constraints, and satisfy pre-specified mission-specific requirements. Ideally, these algorithms are to be implemented onboard the autonomous vehicles in a decentralized fashion, and should scale with the size of the fleet. Also, future developments should include the effect of wind in the problem formulation, which can significantly reduce the amount of replanning required for the successful execution of a cooperative mission. The use of inverse simulation techniques for trajectory generation is also a topic of special interest, as such methods can help evaluate feasibility of the generated trajectories, estimate mission effectiveness, and provide corrections for turning unfeasible maneuvers into feasible ones.

Coordination under Communication Constraints: Future research should also explore the development of coordination algorithms for the effective execution of cooperative missions in communications-limited and communication-denied environments. In particular, it would be interesting to investigate in further de-

tail the stability and convergence properties of the coordination control law proposed in Chapter 6 of this thesis for low-connectivity mission scenarios. The derivation of design constraints under which this control law is able to improve the convergence rate of the closed-loop coordination dynamics appears to be rather challenging, as the proposed approach leads to an evolving network with time-varying link weights and unidirectional communications.

In some cooperative missions, the QoS of the supporting communications network can be adjusted by means of motion-control algorithms for connectivity maintenance. Future efforts will investigate the integration of such algorithms into the framework for cooperative path following described in this thesis. Of particular interest are the motion strategies that arise from a differential game-theoretic formulation of the connectivity-maintenance problem; see, for example, [11, 12] and references therein. These strategies could be designed, for instance, to ensure that the connectivity condition (2.14) is satisfied during the entire execution of the mission, rather than have it assumed a priori. Moreover, because in such a setup the vehicles would be allowed to deviate from the corresponding paths in order to maintain connectivity, the resulting solution would require the integration of algorithms for (online) collision avoidance.

Another interesting direction of future research is the development of coordination algorithms that, in addition to the relative temporal constraints considered in this thesis, can also enforce absolute temporal constraints, such as specifications in the desired final time of the mission. In fact, this extended coordination problem can be addressed by judiciously modifying the coordination control laws presented in this thesis. Absolute temporal constraints can be enforced, for example, by reformulating the consensus problem introduced in Chapter 2 as a collective tracking problem, or by explicitly controlling the desired rate of change of the coordination states. Relevant topics of research include the derivation of stability and performance guarantees for such algorithms, as well as the design of methods capable of monitoring the feasibility of the temporal specifications as the mission unfolds.

Future research efforts will also explore the impact of communication latencies, channel noise, and random link failures on the achievable levels of performance of the cooperative missions considered in this thesis. An exciting and challenging subject of research is the development of a unifying framework that would capture these communication constraints —along with quantization—, while accounting at the same time for the random nature and inherent probabilistic properties of data transmission. Such a framework could be valuable for analysis purposes, but could also be a beneficial tool for the design of new coordination control laws that are less sensitive to link failures and channel constraints.

Autonomy: Finally, thinking in broader terms, it is apparent that the growing complexity of the envisioned mission scenarios poses several new challenges to the design and integration of autonomous systems, especially in terms of autonomy, cooperation, endurance, and resilience. In fact, it is anticipated that future operations will require teams of autonomous systems working in cooperation to achieve common objectives, and being able to safely operate in highly uncertain, remote areas for periods of time that might range from hours to years. It is therefore important to develop energy-harvesting cooperative solutions that provide guaranteed levels of performance in the presence of faulty communications networks, limited sensing capabilities, and partial vehicle failures that might span months. To this end, new breakthroughs will be required in the areas of multi-vehicle cooperative path planning and guidance control; resilient control; battery and solar-panel efficiency; energy management; big data processing, integration, and fusion; wireless communications; numerical weather prediction and analysis; meteorological data assimilation; real-time computation; and aerodynamics. Moreover, the execution of such complex missions also poses new challenges from a human factors perspective. In fact, more research efforts are needed to provide new concepts and tools for designing safe and effective human-machine interaction. Particular emphasis is to be placed on situation awareness interfaces to ensure that automation, whose behavior is too often opaque, is made transparent to system operators.

Appendices

Appendix A

The *Hat* and *Vee* Maps

The *hat map* $(\cdot)^\wedge : \mathbb{R}^3 \rightarrow \mathfrak{so}(3)$ is defined as

$$(\boldsymbol{x})^\wedge = \begin{bmatrix} 0 & -x_3 & x_2 \\ x_3 & 0 & -x_1 \\ -x_2 & x_1 & 0 \end{bmatrix}$$

for $\boldsymbol{x} = [x_1, x_2, x_3]^\top \in \mathbb{R}^3$. The inverse of the hat map is referred to as the *vee map* $(\cdot)^\vee : \mathfrak{so}(3) \rightarrow \mathbb{R}^3$. A property of the hat and vee maps used in this thesis is given below:

$$\text{tr} [\boldsymbol{M}(\boldsymbol{x})^\wedge] = -\boldsymbol{x} \cdot (\boldsymbol{M} - \boldsymbol{M}^\top)^\vee, \quad (\text{A.1})$$

which holds for any $\boldsymbol{x} \in \mathbb{R}^3$, and $\boldsymbol{M} \in \mathbb{R}^{3 \times 3}$. We refer to [63] for further details on the hat and vee maps.

Appendix B

Coordination Dynamics

B.1 Time-Derivative of the Coordination States

The time-derivative of the i th coordination state is given by

$$\dot{\xi}_i(t) = \frac{d}{dt} \left(\eta_i(\ell'_i(t)) \right) = \frac{d\eta_i}{d\ell'_i} \Big|_{\ell'_i(t)} \dot{\ell}'_i(t).$$

From the definitions of $\ell'_{d,i}(\cdot)$ and $\eta_i(\cdot)$ in Section 2.2.3, we have that the following equality holds for all $\ell'_i \in [0, 1]$:

$$\ell'_{d,i}(\eta_i(\ell'_i)) = \ell'_i$$

and, therefore, taking the derivative with respect to ℓ'_i on both sides leads to

$$\frac{d\ell'_{d,i}}{d\eta_i} \Big|_{\eta_i(\ell'_i)} \frac{d\eta_i}{d\ell'_i} \Big|_{\ell'_i} = 1. \quad (\text{B.1})$$

From the definition of $\ell'_{d,i}(\cdot)$, it follows that

$$\frac{d\ell'_{d,i}}{d\eta_i} \Big|_{\eta_i(\ell'_i)} = \frac{1}{\ell_{fi}} v_{d,i}(\eta_i(\ell'_i)), \quad \text{for all } \ell'_i \in [0, 1],$$

which, along with equality (B.1), implies that

$$\frac{d\eta_i}{d\ell'_i} \Big|_{\ell'_i} = \frac{1}{\frac{1}{\ell_{fi}} v_{d,i}(\eta_i(\ell'_i))}, \quad \text{for all } \ell'_i \in [0, 1].$$

Then, the evolution of the i th coordination state can be expressed as

$$\dot{\xi}_i(t) = \frac{1}{\frac{1}{\ell_{fi}} v_{d,i}(\eta_i(\ell'_i(t)))} \dot{\ell}'_i(t),$$

which can be simplified to

$$\dot{\xi}_i(t) = \frac{\dot{l}_i(t)}{v_{d,i}(\xi_i(t))}.$$

B.2 The Coordination Projection Matrix

The equality $\mathbf{Q}^\top \mathbf{Q} = \Pi_\xi$ is used several times throughout this thesis, and is instrumental to derive many of its results. Next, we provide a proof for this equality.

Lemma 7 *Let \mathbf{Q} be an $(n-1) \times n$ matrix such that $\mathbf{Q}\mathbf{1}_n = \mathbf{0}$ and $\mathbf{Q}\mathbf{Q}^\top = \mathbb{I}_{n-1}$. Then, the following equality holds:*

$$\mathbf{Q}^\top \mathbf{Q} = \Pi_\xi := \mathbb{I}_n - \frac{\mathbf{1}_n \mathbf{1}_n^\top}{n}. \quad \diamond$$

Proof: We start by partitioning matrix \mathbf{Q} as

$$\mathbf{Q} = \begin{bmatrix} \tilde{\mathbf{q}}_1^\top \\ \vdots \\ \tilde{\mathbf{q}}_{n-1}^\top \end{bmatrix}, \quad \tilde{\mathbf{q}}_i \in \mathbb{R}^n.$$

From $\mathbf{Q}\mathbf{Q}^\top = \mathbb{I}_{n-1}$, it follows that

$$\begin{aligned} \tilde{\mathbf{q}}_i^\top \tilde{\mathbf{q}}_i &= 1, & i &= 1, \dots, n-1, \\ \tilde{\mathbf{q}}_i^\top \tilde{\mathbf{q}}_j &= 0, & i, j &= 1, \dots, n-1, \quad i \neq j, \end{aligned}$$

which implies that $\{\tilde{\mathbf{q}}_1, \dots, \tilde{\mathbf{q}}_{n-1}\}$ is a set of $(n-1)$ orthonormal vectors in \mathbb{R}^n . From $\mathbf{Q}\mathbf{1}_n = \mathbf{0}$, it also follows that

$$\tilde{\mathbf{q}}_i^\top \mathbf{1}_n = 0, \quad i = 1, \dots, n-1,$$

and $\{\tilde{\mathbf{q}}_1, \dots, \tilde{\mathbf{q}}_{n-1}, \mathbf{1}_n\}$ is thus an orthogonal basis of \mathbb{R}^n .

Next, we prove that vector $\mathbf{1}_n$ spans the null space of matrix \mathbf{Q} . We prove this result by contradiction. To this effect, assume that there exists a vector $\mathbf{v} \in \mathbb{R}^n$, $\mathbf{v} \neq \gamma \mathbf{1}_n$, $\gamma \in \mathbb{R}$, such that $\mathbf{Q}\mathbf{v} = \mathbf{0}$. Since $\{\tilde{\mathbf{q}}_1, \dots, \tilde{\mathbf{q}}_{n-1}, \mathbf{1}_n\}$ forms a basis of \mathbb{R}^n , vector \mathbf{v} can be expressed as a linear combination of these basis vectors

$$\mathbf{v} = \alpha_0 \mathbf{1}_n + \sum_{k=1}^{n-1} \alpha_k \tilde{\mathbf{q}}_k, \quad \alpha_i \in \mathbb{R}.$$

Then, we have

$$\mathbf{0} = \mathbf{Q}\mathbf{v} = \alpha_0 \mathbf{Q}\mathbf{1}_n + \sum_{k=1}^{n-1} \alpha_k \mathbf{Q}\tilde{\mathbf{q}}_k = \mathbf{0} + \begin{bmatrix} \alpha_1 \\ \vdots \\ \alpha_{n-1} \end{bmatrix},$$

which implies that $\alpha_i = 0$, $i = 1, \dots, n - 1$. Therefore, $\mathbf{v} = \alpha_0 \mathbf{1}_n$, which contradicts the assumption $\mathbf{v} \neq \gamma \mathbf{1}_n$, $\gamma \in \mathbb{R}$.

We now note that by multiplying $\mathbf{Q}\mathbf{Q}^\top = \mathbb{I}_{n-1}$ on the right by \mathbf{Q} one obtains $\mathbf{Q}\mathbf{Q}^\top\mathbf{Q} = \mathbf{Q}$, which can be rewritten as $\mathbf{Q}(\mathbf{Q}^\top\mathbf{Q} - \mathbb{I}_n) = \mathbf{0}$. From this last equality, the fact that $\mathbf{Q}^\top\mathbf{Q} - \mathbb{I}_n = (\mathbf{Q}^\top\mathbf{Q} - \mathbb{I}_n)^\top$, and recalling that vector $\mathbf{1}_n$ spans the null space of matrix \mathbf{Q} , it follows that

$$\mathbf{Q}^\top\mathbf{Q} - \mathbb{I}_n = \beta \mathbf{1}_n \mathbf{1}_n^\top, \quad \text{for some } \beta \in \mathbb{R}.$$

Finally, multiplying the equation above on the right by $\mathbf{1}_n$ yields

$$\begin{aligned} (\mathbf{Q}^\top\mathbf{Q} - \mathbb{I}_n) \mathbf{1}_n &= \beta \mathbf{1}_n \mathbf{1}_n^\top \mathbf{1}_n, \\ -\mathbf{1}_n &= n\beta \mathbf{1}_n, \end{aligned}$$

which implies that $\beta = -\frac{1}{n}$ and, hence, we obtain

$$\mathbf{Q}^\top\mathbf{Q} = \mathbb{I}_n - \frac{1}{n} \mathbf{1}_n \mathbf{1}_n^\top.$$

□

B.3 Closed-loop Coordination Error Dynamics

From the definition of $\zeta_1(t)$ and $\zeta_2(t)$ and the closed-loop coordination dynamics (4.5), it follows that

$$\begin{aligned} \dot{\zeta}_1(t) &= -k_P \mathbf{Q} \mathbf{L}(t) \xi(t) + \mathbf{Q} \mathbf{1}_n + \mathbf{Q} \begin{bmatrix} \mathbf{0} \\ \zeta_2(t) \end{bmatrix} \\ &= -k_P \mathbf{Q} \mathbf{L}(t) \xi(t) + \mathbf{Q} \mathbf{C} \zeta_2(t). \end{aligned}$$

The properties of the projection matrix Π_ξ , along with the fact that $\mathbf{Q}\mathbf{Q}^\top = \mathbb{I}_{n-1}$, imply that

$$\begin{aligned} \dot{\zeta}_1(t) &= -k_P \mathbf{Q} \Pi_\xi \mathbf{L}(t) \Pi_\xi \xi(t) + \mathbf{Q} \mathbf{C} \zeta_2(t) \\ &= -k_P \mathbf{Q} \mathbf{Q}^\top \mathbf{Q} \mathbf{L}(t) \mathbf{Q}^\top \mathbf{Q} \xi(t) + \mathbf{Q} \mathbf{C} \zeta_2(t) \\ &= -k_P \bar{\mathbf{L}}(t) \zeta_1(t) + \mathbf{Q} \mathbf{C} \zeta_2(t). \end{aligned} \tag{B.2}$$

Similarly, it follows that

$$\dot{\zeta}_2(t) = -k_I \mathbf{C}^\top \mathbf{L}(t) \xi(t) = -k_I \mathbf{C}^\top \mathbf{Q}^\top \bar{\mathbf{L}}(t) \zeta_1(t). \tag{B.3}$$

Equations (B.2) and (B.3) lead to the dynamics (4.7).

Appendix C

Proofs

C.1 Proof of Lemma 1

We start by noting that over the compact set Ω_{pf} introduced in (3.7) the following upper bounds hold:

$$\|\mathbf{p}_F\| \leq cc_1 < \frac{c_1}{\sqrt{2}}, \quad (\text{C.1})$$

$$\Psi(\tilde{\mathbf{R}}) \leq c^2 < \frac{1}{2}. \quad (\text{C.2})$$

Consider now the Lyapunov function candidate

$$V_{pf}(\mathbf{p}_F, \tilde{\mathbf{R}}) = \Psi(\tilde{\mathbf{R}}) + \frac{1}{c_1^2} \|\mathbf{p}_F\|^2.$$

This function is locally positive-definite about $(\mathbf{p}_F, \tilde{R}_{11}) = (\mathbf{0}, 1)$ within set Ω_{pf} . Moreover, we note that $\|e_{\tilde{\mathbf{R}}}\|$ can be related to the function $\Psi(\tilde{\mathbf{R}})$ as follows:

$$\|e_{\tilde{\mathbf{R}}}\|^2 = \frac{1}{4} (\tilde{R}_{12}^2 + \tilde{R}_{13}^2) = \frac{1}{4} (1 - \tilde{R}_{11}^2) = \frac{1}{4} (1 - \tilde{R}_{11}) (1 + \tilde{R}_{11}) = \Psi(\tilde{\mathbf{R}}) (1 - \Psi(\tilde{\mathbf{R}})).$$

Then, the bound in (C.2) implies that, inside set Ω_{pf} , the function $\Psi(\tilde{\mathbf{R}})$ satisfies

$$\|e_{\tilde{\mathbf{R}}}\|^2 \leq \Psi(\tilde{\mathbf{R}}) \leq \frac{1}{1 - c^2} \|e_{\tilde{\mathbf{R}}}\|^2.$$

It thus follows that, within set Ω_{pf} , the Lyapunov function V_{pf} can be bounded as

$$\|e_{\tilde{\mathbf{R}}}\|^2 + \frac{1}{c_1^2} \|\mathbf{p}_F\|^2 \leq V_{pf} \leq \frac{1}{1 - c^2} \|e_{\tilde{\mathbf{R}}}\|^2 + \frac{1}{c_1^2} \|\mathbf{p}_F\|^2. \quad (\text{C.3})$$

From the dynamics (2.11), the time-derivative of V_{pf} is given by

$$\begin{aligned}\dot{V}_{pf} &= \dot{\Psi}(\tilde{\mathbf{R}}) + \frac{2}{c_1^2} \mathbf{p}_F \cdot \dot{\mathbf{p}}_F \\ &= \mathbf{e}_{\tilde{\mathbf{R}}} \cdot \left(\begin{bmatrix} q \\ r \end{bmatrix} - \boldsymbol{\Pi}_{\tilde{\mathbf{R}}} \tilde{\mathbf{R}}^\top (\mathbf{R}_F^D \{\omega_{F/I}\}_F + \{\omega_{D/F}\}_D) \right) + \frac{2}{c_1^2} \mathbf{p}_F \cdot \left(-\ell \hat{\mathbf{t}} - \omega_{F/I} \times \mathbf{p}_F + v \hat{\mathbf{w}}_1 \right).\end{aligned}$$

In the equation above, $\dot{\mathbf{p}}_F$ denotes the componentwise derivative of the vector \mathbf{p}_F and therefore $\dot{\mathbf{p}}_F = \dot{\mathbf{p}}_F]_F$. The rate commands (3.2), together with the law (3.1) for the rate of progression of the virtual target along the path, lead to

$$\dot{V}_{pf} = -2k_{\tilde{R}} \mathbf{e}_{\tilde{\mathbf{R}}} \cdot \mathbf{e}_{\tilde{\mathbf{R}}} + \frac{2}{c_1^2} \left(-k_\ell (\mathbf{p}_F \cdot \hat{\mathbf{t}})^2 - \mathbf{p}_F \cdot (\omega_{F/I} \times \mathbf{p}_F) + v \mathbf{p}_F \cdot (\hat{\mathbf{w}}_1 - (\hat{\mathbf{w}}_1 \cdot \hat{\mathbf{t}}) \hat{\mathbf{t}}) \right). \quad (\text{C.4})$$

Since $(\mathbf{p}_F \cdot \hat{\mathbf{t}}) = x_F$ and, moreover, we have that $(\mathbf{p}_F \cdot (\omega_{F/I} \times \mathbf{p}_F)) = 0$, then (C.4) reduces to

$$\dot{V}_{pf} = -2k_{\tilde{R}} \mathbf{e}_{\tilde{\mathbf{R}}} \cdot \mathbf{e}_{\tilde{\mathbf{R}}} - \frac{2k_\ell}{c_1^2} x_F^2 + \frac{2v}{c_1^2} (\mathbf{p}_F \cdot (\hat{\mathbf{w}}_1 - (\hat{\mathbf{w}}_1 \cdot \hat{\mathbf{t}}) \hat{\mathbf{t}})). \quad (\text{C.5})$$

Letting $\mathbf{p}_\times(t)$ denote the path-following cross-track error, which can be expressed as

$$\mathbf{p}_\times = (\mathbf{p}_F \cdot \hat{\mathbf{n}}_1) \hat{\mathbf{n}}_1 + (\mathbf{p}_F \cdot \hat{\mathbf{n}}_2) \hat{\mathbf{n}}_2 = y_F \hat{\mathbf{n}}_1 + z_F \hat{\mathbf{n}}_2, \quad (\text{C.6})$$

we have the following equality:

$$\mathbf{p}_F \cdot (\hat{\mathbf{w}}_1 - (\hat{\mathbf{w}}_1 \cdot \hat{\mathbf{t}}) \hat{\mathbf{t}}) = \mathbf{p}_F \cdot ((\hat{\mathbf{w}}_1 \cdot \hat{\mathbf{n}}_1) \hat{\mathbf{n}}_1 + (\hat{\mathbf{w}}_1 \cdot \hat{\mathbf{n}}_2) \hat{\mathbf{n}}_2) = \mathbf{p}_\times \cdot \hat{\mathbf{w}}_1. \quad (\text{C.7})$$

Substituting (C.7) into (C.5), we obtain

$$\dot{V}_{pf} = -2k_{\tilde{R}} \mathbf{e}_{\tilde{\mathbf{R}}} \cdot \mathbf{e}_{\tilde{\mathbf{R}}} - \frac{2k_\ell}{c_1^2} x_F^2 + \frac{2v}{c_1^2} (\mathbf{p}_\times \cdot \hat{\mathbf{w}}_1). \quad (\text{C.8})$$

Consider now the quantity $(\hat{\mathbf{w}}_1 \cdot \hat{\mathbf{b}}_{1D})$, which represents the cosine of the angle ψ_e between the desired direction of the velocity vector $\hat{\mathbf{b}}_{1D}$ and the actual direction of the vehicle's velocity vector $\hat{\mathbf{w}}_1$. From the definition of $\Psi(\tilde{\mathbf{R}})$ in (2.8), we have that

$$\hat{\mathbf{w}}_1 \cdot \hat{\mathbf{b}}_{1D} = \cos \psi_e = \tilde{R}_{11} = 1 - 2\Psi(\tilde{\mathbf{R}}).$$

The bound in (C.2) implies that, within set Ω_{pf} , the quantity $(\hat{\mathbf{w}}_1 \cdot \hat{\mathbf{b}}_{1D})$ is bounded away from zero:

$$\hat{\mathbf{w}}_1 \cdot \hat{\mathbf{b}}_{1D} = 1 - 2\Psi(\tilde{\mathbf{R}}) \geq 1 - 2c^2 > 0.$$

The quantity $\frac{1}{(\hat{\mathbf{w}}_1 \cdot \hat{\mathbf{b}}_{1D})}$ is therefore well defined within set Ω_{pf} . Next, we add and subtract the term $\frac{2v}{c_1^2} \frac{(\mathbf{p}_X \cdot \hat{\mathbf{b}}_{1D})}{(\hat{\mathbf{w}}_1 \cdot \hat{\mathbf{b}}_{1D})}$ to (C.8) to obtain

$$\dot{V}_{pf} = -2k_{\tilde{R}} \mathbf{e}_{\tilde{\mathbf{R}}} \cdot \mathbf{e}_{\tilde{\mathbf{R}}} - \frac{2k_\ell}{c_1^2} x_F^2 + \frac{2v}{c_1^2} \frac{(\mathbf{p}_X \cdot \hat{\mathbf{b}}_{1D})}{(\hat{\mathbf{w}}_1 \cdot \hat{\mathbf{b}}_{1D})} + \frac{2v}{c_1^2} \frac{\mathbf{p}_X \cdot (\hat{\mathbf{w}}_1 \times (\hat{\mathbf{w}}_1 \times \hat{\mathbf{b}}_{1D}))}{(\hat{\mathbf{w}}_1 \cdot \hat{\mathbf{b}}_{1D})}.$$

The definitions of $\hat{\mathbf{b}}_{1D}(t)$ and $\mathbf{p}_X(t)$ in (2.7) and (C.6) lead to

$$\dot{V}_{pf} = -2k_{\tilde{R}} \mathbf{e}_{\tilde{\mathbf{R}}} \cdot \mathbf{e}_{\tilde{\mathbf{R}}} - \frac{2k_\ell}{c_1^2} x_F^2 - \frac{2v}{c_1^2 (\hat{\mathbf{w}}_1 \cdot \hat{\mathbf{b}}_{1D}) (d^2 + \mathbf{p}_X \cdot \mathbf{p}_X)^{\frac{1}{2}}} \mathbf{p}_X \cdot \mathbf{p}_X + \frac{2v}{c_1^2} \frac{\mathbf{p}_X \cdot (\hat{\mathbf{w}}_1 \times (\hat{\mathbf{w}}_1 \times \hat{\mathbf{b}}_{1D}))}{(\hat{\mathbf{w}}_1 \cdot \hat{\mathbf{b}}_{1D})}.$$

Next, we note that, within set Ω_{pf} , the following bounds hold:

$$0 < 1 - 2c^2 \leq (\hat{\mathbf{w}}_1 \cdot \hat{\mathbf{b}}_{1D}) \leq 1, \quad \|\mathbf{p}_X\| \leq \|\mathbf{p}_F\| \leq cc_1.$$

These bounds, together with the assumption on the vehicle speed in (3.3), yield the following bound for \dot{V}_{pf} :

$$\dot{V}_{pf} \leq -2k_{\tilde{R}} \|\mathbf{e}_{\tilde{\mathbf{R}}}\|^2 - \frac{2k_\ell}{c_1^2} x_F^2 - \frac{2v_{\min}}{c_1^2 (d^2 + c^2 c_1^2)^{\frac{1}{2}}} \|\mathbf{p}_X\|^2 + \frac{2v_{\max}}{c_1^2 (1 - 2c^2)} \|\mathbf{p}_X\| \|\hat{\mathbf{w}}_1 \times (\hat{\mathbf{w}}_1 \times \hat{\mathbf{b}}_{1D})\|.$$

The term $\|\hat{\mathbf{w}}_1 \times (\hat{\mathbf{w}}_1 \times \hat{\mathbf{b}}_{1D})\|$ represents the absolute value of the sine of the angle ψ_e . Therefore, we can write

$$\|\hat{\mathbf{w}}_1 \times (\hat{\mathbf{w}}_1 \times \hat{\mathbf{b}}_{1D})\| = |\sin(\psi_e)| = \sqrt{1 - \cos^2(\psi_e)} = \sqrt{1 - \tilde{R}_{11}^2} = \sqrt{\tilde{R}_{12}^2 + \tilde{R}_{13}^2} = 2\|\mathbf{e}_{\tilde{\mathbf{R}}}\|,$$

which yields

$$\dot{V}_{pf} \leq -2k_{\tilde{R}} \|\mathbf{e}_{\tilde{\mathbf{R}}}\|^2 - \frac{2k_\ell}{c_1^2} x_F^2 - \frac{2v_{\min}}{c_1^2 (d^2 + c^2 c_1^2)^{\frac{1}{2}}} \|\mathbf{p}_X\|^2 + \frac{4v_{\max}}{c_1^2 (1 - 2c^2)} \|\mathbf{p}_X\| \|\mathbf{e}_{\tilde{\mathbf{R}}}\|.$$

Letting $\tilde{k}_\ell := \min \left\{ k_\ell, \frac{v_{\min}}{(d^2 + c^2 c_1^2)^{\frac{1}{2}}} \right\}$ and noting that $\|\mathbf{p}_X\| \leq \|\mathbf{p}_F\|$, we have

$$\dot{V}_{pf} \leq -2k_{\tilde{R}} \|\mathbf{e}_{\tilde{\mathbf{R}}}\|^2 - \frac{2\tilde{k}_\ell}{c_1^2} \|\mathbf{p}_F\|^2 + \frac{4v_{\max}}{c_1^2 (1 - 2c^2)} \|\mathbf{p}_F\| \|\mathbf{e}_{\tilde{\mathbf{R}}}\|.$$

From the choice for the characteristic distance d and the path-following control parameters k_ℓ and $k_{\tilde{R}}$ in (3.4),

and the definition of $\bar{\lambda}_{pf}$ in (3.6), it follows that:

$$\begin{bmatrix} k_{\tilde{R}} & -\frac{v_{\max}}{c_1^2(1-2c^2)} \\ -\frac{v_{\max}}{c_1^2(1-2c^2)} & \frac{\tilde{k}_\ell}{c_1^2} \end{bmatrix} \geq \bar{\lambda}_{pf} \begin{bmatrix} \frac{1}{1-c^2} & 0 \\ 0 & \frac{1}{c_1^2} \end{bmatrix},$$

which implies that, within set Ω_{pf} , the following bound holds:

$$\dot{V}_{pf} \leq -2\bar{\lambda}_{pf} \left(\frac{1}{1-c^2} \|e_{\tilde{R}}\|^2 + \frac{1}{c_1^2} \|\mathbf{p}_F\|^2 \right) \leq -2\bar{\lambda}_{pf} V_{pf}.$$

It follows from [54, Theorem 4.10] that both $\|e_{\tilde{R}}\|$ and $\|\mathbf{p}_F\|$ converge exponentially fast to zero for all the initial conditions inside the compact set Ω_{pf} . \square

C.2 Proof of Lemma 2

First, we show that the rate commands $q_c(t)$ and $r_c(t)$ are bounded for all $(\mathbf{p}_F, \tilde{\mathbf{R}}) \in \Omega_{pf}$. To this end, we note that over the compact set Ω_{pf} , introduced in (3.7), the following inequalities hold:

$$\|\mathbf{p}_F\| \leq cc_1, \tag{C.9}$$

$$\Psi(\tilde{\mathbf{R}}) \leq c^2. \tag{C.10}$$

The first inequality above, together with the bound on the vehicle speed in (3.3), implies that $\dot{\ell}(t)$ satisfies

$$|\dot{\ell}| \leq v_{\max} + k_\ell cc_1.$$

From the assumption on the feasibility of the path, we can conclude that both parameters $k_1(\ell)$ and $k_2(\ell)$ are bounded, and therefore the bound on $\dot{\ell}(t)$ implies that $\omega_{D/F}(t)$ is also bounded. It then follows from (2.11) that $\dot{\mathbf{p}}_F(t)$ is bounded, which, along with inequality (C.9), implies that the entries of $\dot{\mathbf{R}}_D^F(t)$ are bounded. From the kinematic equation

$$(\{\omega_{D/F}\}_D)^\wedge = \mathbf{R}_F^D \dot{\mathbf{R}}_D^F,$$

it follows that $\omega_{D/F}(t)$ is also bounded. Moreover, since $\|e_{\tilde{R}}\| \leq \Psi(\tilde{\mathbf{R}})$, inequality (C.10) implies that the attitude error $e_{\tilde{R}}(t)$ satisfies

$$\|e_{\tilde{R}}\| \leq c^2.$$

From the bounds on $\omega_{F/I}(t)$, $\omega_{D/F}(t)$, and $e_{\tilde{R}}(t)$ it follows that, for all $(p_F, \tilde{R}) \in \Omega_{pf}$, the rate commands $q_c(t)$ and $r_c(t)$ are bounded. Then, based on the assumption made in Section 2.2.4 on the tracking capabilities of the vehicle with its autopilot, we have that, for all $(p_F, \tilde{R}) \in \Omega_{pf}$, the following performance bounds hold:

$$|q_c - q| \leq \gamma_q, \quad |r_c - r| \leq \gamma_r. \quad (\text{C.11})$$

Next, we consider again the Lyapunov function candidate

$$V_{pf}(p_F, \tilde{R}) = \Psi(\tilde{R}) + \frac{1}{c_1^2} \|p_F\|^2.$$

From the dynamics (2.11), the time-derivative of V_{pf} is given by

$$\dot{V}_{pf} = e_{\tilde{R}} \cdot \left(\begin{bmatrix} q \\ r \end{bmatrix} - \Pi_R \tilde{R}^\top (R_F^D \{\omega_{F/I}\}_F + \{\omega_{D/F}\}_D) \right) + \frac{2}{c_1^2} p_F \cdot (-\dot{\ell} \hat{\mathbf{t}} - \omega_{F/I} \times p_F + v \hat{\mathbf{w}}_1).$$

We add and subtract the term $e_{\tilde{R}} \cdot [\frac{q_c}{r_c}]$ to the above equation to obtain

$$\dot{V}_{pf} = e_{\tilde{R}} \cdot \left(\begin{bmatrix} q_c \\ r_c \end{bmatrix} - \Pi_R \tilde{R}^\top (R_F^D \{\omega_{F/I}\}_F + \{\omega_{D/F}\}_D) \right) + \frac{2}{c_1^2} p_F \cdot (-\dot{\ell} \hat{\mathbf{t}} - \omega_{F/I} \times p_F + v \hat{\mathbf{w}}_1) - e_{\tilde{R}} \cdot \begin{bmatrix} q_c - q \\ r_c - r \end{bmatrix}.$$

Similar to the proof of Lemma 1, we have that, inside set Ω_{pf} , the following bound holds:

$$\dot{V}_{pf} \leq -2\bar{\lambda}_{pf} \left(\frac{1}{1-c^2} \|e_{\tilde{R}}\|^2 + \frac{1}{c_1^2} \|p_F\|^2 \right) + \|e_{\tilde{R}}\| \left\| \begin{bmatrix} q_c - q \\ r_c - r \end{bmatrix} \right\|,$$

where $\bar{\lambda}_{pf}$ was defined in (3.6). From the performance bounds (C.11) and the definition of γ_ω in (3.8), it follows that

$$\left\| \begin{bmatrix} q_c - q \\ r_c - r \end{bmatrix} \right\| \leq \gamma_\omega,$$

which leads to

$$\dot{V}_{pf} \leq -2\bar{\lambda}_{pf} \left(\frac{1}{1-c^2} \|e_{\tilde{R}}\|^2 + \frac{1}{c_1^2} \|p_F\|^2 \right) + \|e_{\tilde{R}}\| \gamma_\omega.$$

We now rewrite the above inequality as

$$\dot{V}_{pf} \leq -2\bar{\lambda}_{pf}(1-\delta_\lambda) \left(\frac{1}{1-c^2} \|e_{\tilde{\mathbf{R}}}\|^2 + \frac{1}{c_1^2} \|\mathbf{p}_F\|^2 \right) - 2\bar{\lambda}_{pf}\delta_\lambda \left(\frac{1}{1-c^2} \|e_{\tilde{\mathbf{R}}}\|^2 + \frac{1}{c_1^2} \|\mathbf{p}_F\|^2 \right) + \|e_{\tilde{\mathbf{R}}}\| \gamma_\omega ,$$

where $0 < \delta_\lambda < 1$. Then, for all $\mathbf{p}_F(t)$ and $e_{\tilde{\mathbf{R}}}(t)$ satisfying

$$-2\bar{\lambda}_{pf}\delta_\lambda \left(\frac{1}{1-c^2} \|e_{\tilde{\mathbf{R}}}\|^2 + \frac{1}{c_1^2} \|\mathbf{p}_F\|^2 \right) + \|e_{\tilde{\mathbf{R}}}\| \gamma_\omega \leq 0 , \quad (\text{C.12})$$

we have

$$\dot{V}_{pf} \leq -2\bar{\lambda}_{pf}(1-\delta_\lambda) \left(\frac{1}{1-c^2} \|e_{\tilde{\mathbf{R}}}\|^2 + \frac{1}{c_1^2} \|\mathbf{p}_F\|^2 \right) \leq -2\bar{\lambda}_{pf}(1-\delta_\lambda)V_{pf} .$$

Inequality (C.12) is satisfied outside the bounded set D defined by:

$$D := \left\{ (\mathbf{p}_F, \tilde{\mathbf{R}}) \in \mathbb{R}^3 \times \text{SO}(3) \mid \frac{1}{1-c^2} \left(\|e_{\tilde{\mathbf{R}}}\| - \frac{(1-c^2)\gamma_\omega}{4\bar{\lambda}_{pf}\delta_\lambda} \right)^2 + \frac{1}{c_1^2} \|\mathbf{p}_F\|^2 < \frac{(1-c^2)\gamma_\omega^2}{16\bar{\lambda}_{pf}^2\delta_\lambda^2} \right\} .$$

Set D is in the interior of the compact set F given by:

$$F := \left\{ (\mathbf{p}_F, \tilde{\mathbf{R}}) \in \mathbb{R}^3 \times \text{SO}(3) \mid \frac{1}{1-c^2} \|e_{\tilde{\mathbf{R}}}\|^2 + \frac{1}{c_1^2} \|\mathbf{p}_F\|^2 \leq \frac{(1-c^2)\gamma_\omega^2}{4\bar{\lambda}_{pf}^2\delta_\lambda^2} \right\} ,$$

which in its turn is contained in the compact set Ω_b defined by:

$$\Omega_b := \left\{ (\mathbf{p}_F, \tilde{\mathbf{R}}) \in \mathbb{R}^3 \times \text{SO}(3) \mid \Psi(\tilde{\mathbf{R}}) + \frac{1}{c_1^2} \|\mathbf{p}_F\|^2 \leq \frac{(1-c^2)\gamma_\omega^2}{4\bar{\lambda}_{pf}^2\delta_\lambda^2} \right\} .$$

Then, the design constraint for the performance bounds γ_q and γ_r in (3.8) implies that set Ω_b is in the interior of set Ω_{pf} introduced in (3.7), that is, $\Omega_b \subset \Omega_{pf}$.

With the above results and using a proof similar to that of Theorem 4.18 in [54], it can be shown that, for every initial state $(\mathbf{p}_F(0), \tilde{\mathbf{R}}(0)) \in \Omega_{pf}$, there is a time $T_b \geq 0$ such that the following bounds are satisfied:

$$\begin{aligned} V_{pf}(t) &\leq V_{pf}(0)e^{-2\bar{\lambda}_{pf}(1-\delta_\lambda)t}, && \text{for all } 0 \leq t < T_b , \\ V_{pf}(t) &\leq \frac{(1-c^2)\gamma_\omega^2}{4\bar{\lambda}_{pf}^2\delta_\lambda^2}, && \text{for all } t \geq T_b . \end{aligned}$$

The bounds in (3.9) follow immediately from the two bounds above and inequalities (C.3). \square

C.3 Proof of Lemma 3

To prove that the origin of the closed-loop kinematic coordination error dynamics (4.7) is globally uniformly exponentially stable (GUES) under the connectivity condition (2.14), we first consider the system

$$\dot{\phi}(t) = -k_P \bar{\mathbf{L}}(t) \phi(t), \quad \phi(t) \in \mathbb{R}^{n-1}, \quad (\text{C.13})$$

where k_P is the proportional coordination control gain introduced in (4.4). Letting $\mathbf{D}(t)$ be the time-varying incidence matrix, $\mathbf{L}(t) = \mathbf{D}(t) \mathbf{D}^\top(t)$, we can rewrite the system above as

$$\dot{\phi}(t) = -k_P (\mathbf{Q}\mathbf{D}(t))(\mathbf{Q}\mathbf{D}(t))^\top \phi(t).$$

Then, since $\mathbf{Q}\mathbf{D}(t)$ is piecewise constant in time and, in addition, we have that $\|\mathbf{Q}\mathbf{D}(t)\|^2 \leq n$, one can prove that system (C.13) is GUES and the following bound holds:

$$\|\phi(t)\| \leq \kappa_\phi \|\phi(0)\| e^{-\lambda_{cd}^p t}$$

with $\kappa_\phi = 1$ and $\lambda_{cd}^p \geq \bar{\lambda}_{cd}^p := \frac{k_P n \mu}{(1+k_P n T)^2}$. This result can be proven along the same lines as Lemma 5 in [65] or Lemma 3 in [79]. Since $\bar{\mathbf{L}}(t)$ is continuous for almost all $t \geq 0$ and uniformly bounded, and system (C.13) is GUES, then Lemma 1 in [79] and a similar argument as in Theorem 4.12 in [54] imply that, for any constants \bar{c}_3 and \bar{c}_4 satisfying $0 < \bar{c}_3 \leq \bar{c}_4$, there exists a continuous, piecewise-differentiable matrix $\mathbf{P}_{cd_0}(t) = \mathbf{P}_{cd_0}^\top(t)$, such that

$$\bar{c}_1 \mathbb{I}_{n-1} := \frac{\bar{c}_3}{2k_P n} \mathbb{I}_{n-1} \leq \mathbf{P}_{cd_0}(t) \leq \frac{\bar{c}_4}{2\bar{\lambda}_{cd}^p} \mathbb{I}_{n-1} =: \bar{c}_2 \mathbb{I}_{n-1}, \quad (\text{C.14a})$$

$$\dot{\mathbf{P}}_{cd_0}(t) - k_P \bar{\mathbf{L}}(t) \mathbf{P}_{cd_0}(t) - k_P \mathbf{P}_{cd_0}(t) \bar{\mathbf{L}}(t) \leq -\bar{c}_3 \mathbb{I}_{n-1}. \quad (\text{C.14b})$$

Next, we apply the change of variables

$$z(t) := S_\zeta \zeta(t), \quad S_\zeta := \begin{bmatrix} \mathbb{I}_{n-1} & \mathbf{0} \\ -\frac{k_L}{k_P} \mathbf{C}^\top \mathbf{Q}^\top & \mathbb{I}_{n-n_\ell} \end{bmatrix}, \quad (\text{C.15})$$

to the kinematic coordination error dynamics (4.7), which leads to

$$\dot{\mathbf{z}}(t) = \mathbf{S}_\zeta \mathbf{A}_\zeta(t) \mathbf{S}_\zeta^{-1} \mathbf{z}(t) = \begin{bmatrix} -k_P \bar{\mathbf{L}}(t) + \frac{k_I}{k_P} \mathbf{Q} \mathbf{C} \mathbf{C}^\top \mathbf{Q}^\top & \mathbf{Q} \mathbf{C} \\ -\frac{k_I^2}{k_P^2} \mathbf{C}^\top \mathbf{Q}^\top \mathbf{Q} \mathbf{C} \mathbf{C}^\top \mathbf{Q}^\top & -\frac{k_I}{k_P} \mathbf{C}^\top \mathbf{Q}^\top \mathbf{Q} \mathbf{C} \end{bmatrix} \mathbf{z}(t). \quad (\text{C.16})$$

Consider now the Lyapunov function candidate

$$V_{cd}(t, \mathbf{z}) := \mathbf{z}^\top \mathbf{P}_{cd}(t) \mathbf{z}, \quad (\text{C.17})$$

where $\mathbf{P}_{cd}(t)$ is defined as

$$\mathbf{P}_{cd}(t) := \begin{bmatrix} \mathbf{P}_{cd_0}(t) & \mathbf{0} \\ \mathbf{0} & \frac{k_P^3}{k_I^2} (\mathbf{C}^\top \mathbf{Q}^\top \mathbf{Q} \mathbf{C})^{-1} \end{bmatrix}.$$

The time derivative of V_{cd} along the trajectories of the system (C.16) is given by

$$\begin{aligned} \dot{V}_{cd}(t) = \\ z^\top(t) \begin{bmatrix} \dot{\mathbf{P}}_{cd_0}(t) - k_P \bar{\mathbf{L}}(t) \mathbf{P}_{cd_0}(t) - k_P \mathbf{P}_{cd_0}(t) \bar{\mathbf{L}}(t) + \frac{k_I}{k_P} (\mathbf{Q} \mathbf{C} \mathbf{C}^\top \mathbf{Q}^\top \mathbf{P}_{cd_0}(t) + \mathbf{P}_{cd_0}(t) \mathbf{Q} \mathbf{C} \mathbf{C}^\top \mathbf{Q}^\top) (\mathbf{P}_{cd_0}(t) - \frac{k_P}{k_I} \mathbb{I}_{n-1}) \mathbf{Q} \mathbf{C} \\ \mathbf{C}^\top \mathbf{Q}^\top (\mathbf{P}_{cd_0}(t) - \frac{k_P}{k_I} \mathbb{I}_{n-1}) \\ -2 \frac{k_P^2}{k_I^2} \mathbb{I}_{n-n_\ell} \end{bmatrix} \mathbf{z}(t). \end{aligned}$$

Inequality (C.14b) implies that

$$\dot{V}_{cd}(t) \leq z^\top(t) \begin{bmatrix} -\bar{c}_3 \mathbb{I}_{n-1} + \frac{k_I}{k_P} (\mathbf{Q} \mathbf{C} \mathbf{C}^\top \mathbf{Q}^\top \mathbf{P}_{cd_0}(t) + \mathbf{P}_{cd_0}(t) \mathbf{Q} \mathbf{C} \mathbf{C}^\top \mathbf{Q}^\top) (\mathbf{P}_{cd_0}(t) - \frac{k_P}{k_I} \mathbb{I}_{n-1}) \mathbf{Q} \mathbf{C} \\ \mathbf{C}^\top \mathbf{Q}^\top (\mathbf{P}_{cd_0}(t) - \frac{k_P}{k_I} \mathbb{I}_{n-1}) \\ -2 \frac{k_P^2}{k_I^2} \mathbb{I}_{n-n_\ell} \end{bmatrix} \mathbf{z}(t).$$

Now, for any $\rho_k \geq 2$, define

$$\bar{\lambda}_{cd} := \frac{\bar{\lambda}_{cd}^p}{1 + \rho_k \frac{n}{n_\ell}}.$$

Then, letting

$$k_P > 0, \quad k_I = k_P \bar{\lambda}_{cd} \frac{n}{n_\ell} \rho_k, \quad \bar{c}_3 = \bar{c}_4 = \frac{\bar{\lambda}_{cd}^p}{\bar{\lambda}_{cd}} \frac{2n_\ell}{\rho_k n}, \quad (\text{C.18})$$

and noting that $\|\mathbf{Q} \mathbf{C}\| = 1$ and $\lambda_{\min}(\mathbf{C}^\top \mathbf{Q}^\top \mathbf{Q} \mathbf{C}) = \frac{n_\ell}{n}$, one can use inequalities (C.14) and Schur complements to prove that the following inequality holds for all $t \geq 0$:¹

$$\begin{bmatrix} -\bar{c}_3 \mathbb{I}_{n-1} + \frac{k_I}{k_P} (\mathbf{Q} \mathbf{C} \mathbf{C}^\top \mathbf{Q}^\top \mathbf{P}_{cd_0}(t) + \mathbf{P}_{cd_0}(t) \mathbf{Q} \mathbf{C} \mathbf{C}^\top \mathbf{Q}^\top) (\mathbf{P}_{cd_0}(t) - \frac{k_P}{k_I} \mathbb{I}_{n-1}) \mathbf{Q} \mathbf{C} \\ \mathbf{C}^\top \mathbf{Q}^\top (\mathbf{P}_{cd_0}(t) - \frac{k_P}{k_I} \mathbb{I}_{n-1}) \\ -2 \frac{k_P^2}{k_I^2} \mathbb{I}_{n-n_\ell} \end{bmatrix} \leq -2 \bar{\lambda}_{cd} \begin{bmatrix} \bar{c}_2 \mathbb{I}_{n-1} & \mathbf{0} \\ \mathbf{0} & \frac{k_P^3}{k_I^2} (\mathbf{C}^\top \mathbf{Q}^\top \mathbf{Q} \mathbf{C})^{-1} \end{bmatrix}. \quad (\text{C.19})$$

¹The proof of this result can be found at the end of this section.

Then, for the choice of parameters in (C.18), inequality (C.19) implies that

$$\dot{V}_{cd}(t) \leq -2\bar{\lambda}_{cd} \mathbf{z}^\top(t) \begin{bmatrix} \mathbf{P}_{cd0}(t) & \mathbf{0} \\ \mathbf{0} & \frac{k_P^3}{k_I^3} (\mathbf{C}^\top \mathbf{Q}^\top \mathbf{Q} \mathbf{C})^{-1} \end{bmatrix} \mathbf{z}(t) = -2\bar{\lambda}_{cd} V_{cd}(t).$$

Application of the comparison lemma (see [54, Lemma 3.4]) yields

$$V_{cd}(t) \leq V_{cd}(0) e^{-2\bar{\lambda}_{cd} t},$$

and since

$$\min \left\{ \bar{c}_1, \frac{k_P^3}{k_I^3} \right\} \|\mathbf{z}(t)\|^2 \leq V_{cd}(t) \leq \max \left\{ \bar{c}_2, \frac{k_P^3}{k_I^3} \frac{n}{n_\ell} \right\} \|\mathbf{z}(t)\|^2,$$

we find that

$$\|\mathbf{z}(t)\| \leq \left(\frac{\max \left\{ \bar{c}_2, \frac{k_P^3}{k_I^3} \frac{n}{n_\ell} \right\}}{\min \left\{ \bar{c}_1, \frac{k_P^3}{k_I^3} \right\}} \right)^{\frac{1}{2}} \|\mathbf{z}(0)\| e^{-\bar{\lambda}_{cd} t}.$$

The similarity transformation in (C.15) implies that

$$\|\boldsymbol{\zeta}(t)\| \leq \kappa_{\zeta 0} \|\boldsymbol{\zeta}(0)\| e^{-\bar{\lambda}_{cd} t}, \quad \kappa_{\zeta 0} := \|\mathbf{S}_\zeta^{-1}\| \left(\frac{\max \left\{ \bar{c}_2, \frac{k_P^3}{k_I^3} \frac{n}{n_\ell} \right\}}{\min \left\{ \bar{c}_1, \frac{k_P^3}{k_I^3} \right\}} \right)^{\frac{1}{2}} \|\mathbf{S}_\zeta\|, \quad (\text{C.20})$$

and consequently system (4.7) is GUES with (guaranteed) rate of convergence $\bar{\lambda}_{cd}$.

To prove the bounds in (4.10) and (4.11), we note that from the kinematic equations (4.5) and the definition of $\boldsymbol{\zeta}_1(t)$ and $\boldsymbol{\zeta}_2(t)$ in (4.6) we have that

$$\mathbf{Q}^\top \boldsymbol{\zeta}_1(t) = \mathbf{Q}^\top \mathbf{Q} \boldsymbol{\xi}(t) = \boldsymbol{\Pi}_\xi \boldsymbol{\xi}(t) = \boldsymbol{\xi}(t) - \left(\frac{1}{n} \mathbf{1}_n^\top \boldsymbol{\xi}(t) \right) \mathbf{1}_n, \quad (\text{C.21})$$

$$\dot{\boldsymbol{\xi}}(t) - \mathbf{1}_n = -k_P \mathbf{L}(t) \mathbf{Q}^\top \boldsymbol{\zeta}_1(t) + \begin{bmatrix} \mathbf{0} \\ \boldsymbol{\zeta}_2(t) \end{bmatrix}, \quad (\text{C.22})$$

Partitioning matrix \mathbf{Q} as $\mathbf{Q} = [\mathbf{q}_1, \dots, \mathbf{q}_n]$, $\mathbf{q}_i \in \mathbb{R}^{n-1}$, equality (C.21) above yields

$$\xi_i(t) - \xi_j(t) = \mathbf{q}_i^\top \boldsymbol{\zeta}_1(t) - \mathbf{q}_j^\top \boldsymbol{\zeta}_1(t).$$

Then, recalling that $\mathbf{Q}^\top \mathbf{Q} = \boldsymbol{\Pi}_\xi$, which implies that $\|\mathbf{q}_i\|^2 = 1 - \frac{1}{n}$, one obtains the following bound:

$$|\xi_i(t) - \xi_j(t)| \leq 2 \left(1 - \frac{1}{n} \right)^{\frac{1}{2}} \|\boldsymbol{\zeta}_1(t)\| \leq 2 \left(1 - \frac{1}{n} \right)^{\frac{1}{2}} \|\boldsymbol{\zeta}(t)\|, \quad i, j = 1, \dots, n. \quad (\text{C.23})$$

Equality (C.22) leads to

$$|\dot{\xi}_i(t) - 1| \leq k_P \|\mathbf{L}(t)\| \|\mathbf{Q}^\top\| \|\zeta_1(t)\| + \|\zeta_2(t)\|,$$

and recalling that $\lambda_{\max}(\mathbf{L}(t)) \leq n$ and $\mathbf{Q}\mathbf{Q}^\top = \mathbb{I}_{n-1}$, it follows that

$$|\dot{\xi}_i(t) - 1| \leq (k_P n + 1) \|\zeta(t)\|. \quad (\text{C.24})$$

Inequalities (C.20), (C.23), and (C.24) lead to the bounds in (4.10) and (4.11) with

$$\kappa_{\xi 0} = 2 \left(1 - \frac{1}{n}\right)^{\frac{1}{2}} \kappa_{\zeta 0}, \quad \kappa_{\dot{\xi} 0} = (k_P n + 1) \kappa_{\zeta 0}. \quad \square$$

Proof of inequality (C.19)

To prove inequality (C.19), we start by showing that the following inequality

$$\begin{bmatrix} \bar{c}_3 \mathbb{I}_{n-1} - \frac{k_I}{k_P} (\mathbf{Q} \mathbf{C} \mathbf{C}^\top \mathbf{Q}^\top \mathbf{P}_{cd_0}(t) + \mathbf{P}_{cd_0}(t) \mathbf{Q} \mathbf{C} \mathbf{C}^\top \mathbf{Q}^\top) & \left(\frac{k_P}{k_I} \mathbb{I}_{n-1} - \mathbf{P}_{cd_0}(t)\right) \mathbf{Q} \mathbf{C} \\ \mathbf{C}^\top \mathbf{Q}^\top \left(\frac{k_P}{k_I} \mathbb{I}_{n-1} - \mathbf{P}_{cd_0}(t)\right) & 2 \frac{k_P^2}{k_I^2} \mathbb{I}_{n-n_\ell} \end{bmatrix} \geq 2 \bar{\lambda}_{cd} \begin{bmatrix} \bar{c}_2 \mathbb{I}_{n-1} & \mathbf{0} \\ \mathbf{0} & \frac{k_P^3}{k_I^2} \frac{n}{n_\ell} \mathbb{I}_{n-n_\ell} \end{bmatrix}, \quad (\text{C.25})$$

or, equivalently,

$$\begin{bmatrix} (\bar{c}_3 - 2\bar{\lambda}_{cd}\bar{c}_2) \mathbb{I}_{n-1} - \frac{k_I}{k_P} (\mathbf{Q} \mathbf{C} \mathbf{C}^\top \mathbf{Q}^\top \mathbf{P}_{cd_0}(t) + \mathbf{P}_{cd_0}(t) \mathbf{Q} \mathbf{C} \mathbf{C}^\top \mathbf{Q}^\top) & \left(\frac{k_P}{k_I} \mathbb{I}_{n-1} - \mathbf{P}_{cd_0}(t)\right) \mathbf{Q} \mathbf{C} \\ \mathbf{C}^\top \mathbf{Q}^\top \left(\frac{k_P}{k_I} \mathbb{I}_{n-1} - \mathbf{P}_{cd_0}(t)\right) & 2 \frac{k_P^2}{k_I^2} \left(1 - \bar{\lambda}_{cd} \frac{k_P}{k_I} \frac{n}{n_\ell}\right) \mathbb{I}_{n-n_\ell} \end{bmatrix} \geq \mathbf{0}, \quad (\text{C.26})$$

holds for all $t \geq 0$. To this effect, we note that Schur complements can be used to prove that inequality (C.26) holds for all $t \geq 0$ if and only if the following set of inequalities also holds for all $t \geq 0$:

$$(\bar{c}_3 - 2\bar{\lambda}_{cd}\bar{c}_2) \mathbb{I}_{n-1} - \frac{k_I}{k_P} (\mathbf{Q} \mathbf{C} \mathbf{C}^\top \mathbf{Q}^\top \mathbf{P}_{cd_0}(t) + \mathbf{P}_{cd_0}(t) \mathbf{Q} \mathbf{C} \mathbf{C}^\top \mathbf{Q}^\top) \geq \mathbf{0}, \quad (\text{C.27a})$$

$$1 - \bar{\lambda}_{cd} \frac{k_P}{k_I} \frac{n}{n_\ell} > 0, \quad (\text{C.27b})$$

$$\begin{aligned} & (\bar{c}_3 - 2\bar{\lambda}_{cd}\bar{c}_2) \mathbb{I}_{n-1} - \frac{k_I}{k_P} (\mathbf{Q} \mathbf{C} \mathbf{C}^\top \mathbf{Q}^\top \mathbf{P}_{cd_0}(t) + \mathbf{P}_{cd_0}(t) \mathbf{Q} \mathbf{C} \mathbf{C}^\top \mathbf{Q}^\top) \\ & - \left(\frac{k_P}{k_I} \mathbb{I}_{n-1} - \mathbf{P}_{cd_0}(t)\right) \mathbf{Q} \mathbf{C} \frac{1}{2} \frac{k_I^2}{k_P^2} \left(1 - \bar{\lambda}_{cd} \frac{k_P}{k_I} \frac{n}{n_\ell}\right)^{-1} \mathbf{C}^\top \mathbf{Q}^\top \left(\frac{k_P}{k_I} \mathbb{I}_{n-1} - \mathbf{P}_{cd_0}(t)\right) \geq \mathbf{0}. \end{aligned} \quad (\text{C.27c})$$

The last inequality above can be rewritten as

$$\begin{aligned} & (\bar{c}_3 - 2\bar{\lambda}_{cd}\bar{c}_2) \mathbb{I}_{n-1} - \frac{k_I}{k_P} \left(1 - \frac{\alpha}{2}\right) (\mathbf{Q} \mathbf{C} \mathbf{C}^\top \mathbf{Q}^\top \mathbf{P}_{cd_0}(t) + \mathbf{P}_{cd_0}(t) \mathbf{Q} \mathbf{C} \mathbf{C}^\top \mathbf{Q}^\top) \\ & - \frac{\alpha}{2} \mathbf{Q} \mathbf{C} \mathbf{C}^\top \mathbf{Q}^\top - \frac{k_I^2}{k_P^2} \frac{\alpha}{2} \mathbf{P}_{cd_0}(t) \mathbf{Q} \mathbf{C} \mathbf{C}^\top \mathbf{Q}^\top \mathbf{P}_{cd_0}(t) \geq \mathbf{0}, \end{aligned}$$

where we have defined

$$\alpha := \left(1 - \bar{\lambda}_{cd} \frac{k_P}{k_I} \frac{n}{n_\ell}\right)^{-1}.$$

Recalling now that $\mathbf{P}_{cd_0}(t) \leq \bar{c}_2 \mathbb{I}_{\mathbf{n}-\mathbf{1}}$, $\bar{c}_2 = \frac{\bar{c}_4}{2\bar{\lambda}_{cd}^p}$, and $\|\mathbf{Q}\mathbf{C}\| = 1$, it is easy to show that inequalities (C.27) hold for any k_P , k_I , $\bar{\lambda}_{cd}$, \bar{c}_3 , and \bar{c}_4 satisfying

$$\left(\bar{c}_3 - \frac{\bar{\lambda}_{cd}}{\bar{\lambda}_{cd}^p} \bar{c}_4\right) - \frac{k_I}{k_P} \frac{\bar{c}_4}{\bar{\lambda}_{cd}^p} \geq 0, \quad (\text{C.28a})$$

$$\alpha > 0, \quad (\text{C.28b})$$

$$2 - \alpha \geq 0, \quad (\text{C.28c})$$

$$\left(\bar{c}_3 - \frac{\bar{\lambda}_{cd}}{\bar{\lambda}_{cd}^p} \bar{c}_4\right) - \frac{k_I}{k_P} \left(1 - \frac{\alpha}{2}\right) \frac{\bar{c}_4}{\bar{\lambda}_{cd}^p} - \frac{\alpha}{2} - \frac{k_I^2}{k_P^2} \frac{\alpha}{8} \left(\frac{\bar{c}_4}{\bar{\lambda}_{cd}^p}\right)^2 \geq 0, \quad (\text{C.28d})$$

$$\bar{c}_4 - \bar{c}_3 \geq 0, \quad (\text{C.28e})$$

where the last inequality is needed to ensure existence of $\mathbf{P}_{cd_0}(t)$ satisfying (C.14).

Next, we let $X := \frac{\bar{\lambda}_{cd}}{\bar{\lambda}_{cd}^p} \bar{c}_4$ and $Y := \frac{k_I}{k_P} \frac{1}{\bar{\lambda}_{cd}}$, and note that

$$XY = \frac{k_I}{k_P} \frac{\bar{c}_4}{\bar{\lambda}_{cd}^p}, \quad \alpha = \frac{Y n_\ell}{Y n_\ell - n}.$$

Then, inequalities (C.28) can be rewritten as

$$(\bar{c}_3 - X) - XY \geq 0, \quad (\text{C.29a})$$

$$Y - \frac{n}{n_\ell} > 0, \quad (\text{C.29b})$$

$$Y - 2 \frac{n}{n_\ell} \geq 0, \quad (\text{C.29c})$$

$$(\bar{c}_3 - X) - \left(1 - \frac{\alpha}{2}\right) XY - \frac{\alpha}{2} - \frac{\alpha}{8} (XY)^2 \geq 0, \quad (\text{C.29d})$$

$$\frac{\bar{\lambda}_{cd}^p}{\bar{\lambda}_{cd}} X - \bar{c}_3 \geq 0. \quad (\text{C.29e})$$

Clearly, inequality (C.29c) is more strict than inequality (C.29b). It can also be proven that inequality (C.29d) is more strict than inequality (C.29a). Therefore, inequalities (C.29) can be simplified to

$$Y - 2 \frac{n}{n_\ell} \geq 0, \quad (\text{C.30a})$$

$$(\bar{c}_3 - X) - \left(1 - \frac{\alpha}{2}\right) XY - \frac{\alpha}{2} - \frac{\alpha}{8} (XY)^2 \geq 0, \quad (\text{C.30b})$$

$$\frac{\bar{\lambda}_{cd}^p}{\bar{\lambda}_{cd}} X - \bar{c}_3 \geq 0. \quad (\text{C.30c})$$

In particular, we note that the above inequalities have a solution if and only if

$$2\frac{n}{n_\ell} \leq Y \leq \frac{\bar{\lambda}_{cd}^p}{\bar{\lambda}_{cd}} - 1.$$

Let now ρ_k be a positive constant satisfying $\rho_k \geq 2$, and set

$$Y = \rho_k \frac{n}{n_\ell}, \quad X = \frac{2}{Y}, \quad \bar{\lambda}_{cd} = \frac{\bar{\lambda}_{cd}^p}{1+Y}, \quad \bar{c}_3 = \frac{\bar{\lambda}_{cd}^p}{\bar{\lambda}_{cd}} X.$$

It is straightforward to verify that inequalities (C.30) hold for this particular choice of parameters X , Y , $\bar{\lambda}_{cd}$, and \bar{c}_3 . This implies that inequality (C.25) holds for all $t \geq 0$ if k_P , k_I , $\bar{\lambda}_{cd}$, \bar{c}_3 , and \bar{c}_4 are set to satisfy

$$\bar{\lambda}_{cd} = \frac{\bar{\lambda}_{cd}^p}{1 + \rho_k \frac{n}{n_\ell}}, \quad \frac{k_I}{k_P} = \bar{\lambda}_{cd} \frac{n}{n_\ell} \rho_k, \quad \bar{c}_3 = \bar{c}_4 = \frac{\bar{\lambda}_{cd}^p}{\bar{\lambda}_{cd}} \frac{2n_\ell}{\rho_k n}.$$

Finally, we note that $(C^\top Q^\top QC)^{-1} \leq \frac{n}{n_\ell} \mathbb{I}_{n-n_\ell}$, which leads to

$$\begin{bmatrix} \bar{c}_2 \mathbb{I}_{n-1} & \mathbf{0} \\ \mathbf{0} & \frac{k_P^3}{k_I^3} (C^\top Q^\top QC)^{-1} \end{bmatrix} \leq \begin{bmatrix} \bar{c}_2 \mathbb{I}_{n-1} & \mathbf{0} \\ \mathbf{0} & \frac{k_P^3}{k_I^3} \frac{n}{n_\ell} \mathbb{I}_{n-n_\ell} \end{bmatrix}.$$

The inequality above, along with (C.25), implies that inequality (C.19) holds for all $t \geq 0$. \square

C.4 Proof of Lemma 4

Input-to-state stability (ISS) can be proven along the same lines as Lemma 4.6 in [54]. In fact, we can conclude that system (4.12) is ISS because it is a linear system, the Laplacian $L(t)$ is bounded, the unforced system has a globally exponentially stable equilibrium point at the origin (see Lemma 3), and the speed tracking error vector $e_v(t)$ is assumed to be piecewise continuous in t and bounded for all $t \geq 0$. Constants $\kappa_{\zeta 0}$ and $\kappa_{\zeta 1}$ in (4.13) can be derived from a proof similar to that of Lemma 4.6 in [54], and are given by

$$\kappa_{\zeta 0} = \|S_\zeta^{-1}\| \left(\frac{\max \left\{ \bar{c}_2, \frac{k_P^3}{k_I^3} \frac{n}{n_\ell} \right\}}{\min \left\{ \bar{c}_1, \frac{k_P^3}{k_I^3} \right\}} \right)^{\frac{1}{2}} \|S_\zeta\|, \quad \kappa_{\zeta 1} = \frac{1}{v_{d \min}} \|S_\zeta^{-1}\| \left(\frac{\max \left\{ \bar{c}_2, \frac{k_P^3}{k_I^3} \frac{n}{n_\ell} \right\}}{\min \left\{ \bar{c}_1, \frac{k_P^3}{k_I^3} \right\}} \right)^{\frac{3}{2}} \frac{\|S_\zeta\|}{\bar{\lambda}_{cd} \theta_\lambda},$$

where $v_{d \min}$ was introduced in (2.3).

Finally, the bounds in (4.14) and (4.15) follow from the bound in (4.13) and the following inequalities:

$$|\xi_i(t) - \xi_j(t)| \leq 2 \left(1 - \frac{1}{n}\right)^{\frac{1}{2}} \|\zeta(t)\|, \quad i, j = 1, \dots, n, \quad (\text{C.31})$$

$$|\dot{\xi}_i(t) - 1| \leq (k_P n + 1) \|\zeta(t)\| + \frac{1}{v_{d\min}} \|\mathbf{e}_v(t)\|, \quad i = 1, \dots, n. \quad (\text{C.32})$$

□

C.5 Proof of Theorem 1

We prove the claims of the theorem by contradiction. To this effect, we consider one of the vehicles involved in the mission and assume that it is not able to remain inside the pre-specified tube centered on its desired path. Without loss of generality, we assume that this vehicle is the first one that violates this condition and, therefore, we assume that all other vehicles do satisfy the claims of the theorem. In addition, we assume that no vehicle has yet reached its final destination. In what follows, we establish the validity of the theorem by showing that the hypotheses above imply a contradiction.

More precisely, consider the i th vehicle and assume that, at a given time $t > 0$, its path-following errors are such that $(\mathbf{p}_{F,i}(t), \tilde{\mathbf{R}}_i(t)) \notin \Omega_{pf}$. For all other vehicles j , $j = 1, \dots, n$, $j \neq i$, we assume that $(\mathbf{p}_{F,j}(\tau), \tilde{\mathbf{R}}_j(\tau)) \in \Omega_{pf}$ for all $\tau \in [0, t]$. Next, for the i th vehicle, consider the path-following Lyapunov function candidate:

$$V_{pf,i}(\mathbf{p}_{F,i}, \tilde{\mathbf{R}}_i) = \Psi(\tilde{\mathbf{R}}_i) + \frac{1}{c_1^2} \|\mathbf{p}_{F,i}\|^2.$$

Since $(\mathbf{p}_{F,i}(0), \tilde{\mathbf{R}}_i(0)) \in \Omega_{pf}$ by assumption, and $V_{pf,i}$ evaluated along the system trajectories is continuous and differentiable, we have that, if $(\mathbf{p}_{F,i}(t), \tilde{\mathbf{R}}_i(t)) \notin \Omega_{pf}$ for some $t > 0$, then there exists a time t' , $0 \leq t' < t$, such that

$$V_{pf,i}(t') = c^2, \quad (\text{C.33})$$

$$\dot{V}_{pf,i}(t') > 0, \quad (\text{C.34})$$

while

$$V_{pf,i}(\tau) \leq c^2, \quad \text{for all } \tau \in [0, t'). \quad (\text{C.35})$$

Equality (C.33) and the bound in (C.35) imply that the following inequalities hold for all $\tau \in [0, t']$:

$$\|\mathbf{p}_{F,i}(\tau)\| \leq cc_1, \quad \Psi(\tilde{\mathbf{R}}_i(\tau)) \leq c^2. \quad (\text{C.36})$$

These two bounds, along with the choice for the characteristic distance d in (4.16), yield

$$\hat{\mathbf{w}}_{\mathbf{1},i}(\tau) \cdot \hat{\mathbf{t}}_i(\tau) \geq \frac{(1-2c^2)d - 2c(1-c^2)^{\frac{1}{2}}cc_1}{(d^2 + (cc_1)^2)^{\frac{1}{2}}} =: c_2 > 0, \quad \text{for all } \tau \in [0, t']. \quad (\text{C.37})$$

The quantity $\frac{1}{\hat{\mathbf{w}}_{\mathbf{1},i}(\tau) \cdot \hat{\mathbf{t}}_i(\tau)}$ is thus well defined for all $\tau \in [0, t']$, which implies that the speed command $v_{c,i}(\tau)$ in (4.2) is also well defined for all $\tau \in [0, t']$. It follows from Lemma 3 that

$$\|\zeta(\tau)\| \leq \kappa_{\zeta 0} \|\zeta(0)\| e^{-\bar{\lambda}_{cd}\tau}, \quad \text{for all } \tau \in [0, t'],$$

where $\kappa_{\zeta 0}$ was defined in (C.20). This bound, the speed command (4.2), the coordination law (4.4), inequality (C.23), and the bounds in (C.36) and (C.37) lead to

$$v_{d\min}(1 - \kappa_1 \kappa_{\zeta 0} \|\zeta(0)\|) - k_\ell cc_1 \leq v_{c,i}(\tau) \leq \frac{1}{c_2} (v_{d\max}(1 + \kappa_1 \kappa_{\zeta 0} \|\zeta(0)\|) + k_\ell cc_1), \quad \text{for all } \tau \in [0, t'],$$

where $\kappa_1 := 2k_P \left(\frac{(n-1)^3}{n} \right)^{\frac{1}{2}} + 1$. The assumption on the initial condition in (4.19) implies that

$$v_{\min} \leq v_{c,i}(\tau) \leq v_{\max}, \quad \text{for all } \tau \in [0, t']. \quad (\text{C.38})$$

We can now use a proof similar to the one of Lemma 1 to show that, for all $\tau \in [0, t']$, $\dot{V}_{pf,i} < 0$ on the boundary of Ω_{pf} , which contradicts the claim in (C.33)-(C.34).

Therefore, we have that, for all $t \geq 0$ and all $i \in \{1, \dots, n\}$, the path-following errors $\mathbf{p}_{F,i}(t)$ and $\tilde{\mathbf{R}}_i(t)$ satisfy $(\mathbf{p}_{F,i}(t), \tilde{\mathbf{R}}_i(t)) \in \Omega_{pf}$. At the kinematic level, the bounds in (4.20) follow directly from (C.38). Then, Lemmas 1 and 3 can be used to prove exponential stability of the origin of dynamics (2.11) and (4.7), with guaranteed rates of convergence $\bar{\lambda}_{pf}$ and $\bar{\lambda}_{cd}$, respectively. \square

C.6 Proof of Theorem 2

First, in order to simplify the notation in this proof, we define the positive constants $v_{c\min}$ and $v_{c\max}$ as

$$v_{c\min} := v_{\min} + \gamma_v, \quad v_{c\max} := v_{\max} - \gamma_v,$$

which, as will become clear later in the proof, characterize respectively lower and upper bounds on the vehicle speed commands.

We now prove the claims of the theorem by contradiction. To this effect, similar to the proof of Theorem 1,

we consider one of the vehicles involved in the mission and assume that it is not able to remain inside the pre-specified tube centered on its desired path. Without loss of generality, we assume that this vehicle is the first one that violates this condition and, therefore, we assume that all other vehicles do satisfy the claims of the theorem. In addition, we assume that no vehicle has yet reached its final destination. In what follows, we establish the validity of the theorem by showing that the hypotheses above imply a contradiction.

More precisely, consider the i th vehicle and assume that, at a given time $t > 0$, its path-following errors are such that $(\mathbf{p}_{F,i}(t), \tilde{\mathbf{R}}_i(t)) \notin \Omega_{pf}$. For all other vehicles j , $j = 1, \dots, n$, $j \neq i$, we assume that $(\mathbf{p}_{F,j}(\tau), \tilde{\mathbf{R}}_j(\tau)) \in \Omega_{pf}$ for all $\tau \in [0, t]$. Next, for the i th vehicle, consider the path-following Lyapunov function candidate:

$$V_{pf,i}(\mathbf{p}_{F,i}, \tilde{\mathbf{R}}_i) = \Psi(\tilde{\mathbf{R}}_i) + \frac{1}{c_1^2} \|\mathbf{p}_{F,i}\|^2.$$

Since $(\mathbf{p}_{F,i}(0), \tilde{\mathbf{R}}_i(0)) \in \Omega_{pf}$ by assumption, and $V_{pf,i}$ evaluated along the system trajectories is continuous and differentiable, we have that, if $(\mathbf{p}_{F,i}(t), \tilde{\mathbf{R}}_i(t)) \notin \Omega_{pf}$ for some $t > 0$, then there exists a time t' , $0 \leq t' < t$, such that

$$V_{pf,i}(t') = c^2, \quad (\text{C.39})$$

$$\dot{V}_{pf,i}(t') > 0, \quad (\text{C.40})$$

while

$$V_{pf,i}(\tau) \leq c^2, \quad \text{for all } \tau \in [0, t']. \quad (\text{C.41})$$

Equality (C.39) and the bound in (C.41) imply that the following inequalities hold for all $\tau \in [0, t']$:

$$\|\mathbf{p}_{F,i}(\tau)\| \leq cc_1, \quad \Psi(\tilde{\mathbf{R}}_i(\tau)) \leq c^2. \quad (\text{C.42})$$

These two bounds, along with the choice for the characteristic distance d in (4.16), yield

$$\hat{\mathbf{w}}_{1,i}(\tau) \cdot \hat{\mathbf{t}}_i(\tau) \geq c_2 > 0, \quad \text{for all } \tau \in [0, t']. \quad (\text{C.43})$$

The quantity $\frac{1}{\hat{\mathbf{w}}_{1,i}(\tau) \cdot \hat{\mathbf{t}}_i(\tau)}$ is thus well defined for all $\tau \in [0, t']$, which implies that the speed command $v_{c,i}(\tau)$ in (4.2) is also well defined for all $\tau \in [0, t']$.

At this point, we prove (by contradiction) that, with the assumptions made and the results derived so

far, the speed commands of all n vehicles satisfy

$$v_{c\min} \leq v_{c,j}(\tau) \leq v_{c\max}, \quad \text{for all } \tau \in [0, t'], \quad \text{and all } j \in \{1, \dots, n\}.$$

To this end, let t'' , $0 \leq t'' \leq t'$, be the first time at which one of the vehicles, say vehicle k , violates one of the bounds above. This implies that at time t'' one of the following inequalities is satisfied:

$$v_{c\min} > v_{c,k}(t''), \quad \text{or} \quad v_{c,k}(t'') < v_{c\max}, \quad (\text{C.44})$$

while

$$v_{c\min} \leq v_{c,k}(\tau) \leq v_{c\max}, \quad \text{for all } \tau \in [0, t''), \quad (\text{C.45})$$

$$v_{c\min} \leq v_{c,j}(\tau) \leq v_{c\max}, \quad \text{for all } \tau \in [0, t''], \quad \text{and all } j = \{1, \dots, n\}, j \neq k. \quad (\text{C.46})$$

The bounds in (C.45) and (C.46), along with the assumption on the vehicle dynamics in (2.16)-(2.17), yield

$$|v_{c,k}(\tau) - v_k(\tau)| \leq \gamma_v \quad \text{for all } \tau \in [0, t''), \quad (\text{C.47})$$

$$|v_{c,j}(\tau) - v_j(\tau)| \leq \gamma_v \quad \text{for all } \tau \in [0, t''], \quad \text{and all } j = \{1, \dots, n\}, j \neq k, \quad (\text{C.48})$$

which, in turn, lead to

$$v_{\min} \leq v_k(\tau) \leq v_{\max}, \quad \text{for all } \tau \in [0, t''), \quad (\text{C.49})$$

$$v_{\min} \leq v_j(\tau) \leq v_{\max}, \quad \text{for all } \tau \in [0, t''], \quad \text{and all } j = \{1, \dots, n\}, j \neq k. \quad (\text{C.50})$$

Continuity of $v_k(\cdot)$ and the bound in (C.49) above imply that $v_k(t'')$ is bounded. Moreover, since we have assumed that no vehicle has yet reached its final destination at time t , we have that the coordination states $\xi_j(\tau)$, $j = 1, \dots, n$, are bounded for all $\tau \in [0, t'']$. Boundedness of $\xi_j(\tau)$ for all $\tau \in [0, t'']$ and all $j = 1, \dots, n$ implies that, in particular, $u_{\text{coord},k}(t'')$ is bounded, which, together with inequalities (C.42) and (C.43), implies that $v_{c,k}(t'')$ is also bounded. From boundedness of both $v_k(t'')$ and $v_{c,k}(t'')$, we can conclude that $e_{v,k}(t'')$ is bounded. A proof similar to the one of Lemma 4 can now be used to show that the choice of the coordination control gains k_P and k_I in (4.17) ensures that the following bound holds:

$$\|\zeta(\tau)\| \leq \kappa_{\zeta 0} \|\zeta(0)\| e^{-\lambda_{cd}\tau} + \kappa_{\zeta 1} \sup_{s \in [0, \tau)} \|e_{\mathbf{v}}(s)\|, \quad \text{for all } \tau \in [0, t''],$$

which, along with the bounds in (C.47) and (C.48), leads to

$$\|\zeta(t'')\| \leq \kappa_{\zeta 0} \|\zeta(0)\| + \kappa_{\zeta 1} \sqrt{n} \gamma_v .$$

This bound, the speed command (4.2), the coordination law (4.4), inequality (C.31), the bounds in (C.42) and (C.43), and the assumption that $(\mathbf{p}_{F,j}(\tau), \tilde{\mathbf{R}}_j(\tau)) \in \Omega_{pf}$ for all $\tau \in [0, t]$ and all $j \in \{1, \dots, n\}$, $j \neq i$, lead to

$$v_{d \min} (1 - \kappa_1 (\kappa_{\zeta 0} \|\zeta(0)\| + \kappa_{\zeta 1} \sqrt{n} \gamma_v)) - k_{\ell} c c_1 \leq v_{c,k}(t'') \leq \frac{1}{c_2} (v_{d \max} (1 + \kappa_1 (\kappa_{\zeta 0} \|\zeta(0)\| + \kappa_{\zeta 1} \sqrt{n} \gamma_v)) + k_{\ell} c c_1) .$$

The assumption on the initial condition in (4.25) implies that

$$v_{c \min} \leq v_{c,k}(t'') \leq v_{c \max} ,$$

which contradicts the claim in (C.44). Therefore we have that

$$v_{c \min} \leq v_{c,j}(\tau) \leq v_{c \max} , \quad \text{for all } \tau \in [0, t'] , \quad \text{and all } j = \{1, \dots, n\} .$$

Then, the assumption on the vehicle dynamics in (2.16)-(2.17), yields

$$|v_{c,j}(\tau) - v_j(\tau)| \leq \gamma_v \quad \text{for all } \tau \in [0, t'] , \quad \text{and all } j = \{1, \dots, n\} ,$$

which, in turn, leads to

$$v_{\min} \leq v_j(\tau) \leq v_{\max} , \quad \text{for all } \tau \in [0, t'] , \quad \text{and all } j = \{1, \dots, n\} . \quad (\text{C.51})$$

We can now use a proof similar to the one of Lemma 2 to show that, for all $\tau \in [0, t']$, $\dot{V}_{pf,i} < 0$ on the boundary of Ω_{pf} , which contradicts the claim in (C.39)-(C.40).

Therefore, we have that, for all $t \geq 0$ and all $j \in \{1, \dots, n\}$, the path-following errors $\mathbf{p}_{F,j}(t)$ and $\tilde{\mathbf{R}}_j(t)$ satisfy $(\mathbf{p}_{F,j}(t), \tilde{\mathbf{R}}_j(t)) \in \Omega_{pf}$. The bounds in (4.26) follow directly from (C.51), while the bounds in (4.27) and (4.28) can be derived from proofs similar to those of Lemmas 2 and 4. \square

C.7 Proof of Lemma 5

Let $\hat{\xi} \in \mathbb{R}^n$, and note that $\mathbf{q}(\hat{\xi}) = \mathbf{k}\Delta$, for some $\mathbf{k} \in \mathbb{Z}^n$. Also, for any $\mathbf{w} \in K(\mathbf{q}(\hat{\xi}))$, we have that

$$w_i \quad \begin{cases} = k_i\Delta, & \hat{\xi}_i \neq k_i\Delta - \frac{\Delta}{2} \\ \in [(k_i - 1)\Delta, k_i\Delta], & \hat{\xi}_i = k_i\Delta - \frac{\Delta}{2} \end{cases},$$

where $w_i \in \mathbb{R}$, $\hat{\xi}_i \in \mathbb{R}$, $k_i \in \mathbb{Z}$ are the i th components of \mathbf{w} , $\hat{\xi}$, and \mathbf{k} , respectively. Note that $|w_i - \hat{\xi}_i| \leq \frac{\Delta}{2}$.

To prove the result of the lemma, it is enough to show that, if the bound in (5.5) holds, then there exists no 4-tuple $(\hat{\xi}, \mathbf{w}_1, \mathbf{w}_2, \chi_I)$, $\hat{\xi} \in \mathbb{R}^n$, $\mathbf{w}_1, \mathbf{w}_2 \in K(\mathbf{q}(\hat{\xi}))$, and $\chi_I \in \mathbb{R}^{n-n_\ell}$, such that the following equality holds:

$$\mathbf{0} = \begin{bmatrix} -k_P (\mathbf{D}\hat{\xi} - \mathbf{A}\mathbf{w}_1) + [\mathbf{1}_{n_\ell}] \\ -k_I \mathbf{C}^\top (\mathbf{D}\hat{\xi} - \mathbf{A}\mathbf{w}_2) \end{bmatrix}. \quad (\text{C.52})$$

To this end, we first consider the first n rows of equality (C.52) and multiply them on the left by \mathbf{C}^\top to obtain

$$-k_P \mathbf{C}^\top (\mathbf{D}\hat{\xi} - \mathbf{A}\mathbf{w}_1) + \chi_I = \mathbf{0}.$$

Then, noting that the last $(n - n_\ell)$ rows of (C.52) imply that

$$\mathbf{C}^\top (\mathbf{D}\hat{\xi} - \mathbf{A}\mathbf{w}_2) = \mathbf{0},$$

it follows that equality (C.52) can be satisfied only if $\chi_I = k_P \mathbf{C}^\top \mathbf{A} (\mathbf{w}_2 - \mathbf{w}_1)$. This result implies that the existence of a 4-tuple $(\hat{\xi}, \mathbf{w}_1, \mathbf{w}_2, \chi_I)$ satisfying (C.52) is equivalent to the existence of a triple $(\hat{\xi}, \mathbf{w}_1, \mathbf{w}_2)$, $\hat{\xi} \in \mathbb{R}^n$ and $\mathbf{w}_1, \mathbf{w}_2 \in K(\mathbf{q}(\hat{\xi}))$, such that the following equality is satisfied:

$$\mathbf{L}\mathbf{w}_1 - \begin{bmatrix} \frac{1}{k_P} \mathbf{1}_{n_\ell} \\ \mathbf{0} \end{bmatrix} = \mathbf{D} (\mathbf{w}_1 - \hat{\xi}) + \begin{bmatrix} \mathbf{0} \\ \mathbf{C}^\top \mathbf{A} (\mathbf{w}_2 - \mathbf{w}_1) \end{bmatrix}, \quad (\text{C.53})$$

where $\mathbf{L} \in \mathbb{R}^{n \times n}$ is the Laplacian of the network topology, and $\mathbf{D}, \mathbf{A} \in \mathbb{R}^{n \times n}$ are its degree and adjacency matrices, respectively. Recall that, in this lemma, we assume that the topology is static, and therefore both \mathbf{L} , \mathbf{D} , and \mathbf{A} are constant matrices.

The existence of vectors $\hat{\xi}$, \mathbf{w}_1 , and \mathbf{w}_2 such that equality (C.53) holds depends on the quantizer precision. For instance, if $\left\| \frac{1}{k_P} \mathbf{D}^{-1} \begin{bmatrix} \mathbf{1}_{n_\ell} \\ \mathbf{0} \end{bmatrix} \right\|_\infty < \frac{\Delta}{2}$, then the vectors

$$\hat{\xi} = k\Delta \mathbf{1}_n + \frac{1}{k_P} \mathbf{D}^{-1} \begin{bmatrix} \mathbf{1}_{n_\ell} \\ \mathbf{0} \end{bmatrix}, \quad \mathbf{w}_1 = \mathbf{w}_2 = k\Delta \mathbf{1}_n,$$

verify equality (C.53) for any $k \in \mathbb{Z}$. On the contrary, if the bound in (5.5) holds, then there exist no vectors $\hat{\xi}$, \mathbf{w}_1 , and \mathbf{w}_2 such that equality (C.53) holds. To see this, consider the scalar equality

$$\frac{1}{k_P} n_\ell = \mathbf{1}_n^\top \mathbf{D} (\hat{\xi} - \mathbf{w}) + \mathbf{1}_{n-n_\ell}^\top \mathbf{C}^\top \mathbf{A} (\mathbf{w}_1 - \mathbf{w}_2), \quad (\text{C.54})$$

which has been obtained from (C.53) by multiplying on the left by $\mathbf{1}_n^\top$. Noting that $|w_{1i} - w_{2i}| \leq \Delta$, the right-hand side of this equality can be bounded as

$$\left| \mathbf{1}_n^\top \mathbf{D} (\hat{\xi} - \mathbf{w}) + \mathbf{1}_{n-n_\ell}^\top \mathbf{C}^\top \mathbf{A} (\mathbf{w}_1 - \mathbf{w}_2) \right| \leq (3n - 2n_\ell)(n-1) \frac{\Delta}{2}.$$

If the step size of the quantizers is bounded as in (5.5), then we have

$$\left| \mathbf{1}_n^\top \mathbf{D} (\hat{\xi} - \mathbf{w}) + \mathbf{1}_{n-n_\ell}^\top \mathbf{C}^\top \mathbf{A} (\mathbf{w}_1 - \mathbf{w}_2) \right| < \frac{1}{k_P} n_\ell,$$

which implies that no vectors $\hat{\xi}$, \mathbf{w}_1 , and \mathbf{w}_2 satisfy (C.54), and thus (C.53). In turn, this implies that there is no 4-tuple $(\hat{\xi}, \mathbf{w}_1, \mathbf{w}_2, \chi_I)$ such that equality (C.52) holds, and therefore set Θ , defined in (5.4), is empty. \square

C.8 Proof of Proposition 1

Let $\boldsymbol{\eta}(t) := [\boldsymbol{\eta}_1^\top(t), \boldsymbol{\eta}_2^\top(t)]$ be defined as

$$\boldsymbol{\eta}_1(t) := \boldsymbol{\xi}(t) - \hat{\boldsymbol{\xi}},$$

$$\boldsymbol{\eta}_2(t) := \boldsymbol{\chi}_I(t) - \hat{\boldsymbol{\chi}}_I,$$

where $\hat{\boldsymbol{\xi}}$ and $\hat{\boldsymbol{\chi}}_I$ characterize the “zero-speed” equilibrium points introduced in (5.7). Since, by assumption, we have that $\left\| \frac{1}{k_P} \mathbf{D}^{-1} \begin{bmatrix} \mathbf{1}_{n_\ell} \\ \mathbf{0} \end{bmatrix} \right\|_\infty < \frac{\Delta}{2}$, it follows that $\mathbf{q}(\hat{\boldsymbol{\xi}}) = k \Delta \mathbf{1}_n$, $k \in \mathbb{Z}$. Then, the closed-loop kinematic coordination dynamics (5.2) can be rewritten in terms of the states $\boldsymbol{\eta}_1(t)$ and $\boldsymbol{\eta}_2(t)$ as

$$\begin{aligned} \dot{\boldsymbol{\eta}}_1(t) &= -k_P \left(\mathbf{D} \boldsymbol{\eta}_1(t) - \mathbf{A} \mathbf{q}(\boldsymbol{\eta}_1(t) + \hat{\boldsymbol{\xi}}) \right) + \mathbf{C} \boldsymbol{\eta}_2(t) - k_P \mathbf{A} k \Delta \mathbf{1}_n, & \boldsymbol{\eta}_1(0) &= \boldsymbol{\xi}(0) - \hat{\boldsymbol{\xi}}, \\ \dot{\boldsymbol{\eta}}_2(t) &= -k_I \mathbf{C}^\top \left(\mathbf{D} \boldsymbol{\eta}_1(t) - \mathbf{A} \mathbf{q}(\boldsymbol{\eta}_1(t) + \hat{\boldsymbol{\xi}}) \right) - k_I \mathbf{C}^\top \mathbf{A} k \Delta \mathbf{1}_n, & \boldsymbol{\eta}_2(0) &= \boldsymbol{\chi}_I(0) - \hat{\boldsymbol{\chi}}_I. \end{aligned} \quad (\text{C.55})$$

In a sufficiently small neighborhood of the origin $(\boldsymbol{\eta}_1, \boldsymbol{\eta}_2) = (\mathbf{0}, \mathbf{0})$ the nonlinear dynamics (C.55) evolve according to the following linear equation:

$$\dot{\boldsymbol{\eta}} = \mathbf{A}_{\boldsymbol{\eta}} \boldsymbol{\eta}, \quad \mathbf{A}_{\boldsymbol{\eta}} := \begin{bmatrix} -k_P \mathbf{D} & \mathbf{C} \\ -k_I \mathbf{C}^\top \mathbf{D} & \mathbf{0} \end{bmatrix}.$$

The characteristic polynomial of $\mathbf{A}_{\boldsymbol{\eta}}$ is given by

$$p_{\mathbf{A}_{\boldsymbol{\eta}}}(\lambda) = \det(\lambda \mathbb{I}_{2n-n_\ell} - \mathbf{A}_{\boldsymbol{\eta}}) = \prod_{i=1}^{n_\ell} (\lambda + k_P d_i) \prod_{i=n_\ell+1}^n (\lambda^2 + k_P d_i \lambda + k_I d_i),$$

where d_i is the i th diagonal element of the degree matrix \mathbf{D} . Since the communications graph is assumed to be connected, it follows that $1 \leq d_i \leq n-1$, which implies that all of the eigenvalues of $\mathbf{A}_{\boldsymbol{\eta}}$ have negative real part. Therefore, the equilibrium points (5.7) are locally asymptotically stable. \square

C.9 Proof of Theorem 3

Let the function $\zeta(t) = \begin{bmatrix} \mathbf{Q}\xi(t) \\ \chi_{I(t)} - \mathbf{1}_{n-n_\ell} \end{bmatrix}$, $t \in I_t \subset \mathbb{R}$, be a Krasovskii solution of (5.3) on I_t , that is, $\zeta(t)$ is absolutely continuous and satisfies the differential inclusion [43]

$$\dot{\zeta} - \mathbf{A}_\zeta(t)\zeta \in \mathbf{K}(\mathbf{f}_q(t)),$$

for almost every $t \in I_t$. Then, letting $\mathbf{z}(t) := \mathbf{S}_\zeta \zeta(t)$, where \mathbf{S}_ζ was defined in (C.15), we have

$$\dot{\mathbf{z}} - \mathbf{S}_\zeta \mathbf{A}_\zeta(t) \mathbf{S}_\zeta^{-1} \mathbf{z} \in \mathbf{S}_\zeta \mathbf{K}(\mathbf{f}_q(t)), \quad \text{almost everywhere in } I_t.$$

Consider now the same Lyapunov function candidate (C.17) as in the proof of Lemma 3. Then, letting $\mathbf{w}_1(t), \mathbf{w}_2(t) \in \mathbf{K}(\mathbf{q}(\xi(t)))$ and following the same steps as in the proof of Lemma 3, we have that, for the choice of parameters in (C.18), the following inequality holds:

$$\begin{aligned} \dot{V}_{cd} &\leq -2\bar{\lambda}_{cd} V_{cd} + 2\mathbf{z}^\top \mathbf{P}_{cd}(t) \mathbf{S}_\zeta \begin{bmatrix} k_P \mathbf{Q} \mathbf{A}(t) (\mathbf{w}_1 - \xi) \\ k_I \mathbf{C}^\top \mathbf{A}(t) (\mathbf{w}_2 - \xi) \end{bmatrix} \\ &= -2\bar{\lambda}_{cd} V_{cd} + 2\mathbf{z}^\top \begin{bmatrix} k_P \mathbf{P}_{cd0}(t) \mathbf{Q} \mathbf{A}(t) \\ -\frac{k_P^3}{k_I^2} (\mathbf{C}^\top \mathbf{Q}^\top \mathbf{Q} \mathbf{C})^{-1} \mathbf{C}^\top \mathbf{Q}^\top \mathbf{Q} \mathbf{A}(t) \end{bmatrix} (\mathbf{w}_1 - \xi) + 2\mathbf{z}^\top \begin{bmatrix} \mathbf{0} \\ \frac{k_P^3}{k_I^2} (\mathbf{C}^\top \mathbf{Q}^\top \mathbf{Q} \mathbf{C})^{-1} \mathbf{C}^\top \mathbf{A}(t) \end{bmatrix} (\mathbf{w}_2 - \xi). \end{aligned}$$

Noting that $\|\mathbf{w}_1(t) - \boldsymbol{\xi}(t)\| \leq \sqrt{n}\frac{\Delta}{2}$, $\|\mathbf{w}_2(t) - \boldsymbol{\xi}(t)\| \leq \sqrt{n}\frac{\Delta}{2}$, and also that

$$\begin{aligned} \left\| \begin{bmatrix} k_P \mathbf{P}_{cd_0}(t) \mathbf{Q} \mathbf{A} \\ -\frac{k_P^3}{k_I^2} (\mathbf{C}^\top \mathbf{Q}^\top \mathbf{Q} \mathbf{C})^{-1} \mathbf{C}^\top \mathbf{Q}^\top \mathbf{Q} \mathbf{A}(t) \end{bmatrix} \right\| &\leq \sqrt{2} k_P (n-1) \max \left\{ \bar{c}_2, \frac{k_P^2}{k_I^2} \frac{n}{n_\ell} \right\} =: \sigma_{B1}, \\ \left\| \begin{bmatrix} \mathbf{0} \\ \frac{k_P^3}{k_I^2} (\mathbf{C}^\top \mathbf{Q}^\top \mathbf{Q} \mathbf{C})^{-1} \mathbf{C}^\top \mathbf{A}(t) \end{bmatrix} \right\| &\leq k_P (n-1) \frac{k_P^2}{k_I^2} \frac{n}{n_\ell} =: \sigma_{B2}, \end{aligned}$$

it follows that

$$\dot{V}_{cd} \leq -2\bar{\lambda}_{cd} V_{cd} + \sqrt{n}\Delta(\sigma_{B1} + \sigma_{B2})\|\mathbf{z}\|.$$

We can now rewrite the above inequality as

$$\dot{V}_{cd} \leq -2\bar{\lambda}_{cd}(1 - \theta'_\lambda)V_{cd} - 2\bar{\lambda}_{cd}\theta'_\lambda V_{cd} + \sqrt{n}\Delta(\sigma_{B1} + \sigma_{B2})\|\mathbf{z}\|,$$

where $0 < \theta'_\lambda < 1$. Then, for all $\mathbf{z}(t)$ satisfying

$$-2\bar{\lambda}_{cd}\theta'_\lambda V_{cd}(t) + \sqrt{n}\Delta(\sigma_{B1} + \sigma_{B2})\|\mathbf{z}(t)\| \leq 0, \quad (\text{C.56})$$

we have

$$\dot{V}_{cd} \leq -2\bar{\lambda}_{cd}(1 - \theta'_\lambda)V_{cd}.$$

Inequality (C.56) holds outside the bounded set D_Δ defined as

$$D_\Delta := \left\{ \mathbf{z} \in \mathbb{R}^{2n-n_\ell-1} : \|\mathbf{z}\| \leq \frac{\sqrt{n}\Delta(\sigma_{B1} + \sigma_{B2})}{2\bar{\lambda}_{cd}\theta'_\lambda \min \left\{ \bar{c}_1, \frac{k_P^3}{k_I^3} \right\}} \right\}.$$

The set D_Δ is in the interior of the compact set Ω_Δ given by

$$\Omega_\Delta := \left\{ \mathbf{z} \in \mathbb{R}^{2n-n_\ell-1} : V_{cd}(t, \mathbf{z}) \leq \frac{n(\sigma_{B1} + \sigma_{B2})^2 \max \left\{ \bar{c}_2, \frac{k_P^3}{k_I^3} \frac{n}{n_\ell} \right\}}{4\bar{\lambda}_{cd}^2 \theta'^2_\lambda \left(\min \left\{ \bar{c}_1, \frac{k_P^3}{k_I^3} \right\} \right)^2} \Delta^2 =: \kappa_V^2 \Delta^2 \right\}.$$

With this result and using a proof similar to that of Theorem 4.18 in [54], it can be shown that there is a time $T_b \geq 0$ such that

$$V_{cd}(t) \leq V_{cd}(0, \mathbf{z}(0)) e^{-2\bar{\lambda}_{cd}(1-\theta'_\lambda)t}, \quad \text{for all } 0 \leq t < T_b,$$

$$V_{cd}(t) \leq \kappa_V^2 \Delta^2, \quad \text{for all } t \geq T_b.$$

Then, the following inequalities:

$$\min \left\{ \bar{c}_1, \frac{k_P^3}{k_I^3} \right\} \|z(t)\|^2 \leq V_{cd}(t) \leq \max \left\{ \bar{c}_2, \frac{k_P^3}{k_I^3} \frac{n}{n_\ell} \right\} \|z(t)\|^2,$$

along with the similarity transformation in (C.15), yield

$$\|\zeta(t)\| \leq \kappa'_{\zeta 0} \|\zeta(0)\| e^{-\bar{\lambda}_{cd}(1-\theta'_\lambda)t}, \quad \text{for all } 0 \leq t < T_b, \quad (\text{C.57a})$$

$$\|\zeta(t)\| \leq \kappa'_{\zeta 1} \Delta, \quad \text{for all } t \geq T_b, \quad (\text{C.57b})$$

where $\kappa'_{\zeta 0}$ and $\kappa'_{\zeta 1}$ are given by

$$\begin{aligned} \kappa'_{\zeta 0} &:= \|S_\zeta^{-1}\| \left(\frac{\max \left\{ \bar{c}_2, \frac{k_P^3}{k_I^3} \frac{n}{n_\ell} \right\}}{\min \left\{ \bar{c}_1, \frac{k_P^3}{k_I^3} \right\}} \right)^{\frac{1}{2}} \|S_\zeta\|, \\ \kappa'_{\zeta 1} &:= \|S_\zeta^{-1}\| \left(\frac{1}{\min \left\{ \bar{c}_1, \frac{k_P^3}{k_I^3} \right\}} \right)^{\frac{1}{2}} \kappa_V. \end{aligned}$$

The bound in (5.8) follows immediately from the bounds in (C.57). \square

C.10 Proof of Lemma 6

(i) To prove that $\zeta_{\text{eq}} = \mathbf{0}$ is an equilibrium point of the closed-loop kinematic coordination error dynamics (5.11), it is enough to notice that the pair $(\xi_{\text{eq}}(t), \chi_{I,\text{eq}}) = ((\xi_0 + t)\mathbf{1}_n, \mathbf{1}_{n-n_\ell})$, $\xi_0 \in \mathbb{R}$, verifies the following equality for any admissible information flow $L(t)$:

$$\begin{bmatrix} \mathbf{1}_n \\ \mathbf{0} \end{bmatrix} \in K \left(\begin{bmatrix} -k_P L(t) \mathbf{q}(\xi_{\text{eq}}(t)) + \begin{bmatrix} \mathbf{1}_{n_\ell} \\ \chi_{I,\text{eq}} \end{bmatrix} \\ -k_I C^\top L(t) \mathbf{q}(\xi_{\text{eq}}(t)) \end{bmatrix} \right).$$

(ii) To prove this second result, it is enough to show that, if the bound in (5.12) holds, then there exists no 4-tuple $(\beta(t), w_1(t), w_2(t), \chi_I)$, with $\beta(t) \in \mathbb{R}$, $w_1(t), w_2(t) \in K(\mathbf{q}(\xi(t)))$, and $\chi_I \in \mathbb{R}^{n-n_\ell}$, other than $(1, \mathbf{q}((\xi_0 + t)\mathbf{1}_n), \mathbf{q}((\xi_0 + t)\mathbf{1}_n), \mathbf{1}_{n-n_\ell})$, $\xi_0 \in \mathbb{R}$, such that the following equality holds:

$$\begin{bmatrix} \beta(t)\mathbf{1}_n \\ \mathbf{0} \end{bmatrix} = \begin{bmatrix} -k_P L(t) w_1(t) + \begin{bmatrix} \mathbf{1}_{n_\ell} \\ \chi_I \end{bmatrix} \\ -k_I C^\top L(t) w_2(t) \end{bmatrix}. \quad (\text{C.58})$$

To this end, in what follows, we analyze separately the following cases: (1) $\beta(t) \equiv 0$ and $\xi_i \neq k_i\Delta - \frac{\Delta}{2}$ for all $i \in \{1, \dots, n\}$; (2) $\beta(t) \equiv 0$ and $\xi_i = k_i\Delta - \frac{\Delta}{2}$ for (at least) one $i \in \{1, \dots, n\}$; and (3) $\beta(t) \not\equiv 0$.

(1) $\beta(t) \equiv 0$ and $\xi_i \neq k_i\Delta - \frac{\Delta}{2}$ for all $i \in \{1, \dots, n\}$: In this case, the existence of an equilibrium point for the kinematic coordination error dynamics (5.11) is equivalent to the existence of a pair (\mathbf{w}, χ_I) , with $\mathbf{w} \in K(\mathbf{q}(\xi))$ and $\chi_I \in \mathbb{R}^{n-n_\ell}$, such that the following equality holds:

$$\mathbf{0} = \begin{bmatrix} -k_P \mathbf{L}(t) \mathbf{w} + \begin{bmatrix} \mathbf{1}_{n_\ell} \\ \chi_I \end{bmatrix} \\ -k_I \mathbf{C}^\top \mathbf{L}(t) \mathbf{w} \end{bmatrix}. \quad (\text{C.59})$$

Following similar derivations as in the proof of Lemma 5, it can be shown that existence of a pair (\mathbf{w}, χ_I) satisfying (C.59) is equivalent to the existence of a vector \mathbf{w} , $\mathbf{w} \in K(\mathbf{q}(\xi))$, such that the following equality is satisfied:

$$\mathbf{L}(t) \mathbf{w} - \begin{bmatrix} \frac{1}{k_P} \mathbf{1}_{n_\ell} \\ \mathbf{0} \end{bmatrix} = \mathbf{0}. \quad (\text{C.60})$$

Since $\mathbf{L}(t)\mathbf{1}_n = \mathbf{0}$, $\mathbf{L}(t) = \mathbf{L}^\top(t)$, and $\mathbf{L}(t) \geq \mathbf{0}$, it follows that the vector $\begin{bmatrix} \mathbf{1}_{n_\ell} \\ \mathbf{0} \end{bmatrix} \in \mathbb{R}^n$ is not in the column space of any admissible $\mathbf{L}(t)$. Hence, equality (C.60) does not hold for any vector $\mathbf{w} \in \mathbb{R}^n$.

(2) $\beta(t) \equiv 0$ and $\xi_i = k_i\Delta - \frac{\Delta}{2}$ for (at least) one $i \in \{1, \dots, n\}$: In this case, the existence of an equilibrium point for the kinematic coordination error dynamics (5.11) is equivalent to the existence of a triple $(\mathbf{w}_1, \mathbf{w}_2, \chi_I)$, with $\mathbf{w}_1, \mathbf{w}_2 \in K(\mathbf{q}(\xi))$ and $\chi_I \in \mathbb{R}^{n-n_\ell}$, such that the following equality holds:

$$\mathbf{0} = \begin{bmatrix} -k_P \mathbf{L}(t) \mathbf{w}_1 + \begin{bmatrix} \mathbf{1}_{n_\ell} \\ \chi_I \end{bmatrix} \\ -k_I \mathbf{C}^\top \mathbf{L}(t) \mathbf{w}_2 \end{bmatrix}. \quad (\text{C.61})$$

We first consider the first n rows of equality (C.61) and multiply them on the left by \mathbf{C}^\top to obtain $-k_P \mathbf{C}^\top \mathbf{L}(t) \mathbf{w}_1 + \chi_I = \mathbf{0}$. Then, noting that the last $(n-n_\ell)$ rows of (C.61) imply that $\mathbf{C}^\top \mathbf{L}(t) \mathbf{w}_2 = \mathbf{0}$, it follows that equality (C.61) can be satisfied only if the following equality holds:

$$\mathbf{C}^\top \mathbf{L}(t) (\mathbf{w}_1 - \mathbf{w}_2) - \frac{1}{k_P} \chi_I = \mathbf{0}. \quad (\text{C.62})$$

We can now multiply equality (C.62) on the left by $\mathbf{1}_{n-n_\ell}^\top$ to obtain

$$\mathbf{1}_{n-n_\ell}^\top \mathbf{C}^\top \mathbf{L}(t) (\mathbf{w}_1 - \mathbf{w}_2) - \frac{1}{k_P} \mathbf{1}_{n-n_\ell}^\top \chi_I = \mathbf{0} \quad (\text{C.63})$$

and, noting that from equality (C.61) it follows that $n_\ell + \mathbf{1}_{n-n_\ell}^\top \chi_I = \mathbf{0}$ (which has been obtained by

multiplying the first n rows of (C.61) on the left by $\mathbf{1}_n^\top$, we can rewrite equality (C.63) as

$$\frac{1}{k_P} n_\ell = \mathbf{1}_{n-n_\ell}^\top \mathbf{C}^\top \mathbf{L}(t) (\mathbf{w}_2 - \mathbf{w}_1). \quad (\text{C.64})$$

The right-hand side of this equality can be bounded as

$$|\mathbf{1}_{n-n_\ell}^\top \mathbf{C}^\top \mathbf{L}(t) (\mathbf{w}_2 - \mathbf{w}_1)| \leq 2n_\ell(n - n_\ell)\Delta.$$

If the step size of the quantizers is bounded as in (5.12), then we have

$$|\mathbf{1}_{n-n_\ell}^\top \mathbf{C}^\top \mathbf{L}(t) (\mathbf{w}_2 - \mathbf{w}_1)| \leq \frac{1}{k_P} n_\ell,$$

which implies that no vectors \mathbf{w}_1 and \mathbf{w}_2 satisfy equality (C.64). In turn, this implies that, if the bound in (5.12) is satisfied, then there is no triple $(\mathbf{w}_1, \mathbf{w}_2, \chi_I)$ such that equality (C.61) holds.

- (3) $\beta(t) \not\equiv 0$: We start by noting that, in this case, the existence of an equilibrium point for the kinematic coordination error dynamics (5.11) requires that, at any time t' between ‘‘quantization jumps’’, there exist a triple $(\beta(t'), \mathbf{w}(t'), \chi_I)$, with $\beta(t') \in \mathbb{R}$, $\mathbf{w}(t') \in K(\mathbf{q}(\xi(t')))$, and $\chi_I \in \mathbb{R}^{n-n_\ell}$, such that the following equality holds:

$$\begin{bmatrix} \beta(t') \mathbf{1}_n \\ \mathbf{0} \end{bmatrix} = \begin{bmatrix} -k_P \mathbf{L}(t') \mathbf{w}(t') + [\mathbf{1}_{n_\ell} \\ \chi_I] \\ -k_I \mathbf{C}^\top \mathbf{L}(t') \mathbf{w}(t') \end{bmatrix}. \quad (\text{C.65})$$

Following again similar derivations as in the proof of Lemma 5, it can be shown that existence of triple $(\beta(t'), \mathbf{w}(t'), \chi_I)$ satisfying equality (C.65) is equivalent to the existence of a pair $(\beta(t'), \mathbf{w}(t'))$, with $\beta(t') \in \mathbb{R}$ and $\mathbf{w}(t') \in K(\mathbf{q}(\xi(t')))$, such that the following equality is satisfied:

$$\mathbf{L}(t') \mathbf{w}(t') - \left[\begin{smallmatrix} \frac{\beta(t')-1}{k_P} \mathbf{1}_{n_\ell} \\ \mathbf{0} \end{smallmatrix} \right] = \mathbf{0}. \quad (\text{C.66})$$

Since $\mathbf{L}(t) \mathbf{1}_n = \mathbf{0}$, $\mathbf{L}(t) = \mathbf{L}^\top(t)$, and $\mathbf{L}(t) \geq \mathbf{0}$, it follows that the vector $\left[\begin{smallmatrix} \mathbf{1}_{n_\ell} \\ \mathbf{0} \end{smallmatrix} \right] \in \mathbb{R}^n$ is not in the column space of any admissible $\mathbf{L}(t)$. Hence, equality (C.66) can hold only if $\beta(t') = 1$. Moreover, if the network topology is connected at all times, then the null space of $\mathbf{L}(t)$ is equal to the span of $\mathbf{1}_n$ for all $t \geq 0$, which implies that, in this case, equality (C.66) can hold only if $\xi(t') \in \text{span}\{\mathbf{1}_n\}$. This implies that, between ‘‘quantization jumps’’, the coordination state vector $\xi(t)$ is required to evolve continuously according to $\dot{\xi}(t) \in \text{span}\{\mathbf{1}_n\}$ and $\dot{\xi}(t) = \mathbf{1}_n$. From equality (C.65), it further follows that

the integral state $\chi_I = \mathbf{1}_{n-n_\ell}$ is required for $\xi(t) \in \text{span}\{\mathbf{1}_n\}$ and $\dot{\xi}(t) = \mathbf{1}_n$ to hold simultaneously. Finally, because the term $\mathbf{L}(t)\mathbf{w}(t)$ is bounded at the “quantization jumps”, the coordination state vector $\xi(t)$ is continuous for all $t \geq 0$, implying that equality (C.65) only holds if $\beta(t) = 1$ for almost every $t \geq 0$, $\xi(t) = (\xi_0 + t)\mathbf{1}_n$ for some $\xi_0 \in \mathbb{R}$ and all $t \geq 0$, and $\chi_I = \mathbf{1}_{n-n_\ell}$.

We can thus conclude that, if the information flow $\Gamma(t)$ is connected at all times and the step size of the quantizers is bounded as in (5.12), then $\zeta_{\text{eq}} = \mathbf{0}$ is the only equilibrium point of the closed-loop kinematic coordination error dynamics (5.11). \square

References

- [1] A. P. AGUIAR AND J. P. HESPAÑHA, *Position tracking of underactuated vehicles*, in American Control Conference, Denver, CO, June 2003, pp. 1988–1993. 5
- [2] A. P. AGUIAR, J. P. HESPAÑHA, AND P. V. KOKOTOVIĆ, *Performance limitations in reference tracking and path following for nonlinear systems*, Automatica, 44 (2008), pp. 598–610. 11
- [3] A. P. AGUIAR, I. KAMINER, R. GHABCHELOO, A. M. PASCOAL, E. XARGAY, N. HOVAKIMYAN, C. CAO, AND V. DOBROKHODOV, *Time-coordinated path following of multiple UAVs over time-varying networks using \mathcal{L}_1 adaptation*, in AIAA Guidance, Navigation and Control Conference, Honolulu, HI, August 2008. AIAA-2008-7131. 9, 49
- [4] A. P. AGUIAR AND A. M. PASCOAL, *Coordinated path-following control for nonlinear systems with logic-based communication*, in IEEE Conference on Decision and Control, New Orleans, LA, December 2007, pp. 1473–1479. 7
- [5] S. A. AL-HIDDABI AND N. H. McCCLAMROCH, *Tracking and maneuver regulation control for nonlinear non-minimum phase systems*, IEEE Transactions on Control System Technology, 10 (2002), pp. 780–792. 5
- [6] M. ARCAK, *Passivity as a design tool for group coordination*, IEEE Transactions on Automatic Control, 52 (2007), pp. 1380–1390. 1, 26
- [7] F. ARRICIELLO, S. CHIAVERINI, AND T. I. FOSSEN, *Formation control of marine surface vessels using the null-space-based behavioral control*, in Group Coordination and Cooperative Control, K. Y. Pettersen, J. T. Gravdahl, and H. Nijmeijer, eds., vol. 336 of Lecture Notes in Control and Information Sciences, Springer-Verlag Berlin Heidelberg, 2006, pp. 1–19. 2
- [8] H. BAI, M. ARCAK, AND J. T. WEN, *Adaptive design for reference velocity recovery in motion coordination*, Systems & Control Letters, 57 (2008), pp. 602–610. 8
- [9] R. W. BEARD, J. LAWTON, AND F. Y. HADAEGH, *A coordination architecture for spacecraft formation control*, IEEE Transactions on Control System Technology, 9 (2001), pp. 777–790. 2
- [10] R. W. BEARD, T. W. McLAIN, D. B. NELSON, D. KINGSTON, AND D. JOHANSON, *Decentralized cooperative aerial surveillance using fixed-wing miniature UAVs*, Proceedings of the IEEE, 94 (2006), pp. 1306–1324. 2
- [11] S. BHATTACHARYA AND T. BAŞAR, *Graph-theoretic approach for connectivity maintenance in mobile networks in the presence of a jammer*, in IEEE Conference on Decision and Control, Atlanta, GA, December 2010, pp. 3560–3565. 109
- [12] S. BHATTACHARYA, T. BAŞAR, AND N. HOVAKIMYAN, *Singular surfaces in multi-agent connectivity maintenance games*, in IEEE Conference on Decision and Control, Orlando, FL, December 2011, pp. 261–266. 109
- [13] N. BIGGS, *Algebraic Graph Theory*, Cambridge University Press, New York, NY, 1993. 26

- [14] R. L. BISHOP, *There is more than one way to frame a curve*, The American Mathematical Monthly, 82 (1975), pp. 246–251. 20
- [15] V. D. BLONDEL, J. M. HENDRICKX, A. OLSHEVSKY, AND J. N. TSITSIKLIS, *Convergence in multiagent coordination, consensus, and flocking*, in IEEE Conference on Decision and Control, Seville, Spain, December 2005, pp. 2996–3000. 1
- [16] S. BOCCALETI, V. LATORA, Y. MORENO, M. CHAVEZ, AND D.-U. HWANG, *Complex networks: Structure and dynamics*, Physics Reports, 424 (2006), pp. 175–308. 7
- [17] M. BREIVIK, V. E. HOVSTEIN, AND T. I. FOSSEN, *Ship formation control: A guided leader-follower approach*, in IFAC World Congress, Seoul, South Korea, July 2008. 2
- [18] M. CAO, D. A. SPIELMAN, AND A. S. MORSE, *A lower bound on convergence of a distributed network consensus algorithm*, in IEEE Conference on Decision and Control, Seville, Spain, December 2005, pp. 2356–2361. 1
- [19] R. CARLI, A. CHIUSO, L. SCHENATO, AND S. ZAMPIERI, *A PI consensus controller for networked clocks synchronization*, in IFAC World Congress, Seoul, South Korea, July 2008. 8
- [20] A. CENSI AND R. M. MURRAY, *Real-valued average consensus over noisy quantized channels*, in American Control Conference, St. Louis, MO, June 2009, pp. 4361–4366. 8
- [21] F. CERAGIOLI, C. DE PERSIS, AND P. FRASCA, *Discontinuities and hysteresis in quantized average consensus*, Automatica, 47 (2011), pp. 1916–1928. 8, 71
- [22] M. R. CLEMENT, E. BOURAKOV, K. D. JONES, AND V. DOBROKHODOV, *Exploring network-centric information architectures for unmanned systems control and data dissemination*, in AIAA Infotech@Aerospace, Seattle, WA, April 2009. AIAA-2009-1999. 97
- [23] P. DE LELLIS, M. DI BERNARDO, F. GAROFALO, AND M. PORFIRI, *Evolution of complex networks via edge snapping*, IEEE Transactions on Circuits and Systems, 57 (2010), pp. 2132–2143. 85
- [24] P. DE LELLIS, M. DI BERNARDO, AND M. PORFIRI, *Pinning control of complex networks via edge snapping*, Chaos, 21 (2011), p. 033119. 85
- [25] C. DE PERSIS, *On the passivity approach to quantized coordination problems*, in IEEE Conference on Decision and Control, Orlando, FL, December 2011, pp. 1086–1091. 8
- [26] F. DÍAZ DEL RÍO, G. JIMÉNEZ, J. L. SEVILLANO, C. AMAYA, AND A. CIVIT BALCELLS, *A new method for tracking memorized paths: Application to unicycle robots*, in Mediterranean Conference on Control and Automation, Lisbon, Portugal, July 2002. 5
- [27] V. DOBROKHODOV, I. KAMINER, K. D. JONES, AND R. GHABCHELOO, *Vision-based tracking and motion estimation for moving targets using small UAVs*, Journal of Guidance, Control and Dynamics, 31 (2008), pp. 907–917. 101
- [28] V. DOBROKHODOV, I. KAMINER, I. KITSIOS, E. XARGAY, N. HOVAKIMYAN, C. CAO, I. M. GREGORY, AND L. VALAVANI, *Experimental validation of \mathcal{L}_1 adaptive control: The Rohrs counterexample in flight*, Journal of Guidance, Control and Dynamics, 34 (2011), pp. 1311–1328. 29, 30
- [29] W. B. DUNBAR AND R. M. MURRAY, *Distributed receding horizon control for multi-vehicle formation stabilization*, Automatica, 42 (2006), pp. 549–558. 1
- [30] M. EGERSTEDT AND X. HU, *Formation constrained multi-agent control*, IEEE Transactions on Robotics and Automation, 17 (2001), pp. 947–951. 1, 7
- [31] M. EGERSTEDT, X. HU, AND A. STOTSKY, *Control of mobile platforms using a virtual vehicle approach*, IEEE Transactions on Automatic Control, 46 (2001), pp. 1777–1782. 5

- [32] P. ENCARNAÇÃO, *Nonlinear Path Following Control Systems for Ocean Vehicles*, PhD thesis, Instituto Superior Técnico, Lisbon, Portugal, 2002. 5
- [33] P. ENCARNAÇÃO AND A. M. PASCOAL, *Combined trajectory tracking and path following: An application to the coordinated control of autonomous marine craft*, in IEEE Conference on Decision and Control, Orlando, FL, December 2001, pp. 964–969. 6
- [34] L. FANG, P. J. ANTSAKLIS, AND A. TZIMAS, *Asynchronous consensus protocols: Preliminary results, simulations and open questions*, in IEEE Conference on Decision and Control, Seville, Spain, December 2005, pp. 2194–2199. 1
- [35] J. A. FAX AND R. M. MURRAY, *Information flow and cooperative control of vehicle formations*, IEEE Transactions on Automatic Control, 49 (2004), pp. 1465–1476. 1
- [36] M. T. FLYNN, R. JUERGENS, AND T. L. CANTRELL, *Employing ISR: SOF best practices*, Joint Force Quarterly, 50 (2008), pp. 56–61. 97
- [37] T. I. FOSSEN, *Marine Control Systems: Guidance, Navigation and Control of Ships, Rigs and Underwater Vehicles*, Marine Cybernetics, Trondheim, Norway, 2002. 2
- [38] R. A. FREEMAN, P. YANG, AND K. M. LYNCH, *Stability and convergence properties of dynamic average consensus estimators*, in IEEE Conference on Decision and Control, San Diego, CA, December 2006, pp. 398–403. 8
- [39] D. J. GATES, *Nonlinear path following method*, Journal of Guidance, Control and Dynamics, 33 (2010), pp. 321–332. 5
- [40] R. GHACHELOO, A. P. AGUIAR, A. M. PASCOAL, C. SILVESTRE, I. KAMINER, AND J. P. HES-PANHA, *Coordinated path-following in the presence of communication losses and delays*, SIAM Journal on Control and Optimization, 48 (2009), pp. 234–265. 6
- [41] R. GHACHELOO, I. KAMINER, A. P. AGUIAR, AND A. M. PASCOAL, *A general framework for multiple vehicle time-coordinated path following control*, in American Control Conference, St. Louis, MO, June 2009, pp. 3071–3076. 26
- [42] R. GHACHELOO, A. M. PASCOAL, C. SILVESTRE, AND I. KAMINER, *Coordinated path following control of multiple wheeled robots using linearization techniques*, International Journal of Systems Science, 37 (2006), pp. 399–414. 1, 2
- [43] O. HÁJEK, *Discontinuous differential equations, I*, Journal of Differential Equations, 32 (1979), pp. 149–170. 71, 72, 135
- [44] A. J. HANSON AND H. MA, *Parallel transport approach to curve framing*, Tech. Report TR425, Computer Science Department, Indiana University, 1995. 20, 35
- [45] R. HINDMAN AND J. HAUSER, *Maneuver modified trajectory tracking*, in International Symposium on the Mathematical Theory of Networks and Systems, St. Louis, MO, June 1996. 5, 6
- [46] I.-A. F. IHLE, *Coordinated Control of Marine Craft*, PhD thesis, Norwegian University of Science and Technology, Trondheim, Norway, September 2006. 2, 6
- [47] I.-A. F. IHLE, J. JOUFFROY, AND T. I. FOSSEN, *Robust formation control of marine craft using Lagrange multipliers*, in Group Coordination and Cooperative Control, K. Y. Pettersen, J. T. Gravdahl, and H. Nijmeijer, eds., vol. 336 of Lecture Notes in Control and Information Sciences, Springer-Verlag Berlin Heidelberg, 2006, pp. 113–129. 2
- [48] A. JADBABAIE, J. LIN, AND A. S. MORSE, *Coordination of groups of mobile autonomous agents using nearest neighbor rules*, IEEE Transactions on Automatic Control, 48 (2003), pp. 988–1001. 1

- [49] I. KAMINER, A. M. PASCOAL, E. HALLBERG, AND C. SILVESTRE, *Trajectory tracking for autonomous vehicles: An integrated approach to guidance and control*, Journal of Guidance, Control and Dynamics, 21 (1998), pp. 29–38. [1](#), [5](#)
- [50] I. KAMINER, A. M. PASCOAL, E. XARGAY, N. HOVAKIMYAN, C. CAO, AND V. DOBROKHODOV, *Path following for unmanned aerial vehicles using \mathcal{L}_1 adaptive augmentation of commercial autopilots*, Journal of Guidance, Control and Dynamics, 33 (2010), pp. 550–564. [9](#), [29](#), [30](#), [31](#)
- [51] I. KAMINER, O. A. YAKIMENKO, A. M. PASCOAL, AND R. GHACHELOO, *Path generation, path following and coordinated control for time-critical missions of multiple UAVs*, in American Control Conference, Minneapolis, MN, June 2006, pp. 4906–4913. [2](#), [6](#), [7](#), [8](#), [9](#), [25](#), [27](#), [45](#)
- [52] A. KASHYAP, T. BAŞAR, AND R. SRIKANT, *Quantized consensus*, Automatica, 43 (2007), pp. 1192–1203. [8](#)
- [53] T. KEVICZKY, F. BORRELLI, K. FREGENE, D. GODBOLE, AND G. J. BALAS, *Decentralized receding horizon control and coordination of autonomous vehicle formations*, IEEE Transactions on Control System Technology, 16 (2008), pp. 19–33. [1](#)
- [54] H. K. KHALIL, *Nonlinear Systems*, Prentice Hall, Englewood Cliffs, NJ, 2002. [119](#), [121](#), [122](#), [124](#), [127](#), [136](#)
- [55] Y. KIM AND M. MESBAHI, *On maximizing the second smallest eigenvalue of state-dependent graph Laplacian*, IEEE Transactions on Automatic Control, 51 (2006), pp. 116–120. [1](#)
- [56] S. KOTZ AND S. NADARAJAH, *Extreme Value Distributions*, Imperial College Press, London. UK, 2000. [89](#)
- [57] Y. KUWATA AND J. P. HOW, *Cooperative distributed robust trajectory optimization using receding horizon MILP*, IEEE Transactions on Control System Technology, 19 (2011), pp. 423–431. [1](#)
- [58] E. KYRKJEBØ AND K. Y. PETTERSEN, *Ship replenishment using synchronization control*, in IFAC Conference on Manoeuvering and Control of Marine Craft, Girona, Spain, September 2003. [7](#)
- [59] E. KYRKJEBØ, M. WONDERGEM, K. Y. PETTERSEN, AND H. NIJMEIJER, *Experimental results on synchronization control of ship rendezvous operations*, in IFAC Conference on Control Applications in Marine Systems, Ancona, Italy, July 2004, pp. 453–458. [7](#)
- [60] L. LAPIERRE, D. SOETANTO, AND A. M. PASCOAL, *Coordinated motion control of marine robots*, in IFAC Conference on Manoeuvering and Control of Marine Craft, Girona, Spain, September 2003. [2](#), [6](#), [9](#), [11](#)
- [61] ———, *Non-singular path-following control of a unicycle in the presence of parametric modeling uncertainties*, International Journal of Robust and Nonlinear Control, 16 (2006), pp. 485–503. [5](#), [18](#), [19](#)
- [62] D. A. LAWRENCE, E. W. FREW, AND W. J. PISANO, *Lyapunov vector fields for autonomous unmanned aircraft flight control*, Journal of Guidance, Control and Dynamics, 31 (2008), pp. 1220–1229. [5](#)
- [63] T. LEE, M. LEOK, AND N. H. MCCLAMROCH, *Control of complex maneuvers for a quadrotor UAV using geometric methods on $\text{SE}(3)$* , IEEE Transactions on Automatic Control, (2010). Submitted. Available online: [arXiv:1003.2005v4](https://arxiv.org/abs/1003.2005v4). [33](#), [112](#)
- [64] Z. LIN, B. A. FRANCIS, AND M. MAGGIORE, *State agreement for continuous-time coupled nonlinear systems*, SIAM Journal on Control and Optimization, 46 (2007), pp. 288–307. [1](#), [27](#)
- [65] A. LORÍA AND E. PANTELEY, *Uniform exponential stability of linear time-varying systems: Revisited*, Systems & Control Letters, 47 (2002), pp. 13–24. [122](#)

- [66] T. W. McLAIN AND R. W. BEARD, *Coordination variables, coordination functions, and cooperative timing missions*, Journal of Guidance, Control and Dynamics, 28 (2005), pp. 150–161. 1
- [67] M. MESBAHI, *On state-dependent dynamic graphs and their controllability properties*, IEEE Transactions on Automatic Control, 50 (2005), pp. 387–392. 1
- [68] M. MESBAHI AND F. Y. HADAEGH, *Formation flying control of multiple spacecraft via graphs, matrix inequalities, and switching*, Journal of Guidance, Control and Dynamics, 24 (2001), pp. 369–377. 2
- [69] A. MICAELLI AND C. SAMSON, *Trajectory tracking for unicycle-type and two-steering-wheels mobile robot*, Tech. Report 2097, INRIA, Sophia-Antipolis, France, November 1993. 4, 5, 19
- [70] L. MOREAU, *Stability of multiagent systems with time-dependent communication links*, IEEE Transactions on Automatic Control, 50 (2005), pp. 169–182. 1
- [71] S. MORRIS AND E. W. FREW, *Cooperative tracking of moving targets by teams of autonomous unmanned air vehicles*, Tech. Report FA9550-04-C-0107, MLB Company and University of Colorado, July 2004. 101
- [72] A. NEDIĆ, A. OLSHEVSKY, A. OZDAGLAR, AND J. N. TSITSIKLIS, *On distributed averaging algorithms and quantization effects*, IEEE Transactions on Automatic Control, 54 (2009), pp. 2506–2517. 8
- [73] D. R. NELSON, D. B. BARBER, T. W. McLAIN, AND R. W. BEARD, *Vector field path following for miniature air vehicles*, Transactions on Robotics, 23 (2007), pp. 519–529. 5
- [74] D. NETZER AND A. BORDETSKY, *TNT testbed for self-organizing tactical networking and collaboration*, in International Command and Control Research and Technology Symposium, Washington, DC, June 2009. 95
- [75] R. OLFAKI SABER, W. B. DUNBAR, AND R. M. MURRAY, *Cooperative control of multi-vehicle systems using cost graphs and optimization*, in American Control Conference, Denver, CO, June 2003, pp. 2217–2222. 1
- [76] R. OLFAKI SABER, J. A. FAX, AND R. M. MURRAY, *Consensus and cooperation in networked multi-agent systems*, Proceedings of the IEEE, 95 (2007), pp. 215–233. 7
- [77] R. OLFAKI SABER AND R. M. MURRAY, *Consensus problems in networks of agents with switching topology and time-delays*, IEEE Transactions on Automatic Control, 49 (2004), pp. 1520–1533. 1
- [78] J. OUSINGSAWAT AND M. E. CAMPBELL, *Optimal cooperative reconnaissance using multiple vehicles*, Journal of Guidance, Control and Dynamics, 30 (2007), pp. 122–132. 1
- [79] E. PANTELEY AND A. LORÍA, *Uniform exponential stability for families of linear time-varying systems*, in IEEE Conference on Decision and Control, Sydney, Australia, December 2000, pp. 1948–1953. 122
- [80] S. PARK, J. DEYST, AND J. P. HOW, *Performance and Lyapunov stability of a nonlinear path-following guidance method*, Journal of Guidance, Control and Dynamics, 30 (2007), pp. 1718–1728. 5
- [81] F. L. PEREIRA AND J. B. DE SOUSA, *Coordinated control of networked vehicles: An autonomous underwater system*, Automation and Remote Control, 65 (2004), pp. 1037–1045. 2
- [82] E. PEYAMI AND T. I. FOSSEN, *A Lagrangian framework to incorporate positional and velocity constraints to achieve path-following control*, in IEEE Conference on Decision and Control, Orlando, FL, December 2011, pp. 3940–3945. 5
- [83] ———, *Motion control of marine craft using virtual positional and velocity constraints*, in International Conference on Control and Automation, Santiago, Chile, December 2011, pp. 410–416. 5

- [84] Q.-C. PHAM AND J.-J. SLOTINE, *Stable concurrent synchronization in dynamic system networks*, Neural Networks, 20 (2007), pp. 62–77. 1
- [85] A. PIKOVSKY, M. ROSENBLUM, AND J. KURTHS, *Synchronization: A Universal Concept in Nonlinear Sciences*, Cambridge University Press, Cambridge, UK, 2001. 1
- [86] W. REN, *Formation keeping and attitude alignment for multiple spacecraft through local interactions*, Journal of Guidance, Control and Dynamics, 30 (2007), pp. 633–638. 2
- [87] W. REN AND N. SORENSEN, *Distributed coordination architecture for multi-robot formation control*, Robotics and Autonomous Systems, 56 (2008), pp. 324–333. 2
- [88] E. SCHOLTE AND M. E. CAMPBELL, *Robust nonlinear model predictive control with partial state information*, IEEE Transactions on Control System Technology, 16 (2008), pp. 636–651. 1
- [89] T. SCHOUWENAARS, J. P. HOW, AND E. FERON, *Decentralized cooperative trajectory planning of multiple aircraft with hard safety guarantees*, in AIAA Guidance, Navigation and Control Conference, Providence, RI, August 2004. AIAA-2004-5141. 1
- [90] R. SEPULCHRE, D. PALEY, AND N. LEONARD, *Collective Motion and Oscillator Synchronization*, vol. 309 of Lecture Notes in Control and Information Sciences, Springer-Verlag Berlin, 2005, pp. 189–206. 1
- [91] R. SKJETNE, T. I. FOSSEN, AND P. V. KOKOTOVIĆ, *Robust output maneuvering for a class of nonlinear systems*, Automatica, 40 (2004), pp. 373–383. 5
- [92] R. SKJETNE, I.-A. F. IHLE, AND T. I. FOSSEN, *Formation control by synchronizing multiple maneuvering systems*, in IFAC Conference on Manoeuvering and Control of Marine Craft, Girona, Spain, September 2003. 6
- [93] R. SKJETNE, S. MOI, AND T. I. FOSSEN, *Nonlinear formation control of marine craft*, in IEEE Conference on Decision and Control, vol. 2, Las Vegas, NV, December 2002, pp. 1699–1704. 2, 6
- [94] R. SKJETNE, A. R. TEEL, AND P. V. KOKOTOVIĆ, *Stabilization of sets parameterized by a single variable: Application to ship maneuvering*, in Proceedings of the 15th International Symposium on Mathematical Theory of Networks and Systems, Notre Dame, IN, August 2002. 5, 6
- [95] D. SOETANTO, L. LAPIERRE, AND A. M. PASCOAL, *Adaptive, non-singular path-following control of dynamic wheeled robots*, in International Conference on Advanced Robotics, Coimbra, Portugal, June–July 2003, pp. 1387–1392. 5, 6
- [96] Y. D. SONG, Y. LI, AND X. H. LIAO, *Orthogonal transformation based robust adaptive close formation control of multi-UAVs*, in American Control Conference, vol. 5, Portland, OR, June 2005, pp. 2983–2988. 2
- [97] D. STEVENSON, M. WHEELER, M. E. CAMPBELL, W. W. WHITACRE, R. T. RYSDYK, AND R. WISE, *Cooperative tracking flight test*, in AIAA Guidance, Navigation and Control Conference, Hilton Head, SC, August 2007. AIAA-2007-6756. 1
- [98] D. J. STILWELL AND B. E. BISHOP, *Platoons of underwater vehicles*, IEEE Control Systems Magazine, 20 (2000), pp. 45–52. 2
- [99] D. J. STILWELL, E. M. BOLLT, AND D. G. ROBERSON, *Sufficient conditions for fast switching synchronization in time-varying network topologies*, SIAM Journal of Applied Dynamical Systems, 5 (2006), pp. 140–156. 1
- [100] D. M. STIPANOVIĆ, G. İNALHAN, R. TEO, AND C. J. TOMLIN, *Decentralized overlapping control of a formation of unmanned aerial vehicles*, Automatica, 40 (2004), pp. 1285–1296. 2

- [101] J. N. TSITSIKLIS AND M. ATHANS, *Convergence and asymptotic agreement in distributed decision problems*, IEEE Transactions on Automatic Control, 29 (1984), pp. 42–50. [1](#)
- [102] E. XARGAY, R. CHOE, N. HOVAKIMYAN, AND I. KAMINER, *Convergence of a PI coordination protocol in networks with switching topology and quantized measurements*, in IEEE Conference on Decision and Control, Maui, HI, December 2012, pp. 6107–6112. [47](#), [49](#), [51](#), [77](#)
- [103] Y. XU AND J. P. HESPAÑHA, *Communication logics for networked control systems*, in American Control Conference, Boston, MA, June–July 2004, pp. 572–577. [82](#)
- [104] ———, *Communication logic design and analysis for networked control systems*, in Current Trends in Nonlinear Systems and Control, L. Menini, L. Zaccarian, and C. T. Abdallah, eds., Systems and Control: Foundations & Applications, Birkhäuser Boston, Cambridge, MA, 2006, pp. 495–514. [7](#)
- [105] J. K. YOOK, D. M. TILBURY, AND N. R. SOPARKAR, *Trading computation and bandwidth: Reducing communication in distributed control systems using state estimators*, IEEE Transactions on Control System Technology, 10 (2002), pp. 503–518. [7](#), [82](#)
- [106] J. YU, S. M. LAVALLE, AND D. LIBERZON, *Rendezvous without coordinates*, IEEE Transactions on Automatic Control, 57 (2012), pp. 421–434. [8](#)